DEPARTMENT OF ELECTRONIC & ELECTRICAL ENGINEERING

University of Strathclyde Engineering

MULTI-STAGE PROCESSING FOR EFFECTIVE SEGMENTATION OF SAR SEA ICE IMAGES

SOUMITRA SAKHALKAR

In the fulfilment of the requirement for the degree of

Master of Philosophy

Centre for Excellence in Signal and Image Processing

Department of Electronic and Electrical Engineering

University of Strathclyde, Glasgow

Supervised by

Doctor Jinchang Ren

Professor Stephen Marshall

June 12, 2018

I would like to dedicate this thesis
to my loving parents and my elder brother,
who have throughout my study, been a
constant source of support, encouragement
and enlightenment.

मि हे सिध्हान्त माझ्या प्रेमळ पालकांना आणि
माझ्या मोठया भावाला सर्मर्पित करू इच्छितो, जे
माझ्या संपूर्ण शिक्षणात, कायम पाठिंबा,
प्रोत्साहन आणि ज्ञान देत आले आहेत।

DECLARATION

This thesis is the result of the author's original research. It has been composed by the author and has not been previously submitted for examination which has led to the award of a degree.

Soumitra Sakhalkar June 2018

ACKNOWLEDGEMENTS

I would like to thank a number of people for their guidance, support and at times encouragement, throughout my course.

Firstly, I would like to thank my parents for firstly supporting me financially and enabling me to achieve this degree. I would also like to thank them and my brother, Utkarsh, for constantly being supportive and understanding to me, especially during tougher times when I doubted myself a lot.

Secondly, I would like to thank my main Supervisor, Dr. Jinchang Ren, for always being supportive to me and advising me of how to be an effective researcher. I would also like to thank my second Supervisor, Prof. Stephen Marshall, for firstly allowing me the opportunity to do my research and guide me in the right direction, when I was straying away from my research. I would also like to thank my internal and external examiners for accepting my research to be awarded MPhil.

I would like to also extend my gratitude to Dr. Hwang and SAMS for funding me partially in my first year, for the Sea Ice project. I would also like to thank Amanda McLean from the Advice Centre at University of Strathclyde, for helping me with my visa problems at the start of my course and making sure that it didn't affect my study.

Lastly, I would like to thank all of my friends (Rob, Chris, Matty, Amy, Cara, Ashley, Suvi, Dani, Becky, Declan, Lisa, Sarah, Jacob, James, Monika, Marion, Salla, Amine and many more!) at the University, the Students Union and elsewhere for always being there for me, in difficult and fun times. For always helping me de-stress as well as accompany me on my many trips to explore Scotland and beyond.

ABSTRACT

Remote Sensing and Earth Observation became a reality, ever since the launch of NASA's first satellite; Landsat-1 in 1972. Subsequently, numerous other satellites were launched such as the TerraSAR, Sentinel-1 etc, which made possible to acquire High-Resolution imagery of remote areas such as the Arctic region. Consequently, with the accessibility to such large amounts of data, it becomes necessary to develop fast, robust and automated image segmentation algorithms to extract key information as opposed to still relying on time consuming manual expert analysis. As a result, in this thesis, effective algorithms are proposed for efficiently segmenting and extracting information from the Synthetic Aperture Radar (SAR) Sea Ice imagery.

Initially, the contributions for improving the quality of the SAR images itself are introduced. Inspired by the advantages of the Adaptive Median filter (AMF) and the Wiener filter, the Modified Adaptive Median filter (MAMF) is proposed. The MAMF uses local image statistics to identify speckle regions and the Minimum Mean Square Error (MMSE) estimator to suppress speckle. The MAMF is applied to various image types, to test its efficiency and robustness and subsequently compared with other existing techniques such as the Bilateral and Local Sigma filters. Furthermore, additional region-based filtering is suggested, which is based on user-defined threshold values for the quantitative parameters used to determine the performance of the filter.

Another important part of extracting key information from the SAR Sea Ice imagery is "Segmentation". A *Region and Condition* based post processing is proposed for the established algorithm, Kernel Graph Cuts (KGC), for acquiring further improved segmentation results. The post processing incorporates algorithms such as Skeletonisation, Morphology and Active Contours. The proposed algorithm is compared against existing techniques such as the Closeness Degree Cut (CDCut) and Level

Sets with Distance Regularisation (DRLSE). Furthermore, a novel Quantitative Analysis technique is proposed which accurately compares the Regional Accuracy of the various segmented regions.

By the use of local statistics of the SAR images used, the MAMF filter effectively suppresses speckle noise without over-compensating for image features. Similarly, the post processing technique uses a combination of Conditional Morphology and Active Contours, to effectively improve the segmented result obtained with the established KGC algorithm. The results are validated against recently-used algorithms, on real-world and sample images acquired through various datasets by performing objective as well as subjective analysis.

CONTENTS

LIST OF FIGURES

LIST OF TABLES

ABBREVIATIONS

AC	Active Contours
AMF	Adaptive Median filter
ASF	Alaska Space Facility
BF	Bilateral filter
CDCut	Closeness Degree Cut
DRLSE	Level Sets with Distance Regularisation
EEI	Edge Enhancing Index
FPI	Feature Preserving Index
FQA	Filter Quantitative Analysis
FSD	Floe Size Distribution
GC	Graph Cuts
GLCP	Gray-Level Co-occurrence Probabilities
GT	Ground Truth
IDPC	Image Detail Preserving Index
KGC	Kernel Graph Cuts
LSF	Local Sigma filter
MAMF	Modified Adaptive Median filter
MMSE	Minimum Mean Square Error
MRF	Markov Random Fields
MSE	Mean Square Error
ORA	Overall Region Accuracy
PCNN	Pulsed-coupled Neural Networks

PSNR Peak Signal to Noise Ratio

RBF Radial Basis Function

RGB Red-Green-Blue

ROC Receiver Operating Characteristic

SAR Synthetic Aperture Radar

SSI Speckle Suppression Index

SSIM Structural Similarity Index

CHAPTER 1

INTRODUCTION

1.1 Research Motivation

Sea Ice segmentation has been an active research field for more than 25 years. Over the years, many techniques have been proposed to obtain a good Segmentation result for the SAR Sea Ice data [1–5]. In recent years, it has become an increasingly important research topic, primarily owing to the continuing decline of the Sea Ice regions, particularly in the Arctic [6, 7]. This has been largely linked to the increasing number of newer sea ice regions [8] and climate change [9],which is speculatively linked to greenhouse gases [10].

Due to this increasing decline in the Sea Ice regions, it has become even more important in recent years to develop a better understanding of the various environmental and social impacts on these Sea Ice regions like the Arctic.

SAR has been widely used for obtaining the Sea Ice images for several years, owing primarily due to its advantages of not been as affected by harsh weather conditions, illumination changes due to lack of sunlight or cloud cover and its ability to cover large inaccessible areas, such as the Arctic [11]. However, even the most modern SAR images are affected by the phenomenon called ”speckle”, owing to the coherent processing in which they are formed [12]. Speckle is said to be signal dependant and the presence of which affects even the most robust segmentation algorithm’s accuracy.

Figures 1.1 and 1.2, show examples of how the SAR images are affected by speckle. As seen from the figures, it can be seen how the effect of speckle degrades the object

boundaries in the images, thus restricting a segmentation algorithm in detecting different Sea Ice regions and thus affecting the Floe Size Distribution (FSD) calculation.

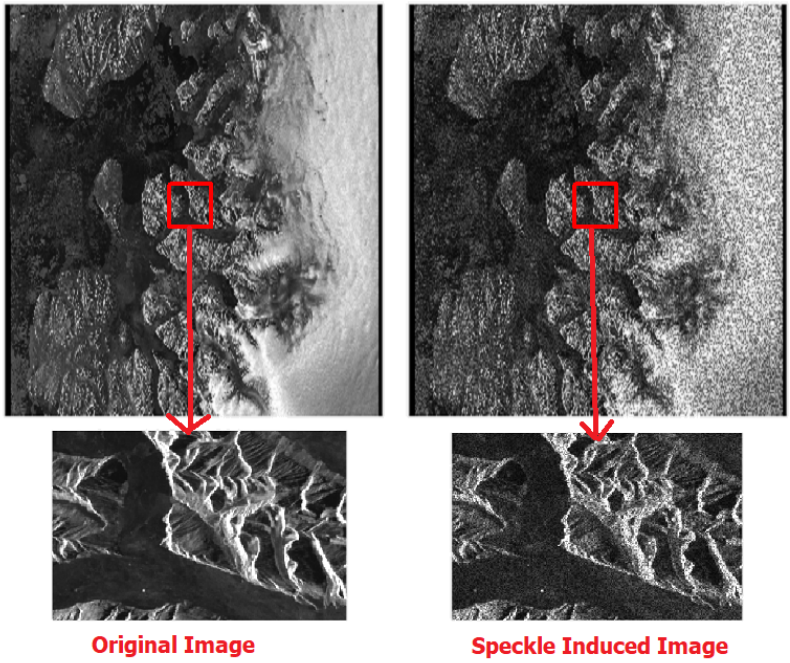

Figure 1.1: Effects of speckle on SAR image: Example 1

FSD is an important parameter used in determining the processes that govern the evolution of Sea Ice as well as validating the parameterization in the Sea Ice models. The models estimate the FSD through the break-up of the various Sea Ice floes and consequently the FSD is then used to calculate the thermodynamic melt [13, 14]. The very first Sea Ice FSD was studied by Rothrock and Thorndike, using aerial photographs [15]. But over the years, due to the advancement in technology and advantages of SAR, FSD can now be achieved using visible satellite and SAR imagery as well [16, 17]. While the aerial photos and visible satellite imagery are restricted and primarily used for examining the effect of lateral melt of small floes, SAR, due to its various advantages can provide flexibility of capturing images even through cloud and darkness and thus making possible the monitoring of continuous evolution of FSD [18].

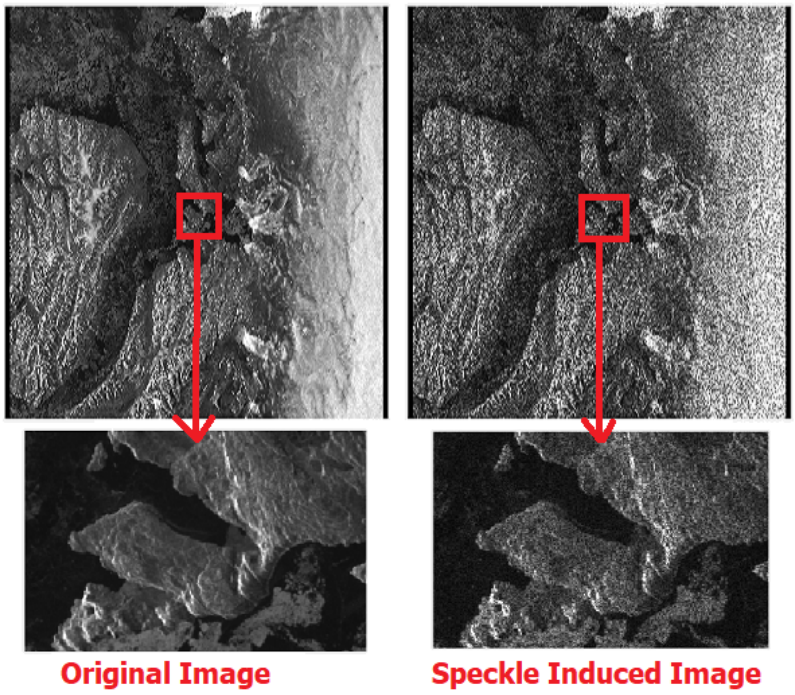

Figure 1.2: Effects of speckle on SAR image: Example 2

Figure 1.3 further explains how the FSD is calculated after acquiring segmentation of the Sea Ice regions.

Furthermore, even with the high demand in literature, scientists and experts still rely on manual segmentation of regions for acquiring an accurate Segmentation of the Sea Ice regions. This can be linked primarily due to the lack of accurate and robust algorithms for finding the Segmentation. Moreover, the Sea Ice regions vary drastically over different periods of the year, due to fracturing of regions caused by peak summer, gale force winds and collision between neighbouring Sea Ice floes [13, 19, 20]. Figure 1.4, shows an example of how the regions vary drastically between early winter and mid-summer period of the year.

As seen from the Figure 1.4, it is important for the Segmentation algorithm to adjust its parameters to changing complexity of the region being assessed. This itself is a challenging task and has been investigated even more in recent years.

Furthermore, it is important to get an accurate measurement of a segmentation al-

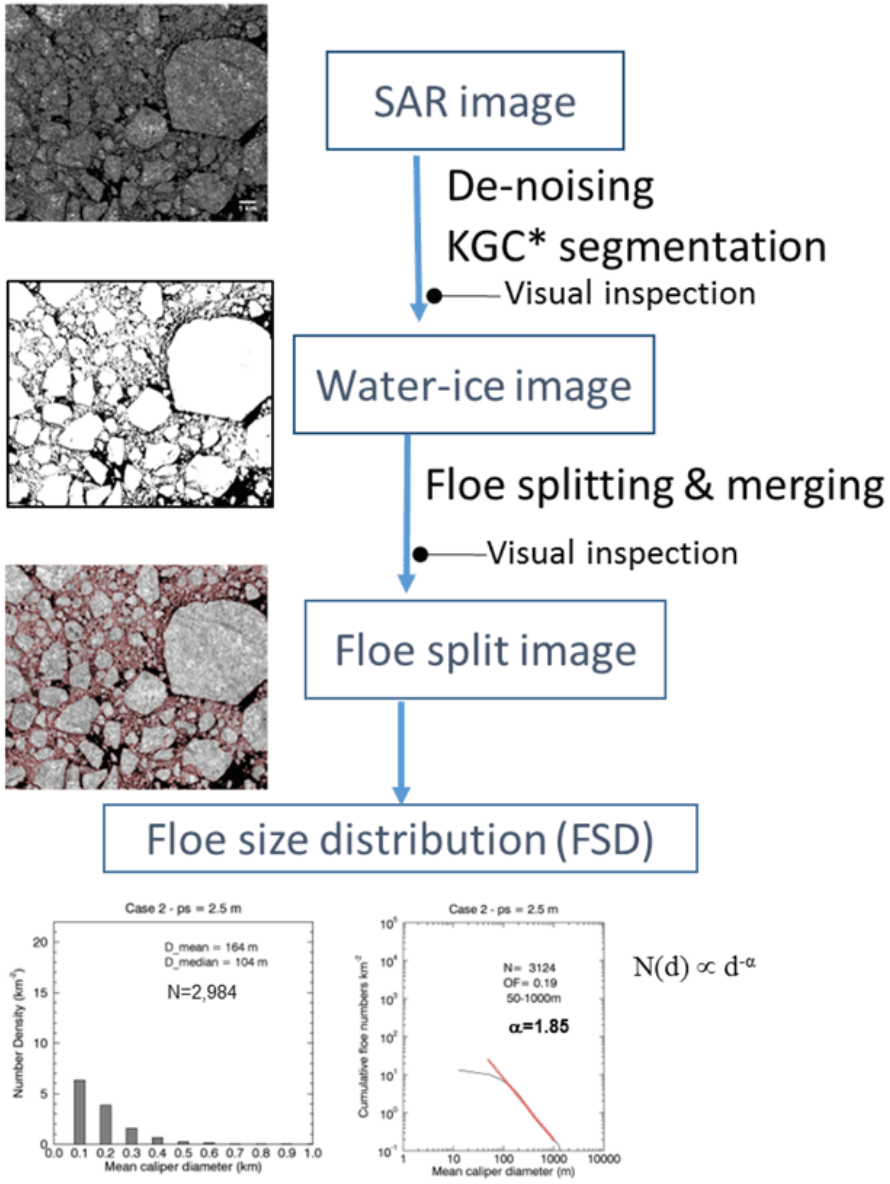

Figure 1.3: Example derivation of the FSD from the Sea Ice imagery

gorithm's ability in detecting the various Sea Ice regions. The most common technique used for measuring the segmentation accuracy is the ROC, which is a measurement of the false versus the true positive rate, discussed further in section 5.3.2.1. Though the ROC is widely used, it only measures the positives cases, i.e. how well the algorithm is able to detect the regions and not how bad they are able to not detect them as well,

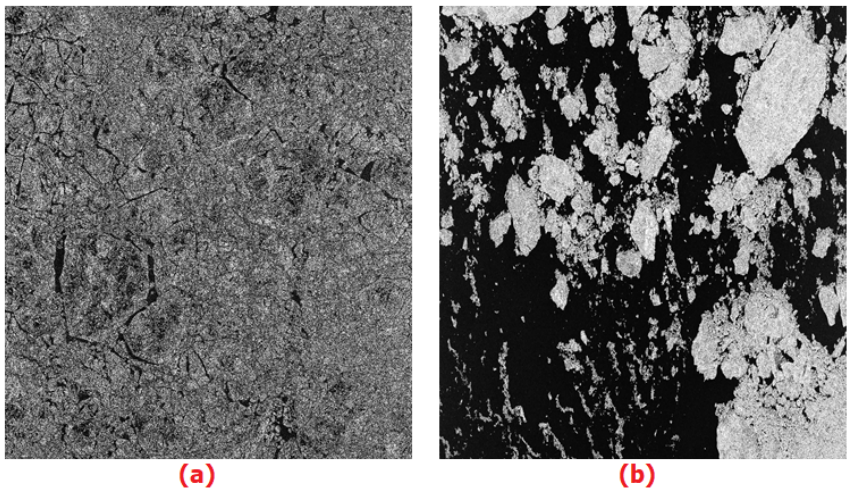

Figure 1.4: Example of difference between the SAR Sea Ice regions (a) Early winter period, (b) Mid-summer period

to give it a fair balance of measurement. In the case of Sea Ice segmentation and acquiring a highly accurate FSD, it is essential that an accurate measurement of Sea Ice segmentation is achieved to effectively understand the various regions. For the purpose of this, a new region based accuracy measurement "ORA" is proposed.

Thus, in summary, the following thesis objectives are defined:

1. To develop a novel Image segmentation algorithm for the Segmentation of SAR Sea Ice images for building the Floe Size Distribution (FSD) analysis. And thus comparing it with previous several years of data.

2. To develop an adaptive speckle filtering algorithm that uses local image statistics to modify/suppress the speckle noise which is evident in almost all SAR images.

3. To develop algorithms which are unsupervised, robust and adjust its parameters automatically according to the variations in the SAR image complexity.

4. To develop an accurate Quantitative Assessment for validating the efficacy of the various algorithms.

1.2 Contributions

In this thesis, several contribution have been discussed with the aim of addressing the various challenges mentioned in the previous section. Improved algorithms for obtaining effective Speckle filtering, Sea Ice Segmentation and Sea ice floe separation are proposed and discussed. The key contributions presented in this thesis are highlighted as follows.

1. Improvement to the Adaptive Median filtering using the advantages of the Weiner filter and the MMSE estimator in effectively suppressing speckle as well as maintaining the edge information used for SAR Sea Ice Segmentation.

2. Using user-specified values for the FQA parameters to perform a second level of speckle filtering, thus modifying only the regions within the image which are lower than the user-specified threshold for the FQA parameters like Edge and Feature Preservation Index in particular.

3. Improvement to the Kernel Graph Cuts algorithm in obtaining the SAR Sea Ice segmentation. By use of easy to implement algorithms, the various "Regions of Interest" are extracted, where the Sea ice floes need to be further separated. Furthermore using local statistics of the image, the regions are separated, thus avoiding over or incorrect segmentation of regions.

4. Using an accurate Quantitative Analysis technique for correctly getting the Segmentation Accuracy of the various algorithms. The technique achieves an accurate measure by calculating the intersection and union of regions of the Segmented result with the Ground Truth (GT) image.

1.3 Organisation of Thesis

The remainder of this thesis is organised as follows.

Chapter 2 provides the mathematical definitions and examples required to understand the various algorithms introduced and compared in this thesis. It also introduces the KGC algorithm which is the benchmark algorithm modified in this thesis to achieve improved segmentation results.

Chapter 3 provides the relevant literature for the research topics presented in this thesis by reviewing popular algorithms used for Speckle Filtering, Sea Ice Segmentation, Image Fusion and Sea Ice floe separation.

Chapter 4 presents an improvement to the Adaptive Median filter by using the MMSE estimator advantages, as used in the Wiener filter. The proposed algorithm utilises the local statistics of the image to identify and modify the speckle pixels within a SAR image. A region based second stage of speckle filtering is also proposed that can be extended to any algorithm by using the FQA techniques used in comparison of speckle filtering results.

Chapter 5 presents an improvement to the KGC algorithm used for the segmentation of SAR Sea Ice floes. The KGC uses local statistics of the image to get the segmentation of various regions, but as the case with even the most robust algorithm, the separation of touching Sea Ice floes is difficult. Thus the proposed improvement of using condition and region based Post Processing algorithm is used to separate these touching Sea Ice floes, without increasing the computing complexity of the whole Segmentation algorithm drastically.

Chapter 6 provides a series of concluding remarks, the original contributions of this thesis and the various directions for future work to further improve the algorithms proposed in this thesis.

CHAPTER 2

SAR SEA ICE PROCESSING AND RELATED TECHNIQUES

Following the motivation behind the present thesis, the fundamental theories and background required to understand the various terms and techniques are introduced in this chapter. Firstly, the background theory for the various speckle filtering algorithms are introduced in sub-section 2.1.1, along with example results on real SAR Sea Ice images. Similarly, in sub-section 2.1.2, the background theory and examples of the various SAR segmentation algorithms are introduced. In section 2.2, the KGC algorithm, which will be enhanced as a result of this thesis, is introduced. In section 2.3, the definitions for the evaluation criteria for speckle filtering as well as segmentation are defined. Finally in section 2.4, a brief summary is provided.

2.1 SAR Data Processing

In this section, the background theory has been mentioned for; Speckle filtering in terms of Pre-Processing and then for Image Segmentation. In section 2.1.1, the various types of speckle filtering algorithms used to compare in this thesis, are mentioned. Similarly, in section 2.1.2, the different algorithms to identify and extract SAR Sea Ice images are mentioned in detail.

2.1.1 Speckle Filtering Methods

Due the coherent process in which a SAR image is formed, it becomes susceptible to a multiplicative noise known as "speckle", which is said to be signal dependant [12]. It is also described as "a grainy salt and pepper noise" [21]. The presence of this noise reduces most segmentation algorithm's ability to detect targets/ objects contained within the SAR images. The concept of the speckle is explained in detail in section 3.1.4.

Many studies have been carried out by researchers, on filtering out this speckle noise and it has been a major research problem for more than 20 years [12, 22–35]. Most of these filters are mentioned in more detail in the following sub-sections.

2.1.1.1 Lee Filter

The most widely known filter for SAR speckle filtering is the Lee filter. Lee [22] first developed a noise filtering algorithm for both additive and multiplicative noise, the multiplicative being used these definitions. It was based on simple calculations of local mean and variances within a local moving window. A MMSE estimator was consequently applied to obtain the noise filtering algorithms. It was consequently extended to real SEASAT SAR images in Lee [12, 25].

It is well known that an image corrupted/ degraded by multiplicative noise can be given by the equation,

$$D_{i,j} = I_{i,j} \times N_{i,j} \tag{2.1}$$

In the Equation 2.1, $D_{i,j}$ is the degraded image produced as a result of the combination of original image $I_{i,j}$ and noise $N_{i,j}$. The noise $N_{i,j}$ has mean equal to 1 and variance θ_N^2. Furthermore, the Multiplicative Noise Model can be derived as follows. For simplification of the notations, the subscripts i, j have been omitted.

Assuming that I and N are uncorrelated, the mean $\hat{D}$ and variance z of D are ex-

pressed as [12],

$$\hat{D} = \bar{I} \,.\, \bar{N} = \bar{I} \tag{2.2}$$

$$z = E\left[(I \,.\, N - \bar{I} \,.\, \bar{N})^2\right] = E\left[I^2\right] E\left[N^2\right] - \bar{I}^2 \,.\, \bar{N}^2 \tag{2.3}$$

Since the window is over an area of constant signal [12], $E\left[I^2\right] = \bar{I}^2$ and thus the variance in Equation 2.3 reduces to,

$$\begin{aligned} z &= \bar{I}^2 \,.\, \theta_N^2 \\ &Or \\ \theta_N &= \frac{\sqrt{z}}{\bar{I}} = \frac{\sqrt{z}}{\mu} \end{aligned} \tag{2.4}$$

Thus from Equations 2.2, 2.3 and 2.4, it can be said that the standard deviation of noise N is equal to the ratio of the standard deviation of D and the mean of D.

The speckle suppression can then be achieved using the local statistics method mentioned in [12]. From Equation 2.1, the a priori mean M and variance V of I are computed as,

$$\mu = \bar{D}/\bar{N} \tag{2.5}$$

$$V = \frac{z + \bar{D}^2}{\theta_N^2 + \bar{N}^2} - \mu^2 \tag{2.6}$$

The observed image D can then be linearised using the first order Taylor series expansion about $(M, \bar{N})$ and given as,

$$D = \bar{N} \,.\, I + \mu(N - \bar{N}) \tag{2.7}$$

The Equation 2.7 is the linear optimal approximation of Equation 2.1 [22]. With the a priori mean and variance from Equations 2.5 and 2.6, along with Equation 2.7, the filter algorithm is derived by minimizing the Mean Square Error by weighted least square estimation [36].

$$\hat{I} = \mu + G(D - \bar{N} \,.\, \mu) \tag{2.8}$$

In Equation 2.5, $\hat{I}_{i,j}$ is the estimate of original noise free image $I_{i,j}$. $G_{i,j}$ is the gain expressed by,

$$G = \frac{\bar{N} \times V}{\mu^2 \theta_N^2 + \bar{N}^2 V} \tag{2.9}$$

Assuming that the Noise $\bar{N}$ equals to 1 in Equations 2.8 and 2.9, the two Equations are simplified as,

$$\hat{I} = M + G(D - M) \tag{2.10}$$

$$G = \frac{V}{M^2 \theta_N^2 + V} \tag{2.11}$$

The θ_N^2 in Equations 2.9 and 2.11 is obtained from the Multiplicative Noise Modelling mentioned in Equation 2.4.

The filter provided a good basis for real-time processing, with the use of parallel processing. Due to its simplicity, it was also very computationally efficient. But despite this, it wasn't very effective with speckle noise noticed in SAR images. Lee [23, 24] then developed an adaptive algorithm that incorporates the sigma factor for better approximation of values for replacing the speckle pixels identified within the image.

The theory is based on the two-sigma property, where a random variable/ image pixel is assumed to be within two standard deviations of its mean. If the pixel is outside this two-sigma range, then it's considered to be noise and is excluded from the calculation of the average that replaces the central pixel value. The two-sigma range can be obtained from a priori mean of the pixel to be smoothed. Since the speckle noise is a multiplicative type of noise and can be given by,

$$\begin{aligned} LowerBound &= D_{i,j} - 2\sigma \\ UpperBound &= D_{i,j} + 2\sigma \end{aligned} \tag{2.12}$$

In Equation 2.12, $D_{i,j}$ is the degraded image mentioned in Equation 2.1. σ is the standard deviation of the noise with mean equal to zero. Using this equation, the central pixel value is then smoothed with the average of the pixel values within the two-sigma

range only. It can be simplified as,

$$R_{k,l} = \begin{cases} 1, & If\ (D_{i,j} - 2\sigma) \leq D_{k,l} \leq (D_{i,j} + 2\sigma) \\ 0, & Otherwise \end{cases} \tag{2.13}$$

In the Equation 2.13, $R_{k,l}$ is the average value used to replace the pixel value within $D(i,j)$ in the filtered image $\hat{I}_{i,j}$. Thus the smoothed pixel value for, this two-sigma range inspired filter, can be expressed as,

$$\hat{I}_{i,j} = \sum_{k=i-n}^{n+i} \sum_{l=j-m}^{m+j} R_{k,l}\, D_{k,l} \Big/ \sum_{k=i-n}^{n+i} \sum_{l=j-m}^{m+j} R_{k,l} \tag{2.14}$$

In Equation 2.14, $\hat{I}_{i,j}$ is the filtered image with the average of the pixels which are in the two-sigma range given in Equation 2.10. To deal with sharp shot noise, Lee modified the Equation 2.14 to only use the central pixel's immediate neighbouring pixels. This was only if the number of pixels within a moving window and within the two sigma range, were less than a user specified value K. Thus,

$$\hat{I}_{i,j} = \begin{cases} two-sigma\ range, & If\ P > K \\ immediate\ neighbour\ average, & If\ P \leq K \end{cases} \tag{2.15}$$

Here P is the number of pixels that lie within the two-sigma range within the moving window. The implementation of the Lee Sigma filter can be further explained by the flowchart in Figure 2.2. Examples of how the filter operates on real SAR images are given in Figure 2.1.

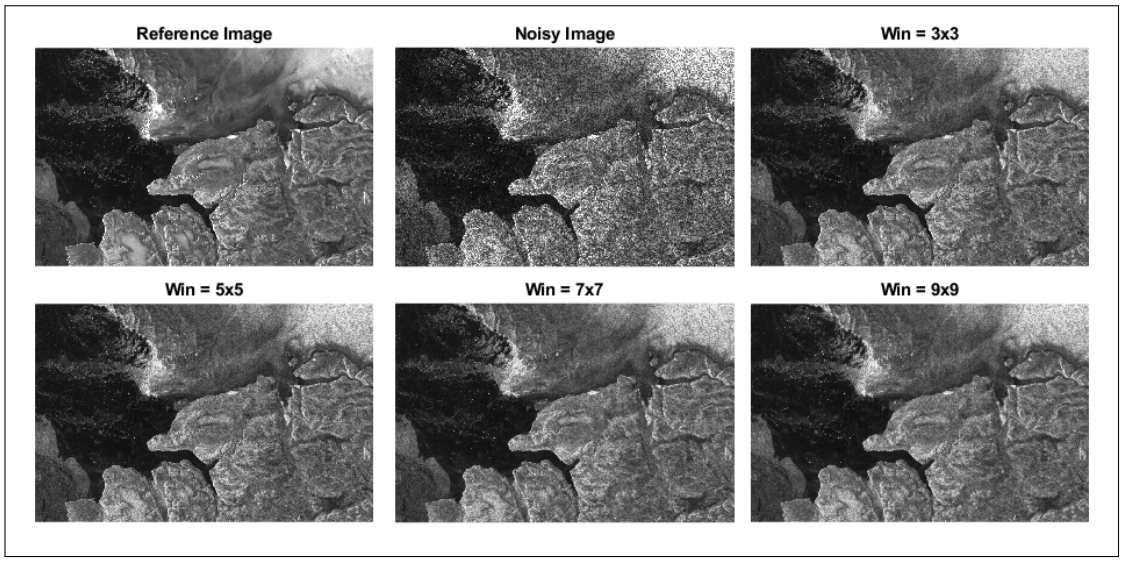

Figure 2.1: Results of the Lee Sigma filter, with increasing window size

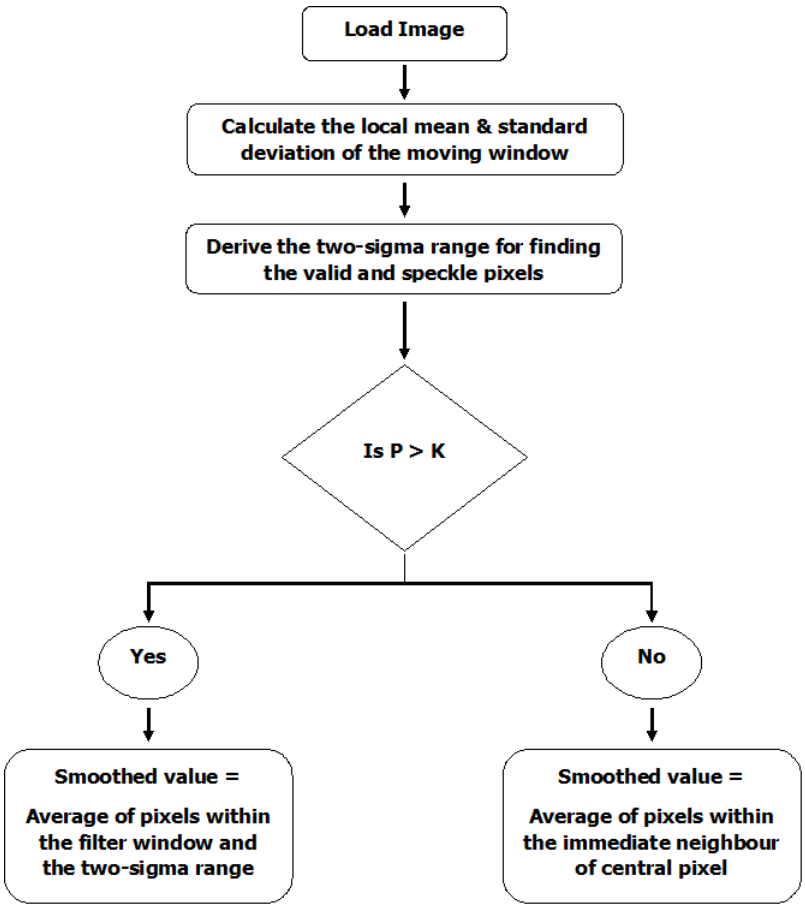

Figure 2.2: Implementation Flowchart for Lee Sigma Filter

2.1.1.2 Local Sigma Filter

The LSF [33] was proposed as an improvement to the Lee Sigma filter [23, 24]. The LSF is one of the two Adaptive Box filters proposed by Eliason. While the LSF is used for smoothing noisy image, the other filter is used for the removal of random bit errors from the image.

The LSF is adaptive in the sense that it uses the standard deviation of the local moving window to calculate the filter value for the central pixel of the moving window. The LSF uses the two sigma range, similar to the one proposed by Lee [23], to predict if the pixel in the image is classed as a speckle or a valid pixel. It can be expressed as [33],

$$\begin{aligned} d(i,j) = 0, \quad if \quad I(i,j) < MIN \quad or \quad D(i,j) > MAX \\ d(i,j) = 1, \quad if \quad MIN \leq D(i,j) \leq MAX \end{aligned} \tag{2.16}$$

In the Equation 2.16, $d(i,j)$ is the delta function used to distinguish between valid and invalid pixels in the filter centered at $D(i,j)$. For a typical 8-bit integer image, MIN and MAX are equal to 1 and 255 respectively, zero indicating a invalid/ empty pixel.

If the central pixel of the moving window is classified as a speckle pixel, it is replaced with the replacement value, given by the following equation [33],

$$R(i,j) = \frac{[S(i,j) - (d(i,j) \times D(i,j))]}{P(i,j) - d(i,j)} \tag{2.17}$$

In the Equation 2.17, R is the replacement value for the central pixel, which is the mean value of the pixels within the filter window, excluding the invalid and central pixel itself for calculating the mean. S is the sum of the valid pixels within the filter window. P is the number of valid pixels within the window.

When the central pixel of the filter window in the LSF is marked as a speckle pixel, it is replaced by the replacement value given in Equation 2.17, rather than the mean

of the pixels within the window. Thus it avoids using the values of pixels marked as speckle and the erroneous value of the central pixel itself. The central pixel is classed as a speckle (invalid) pixel, if it meets the criteria given by,

$$\begin{aligned} |D(i,j) - \mu(i,j)| \quad &> \quad (K \times \sigma(i,j)) \quad And \\ |D(i,j) - \mu(i,j)| \quad &> \quad T \end{aligned} \tag{2.18}$$

In the Equation 2.18, μ is the mean of the valid pixels within the filter window and σ is the standard deviation. The standard deviation of the filter is derived from the μ, the P and the Sum of Square of valid points SS, within the moving filter window. This is a contrast to the Lee Sigma [23], where a fixed sigma value is used for the moving window. K is user defined constant value that typically ranges between 1.0 to 2.0. T is the another user defined constant that typically ranges between 2 to 10 for 8-bit data. It may be set to zero, to avoid over-compensating for potentially valid pixels in low variance areas. The implementation of the LSF is further explained in Figure 2.4. Examples of how the filter operates on real SAR images are given in Figure 2.3.

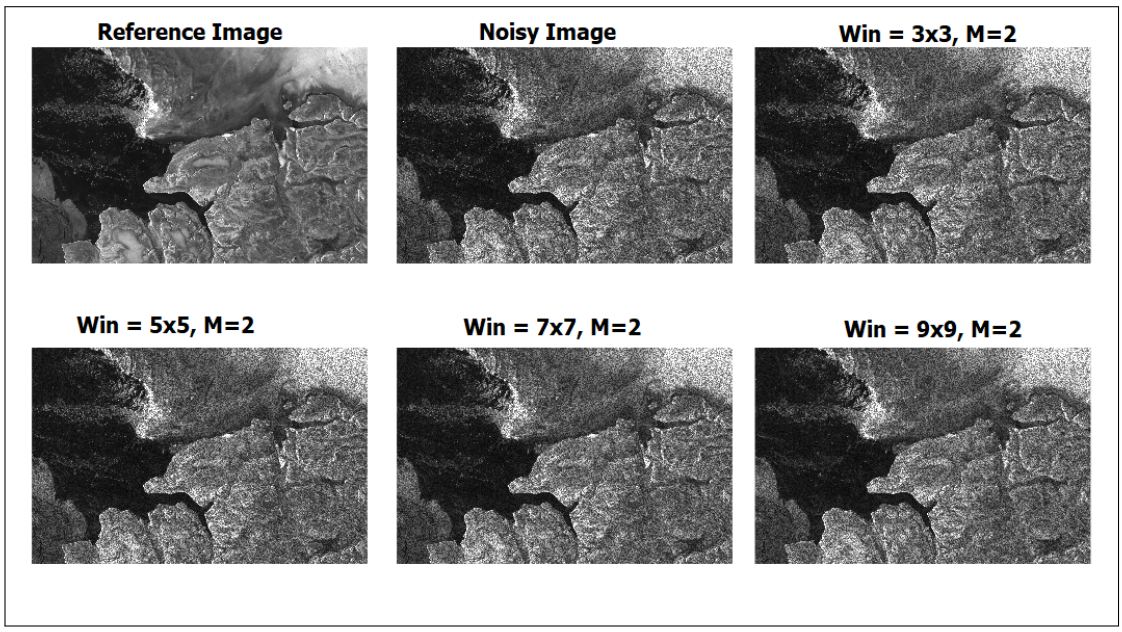

Figure 2.3: Results of the Local Sigma filter, with increasing window size

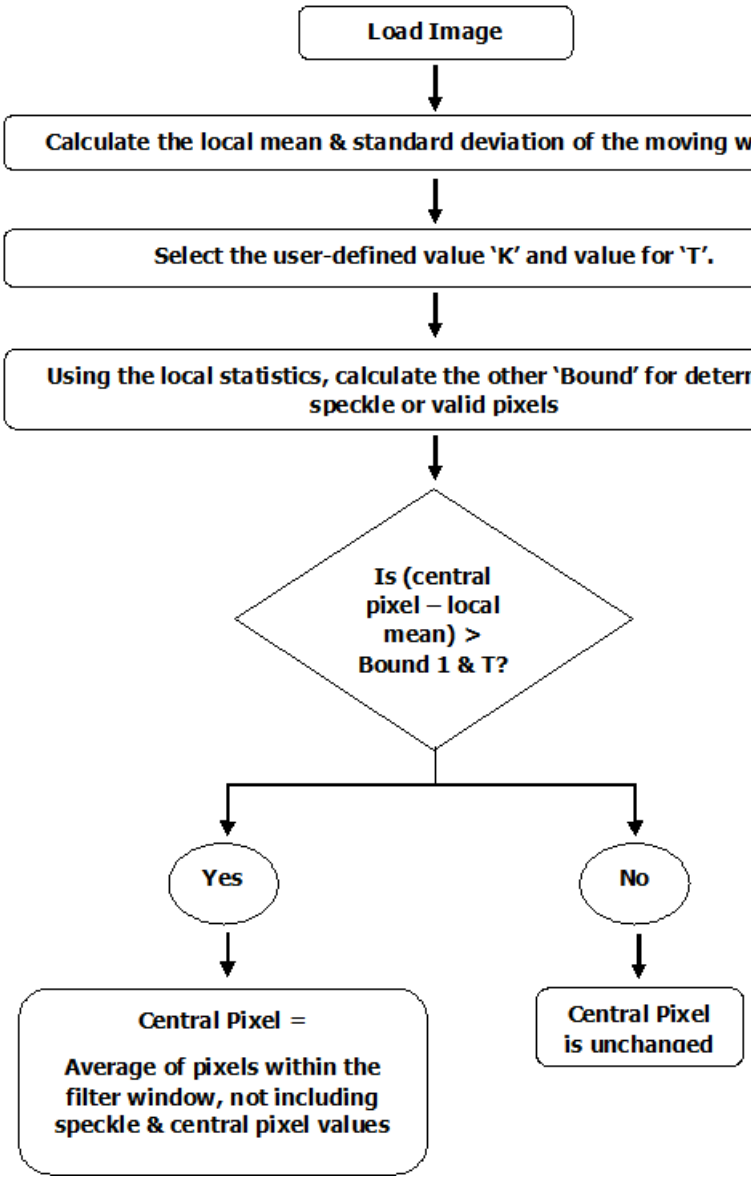

Figure 2.4: Implementation Flowchart for LSF

2.1.1.3 Bilateral Filter

The BF [35] is a non-iterative, non-linear, edge-preserving and smoothing filter. It filters/ smooths the values based on the geometric closeness [domain filtering] and photometric similarity [range filtering].

The BF was introduced as an edge-preserving filter to provide single band, instead

of multi-band filtering for colour images, thus eliminating the corruption of colour pixels of RGB images around the edges. The filter works similarly with grayscale images, where the gray levels of the pixels in the adjacent area of the centred pixel are considered, thus avoiding the blurring of edges.

The BF is a combination of domain filtering and range filtering. The domain filtering can be given by the equation,

$$\hat{I}(x) = k_d^{-1}(x) \int_{-\infty}^{\infty} \int_{-\infty}^{\infty} I(\xi) \times G(\xi, x) d\xi \tag{2.19}$$

In Equation 2.19 [35], $\hat{I}(x)$ is the output of the low-pass domain filter applied to input image $I(x)$. The $G(\xi, x)$ is the measure of the geometric closeness between the central pixel x and its neighbourhood pixel ξ. The $k(x)$ is the normalisation constant for the domain filtering, given by,

$$k_d(x) = \int_{-\infty}^{\infty} \int_{-\infty}^{\infty} G(\xi, x) d\xi \tag{2.20}$$

When the filter is shift-invariant, the geometric closeness $G(\xi, x)$, is a vector difference between ξ and x. The normalisation term in 2.20, "k_d", is then a constant value.

The range filtering can be given by the equation,

$$\hat{I}(x) = k_r^{-1}(x) \int_{-\infty}^{\infty} \int_{-\infty}^{\infty} I(\xi) \times S(I(\xi), I(x)) d\xi \tag{2.21}$$

In Equation 2.21 [35], $\hat{I}(x)$ is the output of the low-pass domain filter applied to input image $I(x)$. The $S(I(\xi), I(x)))$ measures the photometric similarity between the central pixel x and its neighbourhood pixel ξ. The normalisation term in 2.20 is then modified to,

$$k_r(x) = \int_{-\infty}^{\infty} \int_{-\infty}^{\infty} S(I(\xi), I(x)) d\xi \tag{2.22}$$

The normalisation function for the photometric similarity depends on the input image $I(x)$ itself and said to be unbiased when it depends solely on the difference

between the pixels $I(\xi)$ and $I(x)$.

Thus the equation for the BF can then be derived by the combination of Equations 2.19 and 2.21,

$$\hat{I}(x) = k^{-1}(x) \int_{-\infty}^{\infty} \int_{-\infty}^{\infty} I(\xi) \times G(\xi, x) \times S(I(\xi), I(x)) d\xi \tag{2.23}$$

And similarly the normalisation term is given by,

$$k(x) = \int_{-\infty}^{\infty} \int_{-\infty}^{\infty} G(\xi, x) \times S(I(\xi), I(x)) d\xi \tag{2.24}$$

Thus it can be seen how the BF filter modifies the value of pixel x in the Input Image $I(x)$ with the average value in the Output Image $\hat{I}(x)$, calculated using the geometric closeness (domain) and the photometric similarity (range). The implementation of the BF can be further explained by the flowchart in Figure 2.6. Examples of how the filter operates on real SAR images are given in Figure 2.5.

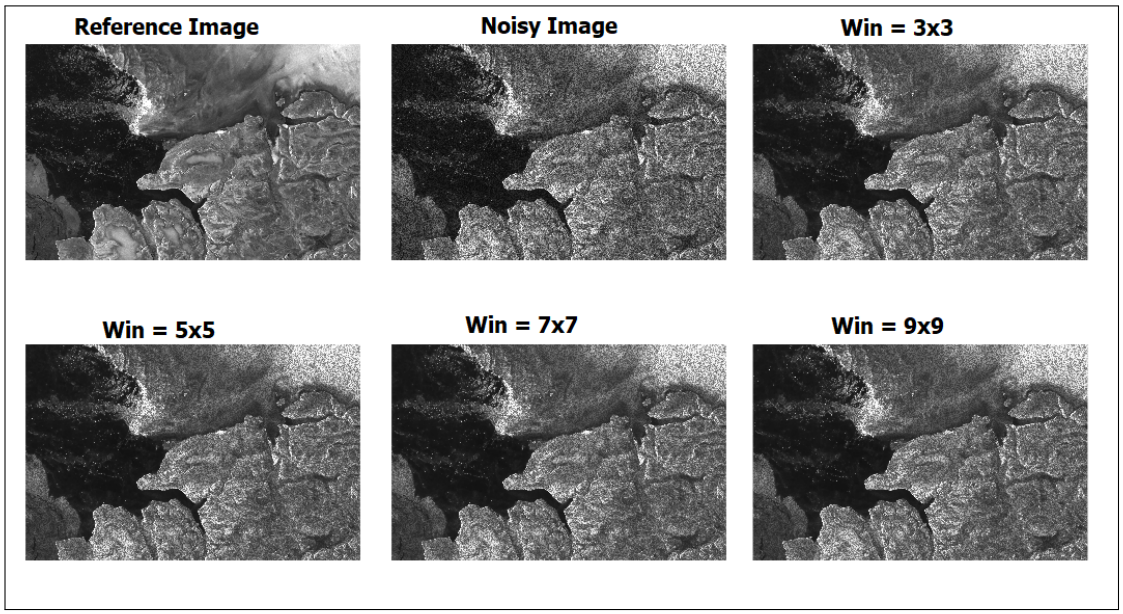

Figure 2.5: Results of the Bilateral filter, with increasing window size

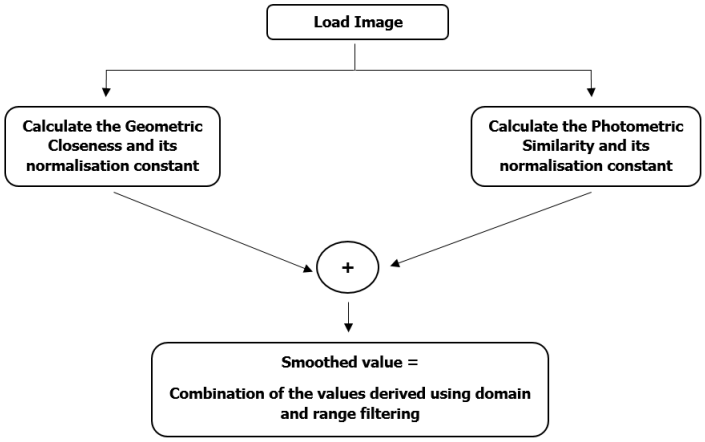

Figure 2.6: Implementation Flowchart for BF

2.1.1.4 Wiener Filter

The Wiener filter [37], is one of the most simple and widely used filter for additive as well as guassian type of noise. It is most commonly used as a restoration filter to remove motion blur caused in RGB images. The Wiener filter is not an adaptive filter but like the Lee, Frost and Kuan filters, uses MMSE estimator to smooth out noise. The equation [38] for the Wiener filter can be given by,

$$O(i,j) = \mu(i,j) + \left(\frac{\sigma^2(i,j) - \theta_N^2}{\sigma^2(i,j)} \times (I(i,j) - \mu(i,j)) \right) \tag{2.25}$$

In the Equation 2.25, i and j are the co-ordinates of the image pixels within Output Image $O(i,j)$ and Input Image $I(i,j)$. $\mu(i,j)$ is the local mean and $\sigma(i,j)$ is the local variance of the moving window. θ_N^2 is the noise variance that is required to be known or estimated for the filter to operate.

The local mean $\mu(i,j)$ and variance $\sigma^2(i,j)$ for the filter are expressed as,

$$\mu(i,j) = \frac{1}{AB} \sum_{i,j \Xi \eta} I(i,j) \tag{2.26}$$

$$\sigma^2(i,j) = \frac{1}{AB} \sum_{i,j \Xi \eta} (I(i,j)^2 - \mu^2) \tag{2.27}$$

In Equations 2.26 and 2.27 [38], η is the A by B local neighbourhood of each pixels in Image $I(i,j)$.

Since this filter is implemented using the Matlab's in-built function, "**wiener2**", the noise variance θ_N^2 in Equation 2.25, is calculated by taking the average of the locally estimated variances of the filter window. Examples of how the filter operates on real SAR images are given in Figure 2.7.

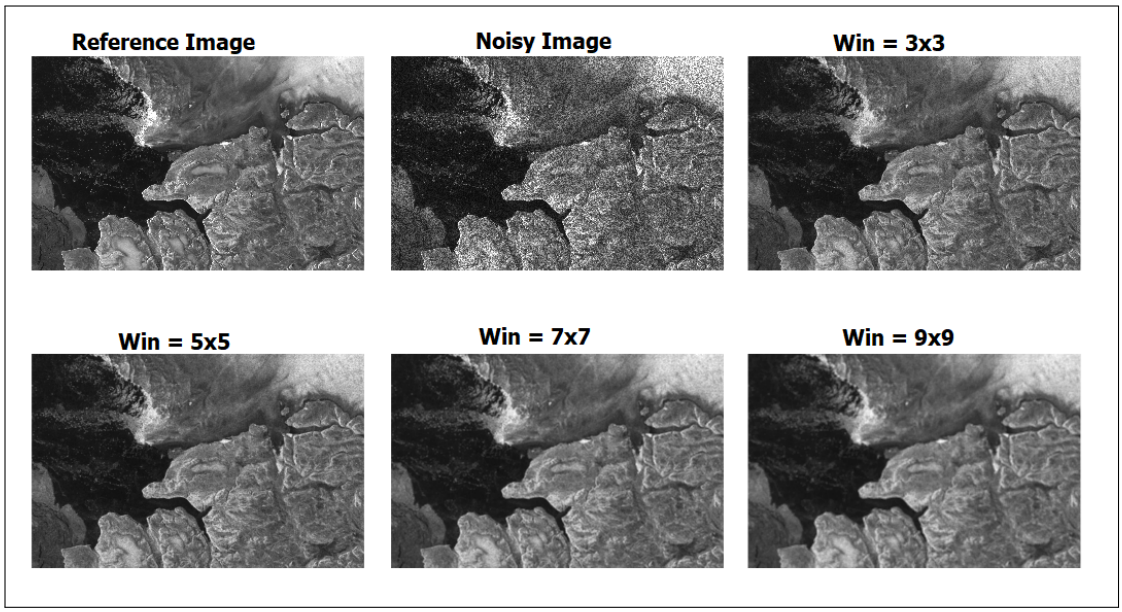

Figure 2.7: Results of the Wiener filter, with increasing window size

2.1.1.5 Adaptive Median Filter

The AMF [34] was proposed by Fang Qui et. al., building on the advantages of the Median filter in retaining the edges within an Image. Edges are particularly important parameter to retain for SAR Sea Ice Images, as they help to separate the ice floes and get an accurate segmentation required for Sea Ice analysis.

The AMF uses local statistics such as mean and standard deviation to calculate valid and speckle pixels within a moving filter window. It is similar to the LSF, aside

from the way it replaces the central pixel value. The filter also replaces the central pixel value with the median value of the pixels within the window, rather than the mean value, as used by most filters. The advantages of these are shown in section 4.2.1.

Similar to the LSF, the AMF uses Lower and Upper bounds to validate if a pixel within a window is valid or speckle. The bounds can be calculated by the equations [34],

$$\begin{aligned} LB(i,j) &= \mu(i,j) - (M \times \sigma(i.j)) \\ UB(i,j) &= \mu(i,j) + (M \times \sigma(i.j)) \end{aligned} \tag{2.28}$$

In Equation 2.28, LB and UB are the Lower and Upper bounds used to determine if a pixel is valid or speckle. μ is the mean and σ is the standard deviation of pixels within the filter window. All the valid and speckle pixels are identified and labelled in the temporary Output Image as [34],

$$\begin{aligned} d(i,j) = 0, \quad if \quad D(i,j) < LB(i,j) \quad or \quad D(i,j) > UB(i,j) \\ d(i,j) = 1, \quad if \quad LB(i,j) \leq D(i,j) \leq UB(i,j) \end{aligned} \tag{2.29}$$

In Equation 2.29, the central pixel is equal to "0" if it is identified as a "speckle pixel" and equal to "1" if it is a "valid pixel". If the central pixel in the moving window is marked as a speckle pixel, the AMF replaces its value with the median value calculated using all the original values of the valid pixels in the Input Image.

$$R(i,j) = Median(I(i,j)) \tag{2.30}$$

The implementation of the AMF is further explained by the flowchart in Figure 2.9. Examples of how the filter operates on real SAR images are given in Figure 2.8.

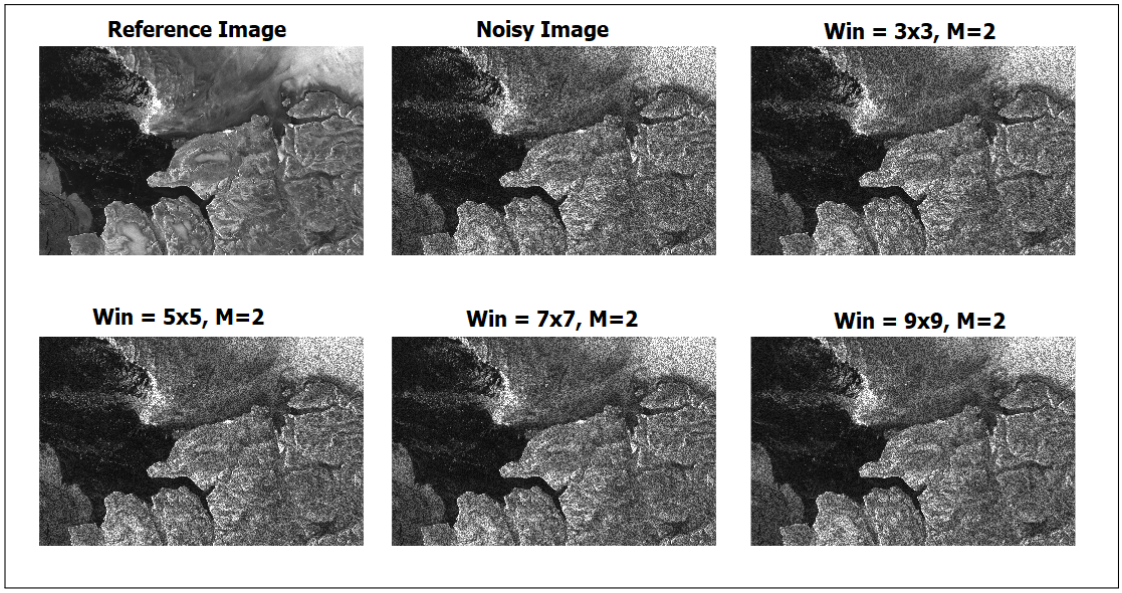

Figure 2.8: Results of the Adaptive Median filter, with increasing window size

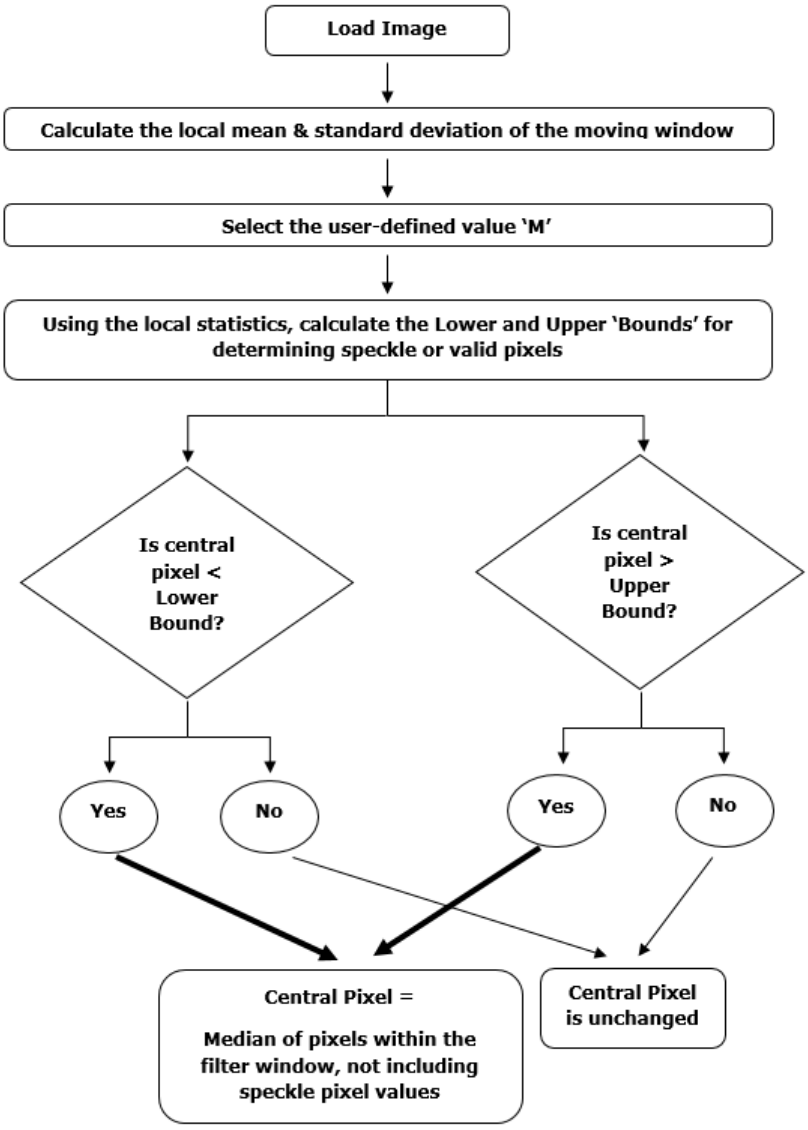

Figure 2.9: Implementation Flowchart for AMF

2.1.2 Segmentation Methods

Synthetic Aperture Radar (SAR) has been widely used for studies related to the Sea Ice imagery; in the Arctic, Antarctic, Baltic Sea, Bohai Sea etc. Due to its various advantages, SAR has been used, over the past as well as present, for identification of sea ice floes, their size and their distribution [15, 39–41]. Some of these have been described in detail in the following sub-sections.

2.1.2.1 Watershed

The watershed algorithm [42] is implemented using Matlab's in-built function, that uses the topographical distance function based specification. The watershed transform identifies the "catchment basins" or also called "watershed ridge lines", in a particular image by means of treating it as a surface where a light pixels represent high elevation and the dark pixels represent low elevation respectively.

Let X be the grayscale digital image with a lower complete (each pixel which is not a minimum has a lower gray value adjacent neighbour/s). The lower slope $L(i)$ of image X at pixel i, can be defined as the maximum slope that links the pixel value with any of its neighbours with a lower altitude. The equation for this can be given as,

$$L(i) = \max_{j \subseteq N_G(i) \cup (i)} \left(\frac{X(i) - X(j)}{d(i,j)} \right) \tag{2.31}$$

In the Equation 2.31, $N_G(i)$ is the set of neighbours of pixel i on the graph $G = (V,E)$. $d(i,j)$ is the associated distance to the edge (i,j). For pixels whose neighbours are all higher grayscale values, the lower slope is equal to zero. The cost associated

with travelling from pixel i to a neighbouring pixel j can be given by,

$$cost(i,j) = \begin{cases} L(i) \times d(i,j) & \text{if } X(i) > X(j) \\ L(j) \times d(i,j) & \text{if } X(i) < X(j) \\ \frac{1}{2}(L(i) + L(j)) \times d(i,j) & \text{if } X(i) = X(j) \end{cases} \tag{2.32}$$

Definition: The set of lower neighbours j of i for which the slope $(X(i)-X(j))/d(i,j)$ is maximal, is denoted by $T(i)$. The set of pixels j for which $i \in T(j)$ is denoted by $T^{-}1(i)$.

The topological distance between $i_0 = i$ and $i_l = j$, along the path $P = i_0, ..., i_l$ is given by,

$$T_X^P(i,j) = \sum_{a=0}^{l-1} d(i_a, i_{a+1})\, cost(i_a, i_{a+1}) \tag{2.33}$$

The topological distance between pixels i and j is the minimum of the topological distances along all the paths between them. Thus,

$$T_X(i,j) = \min_{P \in [i \to j]} T_X^P(i,j) \tag{2.34}$$

In Equation 2.34, $i \to j]$ denotes all the paths from i to j. Also, the topological distance between a set $A \subseteq D$ and point $i \in D$ is given by,

$$T_X(i,A) = \min_{a \in A} T_X(i,a) \tag{2.35}$$

A path $i_0, i_1, ..., i_n$ from $i_0 = i$ to $i_n = j$ is said to be of steepest decent if $i_{a+1} \in T(i_a)$ for each $a = 0, ..., n-1$. Pixel j is said to belong to downstream of i if a path of steepest decent exists from i to j. Pixel j is said to belong to upstream of i if i belongs to the downstream of j. The topological distanced based watershed has the following property:

Preposition: Given that $X(i) > X(j)$, a path P from i to j is of steepest decent, only

if $T_X^P = X(i) - X(j)$. If the path is not of steepest decent, then $T_X^P > X(i) - X(j)$.

The preposition thus implies that the paths of steepest decent as essentially the geodesics of the topological distance function. The Watershed consists of points i which are in the upstream of at least two local minima, i.e. there are at least two paths of steepest decent starting from i that lead to the local minima. Figure 2.10 shows an example of the watershed transform according to the topological distance.

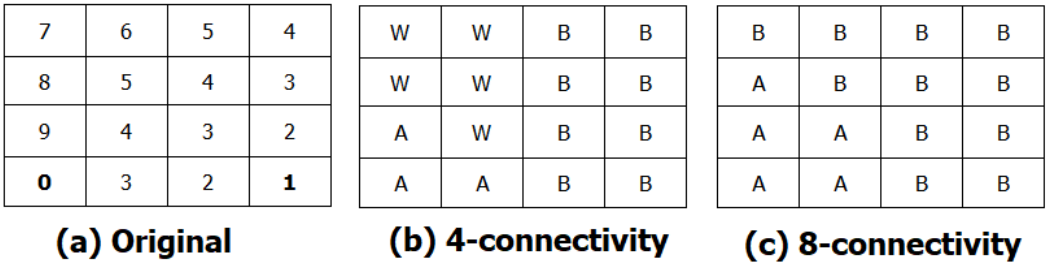

Figure 2.10: Watershed Transform on the square grad with (b)4-connectivity and (c)8-connectivity for original image (a)

The local minima is highlighted in bold in Figure 2.10 (a). The A and B notations in the Figure (b-c), denote the labels of the basins, whereas the W specifies the Watershed pixel. Figures 2.11 and 2.12 give examples of how the Watershed effectively segments sample SAR Sea Ice images used in this thesis.

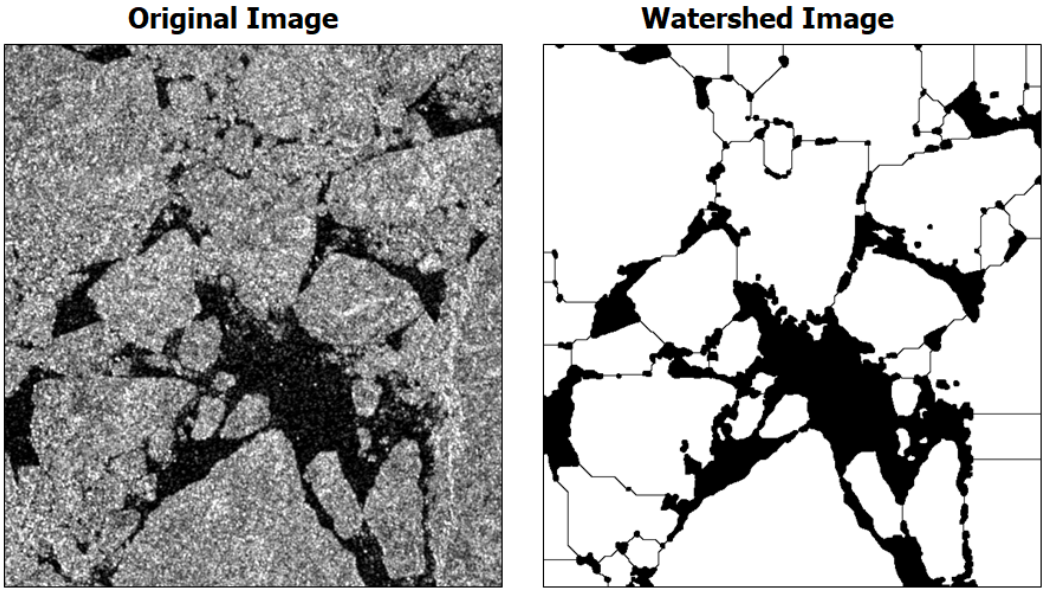

Figure 2.11: Example 1: Segmentation achieved by Watershed

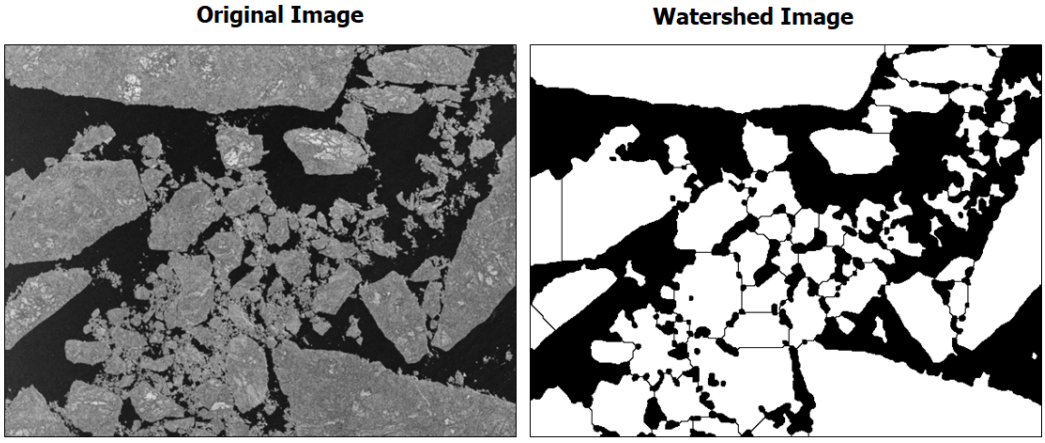

Figure 2.12: Example 2: Segmentation achieved by Watershed

2.1.2.2 Level Sets

The Level Sets [43], is similar to the Active Contours [44] used in this research and mentioned in section 5.2.3. This Level Set algorithm is an improvement to the conventional Level Set algorithm [45], as it introduces distance regularisation to overcome its

evolution irregularities of requiring a reinitialization [46,47] for maintaining its stability of evolution of contours.

The distance regularisation can be of two types; Edge-based or Region-based, but for image segmentation purposes, the Edge-based distance regularisation is used in [43]. This Distance Regularised Level Set Equation (DRLSE) can be described as follows.

Let I represent an image over domain Ψ, for which an edge indicator function can be represented as,

$$E \triangleq \frac{1}{1 + | \bigtriangledown g_\sigma * I |^2} \tag{2.36}$$

In Equation 2.36, g_σ is the Gaussian Kernel with standard deviation σ. The convolution terms in Equation 2.36 is used to smooth the image and decrease the noise. It can also be noted that E takes lower values object boundaries compared to other locations within the image.

Consequently, for a level set function, $\theta : \Psi \rightarrow \Re$, the Energy Functional $\varepsilon(\theta)$ can be expressed as,

$$\varepsilon(\theta) = \mu R_p(\theta) + \lambda L_E(\theta) + \alpha A_E(\theta) \tag{2.37}$$

Where $\alpha \in \Re$ and $\lambda > 0$, are the coefficients of the energy functionals L_E and A_E. The L_E and A_E in Equation 2.37 can be expressed as,

$$L_E(\theta) \triangleq \int_\Psi E\, D(\theta) | \bigtriangledown \theta | dx \tag{2.38}$$

$$A_E(\theta) \triangleq \int_\Psi E\, H(-\theta) dx \tag{2.39}$$

In Equations 2.38 and 2.39, D and H are the Dirac delta function and Heaviside function respectively.

The energy term $L_E(\theta)$, calculates the line integral function of the function E along the zero level contour of θ. The energy L_E is minimized when the zero level contour of θ is located at the boundary of an object.

Whereas the energy functional $A_E(\theta)$, calculates the weighted area of the region $\Psi_\theta^- \triangleq [x : \theta(x) < 0]$. This energy function is introduced to speed up the motion of the zero level contour in the evolution process of the Level Sets, especially when the initial contour has been placed far away from the object boundary.

The Level Set Function, takes a negative value when inside the zero level contour and takes positive values when outside. Thus, if the initial contour is placed outside the object, α in the weighted area term must be positive in order for the contour to shrink inside during the Level Set evolution. Similarly, if the initial contour is placed inside the object, α must be negative in order for the contour to expand the contour during evolution.

The energy functional for the Dirac and Heaviside functions (more information in [43]) can be minimised by solving the gradient flow to give the Level Set Evolution function,

$$\frac{\partial \theta}{\partial t} = \mu div(D_p(|\bigtriangledown \theta|)\bigtriangledown \theta) + \lambda D_E(\theta) div(E\frac{\bigtriangledown \theta}{|\bigtriangledown \theta|} + \alpha E D_E(\theta)) \tag{2.40}$$

The first term in the right side of the Equation 2.40, is the distance regularisation energy $R_p(\theta)$ mentioned in Equation 2.37. Whereas the second term is associated with the $L_E(\theta)$ and the third term with the $A_E(\theta)$ respectively.

Figures 2.13 and 2.14 give examples of how the Level Set function effectively segments sample SAR Sea Ice images used in this thesis.

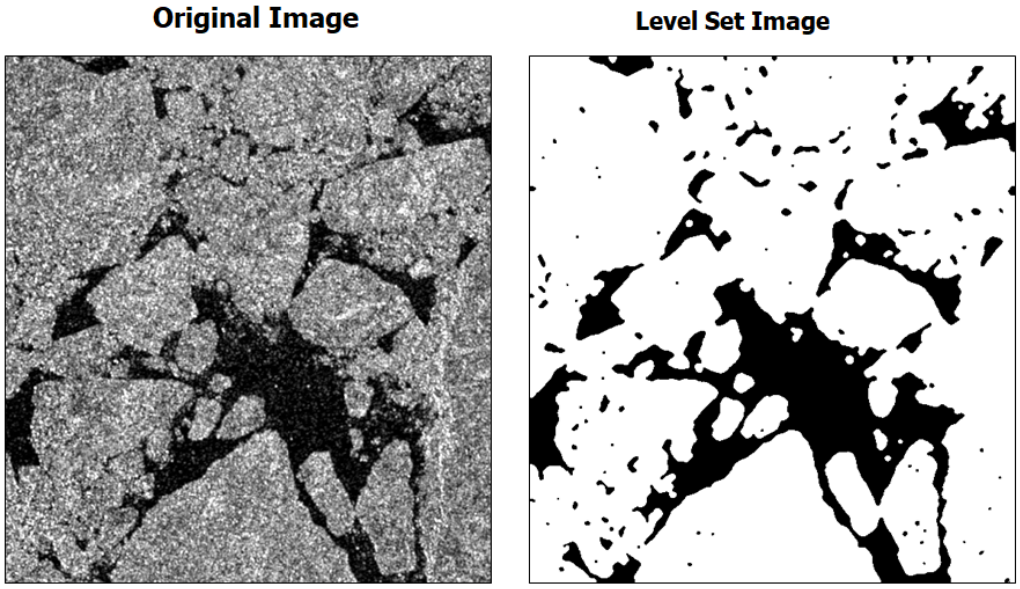

Figure 2.13: Example 1: Segmentation achieved by Level Sets

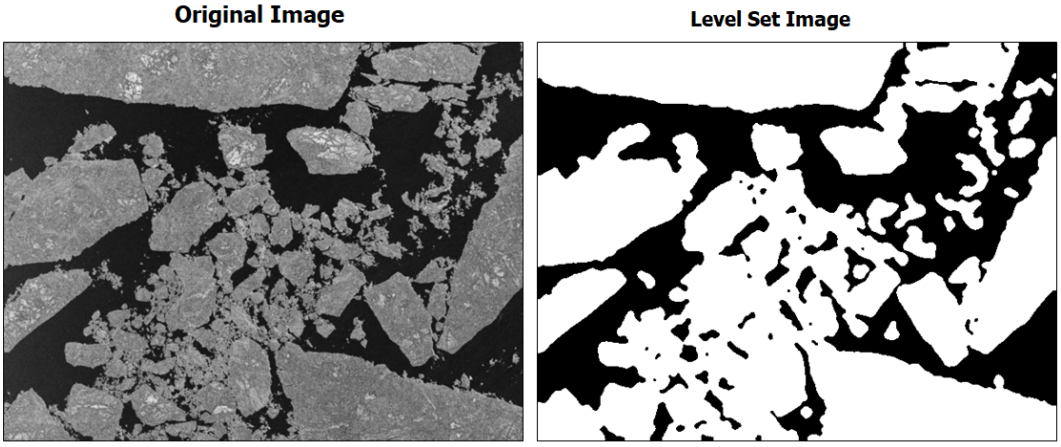

Figure 2.14: Example 2: Segmentation achieved by Level Sets

2.1.2.3 Closeness Degree Cut

The Closeness Degree Cut (CD Cut) algorithm [48] is a combination of two-stage processing, comprising of; Image segmentation achieved using CD Cut model, followed by automatic identification of number of clustering regions using the Minimum Description Length Criterion (MDLC).

The algorithm focuses on extracting an over-segmented image using the Watershed algorithm and then constructing graphs for each of the various identified regions. The graph is then clustered using the spectral clustering algorithm of CD Cut. The MDLC is then used to determine the clustering number by utilising the statistical properties of the speckle noise present in the SAR images.

The CD Cut is based on the closeness degree between the fuzzy sets on the graph [48]. Given the partition of node set $P = \bigcup_{k=1}^{K} P_k$, K fuzzy sets are formed on the partition. The membership degree between the fuzzy set F_k and the node n_i is given by,

$$M_{F_k}(i) = \frac{\sum_{l \in P_k} C_{ij}}{\sum_{k=1}^{K} \sum_{l \in P_k} C_{ij}} = \frac{\sum_{l \in P_k} C_{ij}}{d_i} \tag{2.41}$$

Given the graph $G(P,E)$, let R, S and T be the fuzzy sets derived from nodes P_R, P_S and P_T respectively. $N(S,R)$ is referred to as the closeness degree from S to R, if it satisfies the following conditions,

1. If $R \neq \emptyset, N(R,R) = 1$.
2. If $R \cap S = \emptyset, N(S,R) = N(R,S) = 0$.
3. If $P_T \subseteq P_S \subseteq P_R, N(T,R) \leq N(S,R)$.

The CD Cut algorithm is formulated for spectral clustering as follows,

1. Using the data points, calculate the similarity index S.

2. Calculate the diagonal matrix D, the stochastic matrix S and thus derive the matrix $C = diag(P^T 1_N)$.

3. Calculate the first K set of eigenvectors.

4. Construct the matrix Y with eigenvectors and the orthogonality as well as non-negatively constraints.

5. Obtain the clusters $P_1, ..., P_K$ by applying kmeans clustering of rows of Y or discretization of Y using rotation.

Figures 2.15 and 2.16 give examples of how the CDCut effectively segments sample SAR Sea Ice images used in this thesis.

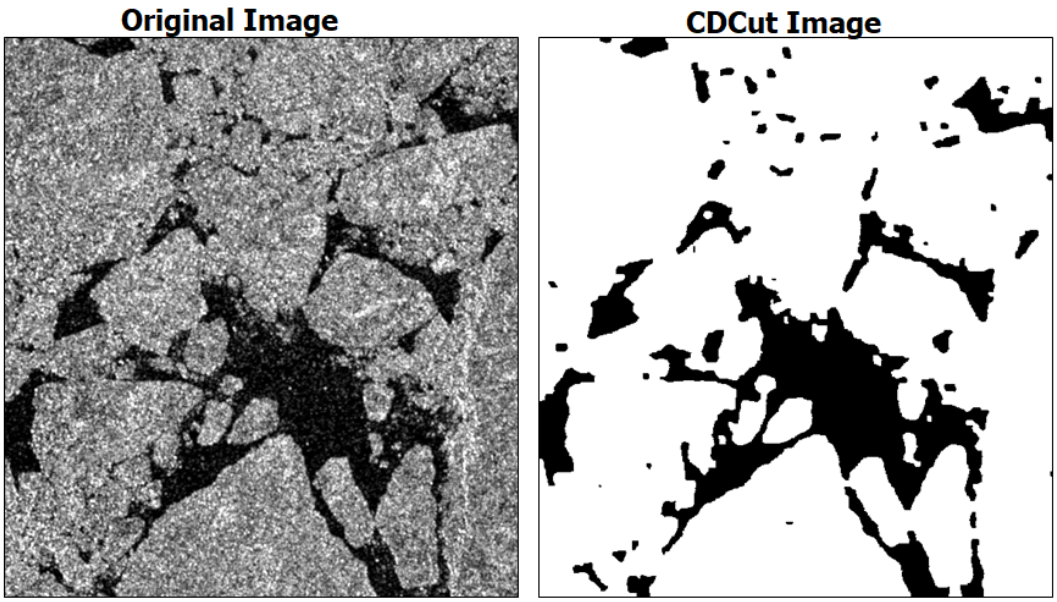

Figure 2.15: Example 1: Segmentation achieved by CDCut

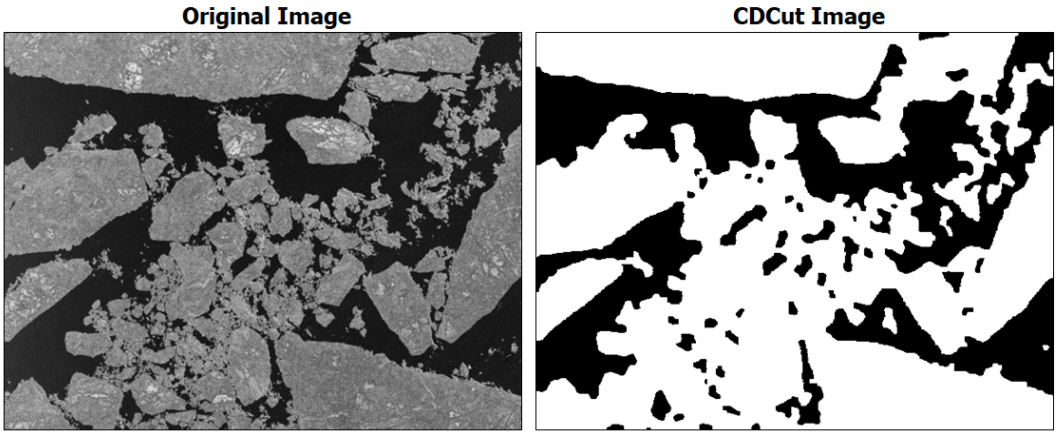

Figure 2.16: Example 2: Segmentation achieved by CDCut

2.2 Kernel Graph Cuts

In this section, the concept and capabilities of the KGC technique are briefly introduced. The KGC was first introduced by Salah et. al. [49], which was an improvement to the GC algorithm suggested in [50].

The algorithm is based on a three stage processing procedure, which incorporates;

1. K-means: For performing the clustering to find the initial clusters and their centroids, for partitioning the regions.

2. Kernel Mapping: For mapping the image data into a higher dimensional feature space, where a linear partition is easier to achieve.

3. Graph Cuts: For segmenting the image data using energy minimization theory.

2.2.1 K-means Classification

K-means [51], is by far the most popular and widely used unsupervised clustering method [52]. The algorithm partitions/ clusters data into k user-defined clusters depending on the user-specified distance of each point from the cluster's centroid. It continues to estimate the user-specified distance of each point from its cluster centroid

and re-assigns them to the respective cluster/s until the process is stabilized. The objective function, also known as the Within-Cluster Sum of Squares (WCSS), which is reduced with every iteration is given by,

$$G(y) = \sum_{j=1}^{K} \sum_{i=1}^{N} \left|\left| X_i^j - Y_j \right|\right|^2 \tag{2.42}$$

In Equation 2.42, K is the number of clusters, N is the number of data points within the ith cluster, X is the dataset (the image), Y is the vector of indices of all these data points, $|| X_i^j - Y_j ||$ is the term which finds the distance between X and Y. $G(y)$ is the objective function which is reduced with every iteration, where y is the set of cluster centres.

The K-means algorithm introduced by Llyod [51], is an iterative refinement algorithm that assigns N data points to each of the clusters K. The value for K is defined before the start of the algorithm. The algorithm steps are defined as follows,

1. Define K initial cluster centroids. This can be done in different ways, by default the algorithm uses the K-means++ algorithm suggested by Arthur and Vassilvitskii [53]. Another way is to select k observations from X at random.

2. Compute the distances of all observations to each of the centroids and then assign each observation to the cluster with the closest centroid location.

3. Compute the average of the observations in each of the newly formed cluster and obtain K new centroid locations.

4. Repeat steps 2 and 3 until there is no change in the cluster assignments or if the maximum number of user-defined iterations has been reached.

An example of a random set of data points clustered into 3 clusters using the default *Squared Euclidean* distance is illustrated in Figure 2.17.

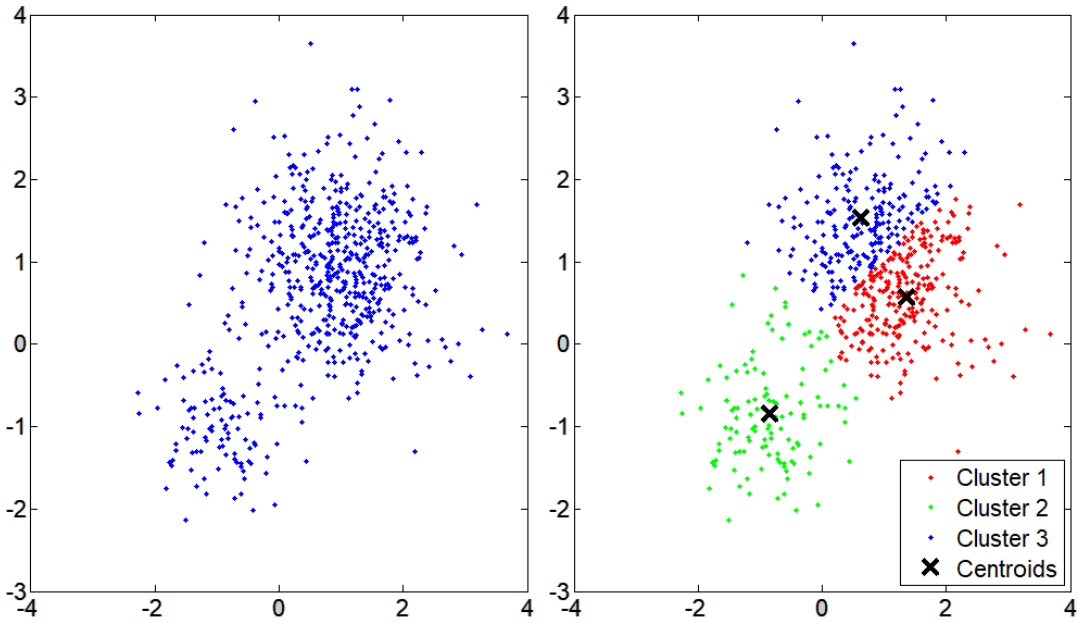

Figure 2.17: Kmeans example: (a) Un-clustered data (b) Data separated in 3 different clusters

2.2.2 Kernel Mapping

Kernel mapping, also referred to as the "kernel trick", has grown in popularity in recent years and has been used in many recent image segmentation algorithms [54–56]. For image segmentation related studies, the partitioning of data is usually non-linearly achieved in the original data space, thus increasing the complexity of the segmentation algorithms. The Kernel mapping is advantageous in these circumstances, as it aids faster segmentation and reducing the mathematical complexity, by transforming the image data into a higher dimensional feature space where a linear partitioning, through a "hyperplane", is possible. Figure 2.18 shows the implementation of the Kernel mapping.

Among the various different types of kernels available, the "Radial Basis Function (RBF)" kernel [57] has been used in the KGC algorithm. The RBF kernel has been used in many pattern data clustering algorithms such as [56, 58]. The equation [49] for

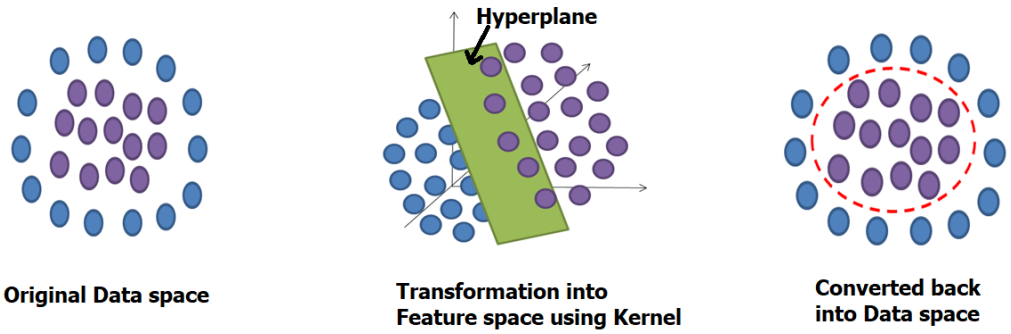

Figure 2.18: Kernel Mapping example

the RBF kernel can be given by,

$$K(X,Y) = \exp\left(\frac{-||X - Y||^2}{\sigma^2}\right) \tag{2.43}$$

The RBF has been used due to its simplicity and ease of implementation. In Equation 2.43, K is the Kernel mapped version of two-dimensional image data X. Y is the vector of centroid locations obtained previously from the K-means clustering. And σ is the user defined sigma value, usually ranging between 0 and 1. $||X - Y||^2$ is the term used to find the Squared Euclidean distance between the vectors X and Y.

Other similar kernels used for kernel mapping include the Polynomial kernel and the Sigmoid kernel, given by the equations [49],

$$K(X,Y) = (X \times Y + C)^d \tag{2.44}$$

$$K(X,Y) = tanh(C(X \times Y) + \theta) \tag{2.45}$$

2.2.3 Graph Cuts based Segmentation

The GC algorithm used in the KGC algorithm was first introduced in [50]. It is based on the energy minimisation principle, which involves reducing the two energy terms given in the following equation,

$$E(k) = S(k) + D(k) \tag{2.46}$$

In the Equation 2.46, S is the Smoothness cost, which measures the extent to which a given label k is no longer piecewise constant. A pixel is said to be piecewise constant if it varies smoothly on the surface of the object but dramatically varies at the object boundary. The smoothness cost can be represented by [50],

$$S(k) = \sum_{p,q \in N} V_{p,q}(k_p, k_q) \tag{2.47}$$

In Equation 2.47, k_p and k_q are the assigned labels for pixels p and q respectively. N is the set of interacting pairs of adjacent pixels p and q. $V_{p,q}$ is the Potts [59] interaction penalty represented by [50],

$$V_{p,q} = u_{p,q} \times T(k_p \neq k_q) \tag{2.48}$$

In Equation 2.48, $T(.)$ is equal to 1 if the argument $k_p \neq k_q$ is true, otherwise equal to 0. $u_{p,q}$ is the penalty for assigning different disparities to the neighbouring pixels p and q. The value of u is smaller for larger intensity differences between neighbouring pixels p and q. $u_{p,q}$ can be further given by [50],

$$u_{p,q} = U\left(|I_p - I_q|\right) \tag{2.49}$$

In Equation 2.49, I_p and I_q are intensities of pixels p and q respectively.

Similarly D in Equation 2.46, is the Data cost, which is the measure of the dis-

agreement between the current pixel label k and the observed data. If the pixel label k and the observed data are similar, the cost is less, otherwise it is high. The data cost can be determined by [50],

$$D(k) = \sum_{p \in P} D_p(k_p) \tag{2.50}$$

In Equation 2.50, D_p is the data penalty that measures how well the defined label k_p fits the given pixel p, given the observed data. The data penalty can be represented as equal to $(k_p - I_p)^2$. Here I_p is the intensity of pixel p.

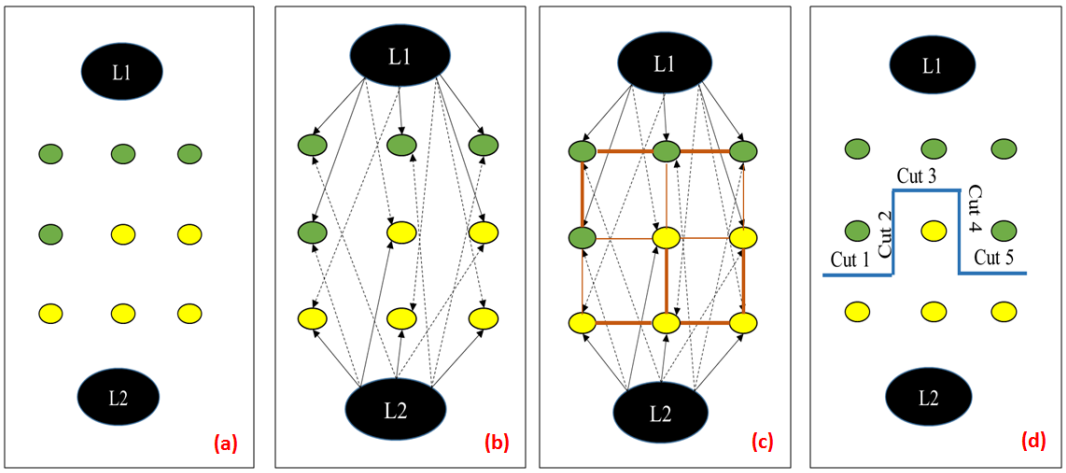

Figure 2.19: Step by Step operation of GC algorithm

Figure 2.19 shows the step by step procedure for the GC algorithm. In (a), the initial labelling for pixels has been shown, with green pixels representing label L1 and yellow pixels representing label L2 respectively. In (b), the *Data* cost for all the pixels is calculated and represented in terms of labellings L1 and L2 respectively. In (c), the *Smoothness* cost is calculated and represented in terms of weights/costs associated with adjacent pixels. Finally in (d), using the calculations from the Data and Smoothness cost, the GC algorithm performs the partitioning of clusters, using the Mini-Max Cut [60, 61] algorithm.

The GC algorithm, as mentioned previously, is based on energy minimisation to achieve optimum and effective segmentation/ partition of regions. The term "*energy*"

here represents the total weight/ cost associated with all the edges connected to the different labels assigned to each pixel within the image. Figure 2.20 [50] shows an example of how a graph is created for different labellings assigned to the pixels within the image.

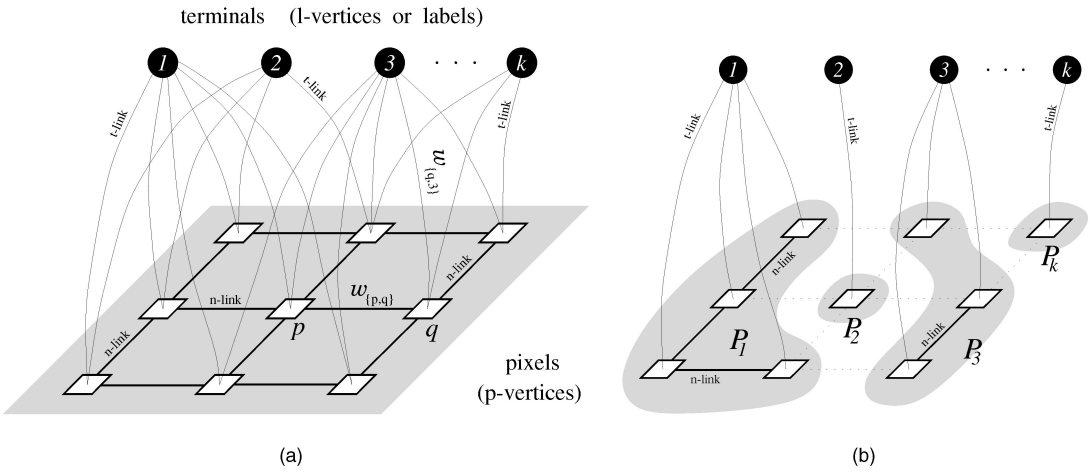

Figure 2.20: A graph constructed for 'k' terminals / labels

In the Figure 2.20, (a) shows the graph constructed for "k" labels, having their edges (weights) connected to each label before a cut is made. In (b) we see how the GC algorithm performs a cut and assigns pixels to each label based on "Minimum Cut Maximum Flow" algorithm.

The GC is a very fast algorithm, to deal with the complexity of the graph created and updating the pixel labels. This is because it performs multiple moves (pixel change) [62] at a time, as compared to standard move used in algorithms like the Iterated Conditional Modes (ICM) [63] and the Simulated Annealing [64]. Figure 2.21 shows how the multiple moves used in the GC algorithm compares with the standard move procedure.

In Figure 2.21, (a) shows the initial labelling of pixels in three different labels α, β and γ respectively. In (b), it can be seen how only one pixel in the circled region is changed with the standard move operation. However in (c) and (d), it can be seen how the GC algorithm's multiple move operation changes multiple pixels at a time. In (c),

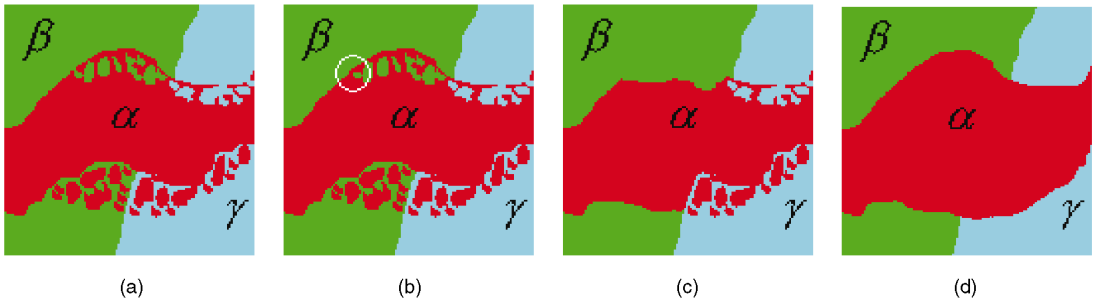

Figure 2.21: Example of standard move vs large moves

the GC algorithm uses the "$\alpha - \beta$ swap" move [50], whereas in (d), the "α expansion" move is used to change the pixel labellings. These moves are further described in detail in [50].

2.3 Evaluation Criteria

In this section, the evaluation criteria commonly used in the context of speckle filtering (2.3.1) and segmentation (2.3.2), are mentioned. These will be used to provide the efficacy of results presented in this thesis.

2.3.1 Speckle Filtering

There have been numerous quantitative parameters that have been used for assessing the filter performance to the speckle induced in SAR images. Of these, the most widely used FQA techniques, which have been mentioned in [65] have been used for forming the quantitative analysis.

2.3.1.1 Speckle Suppression Index

One of the most widely used FQA technique is the Speckle Suppression Index (SSI). It is a measure to determine the amount of speckle that has been successfully suppressed by a filter.

Lee [66] proved how, in homogeneous areas, the ratio of standard deviation to the mean is a good measure of the speckle strength. The value is then normalised with the inverse of the coefficient of variance of the original noise free image. The equation for the SSI can be denoted by,

$$SSI = \frac{\sqrt{Var(I_f)}}{Mean(I_f)} \times \frac{Mean(\hat{I}_f)}{\sqrt{Var(\hat{I}_f)}} \tag{2.51}$$

In Equation 2.51 [65], $Var(I_f)$ and $Mean(I_f)$ are the variance and mean of the filtered image I_f. Similarly $Var(\hat{I}_f)$ and $Mean(\hat{I}_f)$ are the variance and mean of the original speckle free image $\hat{I}_f$. In most cases, the SSI value tends to lower than 1. This is because the variance of the filtered image is reduced due to the speckle suppression achieved by the filter [34]. The smaller the value, the greater is the speckle suppression.

2.3.1.2 Feature Preserving Index

Another important FQA technique for comparing the filtered image with the original image, is the Feature Preserving Index (FPI). It is an important measuring criteria as it measures the filter's ability in retaining important image features such as points, objects, colours and other ridge detail. The equation for the FPI can be given by,

$$FPI = \frac{\sum_{1}^{n} (\, 2 \times I_f - I_{f1} - I_{f2})}{\sum_{1}^{n} (\, 2 \times \hat{I}_f - \hat{I}_{f1} - \hat{I}_{f2})} \tag{2.52}$$

In the Equation 2.52 [65], $\hat{I}_f$ is the value of a pixel in the original image with $\hat{I}_{f1}$ and $\hat{I}_{f2}$ being the values of its neighbouring pixels on either side of this image feature. Similarly, I_f is the value of the pixel in the filtered image with I_{f1} and I_{f2} being the value of pixels in its neighbourhood.

In most of the cases, the value for FPI is derived to below 1.0. The higher the value

of the FPI, greater is the filter's ability in retaining important image features.

2.3.1.3 Edge Enhancing Index

The Edge Enhancing Index (EEI) is similar to the FPI, but in this instance it measures the filter's ability in retaining the edges. The EEI is an important FQA parameter, especially in the Image Segmentation case, as edges greatly help in distinguishing regions apart from each other. Edges, in an image perspective, denote a sharp rise/ peaks in pixels value denoted by the SAR satellite. Thus the EEI measures the filter's response to these sharp pixel changes. The equation for this can be given by,

$$EEI = \frac{\sum |I_{f1} - I_{f2}|}{\sum |\hat{I}_{f1} - \hat{I}_{f2}|} \tag{2.53}$$

In Equation 2.53 [65], $\hat{I}_{f1}$ and $\hat{I}_{f2}$ are values of the pixels on either side of the edge in the original image. Similarly I_{f1} and I_{f2} are values of the pixels on either side of the edge in the filtered image.

Similar to the FPI parameter and due to the division of the filtered image values with the original image pixel values, the value for the EEI is generally below 1.0. The higher the value for the EEI, better is the filter's ability in preserving edges in the image after the filtering process.

2.3.1.4 Image Detail Preserving Index

The Image Detail Preserving Index (IDPC), as the name denotes, measures the correlation between the original image and the filtered image. This correlation provides an indication of a filter's ability in retaining smaller and finer image details within an image after filtering process.

Unlike the FPI and the EEI, the IDPC compares each and every image pixels in the filtered image with the noise free original image. Thus, the higher the value, better is the filter's ability in maintaining these finer image details. The equation for the IDPC

can be given by,

$$IDPC = \frac{\sum_i \sum_j (O_{ij} - \bar{O})(F_{ij} - \bar{F})}{\left(\sum_i \sum_j (O_{ij} - \bar{O})^2\right)\left(\sum_i \sum_j (F_{ij} - \bar{F})^2\right)} \tag{2.54}$$

In Equation 2.54 [65], O is the original noise free image and F is the filtered image. $\bar{O}$ is the mean for original image and $\bar{F}$ is the mean for filtered image respectively.

2.3.1.5 Peak Signal to Noise Ratio

The Peak Signal to Noise Ratio (PSNR) is often used as a quality measurement tool between original and recovered/ reconstructed image. It is the ratio between the maximum value of an image and the Mean Square Error (MSE). The ratio is normalised in the logarithmic process and the result is expressed in the form of Decibels. Higher the value for PSNR, better is the filter's ability to successfully recover the original image from the speckle induced image. The equation for PSNR can be given by,

$$PSNR = 10 \times log_{10}\left(\frac{M^2}{MSE}\right) \tag{2.55}$$

In Equation 2.55, M is the maximum value in the original image and MSE can be calculated by the following equation,

$$MSE = \frac{\sum_{IJ}\left[O(i,j) - F(i,j)\right]^2}{I * J} \tag{2.56}$$

In Equation 2.56, O is the original image and F is the recovered image after filtering. I and J denote the number of rows and columns in both of the images. Thus the MSE is the measure of the cumulative squared error between the two images. Since the PSNR value is inversely proportion to the MSE, a lower value for the MSE denotes a better quality of the image that is recovered after filtering.

2.3.1.6 Structural Similarity Index

In many of the most recent quantitative assessment used for measuring a filter's performance is the Structural Similarity Index (SSIM). The SSIM [67] used for quality assessment of images, measures the similarity between two images which is almost coinciding to that of human perception. This feature is primary reason why it has been widely used, as opposed to MSE or PSNR, in more recent speckle filtering quantitative assessments.

The SSIM computes three terms for performing the quality assessment; Luminance, Contrast and Structure. The equation for this can be given by,

$$SSIM(i,j) = [L(i,j)]^{\alpha} \times [C(i,j)]^{\beta} \times [S(i,j)]^{\gamma} \tag{2.57}$$

In Equation 2.57, L is the Luminance term, C is the Contrast term and S is the Structure term given by the equations below,

$$L(i,j) = \frac{2\mu_i\mu_j + K_1}{\mu_i^2 + \mu_j^2 + K_1} \tag{2.58}$$

$$C(i,j) = \frac{2\sigma_i\sigma_j + K_2}{\sigma_i^2 + \sigma_j^2 + K_2} \tag{2.59}$$

$$S(i,j) = \frac{\sigma_{ij} + K_3}{\sigma_i\sigma_j + K_3} \tag{2.60}$$

In Equations 2.58, 2.59 and 2.60, μ_i and μ_j are the local means for images i and j respectively. Similarly σ_i and σ_j are the local standard deviations for images i and j respectively. σ_{ij} is the cross-covariance for the two images. K_1, K_2 and K_3 are the Regularisation constants, used to stabilise the Image regions where the local mean and standard deviation are close to zero. Thus the values for these constants should be non zero and low values. Matlab, by default, sets $K_1 = (0.01 * D)^2$, where D is the specified Dynamic Range value which is set to 1 by default. Similarly $K_2 = (0.03 * D).^2$ and

$K_3 = K_2/2$. α, β and γ are equal to 1 by Matlab default.

Thus the Equation 2.57 can be simplified using the above Equations 2.58, 2.59 and 2.60 as,

$$SSIM(i,j) = \frac{(2\mu_i\mu_j + K_1)(2\sigma_i\sigma_j + K_2)}{(\mu_i^2 + \mu_j^2 + K_1)(\sigma_i^2 + \sigma_j^2 + K_2)} \tag{2.61}$$

2.3.2 SAR Sea Ice Segmentation

Over the years, there have been numerous techniques introduced and used for calculating the Segmentation accuracy of an algorithm. The most popular one of them, used in Image Processing field, is the ROC (Receiver Operating Characteristic).

It consists of the calculations for "true positives", "false positives", "true negatives" and "false negatives" respectively. The ROC curve is created with the values from the true positive rate versus the false positive values rate plotted on a graph. Figure 2.22 shows a typical example of the ROC curve and how the results for the algorithms are validated against each other.

The True Positive Rate (TPR) is the ratio of True positives versus the total positives identified. Whereas the False Positive Rate (FPR) is the ratio of False Positives versus the Total negatives identified. This can be further explained with the help of the confusion matrix shown in Figure 2.23 and by the equation,

$$\begin{aligned} TPR &= \frac{TruePositives}{TruePositives + FalseNegatives} \\ FPR &= \frac{FalsePositive}{FalsePositive + TrueNegative} \end{aligned} \tag{2.62}$$

The FPR is also referred to as Fall-out and similarly the TPR is also referred to as Recall. Along with Recall and Precision, the F-Measure (also referred to as F1 Score) [68] is used as a common way of analysing segmentation of images. Precision and Recall are important parameters which are used to assess the accuracy of the Seg-

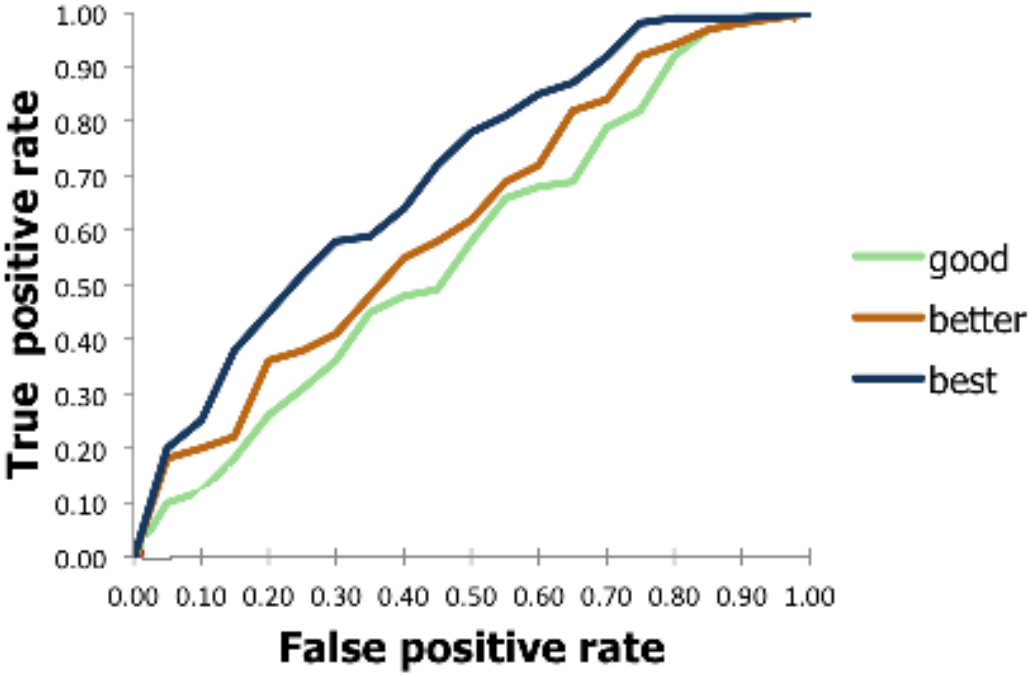

Figure 2.22: An example of the ROC Curve

mentation. A high Precision and low Recall, indicates that the Segmentation algorithm returns a lot of results, but most of them are incorrect. Whereas a high Recall and low Precision, indicates that the Segmentation algorithms returns fewer results but most of them are correct. The ideal result for a Segmentation algorithm is to have High Precision and High Recall values. The equations for calculating Precision and thus the F-Measure is given by,

$$\begin{aligned} Precision &= \frac{TruePositives}{TruePositives + FalsePositives} \\ Fmeasure &= 2 \times \frac{Precision \times Recall}{Precision + Recall} \end{aligned} \tag{2.63}$$

As seen in Equation 2.63, F-measure is the harmonic mean of Precision and Recall. Thus, higher the value for F-measure, better is the Segmentation accuracy of the algorithm. The Precision and Recall rates effectively measure, only the positive cases,

but ignore the negative cases such as the True Negatives [68].

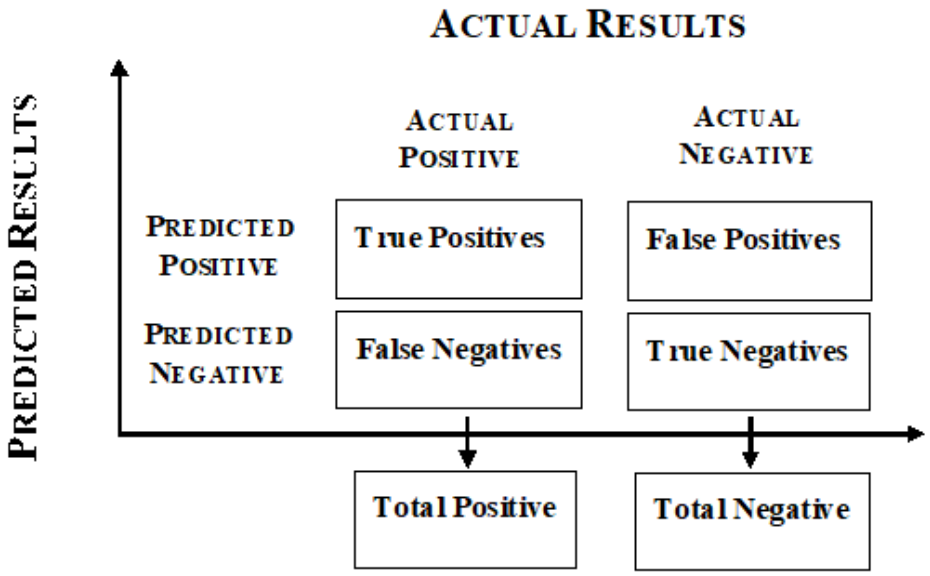

Figure 2.23: The confusion matrix used for the ROC Curve

2.4 Summary

This chapter presented the definitions and examples for various speckle filtering and the SAR Sea Ice segmentation algorithms, used in this thesis to compare with the proposed algorithms used to improve the KGC algorithm. The KGC algorithm is also introduced in this chapter and its process of achieving the segmentation of SAR images is explained. In the following chapter, all these techniques will be compared for their merits and demerits, which helps in outlining the gap in literature for aiding the KGC algorithm further to achieve improved SAR Sea Ice segmentation, which is robust, unsupervised and adjusts its parameters automatically according the Image complexity. The evaluation criteria used to provide the efficacy of the different results, is also introduced in this chapter.

CHAPTER 3

SAR SEA ICE SEGMENTATION: A REVIEW OF THE RELEVANT LITERATURE

The related work in SAR remote sensing applications is briefly introduced in this chapter. The intention of this literature review is to highlight the contributions in the following two chapters of this thesis in context with the relevant research in the particular area. First the various SAR remote sensing data sources for Earth observation is mentioned in section 3.1, along with a brief introduction to SAR Sea Ice imagery and speckle noise. An extensive literature review is then presented in sections 3.2 and 3.3; first in speckle filtering of SAR images in section 3.2 and followed by SAR Sea Ice image segmentation in section 3.3. Finally a brief chapter summary is provided in section 3.4.

3.1 SAR Remote Sensing Earth Observation

Remote sensing, in the image processing sense, is defined as the acquisition and study of information extracted from the images from an area of interest, without the use of any physical contact or using any manipulation. It is an instrument driven technology used for detection, identification and classification of objects in Earth's space [69, 70] and the wider galaxy [71, 72].

Since the launch of National Aeronautics and Space Administration (NASA)'s first satellite; Landsat-1 [73], many more earth observation satellites were launched due to

the high demand in the field, including the satellites used in this study; Sentinel-1 [74] and Terra-SarX [75] by European Space Agency (ESA).

Radar, in the early stages, had been used primarily for military and some non-military applications such as imaging, guidance, remote sensing and global positioning [76]. The first pulse radar system was developed by the Naval Research Laboratory (NRL), USA. At similar times, the United Kingdom and Germany had developed radar systems for tracking and detection of aircraft, particularly for World War II purposes. The first imaging radar system produced was the Side Looking Airborne Radar (SLAR) in the 1950s [77]. However the SLAR lacked the ability to get high resolution images without the need of very large antennas or high image distortion.

Consequently the first SAR image was produced using the advantageous of radar in signal processing. SAR allowed in achieving good image resolution by using longer wavelengths with reasonably sized antennas. Thus SAR is a side-looking radar system that simulates a large antenna or aperture electronically, by making use of the flight path of the platform. An example of radar system is given in Figure 3.1

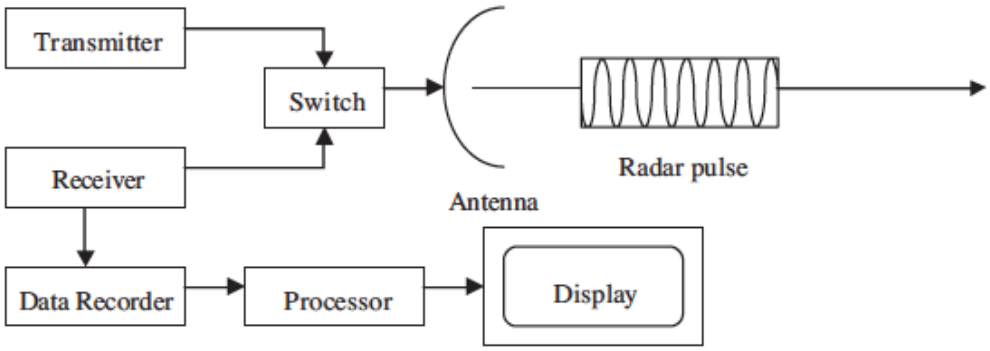

Figure 3.1: Radar system example

3.1.1 Data Sources

An acquisition device or sensor is used for capturing the electromagnetic radiation, which is reflected by various objects in the observation area, under various atmosphere

and temperature conditions. Since every object/ target possesses a unique characteristic, that can be enhanced using the reflected radiation, it is easy to discriminate objects within this observation area for accurate classification or identification. This information can be extracted using different image data types, like optical or radar imagery, using the sensors mounted on "platforms" (sensor carrying vehicles/ devices) orbiting the exploration regions. Figure 3.2 [78] shows an example of the various types of sensor platforms used for remote sensing applications.

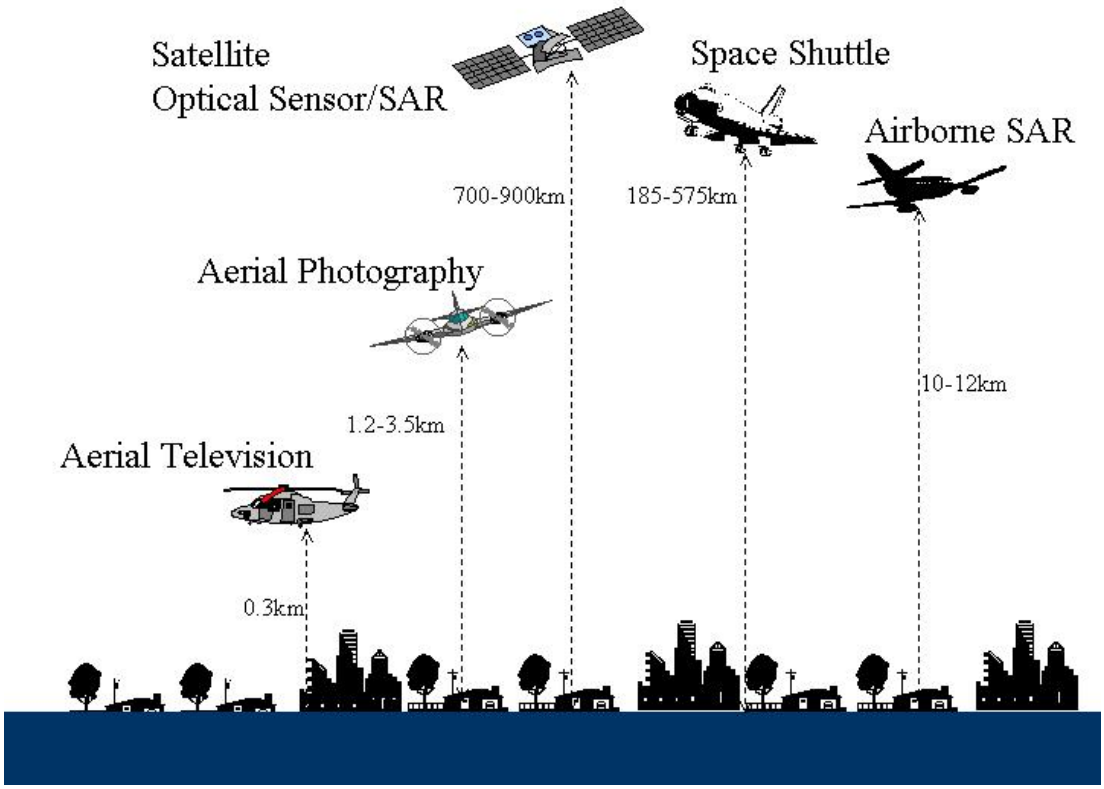

Figure 3.2: Different types of platforms used in remote sensing applications

The information extracted by the remote sensing images is used for various diverse applications, for further analytical studies on better land usage, agriculture development, climate observation, underwater exploration, route planning for ships, among others.

With the advances in technology, improvements to the optical devices and sen-

sors have been made while considering the numerous technical aspects of the observation such as geometric calibration, antenna attenuation, engineering life, embedding structures, observation index etc. With more information provided, potentially better and accurate analysis can be performed on remote sensing applications in the recent decades. This has led the way to the introduction of the multi-spectral as well as hyper-spectral imaging technology being used for better quality and robust image extraction.

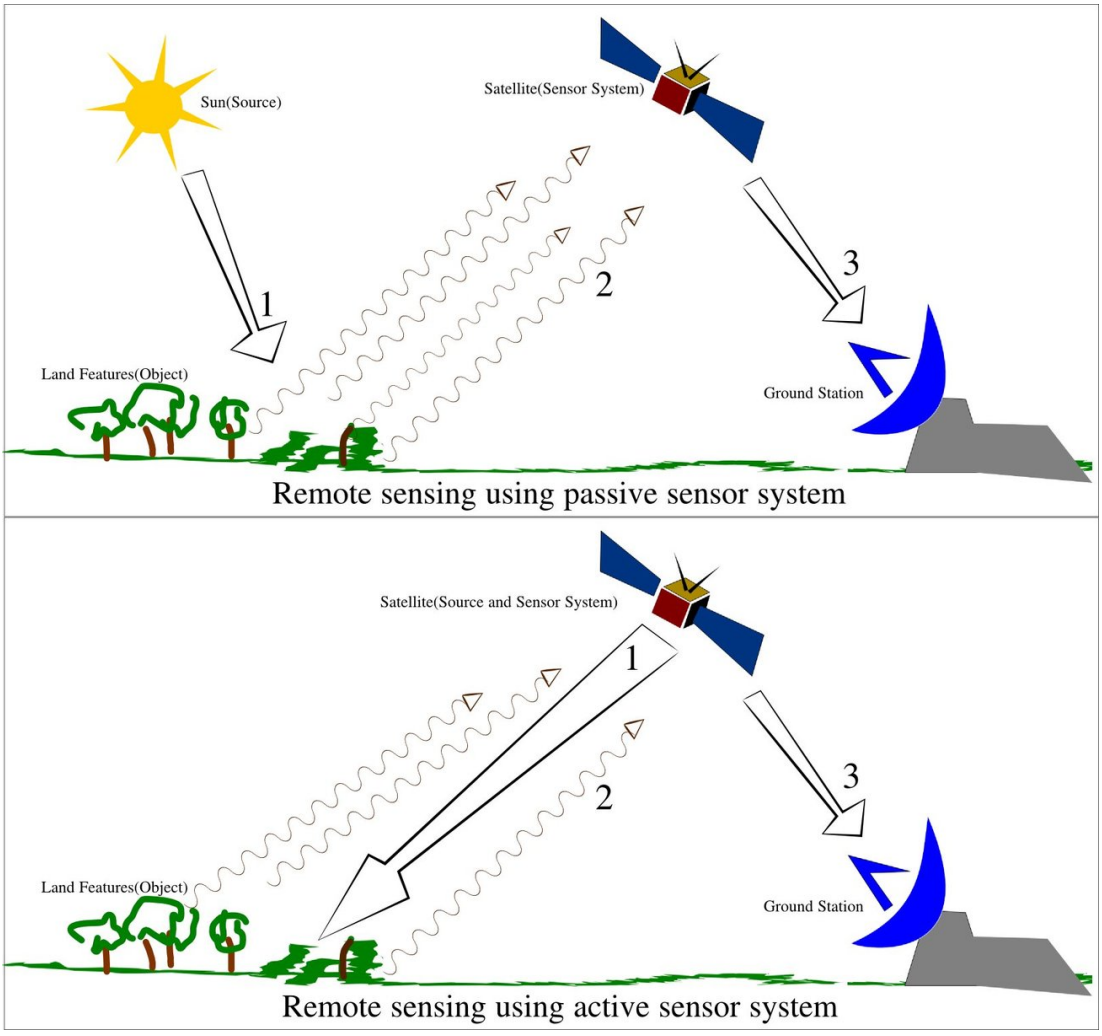

Figure 3.3: Different types of remote sensors

Types of Remote Sensors The remote sensing sensors are primarily divided into two types; active and passive sensors. **Active** sensors like radar, provide their own source of energy for illuminating the objects within the observation area. While **Passive** sensors rely on the natural energy, for example the sun's radiation, for illuminating these objects within the observation area. This can be further explained with the Figure 3.3 [79].

It is difficult to say that an active sensor is better than a passive sensor and vice versa. Each group of sensors have their own benefits and drawbacks, which make them unique to their own applications. While active sensors can be used any time of the day, the data produced isn't as accurate as that of the passive sensor, which give real-life type of accuracy. Whilst active sensors primarily look at the observation point at an angle, passive sensors usually point straight down. Thus the active sensor imagery of a particular region might be completely different to that taken with a passive sensor, each having its own merit and de-merit.

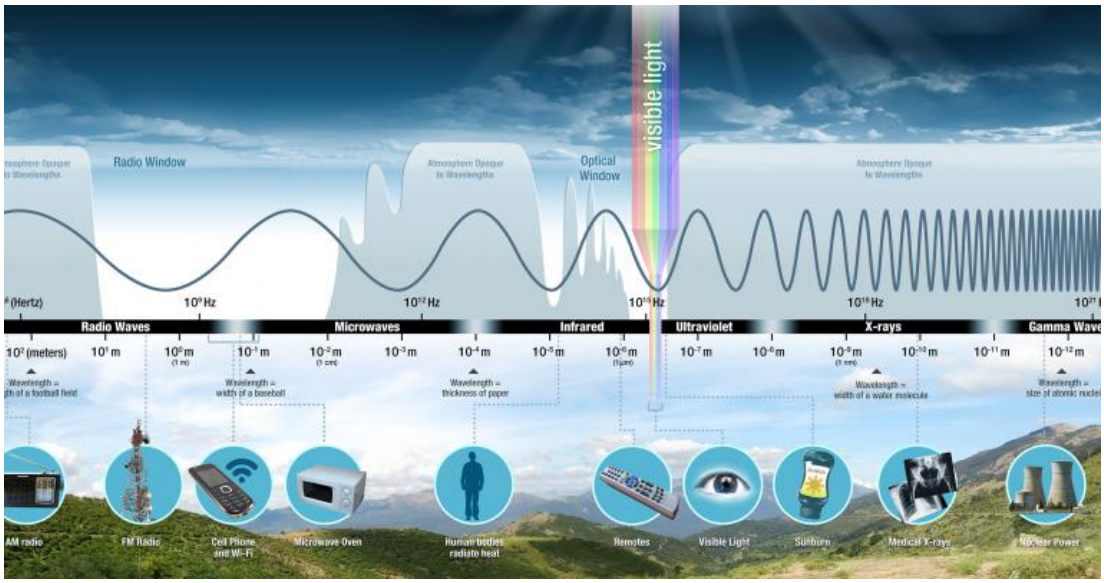

Figure 3.4: The Electro-Magnetic Spectrum defined by NASA

Active sensor data such as SAR images are particularly important for this study, as they help to distinguish the surface roughness of the ice from snow and a trained ob-

server can easily deduce the age and thickness of the ice using this data. Passive sensor on the other hand is not very effective in such cases as it find it difficult to completely distinguish between ice and snow and showing just a bright white region for both.

Passive sensors measure the natural energy at particular frequencies known as wavelengths, for example; visible (390 - 700 nm), infrared (750 nm 1 mm), ultra-violet (100-400 nm) etc. This is further explained in Figure 3.4 [80].

3.1.2 High Resolution Visible Imagery for Quality Improvement

Passive sensors are mostly comprised of optical remote sensing image data and they can be further classified into the three types, based on number of spectral bands used in the image formation process; Panchromatic, Multi-spectral and Hyperspectral.

Panchromatic images are formed when the sensor is single channel detector and sensitive to radiation within a broad wavelength range. If the wavelength range of the sensor coincides with the visible range, a "black and white" image is formed that resembles the apparent brightness of the targets/ objects. The spectral information, however, is lost. The most common examples of Panchromatic imaging systems include IKONOS (from greek term for image "Eikn") [81], SPOT (from french "Satellite pour l'Observation de la Terre") [82], ALOS (Advanced Land Observing Satellite) [83] etc.

Multi-spectral images are produced by sensors that measure the reflected energy with several specific wavelengths of the electro-magnetic spectrum. Multi-spectral sensors usually have around 3 to 10 different band measures for each pixel of the image they produce. Some examples of these bands include; visible green, visible red, near infrared respectively. Each channel is sensitive to radiation within a narrow wavelength band. Some examples of Multi-spectral imaging systems include Landsat [73], SPOT [82], IKONOS [81], Quickbird [84] etc.

Hyperspectral sensors measure energy much more narrower bands than multi-spectral sensors (10-20 nm) and they could contain as many as 200-500 spectral bands which form the "hypercube". The numerous bands of the hyperspectral sensors pro-

vide a uniform spectral measurement across the entire electromagnetic spectrum. This precise spectral information contained in hyperspectral imaging data, enable better identification and classification of targets within the observation area. However, they are more sensitive to subtle variations in the reflected energy. Also due to the increased amount of bands, the hyperspectral imagery comes at the cost of increased computational complexity, although many recent studies aim to tackle with this shortcoming. The Hyperion is the most notable example of the hyperspectral imaging satellite.

Figures 3.5 and 3.6 show the comaprion between the various high-resolution visible images described above.

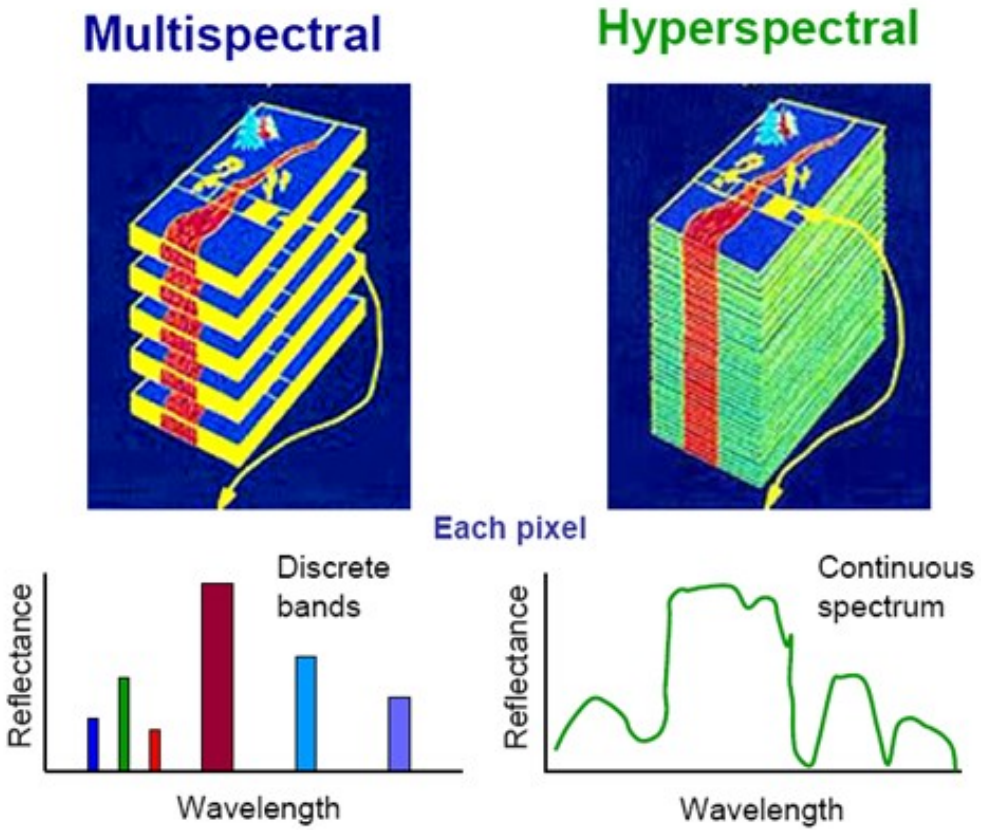

Figure 3.5: Multi-Spectral versus Hyper-Spectral Data

Figure 3.6: Panchromatic (a) versus Multi-Spectral Data (b)

3.1.3 SAR Sea Ice Imagery

Regardless of the various advantages of SAR to cover primarily inaccessible areas, its robustness to harsh weather conditions or illumination changes, many scientists and experts still rely on manual identification for interpretting the sea ice regions. This is usually done in the form of ice charts and egg codes [85]. While interpreting this data, the scientists manually select the regions which are visually homogeneous or that are noticeably separated by a boundary. Each of these regions can have several ice types, e.g. New Ice, Young Ice, First-Year Ice, Old Ice etc. [86].

New Ice is a general term given to recently formed Sea ice at the beginning of winter, which is less than 10 cm thickness and includes frazil or grease ice, slush and

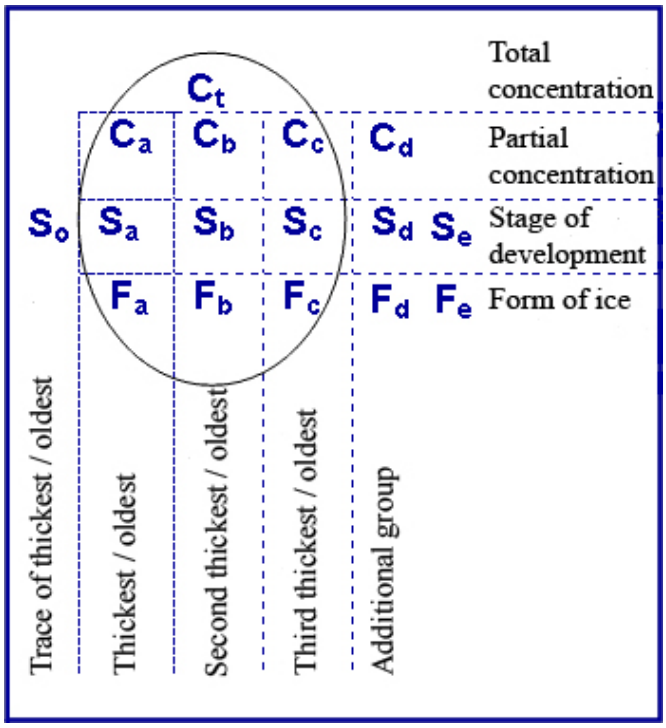

Figure 3.7: WMO defined Egg-Codes for SAR Sea Ice Imagery

shuga. This is the weakest form of ice which after more freezing temperatures forms into *Young Ice*, having thickness ranging between 10 to 30 cm. The Sea Ice which survives near the end of the winter season, then forms into *First-Year Ice*, which has a thickness greater than 30 cm. Ice that survives the harsh summer season and sea waves, forms *Old Ice*, which is sometimes also referred to as "*Multi-Year Ice*". More details about types and forms of Sea Ice can be found in [85] and [86].

The experts associate the Sea Ice region with an "*Egg Code*", shown in Figure 3.7. As seen in Figure 3.7, an Egg Code is an oval shaped symbol that contains the basic information about concentrations, stage of development of Sea Ice and the floe-size/ form of the ice contained within the region [85].

But these type of manual interpretation of data from Sea Ice have several deficiencies and are biased due to the human-element. With increased demand of Sea Ice monitoring in recent years, it has been increasingly important to develop a robust and accurate computer-based system, which is unbiased, to interpret the SAR Sea Ice im-

ages. Some of these have been mentioned extensively in section 2.1.2, some of which are used in comparison with the technique chosen for this study, i.e. the Kernel Graph Cuts (KGC) technique. This research aims to improve the understanding of the different trends as well as conditions affecting the size and shape of the Arctic sea ice floes for the current and developing a further understanding by means of comparison with the past several years data [87].

3.1.4 Speckle Noise

It is a well known fact that SAR images are affected by the "grainy salt and pepper" noise known as "speckle". The speckle is formed due to the coherent processing and dephased reflected wavelets [24], by which a SAR image is formed. More details about the SAR image are given in Section 3.1.1 and also very well documented in [88–90]. Figure 3.8 [89] shows how a speckle is induced into a SAR image.

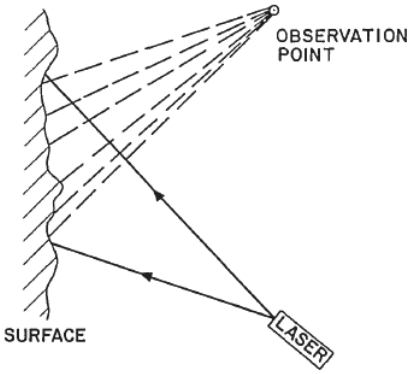

Figure 3.8: Addition of Speckle in a SAR Image

The presence of speckle affecting the SAR images were quickly recognised by early laser technology researchers as early as 1960 [91, 92]. As seen in Figure 3.8, the coherent light used in SAR processing and the roughness of the most surfaces on the optical wavelength, leads to many independent scattering waves being produced. The propagation of the reflected light to a local observation point and the addition of these varying and delayed scattered components produces a granular pattern, we refer

to as “speckle”. The scattering of these components is dependant on the surface and geometry of the observation area.

The presence of speckle greatly reduces a segmentation algorithm’s efficiency to detect targets/ objects within the image, thus creating a major problem for SAR image researchers as ourselves. The Figure 3.9 shows a typical example of a RGB image affected by Speckle. The image in the middle (b) is the speckle induced version of the original RGB image on the left (a) and (c) is the image filtered using a simple Wiener [37] filter with window size 3×3.

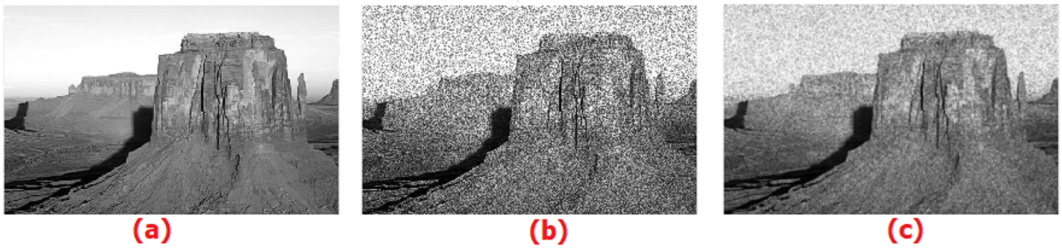

Figure 3.9: Speckle Example: Desert Image

Speckle filtering has been an active research for over 20 years. Over the years, many researchers and experts have proposed various algorithms to deal with speckle, each having their merits and demerits. In the following section 3.2, the merits and demerits of them are discussed.

3.2 Speckle Filtering for SAR Image Improvement

With the advancement in technology, there has been in increase in high resolution SAR images available, more than ever. With speckle noise evident in these images, due to the way it gets embedded in the images, many researchers have proposed various techniques to tackle this issue. Most notable of these is the Lee filter [12, 22], in which the local image statistics are used to identify an image pixel as“valid” or “invalid” pixels. The“invalid” in this term, refers to the speckle identified pixels that need to be removed or smoothed in order to extract useful information of the SAR images.

Frost [29, 30] and Kuan [31, 32] filters are the other popular techniques developed around the time when the first Lee filter was introduced and have been widely used in the context of speckle filtering. The three filters; Lee [12, 22], Frost and Kuan, have been derived from the MMSE filter given by,

$$\hat{I}(i,j) = E[I(i,j)] + \frac{z^2(i,j)}{z^2(i,j) + \sigma_N^2(i,j)} \times (I(i,j) - E[I(i,j)]) \tag{3.1}$$

In the Equation 3.1, $E[I(i,j)]$ is the local mean of the image I. $z^2(i,j)$ is the local variance of the image I and $\sigma_N^2(i,j)$ is the variance of the noise. $\hat{I}$ is the filtered image produced using the MMSE filter.

The Kuan and the Lee filter are almost identical to each other, apart from the way the weighted coefficient is selected for replacing the speckle pixel. The Frost filter is a bit complex as it uses a weighted mean for calculation and can almost be considered as a adaptive weighted mean filter [93]. In Figure 3.10 [22, 30, 31], the filtering formula and calculation of the weighted coefficients for these filters is given.

Filter	Filtering Formula	Weighted Coefficients
Lee	$\hat{I} = I * W + \bar{I}(1 - W)$	$W(x,y) = 1 - \frac{C_{si}^2}{C_I^2(x,y)}$
Kuan	$\hat{I} = I * W + \bar{I}(1 - W)$	$W(x,y) = \frac{1 - C_{si}^2/C_I^2(x,y)}{1 + C_{si}^2}$
Frost	$\hat{I} = I * W$	$W(x,y) = K_1 \exp\left(-K_d C_I(x,y)\sqrt{x^2 + y^2}\right)$

Figure 3.10: Filtering formula and Weighted Coefficients calculation for Lee, Kuan and Frost filter

But due to the various disadvantages of these filters, in particular to blurring the images considerably as compensation for achieving higher speckle suppression, Lee then

proposed the sigma factor added Lee [23–26] filter for identifying and labelling the speckle pixels to be removed from the image. The speckle pixels are identified using the equations given in section 2.1.1.1. This was proposed to deal with the drawbacks of the previous filter in retaining edges and other useful image information. Many authors have since proposed various modifications to this Sigma filter, including the LSF [33], mentioned in section 2.1.1.2, which uses an adaptive box filter for smoothing the noise.

However, both these proposed filters still proved redundant in suppressing speckle without blurring the image information too much, although this was much better tackled by the LSF. Thus, the AMF [34] was proposed which utilises the advantages of the local median filter in retaining edges better than a mean filter, as used in the filters described above. The theory, as explained in section 2.1.1.5, is similar to that of the Lee Sigma and the Local Sigma filters; identify speckle pixels using the local statistics and multiplier value 'M' and then filter only these pixels using the "valid" pixels for calculation only. The difference in the AMF is that it uses the median value of the pixel to replace the erroneous speckle pixel value. The AMF as presented in [34], has various advantages over all of the previous filters but comes at a cost of slight increase in computation times. It is very good in retaining the object edges which are vital for a segmentation algorithm, along with suppressing speckle.

Another widely used filter is the Wiener filter described in 2.1.1.4, commonly used to remove motion blur caused in RGB images. Similar to that of the original Lee filter, the Wiener filter uses MMSE to filter the noise present in the image. It is the most basic of filters used throughout the literature and thus predictably has many drawbacks, such as significantly higher blurring of images, loss of object boundaries etc. These are similar as noted in the Kuan, Frost and the standard Lee filter.

Finally, the BF which is not very commonly used for SAR images, is mentioned in section 2.1.1.3. It works relatively well on speckle noise despite the fact that it was originally introduced as an edge-preserving filter to provide single band, instead of multi-band filtering for colour images. It is a combination of domain filtering (geo-

metric closeness) and range filtering (photometric similarity). However this filter also has significantly increased computation times, which are even more than the AMF.

Apart from the above filters, in recent literature, more SAR specific algorithms have been proposed by authors to suppress speckle and also preserve vital image information. These usually involve conversion into a different domain space such as the wavelet domain [94, 95] or the PCA induced space [96], as they have proven to be more efficient in denoising the image as the signal and noise are easier to separate [96]. In [94], the Wavelet Based Image Denoising Nonlinear SAR (WIN-SAR) filter, is proposed which incorporates the Bayesian based algorithm within the Wavelet analysis. They designed a maximum a posteriori (MAP) processor which relies on heavy-tailed alpha-stable models. This provided an increase in speckle reduction and signal detail preservation than traditional wavelet shrinkage methods. The processor is based on a solid statistical theory rather than using an ad-hoc thresholding parameter. However, the authors reported that the filtering is significantly time consuming due to the various calculations for the prior distribution parameters needed for each wavelet decomposition scale of interest and thus best used for off-line processing.

In [96], a SAR image denoising technique is proposed, based on clustering the noise-induced image into disjoint local regions and denoising each of these regions by Linear Minimum Mean-Square Error (LMMSE) filtering in the PCA domain. The K-means algorithm is used for clustering and to reduce the dimensionality, and is fed with several leading principal components in the logarithmic domain, identified by the Minimum Description Length (MDL) criterion. The denoising, which is the first in its case, is based on the Additive Signal-Dependent Noise (ASDN) model to derive PCA-based LMMSE denoising for multiplicative noise. This filter requires less computation and is capable of adaptively identifying patches similar to each other by considering the closeness to different cluster centres using Euclidean distance. Similar to the WIN-SAR filter, the noisy image is split into several patches in the transformed domain where filtering takes place and the patches are reconstructed back into the orig-

inal domain.

Finally in [95], an extension to the Block Matching 3-D (BM3-D) filter [97] is proposed and thus called the SAR-BM3-D filter. The filter is based on the non-local filtering and wavelet domain shrinkage. As opposed to the BM3-D filter, the SAR-BM3-D filter uses: 1) Ad-hoc measure to form similar image block groups, 2) Using Local Linear MMSE (LLMMSE) criterion in the shrinkage phase and 3) Use of Undecimated Discrete Wavelet Transform (UDWT) to improve estimation reliability in step 1. This technique however doesn't correctly estimate the speckle statistics, especially at higher resolution and thus them being different than the ones mentioned in the simplified model. This is visible from the difference in performance observed on the various tests conducted on similated as well as real SAR images.

Consequently, although wavelet-based denoising methods have proved better efficiency than classical filters, limitations reside in the inadequate representation of various local spatial structures in images using the fixed wavelet bases [98, 99].

3.3 SAR Sea Ice Segmentation

Due to the decline in the Arctic region, it has increasingly become important to develop a better understanding of the various environmental as well as social impacts on the sea ice extent. Consequently, many authors have performed their studies on the SAR sea ice floe segmentation.

Studies for SAR Sea Ice Segmentation have been done using dynamic thresholding and coded human expert knowledge [2], using two bands, each consisting of brightness and variance measures respectively [3] and also using mathematical morphology [1]. In recent years, similar studies have been done; Using a combination of two texture analysis methods; Markov Random Fields (MRF) and Gray-Level Co-occurrence Probabilities (GLCP) [100], Stochastic Ensemble Consensus approach [5], MRF on its own [4] and finally Pulsed-coupled Neural Networks (PCNN) [101].

Although these traditional approaches have been proposed, implemented and tested for various types of images including the SAR Sea Ice images, they still face some disadvantages as they only consider the local information of pixels such as intensities for segmentation [102]. To improve the segmentation results by considering the spatial position and other similar information, couple of graph based approaches have been proposed in [103, 104]. The segmentation criterion for the first graph based approach was based on breaking of Minimum Spanning Tree (MST) edges with large weights [103]. These posed some drawbacks of wrong region merging and splitting, which were later addressed by normalizing the weights of the edges [104].

Recent developments in energy based image segmentation techniques, have led to several new algorithms like the energy minimization based GC [50] for Image Segmentation. GC based on an iterative and interactive model [105] has been used for foreground extraction, whereas GC based on image histogram analysis is used for segmenting the regions in an image [50, 106]. Similar energy based techniques have also been used for image segmentation; Region Competition [107], Active Contours (AC) [44, 108] and Level Set using Mumford and Shah model [45].

In many recent studies, kernel mapping or popularly known as the"kernel trick", has been used for effectively getting better and faster segmentation results [54, 55, 109, 110]. The kernel function is popular because it implicitly maps the data into higher dimensional space, known as the feature space, so that a linear partition is possible before being mapped back into the original input space [111]. Thus, this implicit mapping, overcomes the huge computation overload caused by the various calculations required for graph based techniques. Based on this advantage, the KGC [49] has been proposed and implemented for Image segmentation, which incorporates the advantages of the kernel mapping and the GC algorithm [50].

After its initial implementation and consequent adaptations in Medical Imagery [112–115], the KGC has been used for comparison in few very recent SAR Sea Ice based image segmentation studies. It has been used for comparison with a newly pro-

posed technique, Kernel Fuzzy C-means algorithm with pixel intensity and local information [ILKFCM] [116],which is based on the pixel intensities and other pixel related information for effective SAR Sea Ice segmentation. The technique also incorporates the weighted fuzzy factor and kernel metric measures for improving the segmentation results. Similarly, the KGC has been used for comparison with Multi-kernel Level Set Method (MK-LSM) [117], which comprises of combination of the advantages of the Level Set method (LSM) and the Multi Kernel (MK) technique for segmentation of Very High Resolution (VHR) SAR Sea Ice imagery. The MK technique is useful for selecting an appropriate stopping function for the evolving curve in the LSM.

Also more recently, the KGC has been compared with Closeness Degree Cut (CD-cut) and Minimum Description Length Criterion (MDLC) based algorithm [48]. It proposes a new clustering algorithm, which first over segments the data using Watershed [42] algorithm, then builds a graph using the nodes in the over segmented image followed by spectral clustering based on CDcut and finally using the MDLC for efficiently determining the clustering number. Some of these algorithms used for comparison with the initial segmentation results, are mentioned in the section 2.1.2.

Watershed algorithm, as mentioned previously, provides a highly over-segmented result and to achieve any better results, the threshold parameter for identifying the various regions need to be modified through various testing. This can be very time consuming as well as being semi-supervised technique. However, the watershed algorithm is very good at eliminating the under-segmented regions and thus has been used for making the Ground Truth images for the various SAR datasets. Similarly, the Level Set algorithm mentioned in 2.1.2, is somewhat similar but mostly provides worse segmentation results than the KGC algorithm. It is also very time consuming algorithm, again dependant on semi-supervision and increased computation times to achieve better results. Unlike the Watershed, the Level Set algorithm provides a decrease in over-segmentation but at the cost of increase in under-segmentation. The CD-Cut algorithm has been proposed as an improvement to the KGC by using the

MDLC criterion for performing clustering. But this improvement is yet again met with increased computation times and more often, as mentioned in the following chapters, the KGC still provides comparative and sometimes better results than the CD-Cut algorithm.

In all of these comparative studies, the KGC has continued to give optimum segmentation results and in some cases given comparable or better results. It is also worth noting that most authors have opted to propose redefined algorithms for the KGC rather than opting to aid the algorithm itself to produce comprehensive segmentation results, which is done in this study.

Apart from the above SAR Sea Ice image specific algorithms, in recent literature, two SAR image specific algorithms are also introduced [118, 119]. In [118], the use of an Artificial Bee Colony (ABC) algorithm [120–122] is employed for providing a fast segmentation of SAR images. The algorithm uses the ABC to estimate the threshold for the image segmentation, using gray levels. Discrete wavelet transform, combined with Grey Theory to produce 2-D Grey Entropy, is employed to suppress the influence of speckle on the segmentation result, thus aiding the forging guide for the bee colony of the ABC algorithm. The technique is very fast due to the high convergence ratio of the ABC algorithm. However despite these advantages, the technique is weak as it requires user-experience to define the control parameters and due to the use of a single threshold in the global thresholding procedure, the image is sub-divided into foreground and background only, which maybe ideal for simple SAR images but highly problematic for complex SAR images as that for identifying Sea Ice floes.

Similarly in [119], SAR segmentation is achieved using the Maximally Stable Extremal Regions (MSER) and improved spectral clustering. First the input image is filtered using the Frost filter, followed by Morphological Closing to remove noise and yield a smoother image for further processing. Next, the image is transformed from the pixel domain to multiple disjointed regions using the MSER. All the different regions after this procedure, are treated as nodes to construct a graph structure. Different num-

ber of nodes are assigned to represent each region according to area ratio between the regions rather than considering it as only one graph node. This takes into account the area differences among the regions and retains more image information after MSER. Smaller the distance between two spatial regions, greater is the likelihood of clustering two regions into one class. Finally, the improved spectral clustering is performed to generate the image segmentation. K-Harmonic means (KHM) is used instead of K-means, in the clustering method. This is due to KHM uses harmonic averages of distances from each data point to the centres, as components to its function. Thus, by replacing the minimum distances from data point to centres, the KHM addresses its intrinsic problem and is less prone to initialisation error as noticed in K-means. However, the choice of the adjusting parameters is a bit ambiguous and not adjustable, for *Scaling Factor S* determining the sensitivity of intensity differences and *Adjusting Constant H* determining the sensitivity of spatial distances between regions. This thus suggests that the algorithm works only if these parameters are known or derived through various testing.

3.4 Summary

This chapter reviews the related work on SAR remote sensing earth applications. First, the concept of SAR and other forms of remote sensing data sources are described, highlighting the various advancements in the area.

The data acquisition and conditioning is addressed by the satellite data providers like NASA, ESA, ASF, JPL etc. Thus, the researchers focus their knowledge on important feature and target extraction from the data provided. Subsequently, the relevant and popular techniques in speckle filtering is discussed, including the necessity for performing speckle filtering. Various algorithms past and present are shown, along with flowcharts and examples of their implementation.

Similarly, the relevant literature in SAR image segmentation is discussed. It is shown how many studies have been done to suggest improvements to the KGC algorithm, yet the KGC has proven to be equally or almost in par with the proposed algorithms. Finally, numerous types of image fusion, whether level-based or domain-based, are mentioned and reviewed.

The various techniques mentioned in this chapter have been used for comparison in chapters 4 and 5. This has been primarily done to highlights the merits and contribution of this thesis with the relevant literature in the field of research.

CHAPTER 4

ADAPTIVE FILTERING FOR EFFECTIVE PRE PROCESSING OF SAR IMAGES

4.1 Introduction

Speckle is a common noise phenomenon affecting SAR images and the "speckle filtering" has been an active research field for over 20 years. Due to the fact that noise is a product of the the mean and standard deviation, associated with the SAR image, most of the early filters were developed on the theory of reducing these parameters. In section 2.1.1, some of these popular filtering algorithms used in speckle filtering are mentioned. Whilst many researchers have proposed various solutions on tackling the speckle, this has so far still not been adequate in helping to solve the main problem caused for extracting the data out of the images itself.

The use of an adaptive region-based filter is proposed, which incorporates the merits of both the AMF [34] and the Wiener filter [37]. The AMF has advantages of retaining the important edge and feature information contained within the image, whilst the Wiener filter has the ability of achieving high level of speckle suppression.

This chapter is organised as follows; Section 4.2 gives information of the proposed technique for tackling speckle noise, Section 4.3 describes the image datasets used, as well as the evaluation criteria. Experimental results and analysis of the various images used are given in Section 4.4 and Section 4.5 gives the summary of the findings and contributions.

4.2 Proposed Region and Adaptive Speckle Filter

In this section, the advantages of the AMF [34] and Wiener filter [37] are combined together to form a Modified Adaptive Median filter (MAMF). It uses the MMSE estimator to effective reduce speckle from the SAR images and uses local image statistics to identify the speckle pixels. The proposed filter is thus a further modification to the AMF using MMSE estimation, for getting even better accuracy in terms of edge and feature preservation.

4.2.1 Modified Adaptive Median Filter

The proposal of an adaptive and region based speckle filtering algorithm is inspired by the latest trend to build more robust algorithms, especially for retaining edges. The proposed adaptive algorithm "'MAMF" is based on the theory and advantages of the Wiener [37] and the AMF [34]. It is a combination of the MMSE estimation used in the Wiener filter and the identification of speckle pixels from the AMF.

Assuming a moving window centred at pixel $I(i,j)$ and with window size given by $2m+1$, where m is the user defined value for the window size equal to odd values such as $3,5,7$ etc. The local mean $\hat{D}(i,j)$ and standard deviation $\sigma(i,j)$ can be calculated by,

$$\hat{D}(i,j) = \frac{S(i,j)}{n(i,j)} \tag{4.1}$$

$$\sigma(i,j) = \sqrt{\frac{\sum_{a=i-m}^{i+m}\sum_{b=i-m}^{i+m}\Big(I(i,j) - S(i,j)\Big)^2}{n(i,j)}} \tag{4.2}$$

In the Equations 4.1 and 4.2, $S(i,j)$ is the sum of pixels in the moving window, whereas $n(i,j)$ is the number of pixels within this window.

Thus the bounds are created for identifying and labelling the pixels within the im-

age I as "valid" or "speckle" pixels, given by the Equation,

$$\begin{aligned} LB(i,j) &= \hat{D}(i,j) - (K \times \sigma(i.j)) \\ UB(i,j) &= \hat{D}(i,j) + (K \times \sigma(i.j)) \end{aligned} \tag{4.3}$$

With the window centred at $\bar{I}(i,j)$, the valid and speckle pixels are identified and labelled for every pixel $\bar{I}(i,j)$. Where "0" indicates speckle pixels, whereas "1" indicates a valid pixel respectively.

$$\begin{aligned} S(i,j) = 0, \quad if \quad I(i,j) < LB(i,j) \quad or \quad I(i,j) > UB(i,j) \\ S(i,j) = 1, \quad if \quad LB(i,j) \leq I(i,j) \leq UB(i,j) \end{aligned} \tag{4.4}$$

The Equation 4.3 is exactly similar to that given in Equation 2.28 [34], where K is the user defined constant which ranges between 1 and 2. Similarly Equation 4.4 is exactly similar to that given in Equation 2.29

However, contrary to the AMF, the replacement value $R(i,j)$ is derived using the MMSE estimation shown in Equation 3.1. However, instead of using the mean value as given in the equation, the median value (as used in AMF) of the filter window is used. Thus the MMSE filter estimation can be thus rewritten as,

$$R(i,j) \; = \; T(i,j) \; + \; \frac{z^2(i,j)}{z^2(i,j) \; + \; \sigma_N^2(i,j)} \; \times \; (I(i,j) - \delta(i,j)) \tag{4.5}$$

In the Equation 4.5, $R(i,j)$ is the replacement value for the central pixel. $T(i,j)$ is the median value of all the valid pixels within the filter window. Similarly $z^2(i,j)$ is the variance of the filter window and $\sigma_N^2(i,j)$ is the corresponding noise variance.

Thus the proposed MAMF identifies speckle and valid pixels using the local statistics, this being similar to the AMF. But unlike the AMF, the proposed filter uses the MMSE estimation used in the Wiener filter to use as the replacement value for the central pixel. Furthermore, unlike the Wiener filter, which uses the mean value for

calculation in the MMSE estimation, a median value is used, which has been proven to be better way of estimating the replacement value [34].

It is important to note here that, the central pixel value is only replaced if it has been identified as a "speckle" pixel in the above process and using the calculations derived from the "valid" pixels identified only. Thus the erroneous values are removed and not used in the calculation of the filter parameters for the replacement value. The implementation of the proposed filter can be further explained by the flowchart in Figure 4.1.

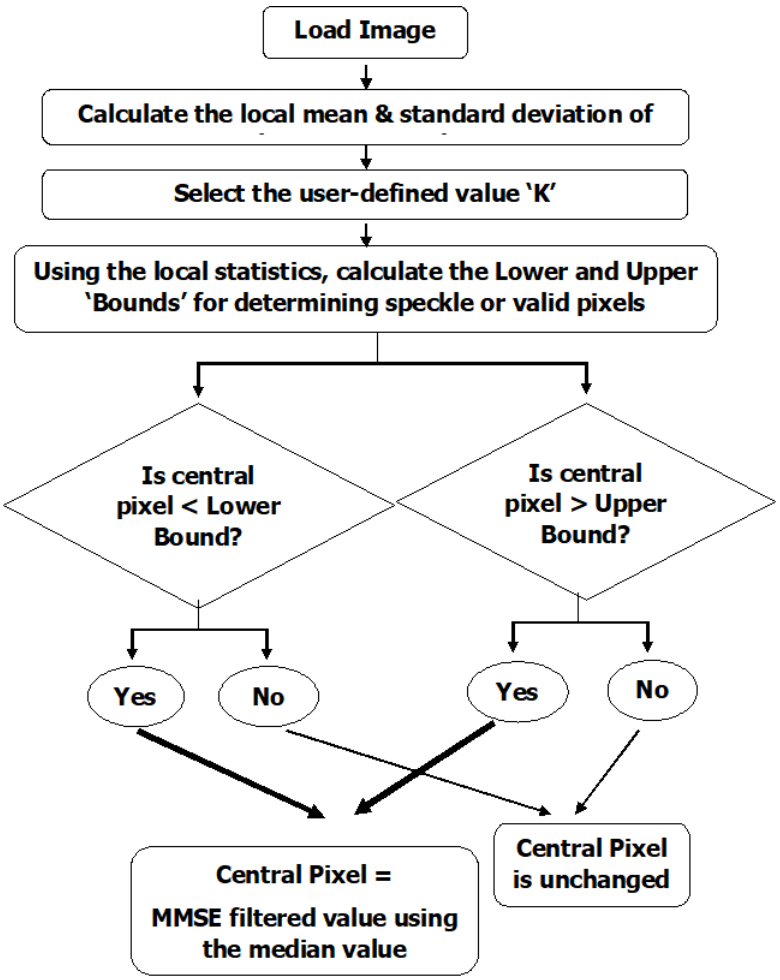

Figure 4.1: Implementation Flowchart for proposed filter

4.2.2 Region based Filtering

In recent speckle filtering literature, it has been seen how a region based algorithm and use of local statistics (mean and standard deviation) of an image are used to get improved filtered image. Thus in relation to that and the proposed "MAMF" described in the previous section, a region based filtering approach is also proposed. This acts as a second level of filtering to improve an already filtered image, to further boost its filtered image result. The flowchart of this implementation is given in Figure 4.2.

As seen in the flowchart, the region based filtering only works if there is a necessity to improve upon an already filtered image and is dependent on a user-defined Threshold value for the FQA parameters, which are discussed in section 2.3.1. These usually range between 0 and 1, 1 being the best result.

The regions are also split into user-defined number of regions for performing the second stage of filtering. The greater the number of regions, the greater is the time required to process them, thus the processing times are increased considerably as a result of this approach.

Through experimental results shown in section 4.4.1, a filter with window size 3x3 gave the best result for that particular algorithm in use and hence the region based approach uses a user-defined filter with window size fixed to 3x3. The image is then split into user-defined regions, which in this case has been set to 64 regions for most cases for image resolution near to 1000x1000 pixels. The FQA of these regions is derived and if it is below the user-defined threshold, then additional filtering is done using the user-defined filtering algorithm.

The FQA of the newly filtered region is then derived and compared with the previous to conclude if the region needs to be updated. If the updated FQA is increased than previous and if there is no drop in EEI and FPI, then the region is updated. This is done for each and every region within the image.

The effects of varying the user-defined threshold in terms of FQA are given in Tables 4.1 and 4.3. Tables 4.2 and 4.4 show how this affects in terms of the number of

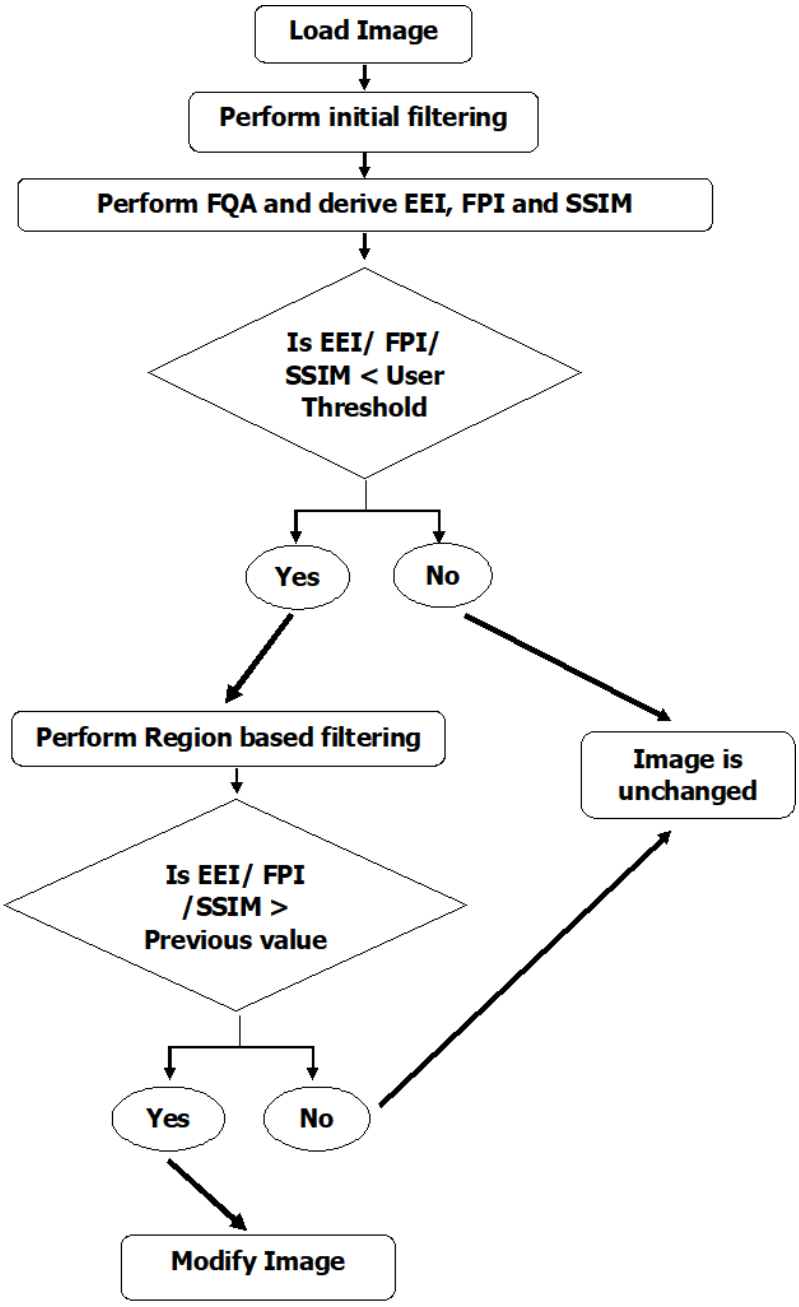

Figure 4.2: Implementation Flowchart for region filter

regions extracted, increased and updated. Tables 4.1 and 4.2 show the result for sample images from SAR Sea Ice image dataset, whereas Tables 4.3 and 4.4 show the result for sample RGB images, given in 4.3.1.

From Table 4.1 it can be seen that the best set of results are achieved with the

Table 4.1: FQA for Region Filtering of SAR Sea Ice Images

Average											
FQA parameter	Window Size	M=1		M=2		AMF&MAMF, M=1			AMF&MAMF, M=2		
		AMF	MAMF	AMF	MAMF	Thresh=0.7	Thresh=0.8	Thresh=0.9	Thresh=0.7	Thresh=0.8	Thresh=0.9
SSI	3 x 3	1.0001	1.3920	1.0845	1.0927	1.0001	1.0001	1.0001	1.0845	1.0845	1.0845
	5 x 5	0.9175	1.3472	1.0743	1.0905	0.9175	0.9175	0.9175	1.0743	1.0743	1.0743
	7 x 7	0.8729	1.2985	1.0644	1.0867	0.8729	0.8729	0.8729	1.0644	1.0644	1.0644
	9 x 9	0.8467	1.2533	1.0570	1.0829	0.8467	0.8467	0.8467	1.0570	1.0570	1.0570
	11 x 11	0.8283	1.2165	1.0513	1.0798	**0.8283**	**0.8283**	**0.8283**	1.0513	1.0513	1.0513
EEI	3 x 3	0.8327	**1.0994**	1.0198	1.0392	0.8062	0.8062	0.8062	0.9892	0.9892	0.9892
	5 x 5	0.5921	0.9688	0.9924	1.0162	0.5620	0.5620	0.5620	0.9610	0.9610	0.9610
	7 x 7	0.4720	0.8843	0.9605	0.9889	0.4376	0.4376	0.4376	0.9248	0.9248	0.9248
	9 x 9	0.4277	0.8373	0.9400	0.9705	0.3905	0.3905	0.3905	0.9038	0.9038	0.9038
	11 x 11	0.4104	0.8011	0.9326	0.9630	0.3734	0.3734	0.3734	0.8967	0.8967	0.8967
FPI	3 x 3	0.6658	0.6267	0.9766	0.9765	0.6659	0.6659	0.6659	**0.9766**	0.9766	0.9766
	5 x 5	0.4235	0.5247	0.9447	0.9460	0.4235	0.4235	0.4235	0.9446	0.9446	0.9446
	7 x 7	0.3409	0.5121	0.9274	0.9289	0.3409	0.3409	0.3409	0.9274	0.9274	0.9274
	9 x 9	0.3250	0.5053	0.9242	0.9250	0.3250	0.3250	0.3250	0.9240	0.9240	0.9240
	11 x 11	0.3213	0.4932	0.9251	0.9250	0.3213	0.3213	0.3213	0.9249	0.9249	0.9249
IDPC	3 x 3	**0.8875**	0.6119	0.8812	0.8824	0.8875	0.8875	0.8875	0.8812	0.8812	0.8812
	5 x 5	0.8395	0.5344	0.8754	0.8779	0.8395	0.8395	0.8395	0.8754	0.8754	0.8754
	7 x 7	0.7977	0.5124	0.8670	0.8705	0.7977	0.7977	0.7977	0.8670	0.8670	0.8670
	9 x 9	0.7712	0.5094	0.8606	0.8649	0.7712	0.7712	0.7712	0.8606	0.8606	0.8606
	11 x 11	0.7528	0.5103	0.8559	0.8612	0.7528	0.7528	0.7528	0.8559	0.8559	0.8559
PSNR	3 x 3	**18.8896**	12.1026	18.2210	18.2239	18.8895	18.8895	18.8895	18.2210	18.2209	18.2209
	5 x 5	17.5345	11.5633	18.0932	18.0996	17.5345	17.5345	17.5345	18.0934	18.0934	18.0934
	7 x 7	16.6398	11.5416	17.8743	17.8819	16.6398	16.6398	16.6398	17.8743	17.8743	17.8743
	9 x 9	16.1761	11.6619	17.7094	17.7266	16.1761	16.1761	16.1761	17.7096	17.7096	17.7096
	11 x 11	15.8875	11.7851	17.5910	17.6251	15.8875	15.8875	15.8875	17.5912	17.5912	17.5912
SSIM	3 x 3	0.6967	0.3774	0.7196	**0.7246**	0.6967	0.6967	0.6967	0.7196	0.7196	0.7196
	5 x 5	0.5127	0.2624	0.6952	0.7055	0.5127	0.5127	0.5127	0.6952	0.6952	0.6952
	7 x 7	0.3919	0.2276	0.6715	0.6855	0.3919	0.3919	0.3919	0.6715	0.6715	0.6715
	9 x 9	0.3435	0.2209	0.6588	0.6758	0.3435	0.3435	0.3435	0.6588	0.6588	0.6588
	11 x 11	0.3237	0.2222	0.6515	0.6713	0.3237	0.3237	0.3237	0.6514	0.6514	0.6514

proposed filter on its own, with M=2 and window size 3x3, although the proposed filter with M=1 and window size 3x3 has a slightly better EEI but a very low FPI. The proposed filter on its own with M=2 and window size 3x3 also has the best SSIM, which are the three main criteria of FQA chosen while performing the region filtering.

However, the region filtering (AMF and MAMF, M=2, Thresh=0.7, window size 3x3) does improve slightly the FPI for the AMF but at the cost of slight decrease in the EEI. The updation is not quite substantial as evident from Table 4.2, where out of 24 regions identified and with 10 of them showing increase in FQA, only 7 of these regions are modified. Also from the table is quite evident that even with high number

Table 4.2: Regions Identified, Increased and Updated for Region Filtering of SAR Sea Ice Images

Average							
Parameter	Window Size	AMF&MAMF, M=1			AMF&MAMF, M=2		
		Thresh=0.7	Thresh=0.8	Thresh=0.9	Thresh=0.7	Thresh=0.8	Thresh=0.9
Reg Iden	3 x 3	40	63	64	24	60	64
	5 x 5	64	64	64	35	64	64
	7 x 7	64	64	64	53	64	64
	9 x 9	64	64	64	60	64	64
	11 x 11	64	64	64	62	64	64
Reg Inc	3 x 3	34	41	41	10	22	23
	5 x 5	60	60	60	6	10	10
	7 x 7	62	62	62	7	9	9
	9 x 9	62	62	62	10	10	10
	11 x 11	62	62	62	10	10	10
Reg Accep	3 x 3	0	0	0	7	14	14
	5 x 5	0	0	0	1	1	1
	7 x 7	0	0	0	0	0	0
	9 x 9	0	0	0	1	1	1
	11 x 11	0	0	0	1	1	1

of regions identified to be modified and almost half or more of them having increased FQA after region filtering, only handful of them are actually updated. For the cases with M=1, none of the regions which are increased have been updated. It can also be noted, especially with lower threshold, more regions are identified and increased with growing window size, thus 11x11 region being the highest. This again indicates of how a filter degrades the image quality with increasing window size.

For the results of Sample RGB images shown in Table 4.3, similar phenomenon are noted as that for the SAR Sea Ice image results in 4.1. The proposed filter on its own with window size 3x3 and M=2 is again the most ideal. The region filtering performs some improvement to the FPI but the decrease in the EEI is not as low as that for the SAR Sea Ice image results. Also in Table 4.4, more number of regions are updated, even with M=1 conditions.

Table 4.3: FQA for Region Filtering of Sample RGB Images

Average											
FQA parameter	Window Size	M=1		M=2		AMF&MAMF, M=1			AMF&MAMF, M=2		
		AMF	MAMF	AMF	MAMF	Thresh=0.7	Thresh=0.8	Thresh=0.9	Thresh=0.7	Thresh=0.8	Thresh=0.9
SSI	3 x 3	1.0203	1.2882	1.0397	1.0404	1.0220	1.0224	1.0224	1.0398	1.0398	1.0398
	5 x 5	1.0137	1.2679	1.0399	1.0410	1.0160	1.0160	1.0160	1.0401	1.0401	1.0401
	7 x 7	1.0122	1.2409	1.0407	1.0419	1.0153	1.0153	1.0158	1.0409	1.0409	1.0409
	9 x 9	1.0121	1.2193	1.0413	1.0426	**1.0121**	**1.0121**	**1.0121**	1.0416	1.0416	1.0416
	11 x 11	1.0123	1.2039	1.0419	1.0433	1.0123	1.0123	1.0123	1.0421	1.0421	1.0421
EEI	3 x 3	1.0083	**1.5029**	1.2462	1.2486	0.9642	0.9646	0.9646	1.1701	1.1701	1.1701
	5 x 5	0.8074	1.3481	1.2066	1.2121	0.7753	0.7753	0.7753	1.1309	1.1309	1.1309
	7 x 7	0.7117	1.2365	1.1755	1.1826	0.6838	0.6838	0.6840	1.0990	1.0990	1.0990
	9 x 9	0.6632	1.1584	1.1555	1.1632	0.6320	0.6320	0.6320	1.0766	1.0766	1.0766
	11 x 11	0.6359	1.1103	1.1415	1.1502	0.6045	0.6045	0.6045	1.0635	1.0635	1.0635
FPI	3 x 3	0.7625	0.5918	0.9561	**0.9570**	0.7622	0.7622	0.7622	0.9561	0.9561	0.9561
	5 x 5	0.5801	0.3920	0.9069	0.9095	0.5790	0.5790	0.5790	0.9069	0.9069	0.9069
	7 x 7	0.4990	0.3105	0.8602	0.8629	0.4978	0.4978	0.4978	0.8600	0.8600	0.8600
	9 x 9	0.4512	0.2651	0.8255	0.8292	0.4512	0.4512	0.4512	0.8253	0.8253	0.8253
	11 x 11	0.4233	0.2532	0.7990	0.8034	0.4233	0.4233	0.4233	0.7990	0.7990	0.7990
IDPC	3 x 3	0.9659	0.7670	0.9377	0.9375	0.9643	0.9643	0.9643	0.9379	0.9379	0.9379
	5 x 5	0.9728	0.7705	0.9389	0.9385	0.9713	0.9713	0.9713	0.9398	0.9398	0.9398
	7 x 7	**0.9735**	0.7799	0.9387	0.9385	0.9718	0.9718	0.9717	0.9396	0.9396	0.9396
	9 x 9	0.9724	0.7888	0.9384	0.9382	0.9724	0.9724	0.9724	0.9393	0.9393	0.9393
	11 x 11	0.9708	0.7956	0.9380	0.9380	0.9708	0.9708	0.9708	0.9389	0.9389	0.9389
PSNR	3 x 3	22.2003	12.9343	19.5065	19.4880	22.0756	22.0630	22.0630	19.5240	19.5240	19.5240
	5 x 5	23.1348	13.0916	19.5881	19.5559	22.9727	22.9727	22.9727	19.6545	19.6546	19.6546
	7 x 7	**23.1975**	13.3722	19.5715	19.5433	22.9773	22.9773	22.9606	19.6384	19.6384	19.6384
	9 x 9	23.0071	13.6281	19.5421	19.5225	23.0071	23.0071	23.0071	19.6146	19.6146	19.6147
	11 x 11	22.7614	13.8234	19.5083	19.4968	22.7614	22.7614	22.7614	19.5744	19.5744	19.5744
SSIM	3 x 3	0.5098	0.3149	0.4338	0.4345	0.5089	0.5073	0.5073	0.4340	0.4340	0.4340
	5 x 5	**0.5163**	0.3003	0.4298	0.4303	0.5153	0.5153	0.5153	0.4308	0.4308	0.4308
	7 x 7	0.4980	0.3030	0.4234	0.4241	0.4950	0.4950	0.4929	0.4245	0.4245	0.4245
	9 x 9	0.4804	0.3082	0.4180	0.4197	0.4804	0.4804	0.4804	0.4191	0.4191	0.4191
	11 x 11	0.4660	0.3129	0.4140	0.4164	0.4660	0.4660	0.4660	0.4150	0.4150	0.4150

Consequently, if there is a need for second stage of filtering, that part of the image is then filtered separately using a user-selected filter. For this research, the proposed MAMF filter in the previous section is used, although tests with various combination of filters used in thesis have been done. It has observed to produce improved accuracy, although minor, in terms of feature and edge information retention. It thus provides a basis for future applications where this process can be used to further improve a filtered image result and only to regions where an improvement is deemed necessary, but as a trade-off for increased computation time.

Table 4.4: Regions Identified, Increased and Updated for Region Filtering of Sample RGB Images

Average							
Parameter	Window Size	AMF&MAMF, M=1			AMF&MAMF, M=2		
		Thresh=0.7	Thresh=0.8	Thresh=0.9	Thresh=0.7	Thresh=0.8	Thresh=0.9
Reg Iden	3 x 3	45	56	63	46	52	61
	5 x 5	52	57	63	46	56	63
	7 x 7	56	58	64	50	59	63
	9 x 9	58	60	64	53	62	63
	11 x 11	58	61	64	54	62	64
Reg Inc	3 x 3	24	29	33	45	49	54
	5 x 5	34	37	41	46	52	57
	7 x 7	40	42	46	47	53	57
	9 x 9	44	46	50	49	56	58
	11 x 11	43	46	48	50	57	59
Reg Accep	3 x 3	0	1	1	14	14	14
	5 x 5	0	0	0	14	14	14
	7 x 7	1	1	1	14	14	14
	9 x 9	0	0	0	13	13	13
	11 x 11	0	0	0	13	13	13

4.3 Experimental Setup for Speckle Filtering

The Speckle filtering algorithm proposed in the previous section is compared with numerous real-world SAR images, with computer generated simulated SAR images as well as RGB images to effectively evaluate the filter's performance. The dataset preparation for the various test conducted, is discussed in detail in this section.

4.3.1 Dataset preparation

There have been in total 4 datasets used in the FQA done, these include some publicly available Sentinel-1A satellite data on NASA's Alaska Space Facility (ASF) website [123], some satellite data acquired from TerraSAR-X satellite, some computer generated simulated SAR images and finally some sample RGB images available on Windows operating computers. The RGB images have been used in this context to show the performance of the filter with non-satellite images.

The first and primary dataset used is from the TerraSar-X satellite, acquired on 29 June 2012 from the northern Chukchi Sea. The images represent the Sea Ice condition during early summer breakup, some of area which are tightly packed with Sea Ice floes and some more loosely packed with more water regions. The acquired image has dimensions 16303 x 16181 and has been cropped in the top right corner, as shown in Figure 4.3. Three subsequent images have been created with dimensions 570 x 620, 699 x 554 and 610 x 694 respectively, for means for easy processing for the filtering algorithms, before being applied on the bigger image. To test the performance of the speckle filters, pseudo speckle noise has been added to the images before testing the performance. The noise added has zero mean and variance equal to 0.05, 0.07 and 0.09 respectively.

The second dataset is from the publicly available Sentinel-1A satellite data from NASA supplied ASF's vertex portal [123]. Nine very high resolution images were collected, which were acquired on 10th and 11th January 2017. Each of the nine SAR

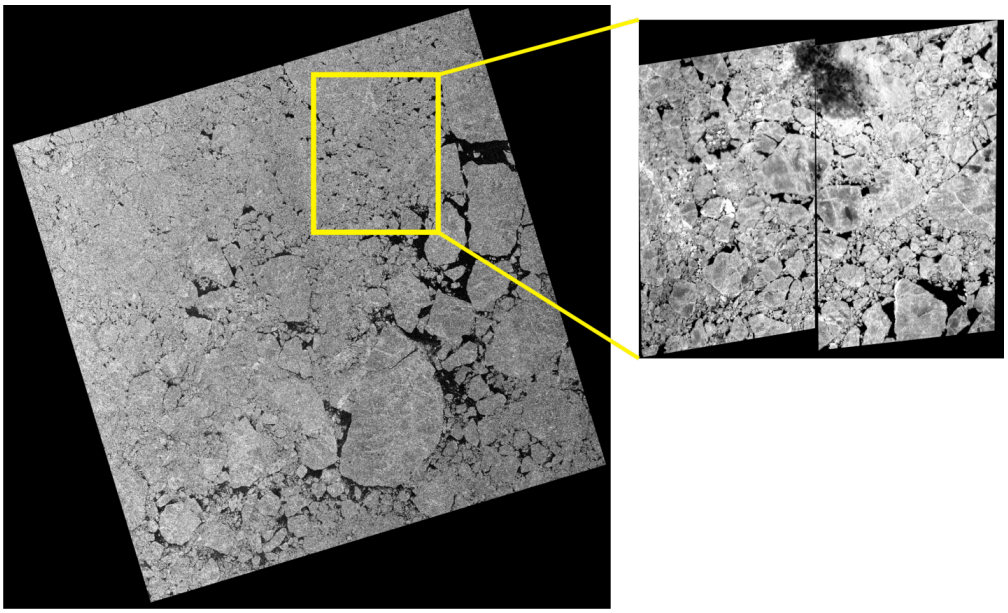

Figure 4.3: Sample TerraSar-X image acquired on 29th June 2012

images acquired are of dimensions exceeding 25k x 16k pixels respectively. Thus for faster means of processing, they have been reduced by a factor of 10 percent with bilinear interpolation, thus producing images of dimensions 2.5k x 1.6k pixels respectively. Similar to the first dataset, pseudo noise has been added to test the performance of the filter.

The third dataset is created using computer generated simulation program. Random drawings and figures created in the Windows' software have been used to create mock SAR images. The drawings created have been varied to test the performance of the retaining edges in particular, which are required for the next part of this research. The three simulated SAR generated have dimensions; 217 x 181, 248 x 204 and 1034 x 900 respectively . Again computer generated pseudo noise is added to test the filter's performance.

The final dataset are everyday sample RGB images available on any Windows operating-systems' computer. Out of the available eight images, five have been used for testing the performance of the filter, shown in Figure 4.4. The RGB images have been chosen to test the performance of the filter with non-satellite images and to check

its performance on retaining edges with objects much closer to each other, as seen in most of the images used. Pseudo speckle noise with the variances described above is added and then average of the performance is tested to form the filter's performance conclusion.

Figure 4.4: Sample RGB images available on Windows PC

4.4 Experimental results and analysis

The proposed filter described in the previous section, is now subject to objective as well as subjective analysis in order to prove the benefits of the contribution. This is done using Matlab and using the various FQA techniques described in section 2.3.1. For completeness, the processing time comparison is also done to show the computation times for each filtering algorithms.

4.4.1 Filter Quantitative Analysis

In this section, the FQA results are shown for the various filters described in sections 2.1.1. The results are then compared with the proposed filter mentioned in section 4.2.1. The FQA is performed on the four data sets mentioned in the previous section; Sea Ice images, Sentinel-1A SAR, simulated SAR and Windows PC available RGB images. Followed by these results, a sub-divided category of results are compared with the results of the region based filtering proposed in section 4.2.2.

4.4.1.1 Sea Ice SAR Images

The primary FQA were performed on the Sea-Ice images and have been presented in the Table 4.5 and the graphs shown in Figures 4.5 and 4.6. These results are the average for the FQA performed on the three different noise addition mentioned in section 4.3.1.

From Table 4.5, it can be seen how the Wiener filter has the best SSI, IDPC, PSNR and SSIM values respectively. However, the poor performance for the FPI and EEI values can also be seen, which are the worst results produced.

Although the proposed MAMF with user-defined Multiplier value (M) equal to 1 has the best EEI, but due to its very poor FPI value, we ignore this result. It can be seen how the proposed filter, with M = 2, marginally outperforms the AMF and thus is the second best filter to get high EEI. It is however the opposite case in terms of the

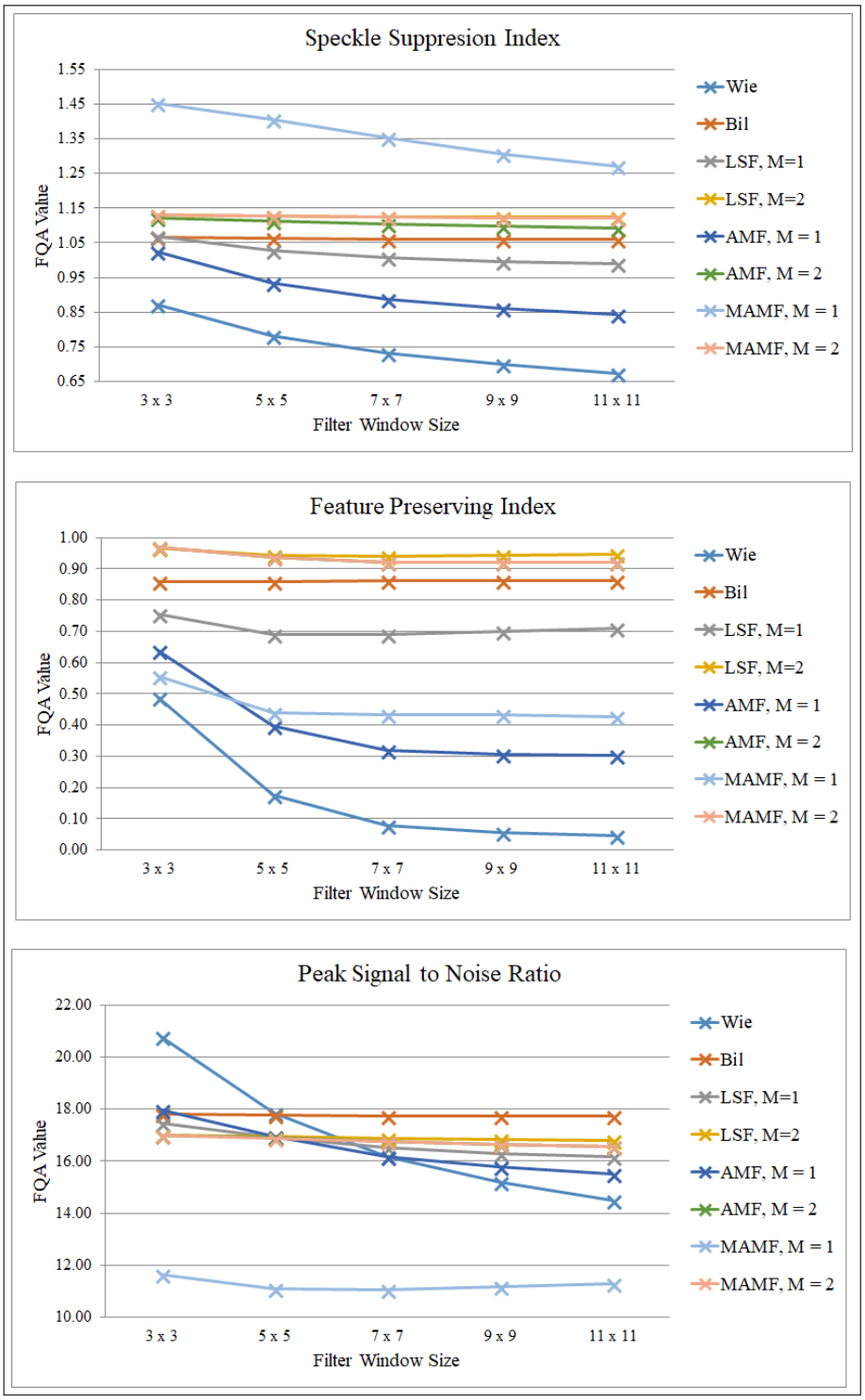

Figure 4.5: Graph of the FQA values for SAR Sea-Ice Images

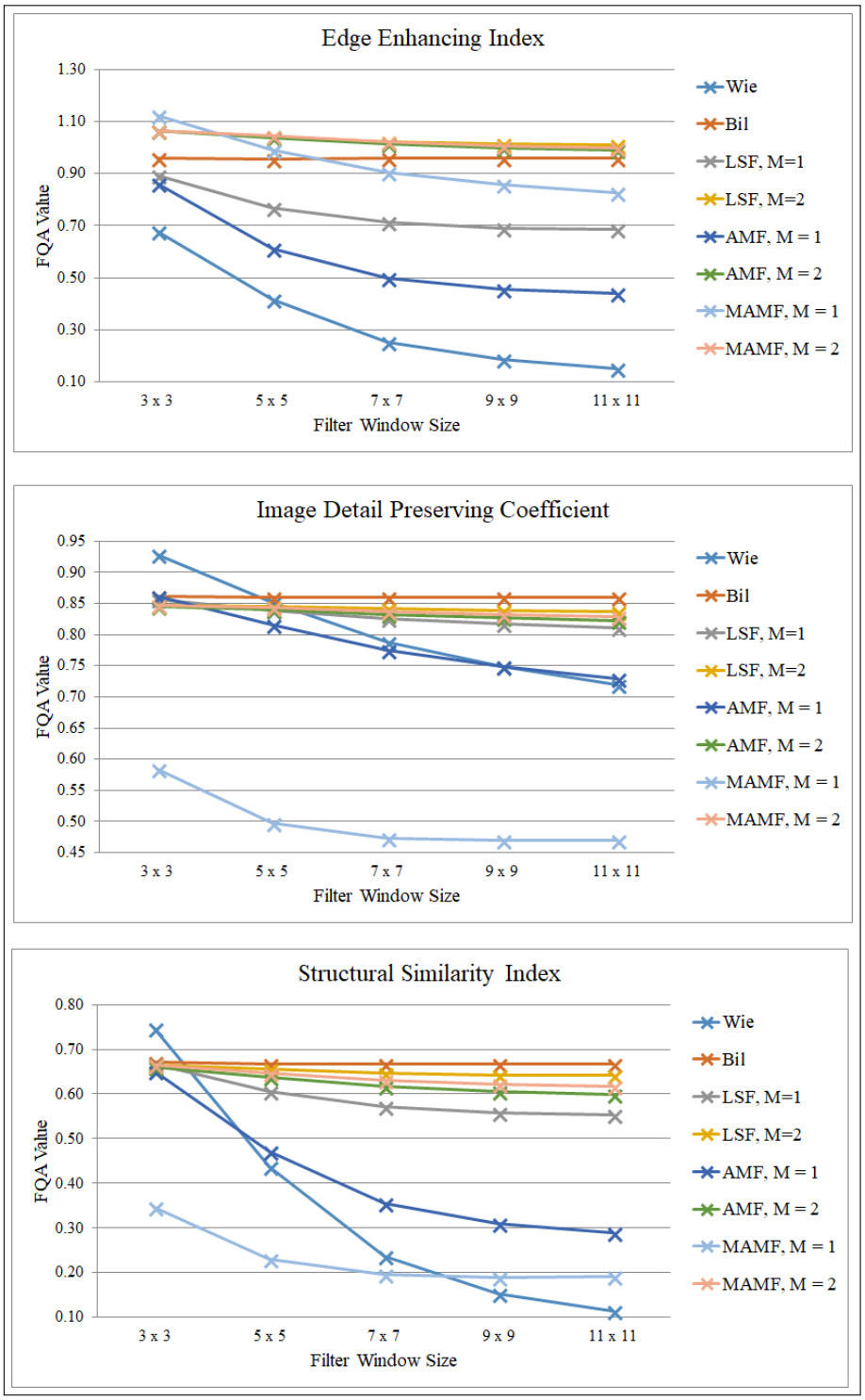

Figure 4.6: Graph of the FQA values for SAR Sea-Ice Images (continued)

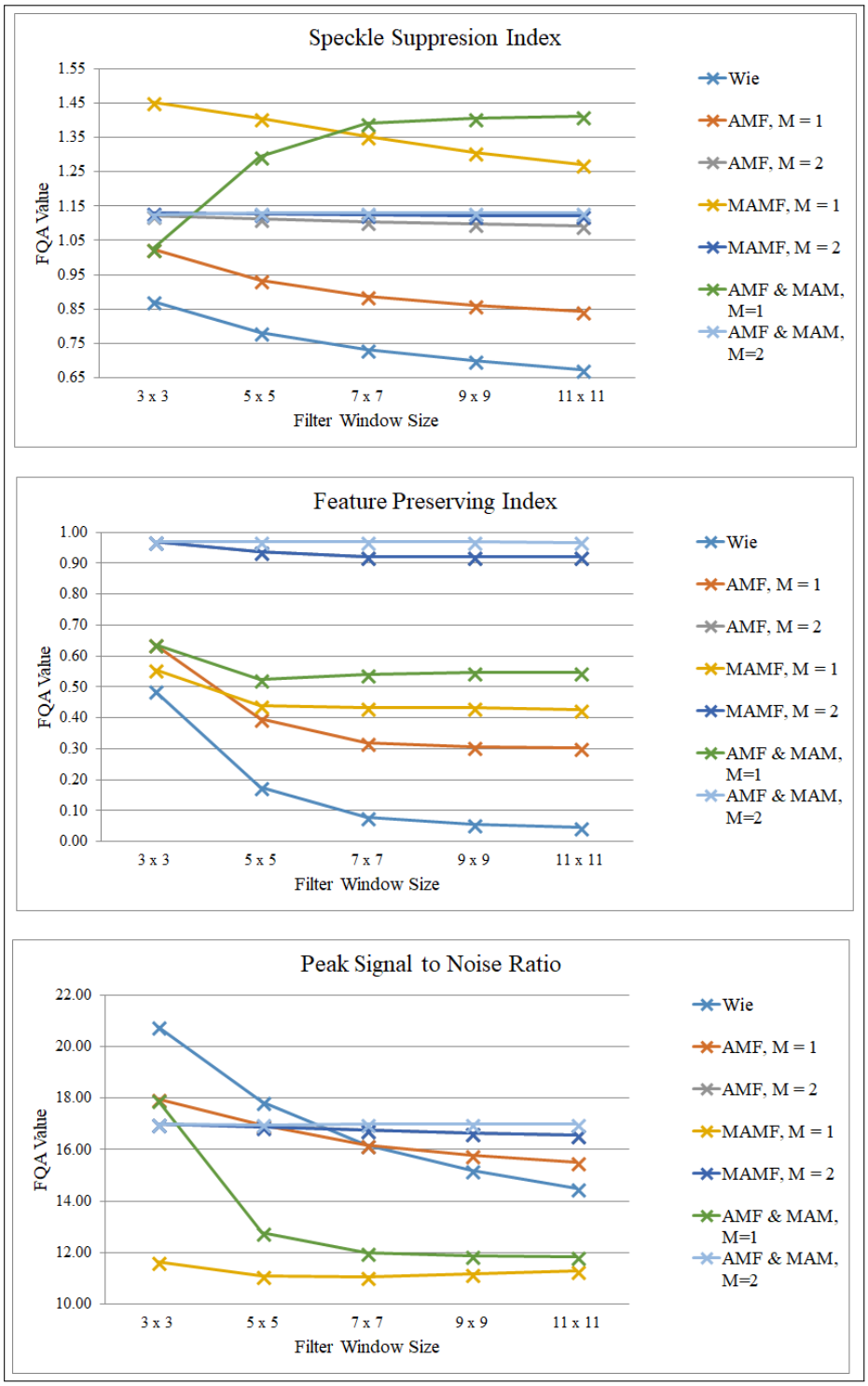

Figure 4.7: Graph of the Region based FQA values for SAR Sea-Ice Images

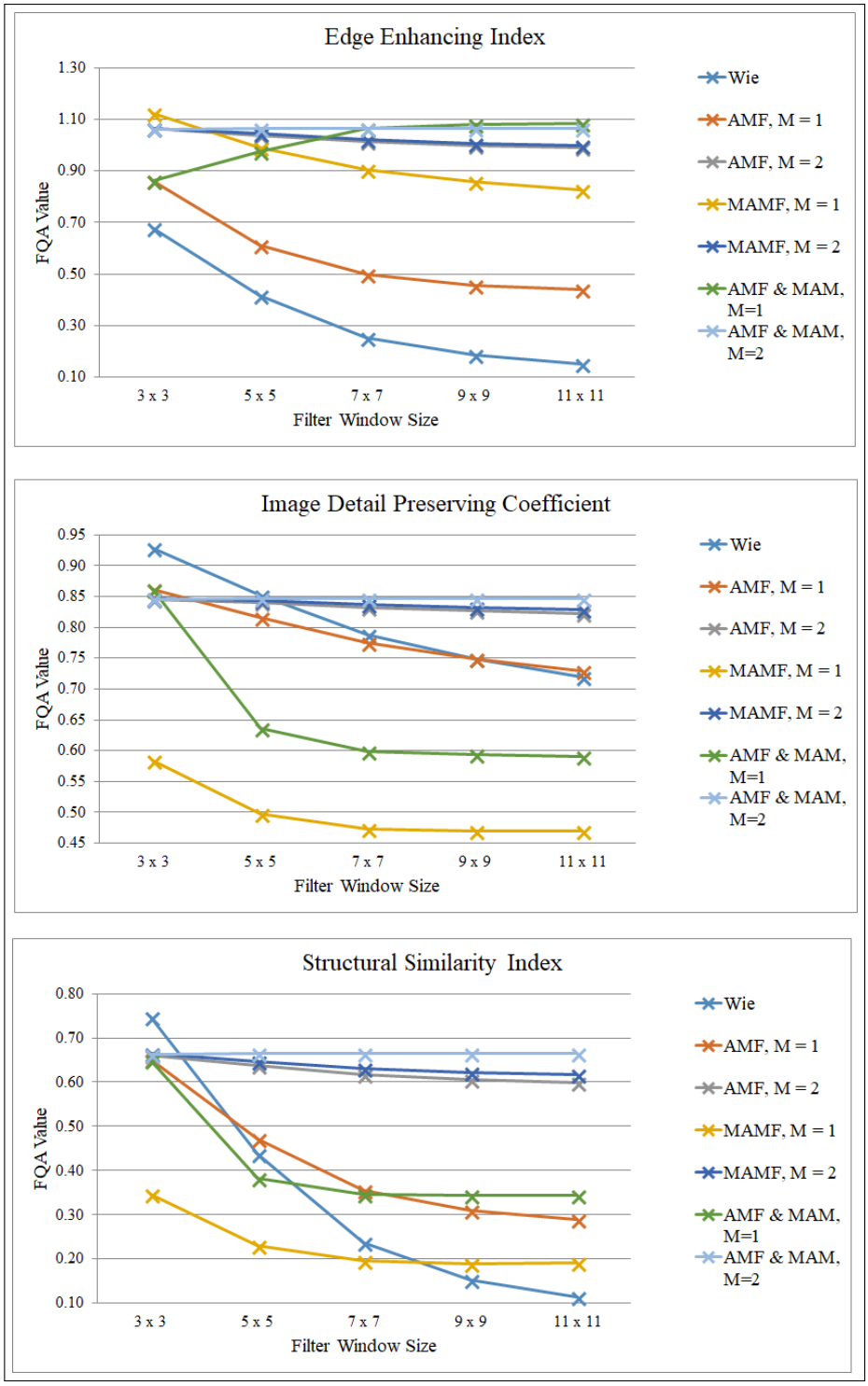

Figure 4.8: Graph of the Region based FQA values for SAR Sea-Ice Images (continued)

Table 4.5: FQA of SAR Sea Ice Images

Average of all noises									
FQA parameter	Window Size	Wie	Bil	LSF, M=1	LSF, M=2	AMF, M = 1	AMF, M = 2	MAMF, M = 1	MAMF, M = 2
SSI	3 x 3	0.87	1.07	1.07	1.13	1.02	1.12	1.45	1.13
	5 x 5	0.78	1.06	1.03	1.13	0.94	1.11	1.41	1.13
	7 x 7	0.73	1.06	1.01	1.13	0.89	1.10	1.35	1.13
	9 x 9	0.70	1.06	1.00	1.12	0.86	1.10	1.31	1.12
	11 x 11	**0.68**	1.06	0.99	1.12	0.84	1.09	1.27	1.12
EEI	3 x 3	0.68	0.96	0.89	1.06	0.86	1.06	**1.12**	1.07
	5 x 5	0.42	0.96	0.77	1.04	0.61	1.04	0.99	1.04
	7 x 7	0.25	0.96	0.71	1.02	0.50	1.01	0.91	1.02
	9 x 9	0.18	0.96	0.69	1.01	0.46	1.00	0.86	1.01
	11 x 11	0.15	0.96	0.68	1.01	0.44	0.99	0.83	1.00
FPI	3 x 3	0.49	0.86	0.75	0.97	0.64	**0.97**	0.56	0.97
	5 x 5	0.17	0.86	0.69	0.94	0.40	0.94	0.44	0.94
	7 x 7	0.08	0.86	0.69	0.94	0.32	0.92	0.43	0.92
	9 x 9	0.06	0.86	0.70	0.94	0.31	0.92	0.43	0.92
	11 x 11	0.05	0.86	0.71	0.95	0.30	0.92	0.43	0.92
IDPC	3 x 3	**0.93**	0.86	0.86	0.85	0.86	0.85	0.58	0.85
	5 x 5	0.85	0.86	0.84	0.84	0.82	0.84	0.50	0.84
	7 x 7	0.79	0.86	0.82	0.84	0.77	0.83	0.47	0.84
	9 x 9	0.75	0.86	0.82	0.84	0.75	0.83	0.47	0.83
	11 x 11	0.72	0.86	0.81	0.84	0.73	0.82	0.47	0.83
PSNR	3 x 3	**20.76**	17.81	17.44	16.99	17.97	16.98	11.63	16.98
	5 x 5	17.83	17.76	16.91	16.95	16.94	16.89	11.09	16.89
	7 x 7	16.16	17.74	16.51	16.87	16.18	16.75	11.07	16.75
	9 x 9	15.19	17.74	16.31	16.82	15.76	16.63	11.18	16.64
	11 x 11	14.49	17.74	16.18	16.78	15.50	16.55	11.29	16.57
SSIM	3 x 3	**0.75**	0.67	0.67	0.66	0.65	0.66	0.35	0.66
	5 x 5	0.44	0.67	0.61	0.65	0.47	0.64	0.23	0.65
	7 x 7	0.24	0.67	0.57	0.65	0.36	0.62	0.20	0.63
	9 x 9	0.15	0.67	0.56	0.64	0.31	0.61	0.19	0.62
	11 x 11	0.11	0.67	0.55	0.64	0.29	0.60	0.19	0.62

FPI where, the AMF with M = 2, marginally outperforms the MAMF with M = 2. The MAMF marginally outperforms the AMF in terms of the IDPC, PSNR and SSIM as well.

It is important to note how all the best results are produced with filter window value 3x3, except for the SSI, where the Wiener filter with filter window 11x11 is the best.

The FQA results for the Region based filtering proposed in section 4.2.2 are shown in Table 4.6 and Figures 4.7, 4.8 . It can be seen how the AMF followed by MAMF

Table 4.6: FQA for Region Filtering of SAR Sea Ice Images

Average of all noises								
FQA parameter	Window Size	Wie	AMF, M = 1	AMF, M = 2	MAMF, M = 1	MAMF, M = 2	AMF & MAMF, M=1	AMF & MAMF, M=2
SSI	3 x 3	0.87	1.02	1.12	1.45	1.13	1.03	1.12
	5 x 5	0.78	0.94	1.11	1.41	1.13	1.29	1.13
	7 x 7	0.73	0.89	1.10	1.35	1.13	1.39	1.13
	9 x 9	0.70	0.86	1.10	1.31	1.12	1.41	1.13
	11 x 11	**0.68**	0.84	1.09	1.27	1.12	1.41	1.13
EEI	3 x 3	0.68	0.86	1.06	**1.12**	1.07	0.86	1.06
	5 x 5	0.42	0.61	1.04	0.99	1.04	0.98	1.07
	7 x 7	0.25	0.50	1.01	0.91	1.02	1.06	1.07
	9 x 9	0.18	0.46	1.00	0.86	1.01	1.08	1.07
	11 x 11	0.15	0.44	0.99	0.83	1.00	1.08	1.07
FPI	3 x 3	0.49	0.64	0.97	0.56	0.97	0.64	**0.97**
	5 x 5	0.17	0.40	0.94	0.44	0.94	0.52	0.97
	7 x 7	0.08	0.32	0.92	0.43	0.92	0.54	0.97
	9 x 9	0.06	0.31	0.92	0.43	0.92	0.55	0.97
	11 x 11	0.05	0.30	0.92	0.43	0.92	0.55	0.97
IDPC	3 x 3	**0.93**	0.86	0.85	0.58	0.85	0.86	0.85
	5 x 5	0.85	0.82	0.84	0.50	0.84	0.64	0.85
	7 x 7	0.79	0.77	0.83	0.47	0.84	0.60	0.85
	9 x 9	0.75	0.75	0.83	0.47	0.83	0.59	0.85
	11 x 11	0.72	0.73	0.82	0.47	0.83	0.59	0.85
PSNR	3 x 3	**20.76**	17.97	16.98	11.63	16.98	17.94	16.98
	5 x 5	17.83	16.94	16.89	11.09	16.89	12.76	16.98
	7 x 7	16.16	16.18	16.75	11.07	16.75	11.98	16.98
	9 x 9	15.19	15.76	16.63	11.18	16.64	11.88	16.98
	11 x 11	14.49	15.50	16.55	11.29	16.57	11.84	16.98
SSIM	3 x 3	**0.75**	0.65	0.66	0.35	0.66	0.65	0.66
	5 x 5	0.44	0.47	0.64	0.23	0.65	0.38	0.66
	7 x 7	0.24	0.36	0.62	0.20	0.63	0.35	0.66
	9 x 9	0.15	0.31	0.61	0.19	0.62	0.34	0.66
	11 x 11	0.11	0.29	0.60	0.19	0.62	0.34	0.66

produces minor improvements to the FPI, IDPC and SSIM values, although this is lower than the proposed filter value on its own. However, the region filtering produces the best FPI value, all with M = 2. The PSNR value for the region filtering is better than the AMF or the MAMF on its own, but is second best to the Wiener filter. The SSI again has the best value with Wiener filter with filter window 11x11.

As mentioned in the FQA in section 2.3.1, a filter with lowest SSI is said to have the best speckle suppression but this also comes at a cost of degrading and blurring the image boundaries and thus is not ideal for segmentation algorithms. The EEI, FPI, IDPC, PSNR and the SSIM however are a good indication of how good a filter is in

retaining original valid pixels within the Image and maintaining its object boundaries which are vital for segmentation. The EEI, FPI and SSIM are particularly important in this research for Image Segmentation purposes and quantifying the filter's ability to accurately retain important image features after filtering.

Thus, for the speckle filtering without region based approach, the proposed MAMF, M=2, closely followed by AMF, M=2, with window size 3x3 are the most ideal as they have really good EEI and FPI as well as good SSIM. The Wiener filter with window size 11x11 has the best SSI but the EEI and FPI are very low, even for result with window size 3x3, which concurrently have the best SSIM and PSNR. For the region based approach, the addition of the proposed filter to improve the AMF result produces a good result but the result with MAMF on its own is still the most ideal with window size 3x3 and M=2.

4.4.1.2 Sentinel-1A SAR Images

The next set of FQA results were performed on Sentinel 1-A SAR images, which are given in Table 4.7 and shown in the graph in Figures 4.9 and 4.10. These results are the average for the FQA performed on the three different noise addition mentioned in section 4.3.1.

From the Table 4.7, it can be seen how the Wiener filter has the best SSI, IDPC, PSNR and SSIM values respectively. However, it is similarly noted the poor performance for the FPI and EEI values, which are the worst results produced. This is exactly similar to that witnessed with the Sea Ice images. Similar to the Sea Ice images, the proposed filter with M = 2 is the most ideal with high EEI and FPI. The AMF marginally outperforms the proposed filter in terms of FPI.

The FQA results for the Region based filtering proposed in section 4.2.2 are shown in Table 4.8 and Figures 4.11 and 4.12. It can be seen how the region filtering produces marginal improvement to the EEI as well as now has the best FPI. The IDPC and SSIM values for both the AMF and region filtered result are same and marginally

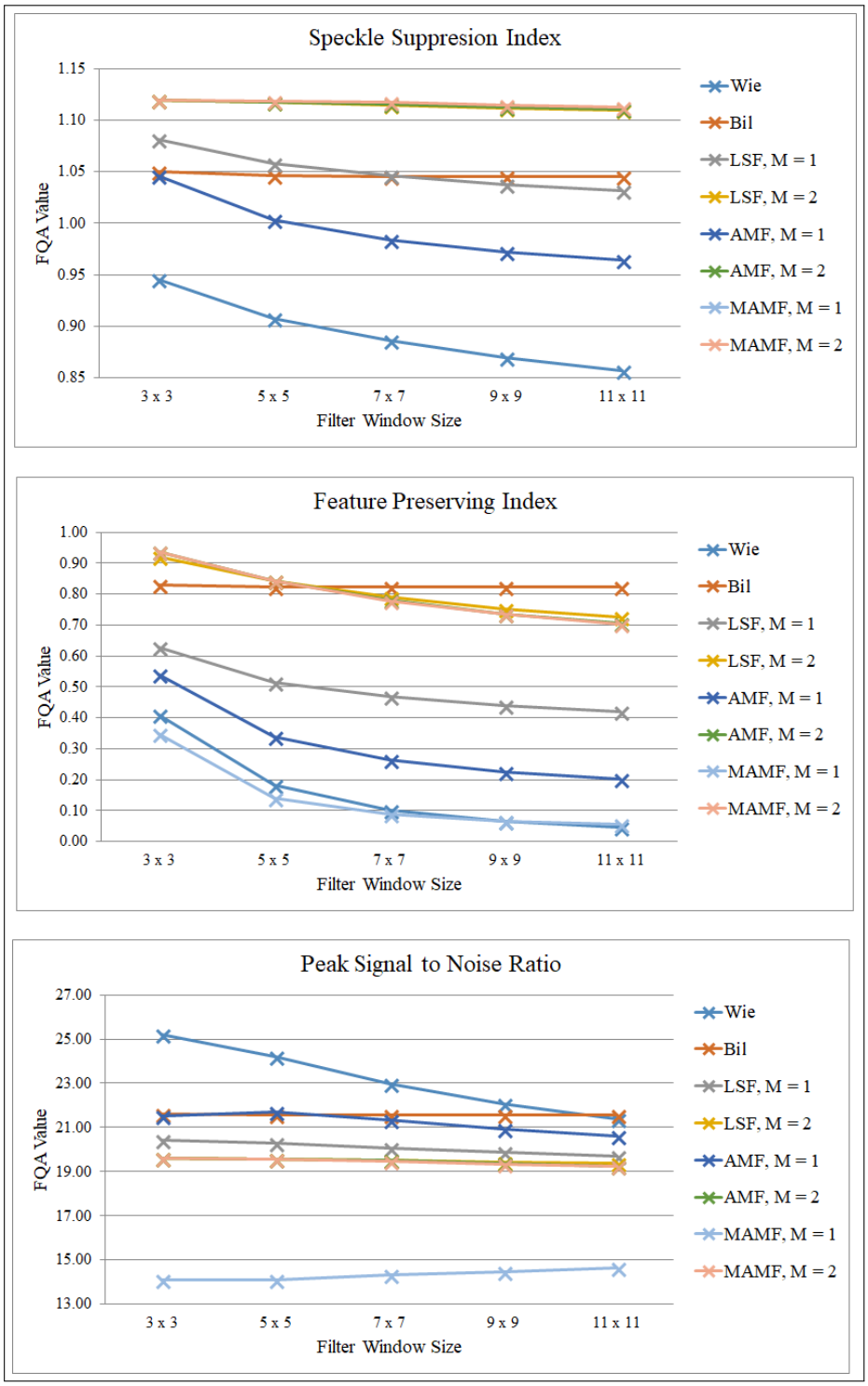

Figure 4.9: Graph of the FQA values for Sentinel 1-A SAR Images

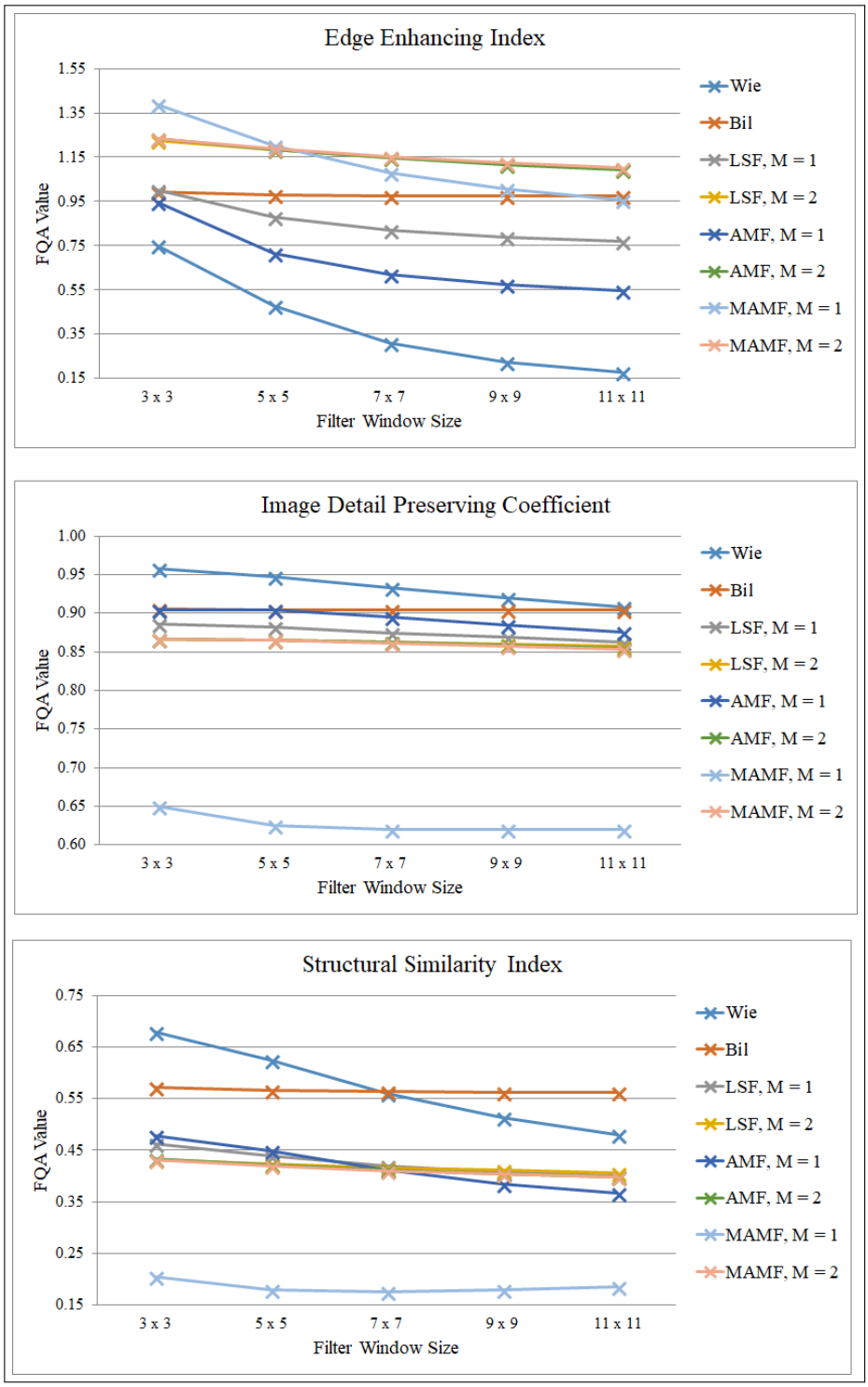

Figure 4.10: Graph of the FQA values for Sentinel 1-A SAR Images (continued)

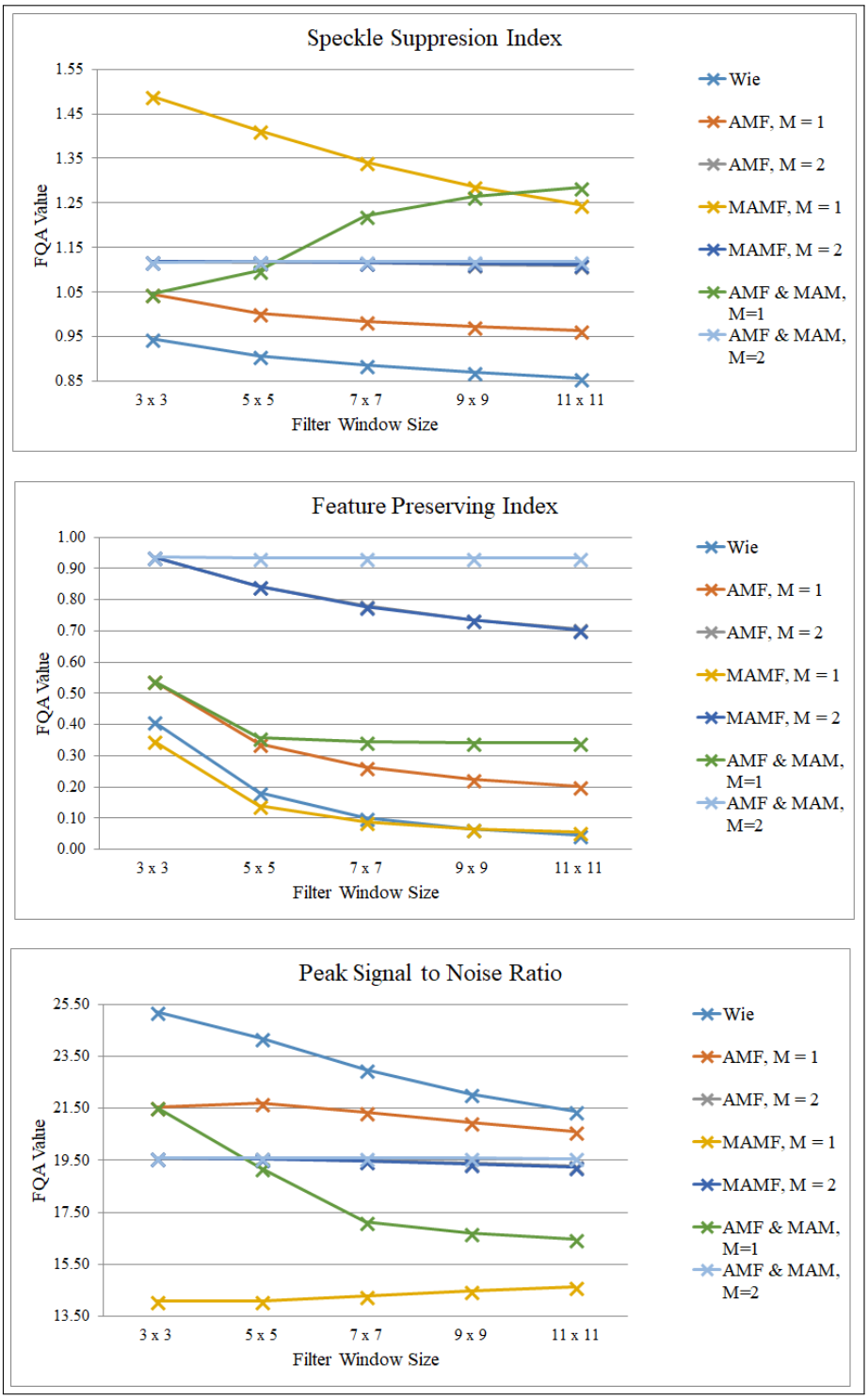

Figure 4.11: Graph of the Region based FQA values for Sentinel 1-A SAR Images

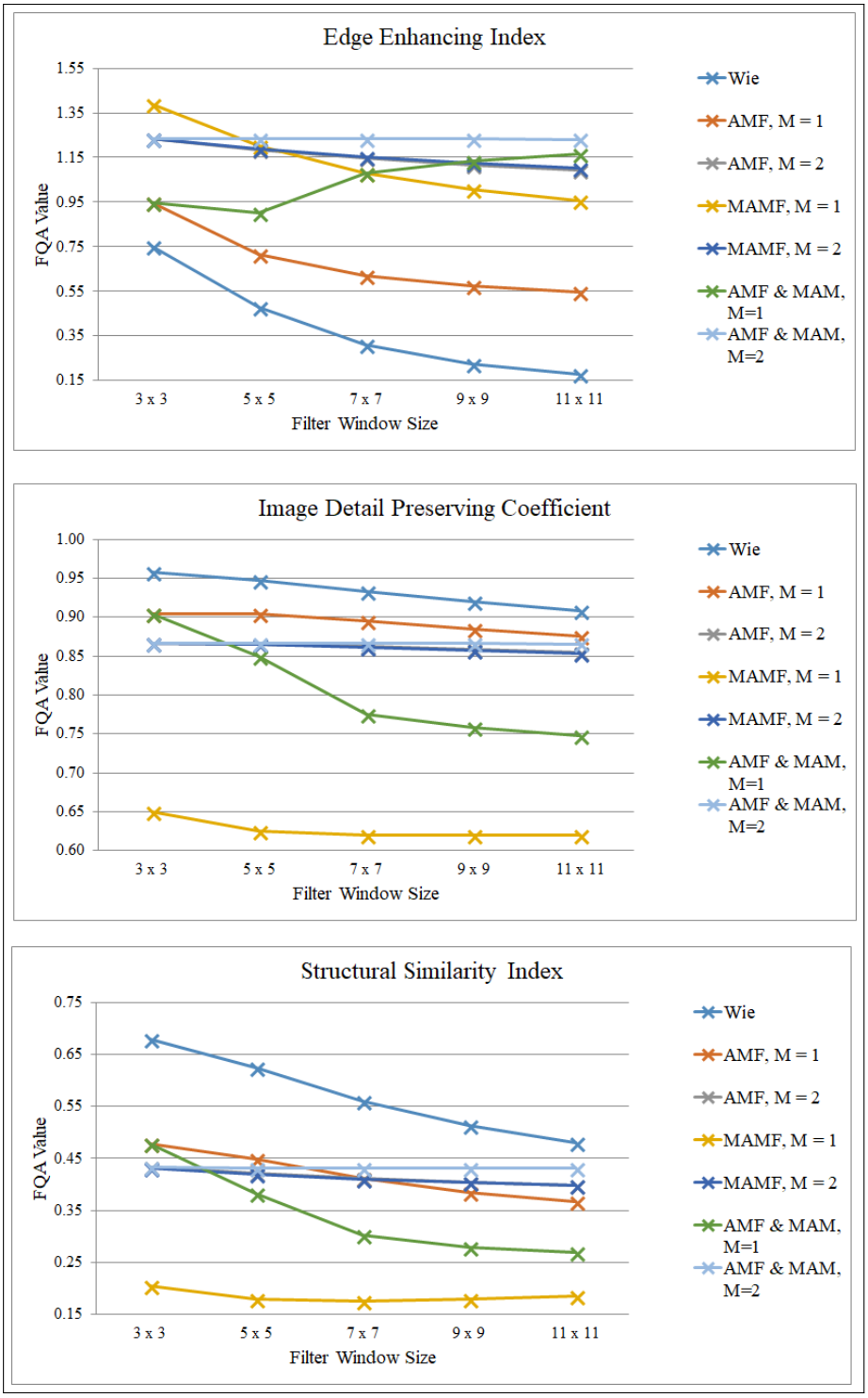

Figure 4.12: Graph of the Region based FQA values for Sentinel 1-A SAR Images (continued)

Table 4.7: FQA of Sentinel-1A SAR Images

Average of all noises									
FQA parameter	Window Size	Wie	Bil	LSF, M=1	LSF, M=2	AMF, M = 1	AMF, M = 2	MAMF, M = 1	MAMF, M = 2
SSI	3 x 3	0.95	1.05	1.08	1.12	1.05	1.12	1.49	1.12
	5 x 5	0.91	1.05	1.06	1.12	1.00	1.12	1.41	1.12
	7 x 7	0.89	1.05	1.05	1.11	0.98	1.12	1.34	1.12
	9 x 9	0.87	1.05	1.04	1.11	0.97	1.11	1.29	1.11
	11 x 11	**0.86**	1.05	1.03	1.11	0.96	1.11	1.25	1.11
EEI	3 x 3	0.75	0.99	1.00	1.23	0.95	1.23	**1.39**	1.23
	5 x 5	0.48	0.98	0.88	1.18	0.72	1.18	1.20	1.19
	7 x 7	0.31	0.98	0.82	1.15	0.62	1.15	1.08	1.15
	9 x 9	0.22	0.98	0.79	1.12	0.57	1.11	1.01	1.12
	11 x 11	0.18	0.98	0.77	1.10	0.55	1.09	0.96	1.10
FPI	3 x 3	0.41	0.83	0.63	0.92	0.54	**0.94**	0.35	0.94
	5 x 5	0.18	0.82	0.52	0.84	0.34	0.84	0.14	0.84
	7 x 7	0.10	0.82	0.47	0.79	0.26	0.78	0.09	0.78
	9 x 9	0.07	0.82	0.44	0.75	0.23	0.74	0.07	0.73
	11 x 11	0.05	0.82	0.42	0.73	0.20	0.71	0.06	0.70
IDPC	3 x 3	**0.96**	0.90	0.89	0.87	0.90	0.87	0.65	0.87
	5 x 5	0.95	0.90	0.88	0.86	0.90	0.87	0.63	0.86
	7 x 7	0.93	0.90	0.87	0.86	0.90	0.86	0.62	0.86
	9 x 9	0.92	0.90	0.87	0.86	0.88	0.86	0.62	0.86
	11 x 11	0.91	0.90	0.86	0.86	0.88	0.85	0.62	0.85
PSNR	3 x 3	**25.22**	21.60	20.42	19.59	21.53	19.60	14.11	19.59
	5 x 5	24.19	21.58	20.31	19.58	21.71	19.58	14.11	19.57
	7 x 7	22.99	21.57	20.09	19.52	21.34	19.49	14.30	19.47
	9 x 9	22.06	21.56	19.88	19.44	20.95	19.38	14.48	19.35
	11 x 11	21.39	21.56	19.71	19.36	20.61	19.26	14.63	19.24
SSIM	3 x 3	**0.68**	0.57	0.46	0.43	0.48	0.43	0.20	0.43
	5 x 5	0.63	0.56	0.44	0.42	0.45	0.42	0.18	0.42
	7 x 7	0.56	0.56	0.42	0.42	0.41	0.41	0.17	0.41
	9 x 9	0.51	0.56	0.41	0.41	0.39	0.40	0.18	0.40
	11 x 11	0.48	0.56	0.40	0.41	0.37	0.40	0.19	0.40

better than the MAMF on its own. The PSNR value for the region filtering is better than the MAMF on its own but marginally lower than AMF on its own.

It is again important to note how all the best results are produced with filter window value 3x3, except for the SSI, where the Wiener filter with filter window 11x11 is the best. For the AMF, MAMF and the region filtering, M = 2 with window size 3x3, has the best set of results as opposed to M = 1.

As mentioned in section 2.3.1, although the Wiener filter with window size 11x11

Table 4.8: FQA for Region Filtering of Sentinel-1 SAR Images

Average of all noises								
FQA parameter	Window Size	Wie	AMF, M = 1	AMF, M = 2	MAMF, M = 1	MAMF, M = 2	AMF & MAMF, M=1	AMF & MAMF, M=2
SSI	3 x 3	0.95	1.05	1.12	1.49	1.12	1.05	1.12
	5 x 5	0.91	1.00	1.12	1.41	1.12	1.10	1.12
	7 x 7	0.89	0.98	1.12	1.34	1.12	1.22	1.12
	9 x 9	0.87	0.97	1.11	1.29	1.11	1.26	1.12
	11 x 11	**0.86**	0.96	1.11	1.25	1.11	1.29	1.12
EEI	3 x 3	0.75	0.95	1.23	**1.39**	1.23	0.95	1.23
	5 x 5	0.48	0.72	1.18	1.20	1.19	0.90	1.23
	7 x 7	0.31	0.62	1.15	1.08	1.15	1.08	1.23
	9 x 9	0.22	0.57	1.11	1.01	1.12	1.13	1.23
	11 x 11	0.18	0.55	1.09	0.96	1.10	1.16	1.23
FPI	3 x 3	0.41	0.54	0.94	0.35	0.94	0.54	**0.94**
	5 x 5	0.18	0.34	0.84	0.14	0.84	0.36	0.93
	7 x 7	0.10	0.26	0.78	0.09	0.78	0.34	0.93
	9 x 9	0.07	0.23	0.74	0.07	0.73	0.34	0.94
	11 x 11	0.05	0.20	0.71	0.06	0.70	0.34	0.93
IDPC	3 x 3	**0.96**	0.90	0.87	0.65	0.87	0.90	0.87
	5 x 5	0.95	0.90	0.87	0.63	0.86	0.85	0.87
	7 x 7	0.93	0.90	0.86	0.62	0.86	0.78	0.87
	9 x 9	0.92	0.88	0.86	0.62	0.86	0.76	0.87
	11 x 11	0.91	0.88	0.85	0.62	0.85	0.75	0.87
PSNR	3 x 3	**25.22**	21.53	19.60	14.11	19.59	21.53	19.60
	5 x 5	24.19	21.71	19.58	14.11	19.57	19.22	19.59
	7 x 7	22.99	21.34	19.49	14.30	19.47	17.14	19.59
	9 x 9	22.06	20.95	19.38	14.48	19.35	16.69	19.59
	11 x 11	21.39	20.61	19.26	14.63	19.24	16.46	19.59
SSIM	3 x 3	**0.68**	0.48	0.43	0.20	0.43	0.48	0.43
	5 x 5	0.63	0.45	0.42	0.18	0.42	0.38	0.43
	7 x 7	0.56	0.41	0.41	0.17	0.41	0.30	0.43
	9 x 9	0.51	0.39	0.40	0.18	0.40	0.28	0.43
	11 x 11	0.48	0.37	0.40	0.19	0.40	0.27	0.43

has the best SSI, it is not ideal as it comes at the cost of extremely low other FQA parameters. Although the Wiener filter with window size 3x3 has the best IDPC, PSNR and SSIM, it still has the lowest EEI and FPI, which are more ideal for Image Segmentation. This is the same case for the region based filtering approach.

Thus for Sentinel-1 SAR images, the proposed filter with M=2 and window size 3x3 is the most ideal for filtering without region based approach and for region based approach, the AMF modified with the proposed filter produces the better results. The AMF with M=2 and window size 3x3 closely follows the proposed filter results.

4.4.1.3 Simulated SAR Images

The FQA results for simulated SAR images are given in Table 4.9 and shown in the graphs in Figures 4.13 and 4.14. These results are the average for the FQA performed on the three different noise addition mentioned in section 4.3.1.

Table 4.9: FQA of Simulated SAR Images

Average of all noises									
FQA parameter	Window Size	Wie	Bil	LSF, M=1	LSF, M=2	AMF, M = 1	AMF, M = 2	MAMF, M = 1	MAMF, M = 2
SSI	3 x 3	0.94	1.02	1.01	1.02	0.99	1.01	1.10	1.02
	5 x 5	0.91	1.02	1.00	1.02	0.98	1.00	1.12	1.02
	7 x 7	0.88	1.02	0.99	1.02	0.98	1.00	1.11	1.02
	9 x 9	0.86	1.02	1.00	1.02	0.99	1.00	1.11	1.02
	11 x 11	**0.84**	1.02	1.00	1.02	0.99	0.99	1.12	1.02
EEI	3 x 3	0.71	1.03	0.89	**1.06**	0.88	1.05	0.97	1.06
	5 x 5	0.48	1.03	0.80	1.05	0.72	1.02	0.83	1.04
	7 x 7	0.35	1.03	0.78	1.05	0.65	1.01	0.75	1.04
	9 x 9	0.29	1.03	0.77	1.05	0.60	1.00	0.69	1.03
	11 x 11	0.25	1.03	0.75	1.03	0.56	0.96	0.66	1.00
FPI	3 x 3	0.38	0.93	0.74	0.91	0.73	0.89	0.62	0.91
	5 x 5	0.17	0.93	0.65	0.91	0.55	0.87	0.38	0.90
	7 x 7	0.14	0.93	0.62	0.91	0.47	0.86	0.31	0.89
	9 x 9	0.10	**0.93**	0.60	0.90	0.40	0.83	0.26	0.86
	11 x 11	0.07	0.93	0.57	0.87	0.33	0.77	0.22	0.80
IDPC	3 x 3	0.96	**0.97**	0.96	0.97	0.96	0.97	0.86	0.97
	5 x 5	0.93	0.97	0.95	0.97	0.94	0.96	0.81	0.97
	7 x 7	0.92	0.97	0.95	0.97	0.93	0.96	0.80	0.96
	9 x 9	0.90	0.97	0.94	0.97	0.91	0.96	0.79	0.96
	11 x 11	0.89	0.97	0.93	0.96	0.90	0.95	0.78	0.95
PSNR	3 x 3	24.77	**26.32**	24.78	25.82	25.26	25.69	19.61	25.80
	5 x 5	21.72	26.15	23.93	25.76	23.83	25.51	18.46	25.75
	7 x 7	20.57	26.15	23.46	25.75	22.93	25.39	18.24	25.60
	9 x 9	19.81	26.14	23.01	25.69	21.85	24.86	18.06	25.19
	11 x 11	19.17	26.14	22.66	25.29	21.08	23.96	17.87	24.25
SSIM	3 x 3	0.92	**0.94**	0.92	0.94	0.93	0.93	0.90	0.94
	5 x 5	0.87	0.94	0.92	0.94	0.90	0.93	0.87	0.94
	7 x 7	0.85	0.93	0.92	0.94	0.90	0.93	0.87	0.93
	9 x 9	0.84	0.93	0.91	0.94	0.89	0.93	0.86	0.93
	11 x 11	0.82	0.93	0.91	0.93	0.88	0.92	0.86	0.93

From the Table 4.9, it can be seen Bilateral filter with window size 3x3 has the best IDPC, PSNR and SSIM values. The bilateral filter also has the best FPI value, but with filter window 9x9 and filter window 3x3 having marginally lower result than that. The

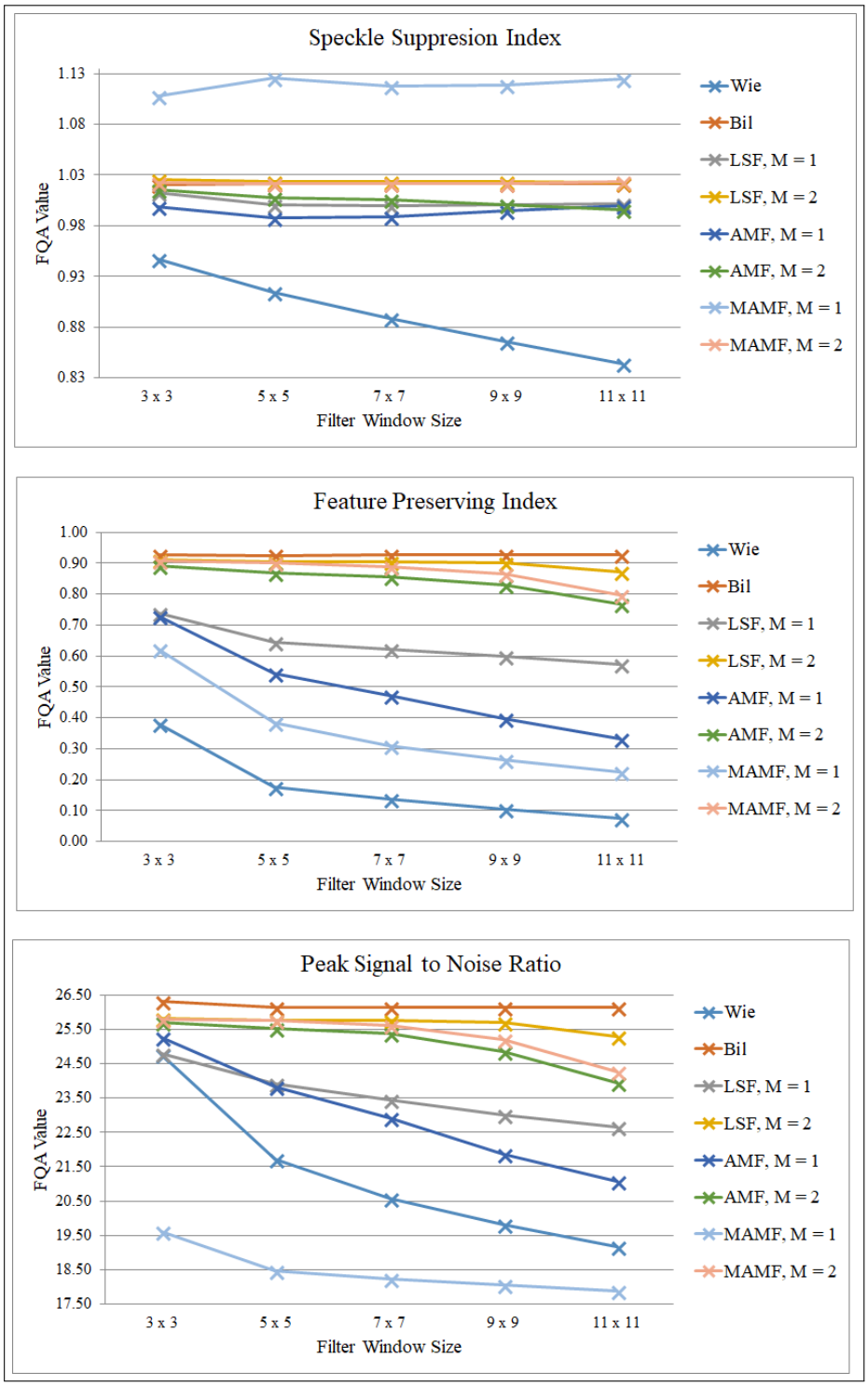

Figure 4.13: Graph of the FQA values for Simulated SAR Images

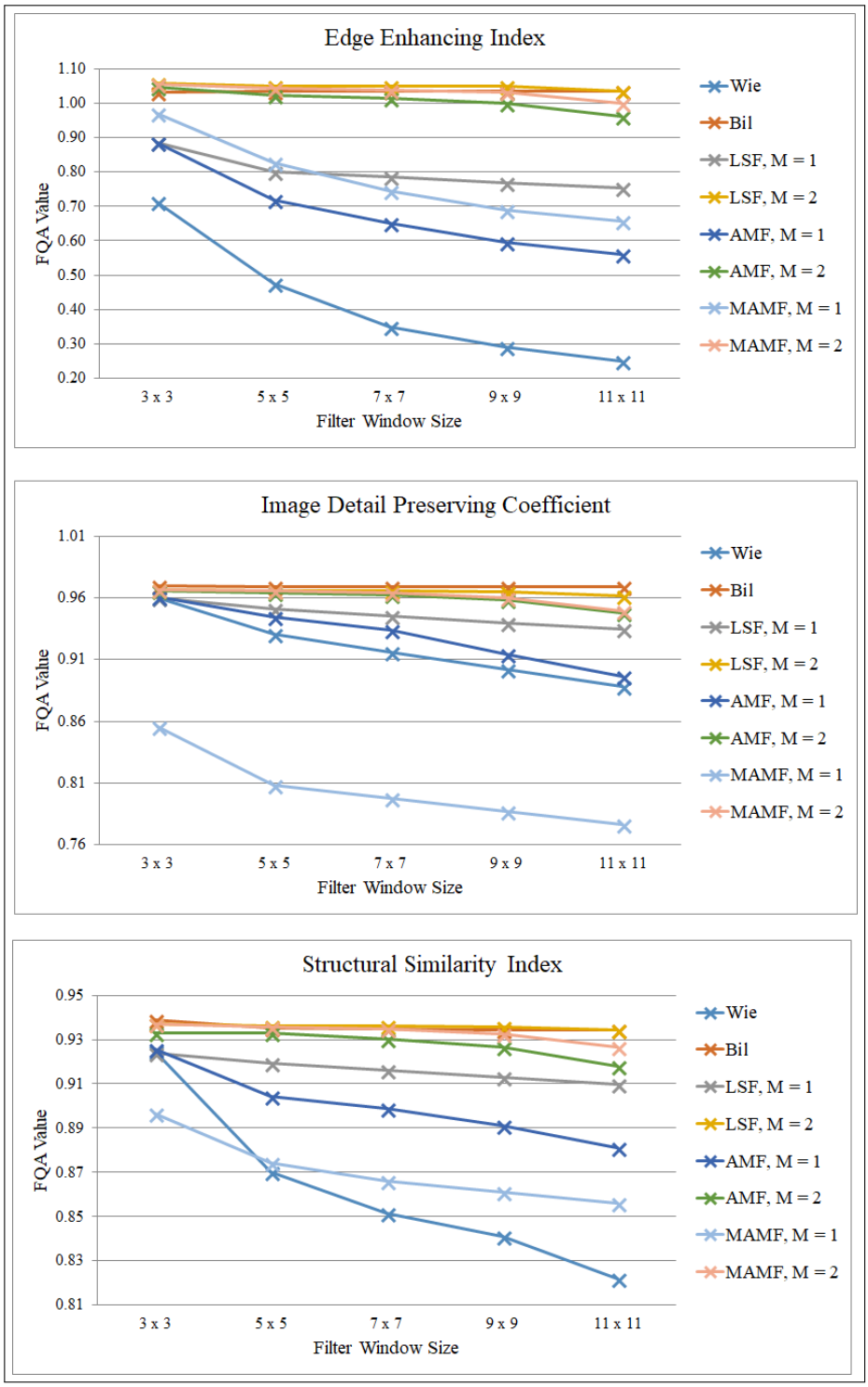

Figure 4.14: Graph of the FQA values for Simulated SAR Images (continued)

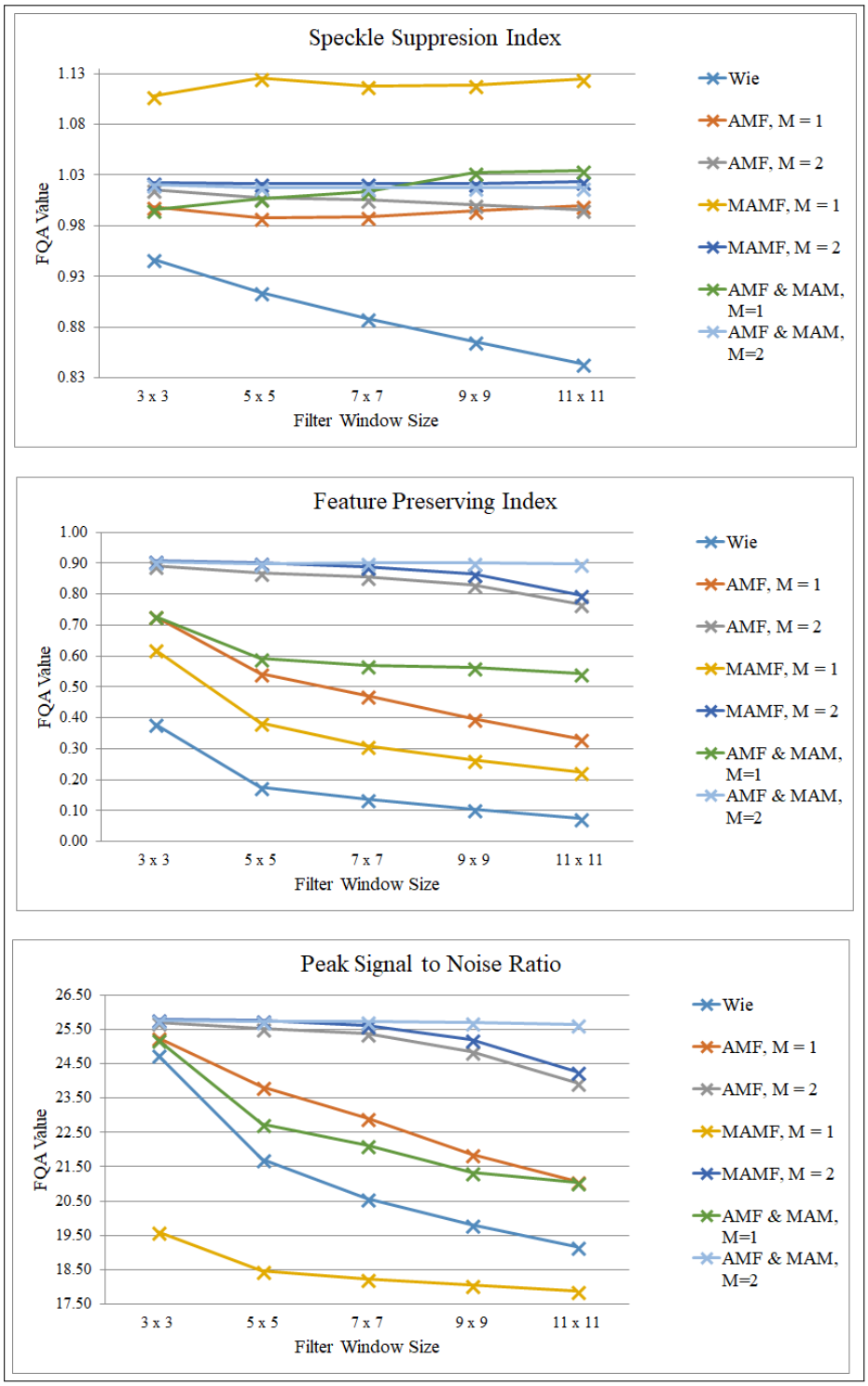

Figure 4.15: Graph of the Region based FQA values for Simulated SAR Images

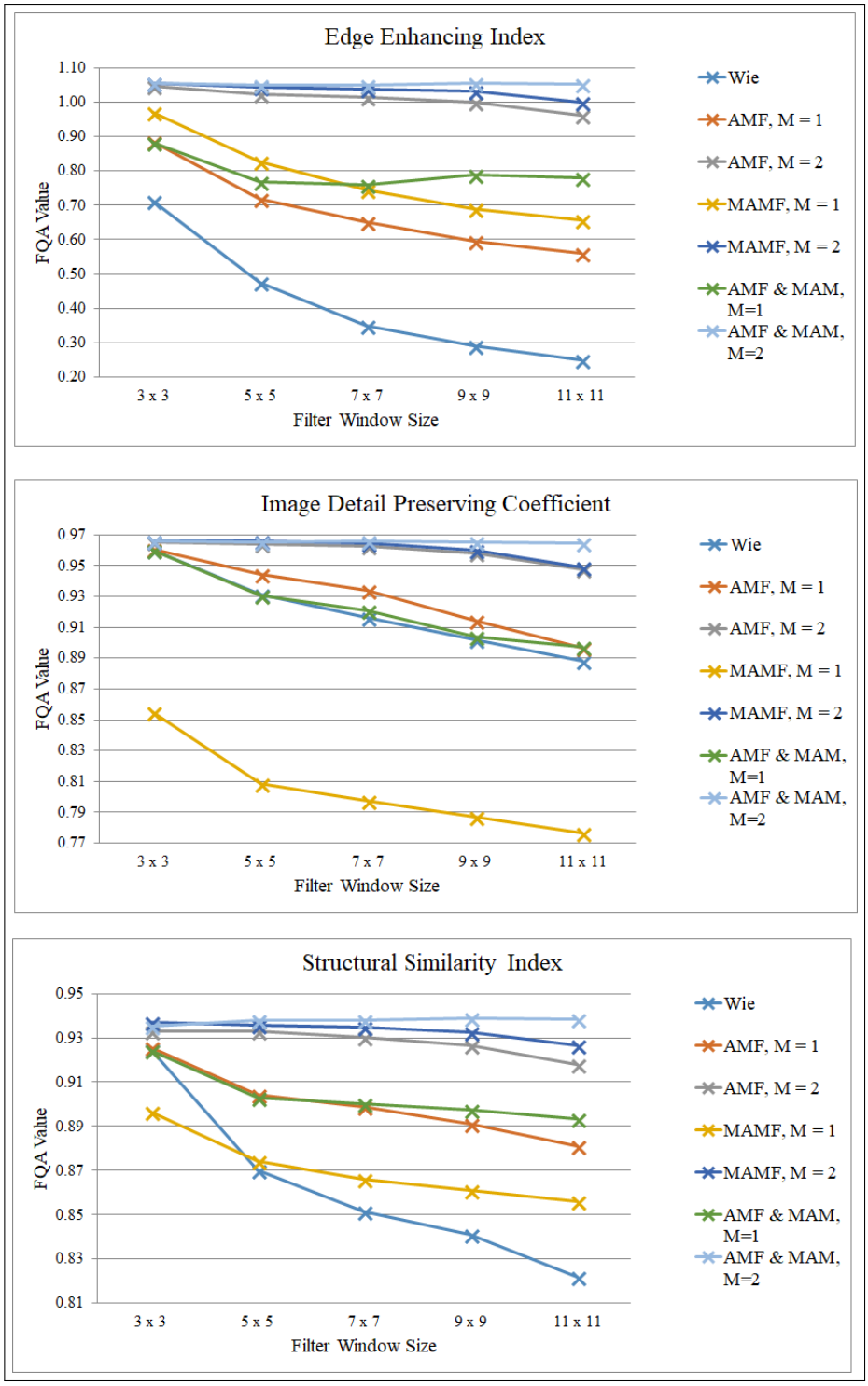

Figure 4.16: Graph of the Region based FQA values for Simulated SAR Images (continued)

Table 4.10: FQA for Region Filtering of Simulated SAR Images

Average of all noises								
FQA parameter	Window Size	Wie	AMF, M = 1	AMF, M = 2	MAMF, M = 1	MAMF, M = 2	AMF & MAMF, M=1	AMF & MAMF, M=2
SSI	3 x 3	0.94	0.99	1.01	1.10	1.02	0.99	1.02
	5 x 5	0.91	0.98	1.00	1.12	1.02	1.00	1.01
	7 x 7	0.88	0.98	1.00	1.11	1.02	1.01	1.01
	9 x 9	0.86	0.99	1.00	1.11	1.02	1.03	1.01
	11 x 11	**0.84**	0.99	0.99	1.12	1.02	1.03	1.01
EEI	3 x 3	0.71	0.88	1.05	0.97	**1.06**	0.88	1.05
	5 x 5	0.48	0.72	1.02	0.83	1.04	0.77	1.05
	7 x 7	0.35	0.65	1.01	0.75	1.04	0.76	1.05
	9 x 9	0.29	0.60	1.00	0.69	1.03	0.79	1.05
	11 x 11	0.25	0.56	0.96	0.66	1.00	0.78	1.05
FPI	3 x 3	0.38	0.73	0.89	0.62	**0.91**	0.73	0.90
	5 x 5	0.17	0.55	0.87	0.38	0.90	0.59	0.90
	7 x 7	0.14	0.47	0.86	0.31	0.89	0.57	0.90
	9 x 9	0.10	0.40	0.83	0.26	0.86	0.56	0.90
	11 x 11	0.07	0.33	0.77	0.22	0.80	0.54	0.90
IDPC	3 x 3	0.96	0.96	0.97	0.86	**0.97**	0.96	0.97
	5 x 5	0.93	0.94	0.96	0.81	0.97	0.93	0.97
	7 x 7	0.92	0.93	0.96	0.80	0.96	0.92	0.97
	9 x 9	0.90	0.91	0.96	0.79	0.96	0.90	0.97
	11 x 11	0.89	0.90	0.95	0.78	0.95	0.90	0.96
PSNR	3 x 3	24.77	25.26	25.69	19.61	**25.80**	25.20	25.77
	5 x 5	21.72	23.83	25.51	18.46	25.75	22.75	25.72
	7 x 7	20.57	22.93	25.39	18.24	25.60	22.14	25.74
	9 x 9	19.81	21.85	24.86	18.06	25.19	21.33	25.70
	11 x 11	19.17	21.08	23.96	17.87	24.25	21.05	25.63
SSIM	3 x 3	0.92	0.93	0.93	0.90	0.94	0.92	0.94
	5 x 5	0.87	0.90	0.93	0.87	0.94	0.90	0.94
	7 x 7	0.85	0.90	0.93	0.87	0.93	0.90	0.94
	9 x 9	0.84	0.89	0.93	0.86	0.93	0.90	**0.94**
	11 x 11	0.82	0.88	0.92	0.86	0.93	0.89	0.94

Wiener filter with window size 11x11 has the best SSI, but with extremely low FPI and EEI, even with window size 3x3.

The best EEI is produced by the LSF, M = 2. The proposed filter with M = 2 is again marginally second, followed by the AMF with M = 2. It is a similar case in terms of IDPC, PSNR and SSIM values, with LSF being the best of the three filters, the MAMF second and last being the AMF, all with M=2.

The FQA results for the Region based filtering proposed in section 4.2.2 are shown in Table 4.10 and Figures 4.15 and 4.16. It can be seen how region filtering improves the performance of the AMF but is still marginally behind the MAMF on its own. Only

for the SSIM, the region filtering with window size 9x9 is better than the MAMF on its own.

It can be noted how almost all the best results are produced with filter window value 3x3, except for the SSI, where the Wiener filter with window 11x11 is the best. For the AMF, MAMF and the region filtering, M = 2, has the best set of results as opposed to M = 1.

As mentioned in section 2.3.1, although the Wiener filter with window size 11x11 has the best SSI, it is not ideal as it comes at the cost of extremely low other FQA parameters. Although the Wiener filter with window size 3x3 has better IDPC, PSNR and SSIM, it still has the lowest EEI and FPI, which are more ideal for Image Segmentation. This is the same case for the region based filtering approach.

Thus for Simulated SAR images, the proposed filter with M=2 and window size 3x3 as well as the Bilateral filter are the most ideal for filtering without region based approach and for region based approach, the proposed filter with M=2 and window size 3x3 produces the better results, closely followed by its use to enhance the AMF results.

4.4.1.4 Sample RGB Images

The final FQA analysis were performed on sample RGB images and are given in Table 4.11 as well as the graphs in Figures 4.17 and 4.18. These results are the average for the FQA performed on the three different noise addition mentioned in section 4.3.1.

From the Table 4.11, it can be seen that yet again the Wiener filter produces the best IDPC, PSNR, SSIM and SSI results. Whilst the best values for IDPC, PSNR and SSIM are produced with Wiener filter window size 5x5, the best best SSI are yet again produced by window size 11x11. Also yet again the Wiener filter is really poor in terms of EEI and FPI.

Similar to what is seen with the Sea Ice images, the proposed MAMF marginally produces better results when compared with the AMF with M = 2, for EEI and FPI.

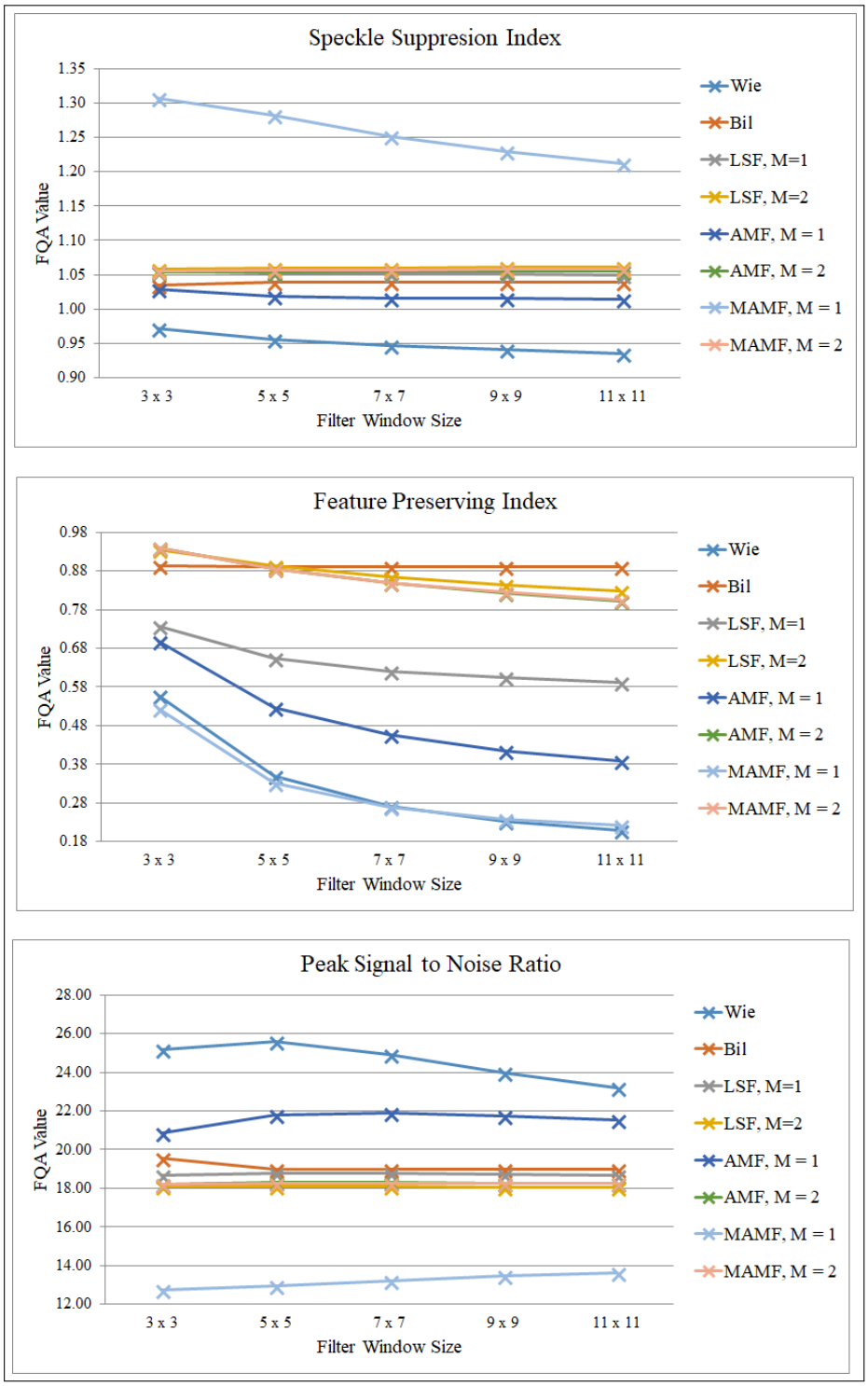

Figure 4.17: Graph of the FQA values for RGB Images

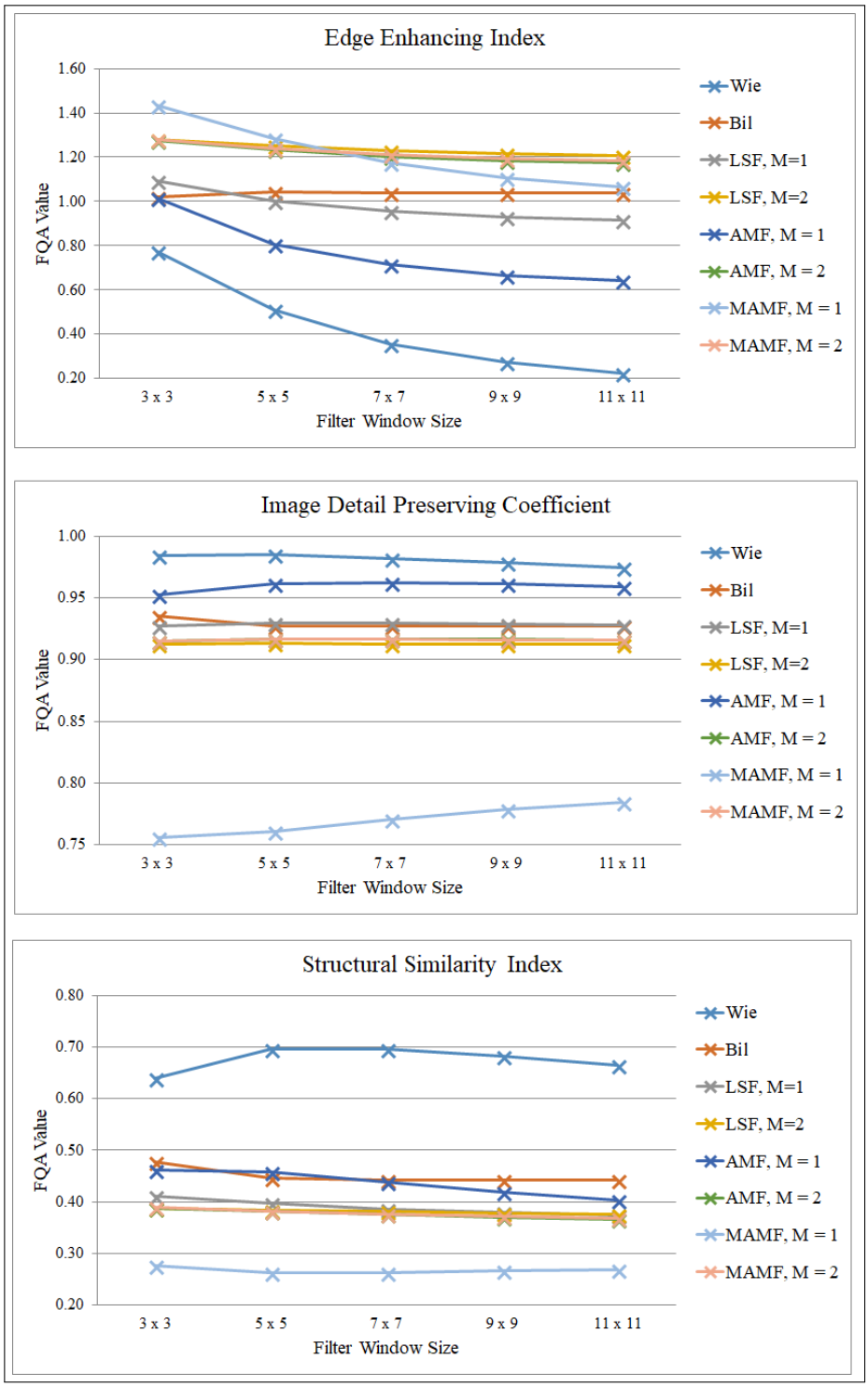

Figure 4.18: Graph of the FQA values for RGB Images (continued)

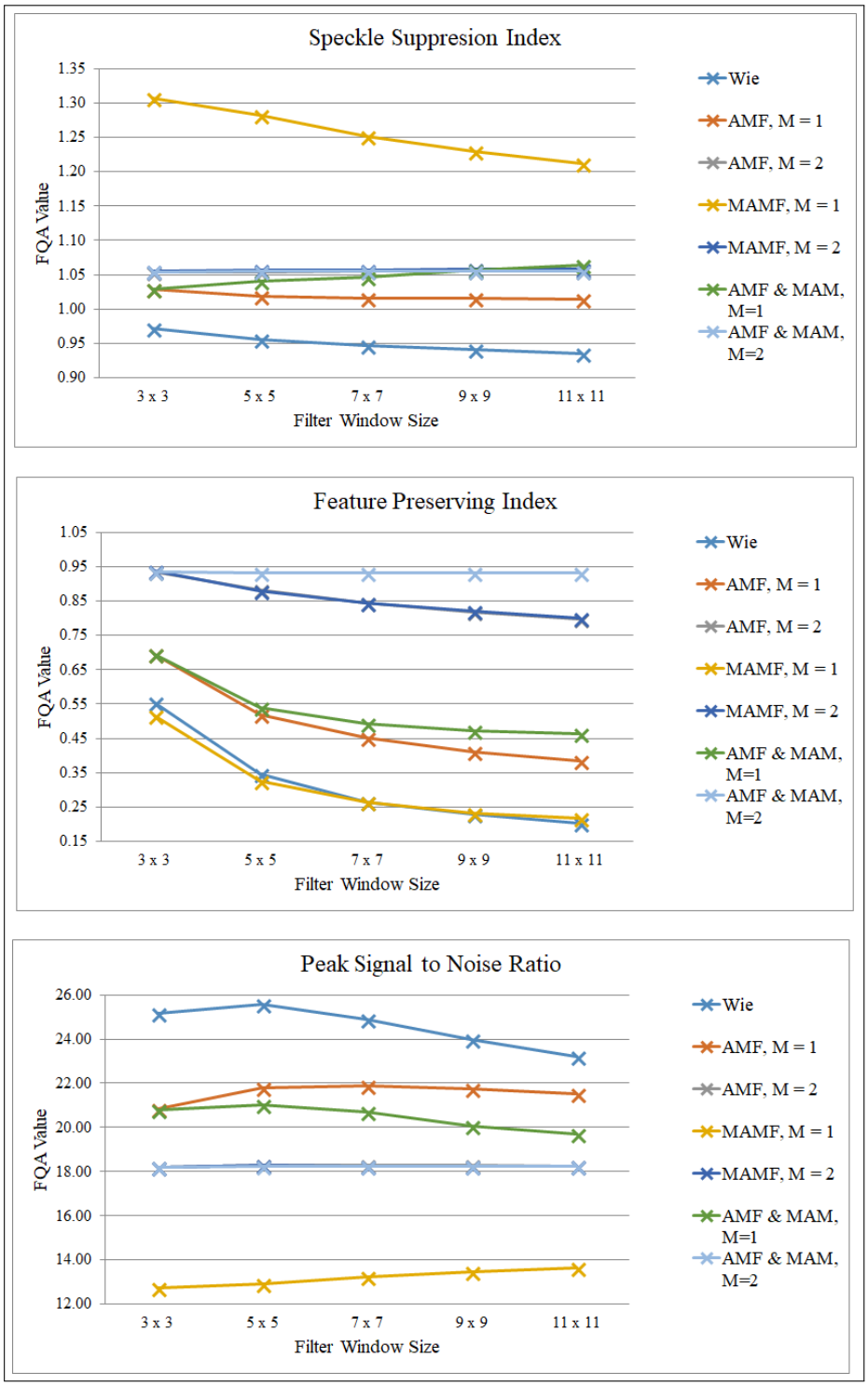

Figure 4.19: Graph of the Region based FQA values for RGB Images

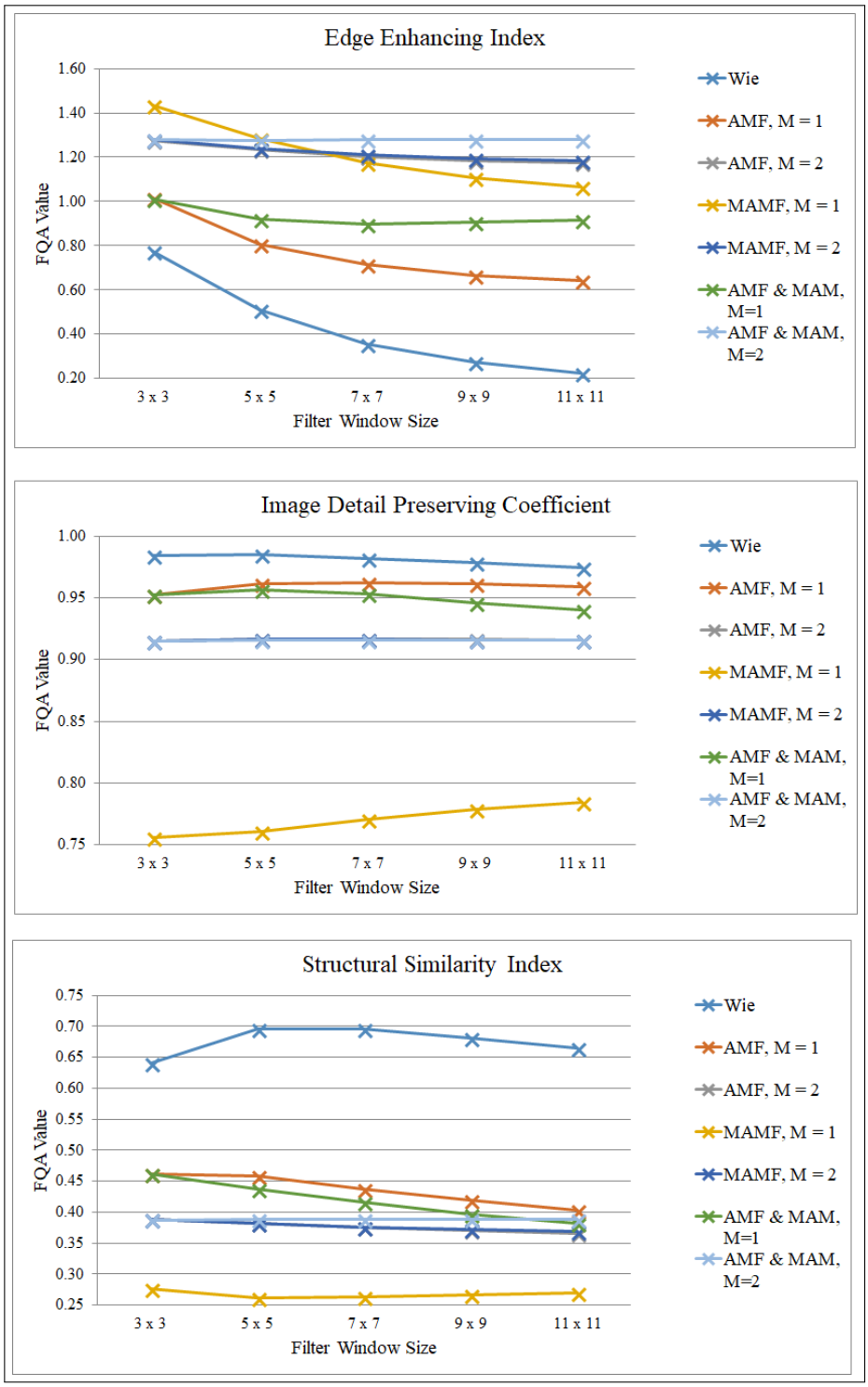

Figure 4.20: Graph of the Region based FQA values for RGB Images (continued)

Table 4.11: FQA of RGB Images

Average of Noises									
FQA parameter	Window Size	Wiener	Bilateral	LSF, M=1	LSF, M=2	AMF, M = 1	AMF, M = 2	Mod AMF, M = 1	Mod AMF, M = 2
SSI	3 x 3	0.97	1.03	1.06	1.06	1.03	1.05	1.31	1.06
	5 x 5	0.96	1.04	1.05	1.06	1.02	1.05	1.28	1.06
	7 x 7	0.95	1.04	1.05	1.06	1.02	1.06	1.25	1.06
	9 x 9	0.94	1.04	1.05	1.06	1.02	1.06	1.23	1.06
	11 x 11	**0.94**	1.04	1.05	1.06	1.01	1.06	1.21	1.06
EEI	3 x 3	0.77	1.02	1.09	1.28	1.01	1.28	**1.44**	1.28
	5 x 5	0.51	1.04	1.00	1.25	0.81	1.23	1.28	1.24
	7 x 7	0.36	1.04	0.96	1.23	0.71	1.20	1.18	1.21
	9 x 9	0.27	1.04	0.93	1.22	0.67	1.19	1.11	1.19
	11 x 11	0.23	1.04	0.91	1.21	0.64	1.17	1.06	1.18
FPI	3 x 3	0.55	0.89	0.73	0.93	0.69	0.94	0.52	**0.94**
	5 x 5	0.35	0.89	0.65	0.89	0.52	0.88	0.33	0.88
	7 x 7	0.27	0.89	0.62	0.86	0.45	0.84	0.26	0.84
	9 x 9	0.23	0.89	0.60	0.84	0.41	0.82	0.23	0.82
	11 x 11	0.20	0.89	0.59	0.82	0.38	0.80	0.22	0.80
IDPC	3 x 3	0.98	0.94	0.93	0.91	0.95	0.92	0.76	0.91
	5 x 5	**0.99**	0.93	0.93	0.91	0.96	0.92	0.76	0.92
	7 x 7	0.98	0.93	0.93	0.91	0.96	0.92	0.77	0.92
	9 x 9	0.98	0.93	0.93	0.91	0.96	0.92	0.78	0.92
	11 x 11	0.97	0.93	0.93	0.91	0.96	0.92	0.78	0.92
PSNR	3 x 3	25.15	19.56	18.65	18.08	20.83	18.22	12.75	18.20
	5 x 5	**25.59**	18.99	18.77	18.09	21.79	18.30	12.93	18.27
	7 x 7	24.89	18.98	18.75	18.08	21.89	18.30	13.22	18.26
	9 x 9	23.98	18.98	18.71	18.07	21.74	18.27	13.46	18.25
	11 x 11	23.22	18.98	18.66	18.05	21.52	18.24	13.63	18.23
SSIM	3 x 3	0.64	0.48	0.41	0.39	0.46	0.39	0.28	0.39
	5 x 5	**0.70**	0.45	0.40	0.38	0.46	0.38	0.26	0.38
	7 x 7	0.70	0.44	0.39	0.38	0.44	0.38	0.26	0.38
	9 x 9	0.68	0.44	0.38	0.38	0.42	0.37	0.27	0.37
	11 x 11	0.67	0.44	0.37	0.38	0.40	0.37	0.27	0.37

The results are also very marginally better for the SSIM value but the opposite is the case for PSNR and IDPC values, where the AMF is better out of the two. The best results for these two filters are produced with filter window 3x3 and M = 2 respectively.

The FQA results for the Region based filtering proposed in section 4.2.2 are shown in Table 4.12 and Figures 4.19 and 4.20. It can be seen how the region filtering slightly improves the performance of the AMF (window size 5x5 and above) in terms of EEI, FPI and the SSIM values. However for the PSNR value, there is a moderate decline in the performance. It is also noticable that the MAMF performs better on its own as opposed to the region filtering used to improve the performance of the AMF.

Table 4.12: FQA for Region Filtering of RGB Images

Average of all noises								
FQA parameter	Window Size	Wie	AMF, M = 1	AMF, M = 2	MAMF, M = 1	MAMF, M = 2	AMF & MAMF, M=1	AMF & MAMF, M=2
SSI	3 x 3	0.97	1.03	1.05	1.31	1.06	1.03	1.05
	5 x 5	0.96	1.02	1.05	1.28	1.06	1.04	1.05
	7 x 7	0.95	1.02	1.06	1.25	1.06	1.05	1.06
	9 x 9	0.94	1.02	1.06	1.23	1.06	1.06	1.06
	11 x 11	**0.94**	1.01	1.06	1.21	1.06	1.06	1.06
EEI	3 x 3	0.77	1.01	1.28	**1.44**	1.28	1.01	1.28
	5 x 5	0.51	0.81	1.23	1.28	1.24	0.92	1.28
	7 x 7	0.36	0.71	1.20	1.18	1.21	0.90	1.28
	9 x 9	0.27	0.67	1.19	1.11	1.19	0.91	1.28
	11 x 11	0.23	0.64	1.17	1.06	1.18	0.92	1.28
FPI	3 x 3	0.55	0.69	0.94	0.52	**0.94**	0.69	0.94
	5 x 5	0.35	0.52	0.88	0.33	0.88	0.54	0.93
	7 x 7	0.27	0.45	0.84	0.26	0.84	0.49	0.93
	9 x 9	0.23	0.41	0.82	0.23	0.82	0.47	0.93
	11 x 11	0.20	0.38	0.80	0.22	0.80	0.46	0.93
IDPC	3 x 3	0.98	0.95	0.92	0.76	0.91	0.95	0.91
	5 x 5	**0.99**	0.96	0.92	0.76	0.92	0.96	0.92
	7 x 7	0.98	0.96	0.92	0.77	0.92	0.95	0.92
	9 x 9	0.98	0.96	0.92	0.78	0.92	0.95	0.92
	11 x 11	0.97	0.96	0.92	0.78	0.92	0.94	0.92
PSNR	3 x 3	25.15	20.83	18.22	12.75	18.20	20.81	18.19
	5 x 5	**25.59**	21.79	18.30	12.93	18.27	21.02	18.23
	7 x 7	24.89	21.89	18.30	13.22	18.26	20.69	18.24
	9 x 9	23.98	21.74	18.27	13.46	18.25	20.09	18.24
	11 x 11	23.22	21.52	18.24	13.63	18.23	19.72	18.24
SSIM	3 x 3	0.64	0.46	0.39	0.28	0.39	0.46	0.39
	5 x 5	**0.70**	0.46	0.38	0.26	0.38	0.44	0.39
	7 x 7	0.70	0.44	0.38	0.26	0.38	0.42	0.39
	9 x 9	0.68	0.42	0.37	0.27	0.37	0.40	0.39
	11 x 11	0.67	0.40	0.37	0.27	0.37	0.38	0.39

As mentioned in section 2.3.1, although the Wiener filter with window size 11x11 has the best SSI, it is not ideal as it comes at the cost of extremely low other FQA parameters. Although the Wiener filter with window size 3x3 has better IDPC, PSNR and SSIM, it still has the lowest EEI and FPI, which are more ideal for Image Segmentation. This is the same case for the region based filtering approach.

Thus for Sample RGB images, the proposed filter with M=2 and window size 3x3 is the most ideal for filtering without and with region based approach, closely followed by its use to enhance the AMF results.

4.4.2 Filter Subjective Analysis

In this section, the visual results for the various filtering techniques are shown and then the results of the proposed filter are compared. Figure 4.21 shows the sample results for the proposed MAMF with increasing window sizes. It can be seen how the increasing filter window size decreases the accuracy of the filtered image and also producing a blurred result.

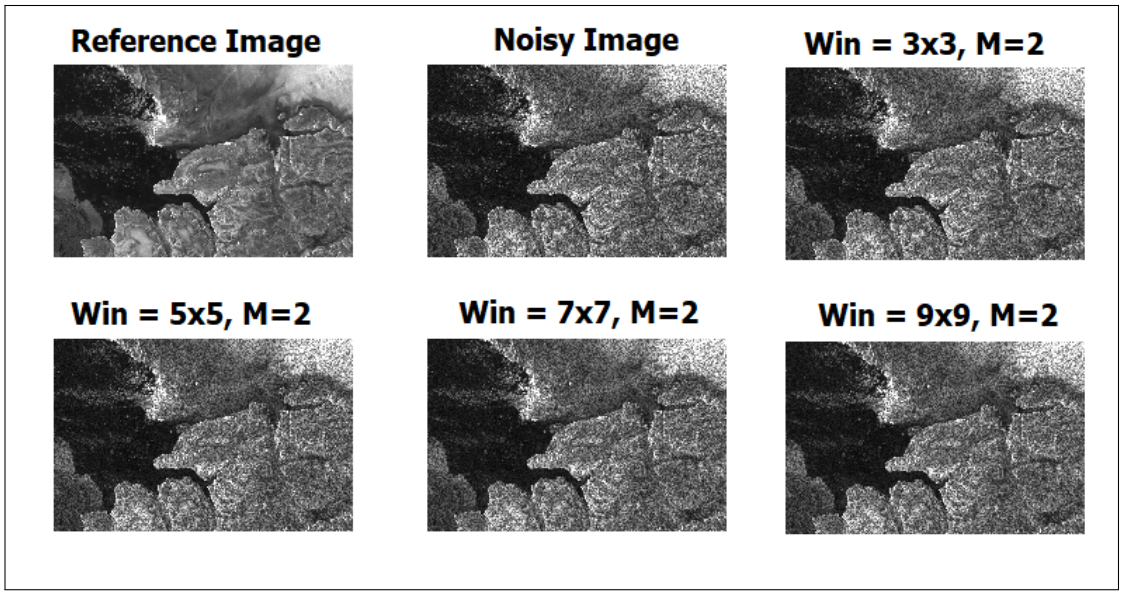

Figure 4.21: Results of the Proposed MAMF, with increasing window size

The results shown in Figure 4.22 are for Sample3 of the SAR Sea Ice image, which has dimensions of 570x620 pixels. The Wiener as well as the Bilateral filter results shows a bit of blurriness. The results for the LSF and the AMF look almost identical to each other. Similarly the MAMF and region filtered result look very similar to each other. However, subjectively it can be said that the region based filtering done to improve the AMF result using the proposed MAMF produces the best result.

The results shown in Figure 4.23 are for Sample 2 of the Sentinel-1A SAR image, which has dimensions of 2560x1664 pixels. The results for the Wiener filter, subjectively, look very much similar to that of the original reference image.

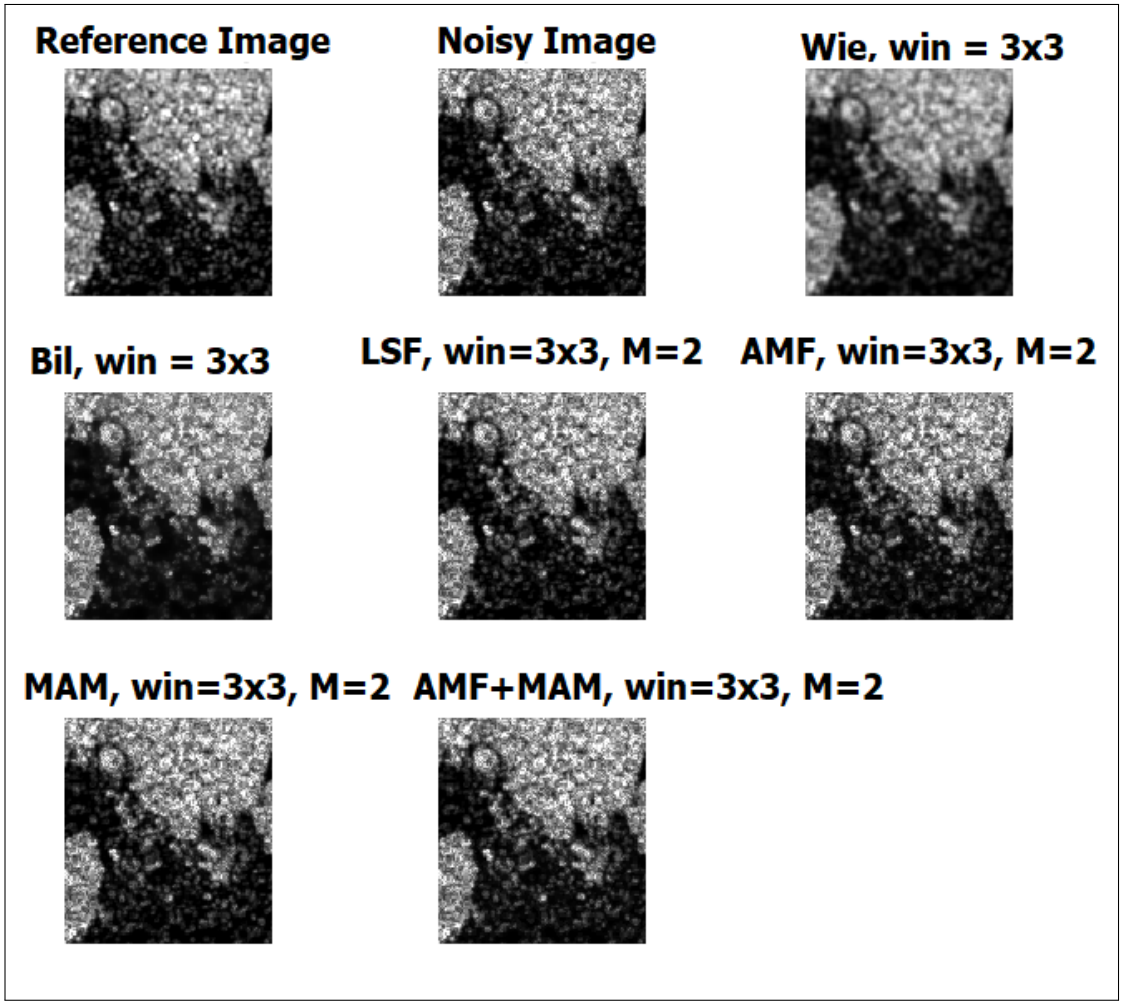

Figure 4.22: FQA Results for all the filters, with window size = 3x3 and Multiplier value = 2, for SAR Sea Ice Image

Very minute changes can be noticed between the LSF, AMF and the MAMF result. The region filtered result as well doesn't show much difference to the MAMF result produced.

The results shown in Figure 4.24 are for Sample 2 of the Simulated SAR image generated, which has dimensions of 217x181 pixels. The Wiener filter can be clearly seen to show visibly the worst results. The Bilateral filter looks the most similar to the reference image, followed by proposed MAMF, the LSF and the AMF results.

The results shown in Figure 4.25 are for the Desert sample of the Windows PC

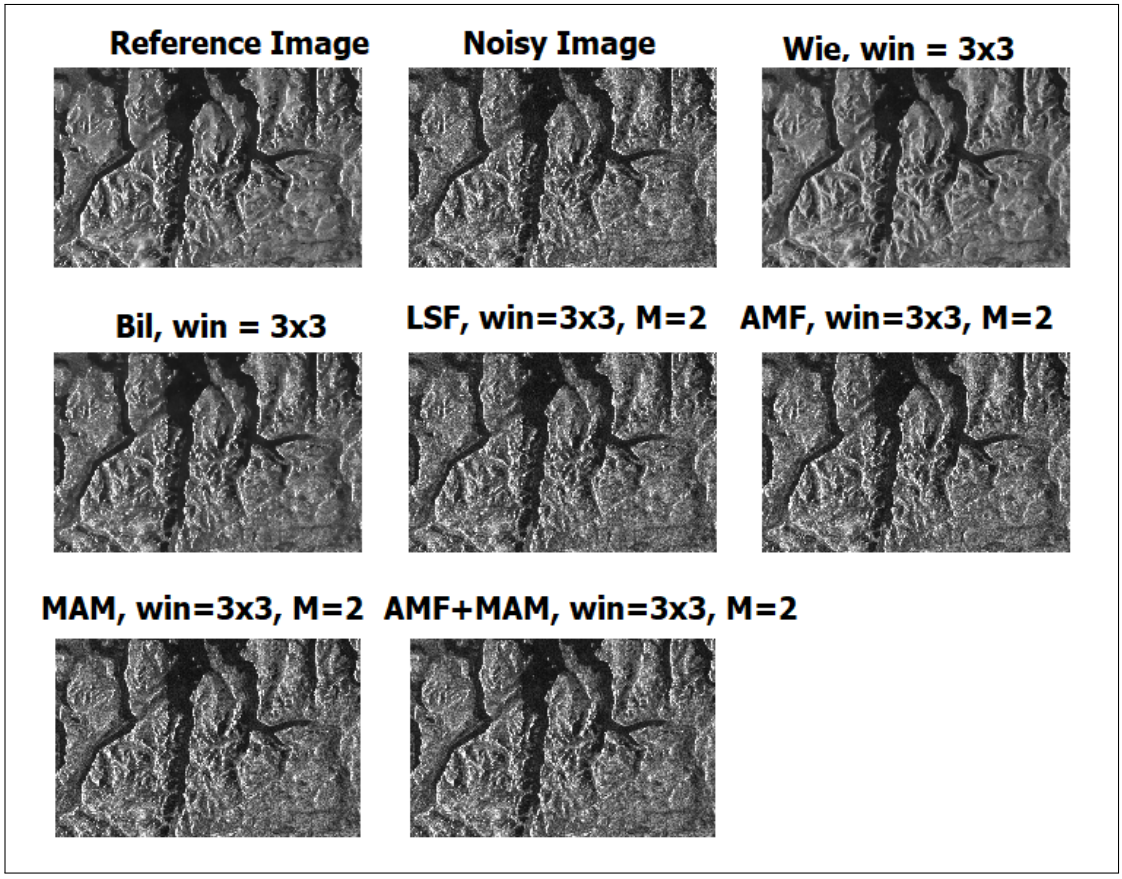

Figure 4.23: FQA Results for all the filters, with window size = 3x3 and Multiplier value = 2, for Sentinel-1A SAR Image

sample RGB images which has dimensions of 1024x768 pixels. The Wiener filter here appears to be the most cleanest image in terms of noise removed, however it also looks worse in terms of edges retained with the reference image.

In terms of edge retention as well as speckle noise reduction, the proposed MAMF and the region filtering produced result show the best results for the image.

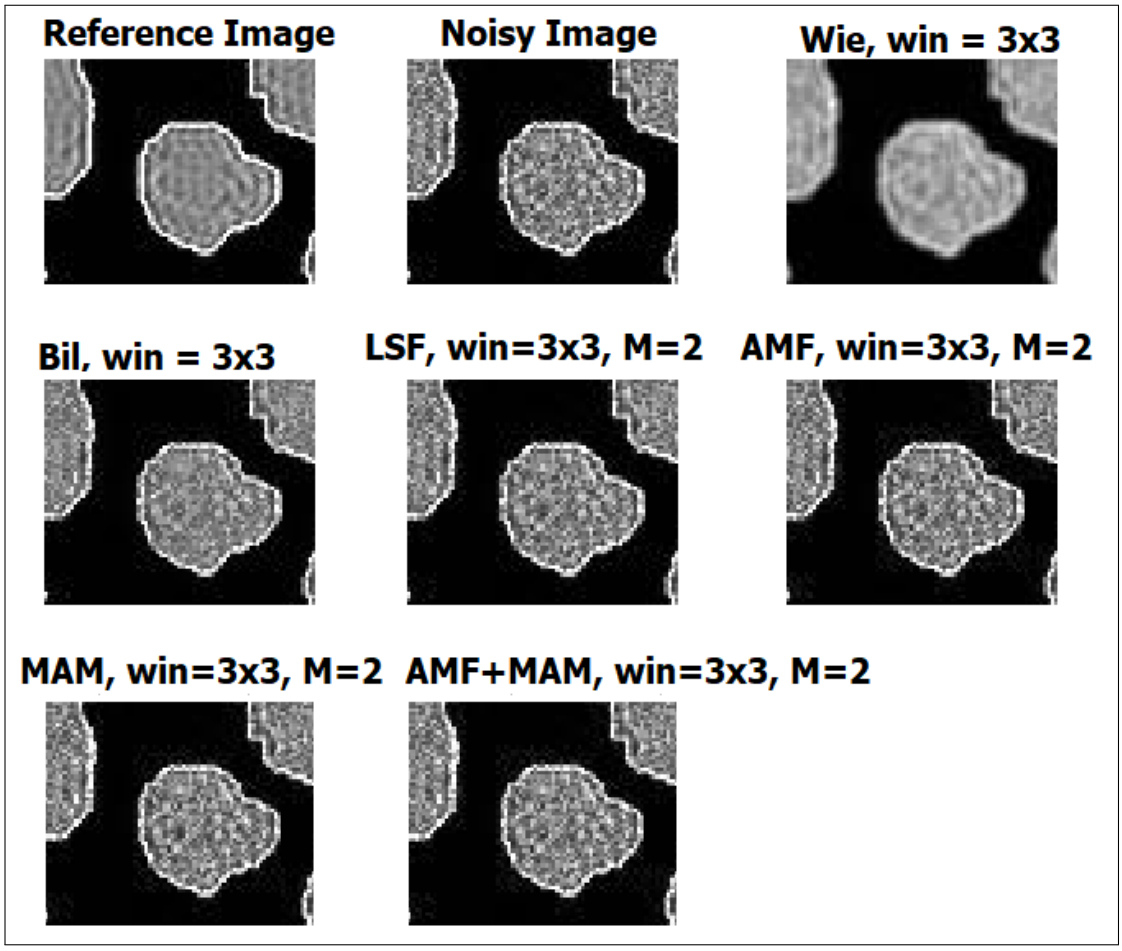

Figure 4.24: FQA Results for all the filters, with window size = 3x3 and Multiplier value = 2, for Simulated SAR Image

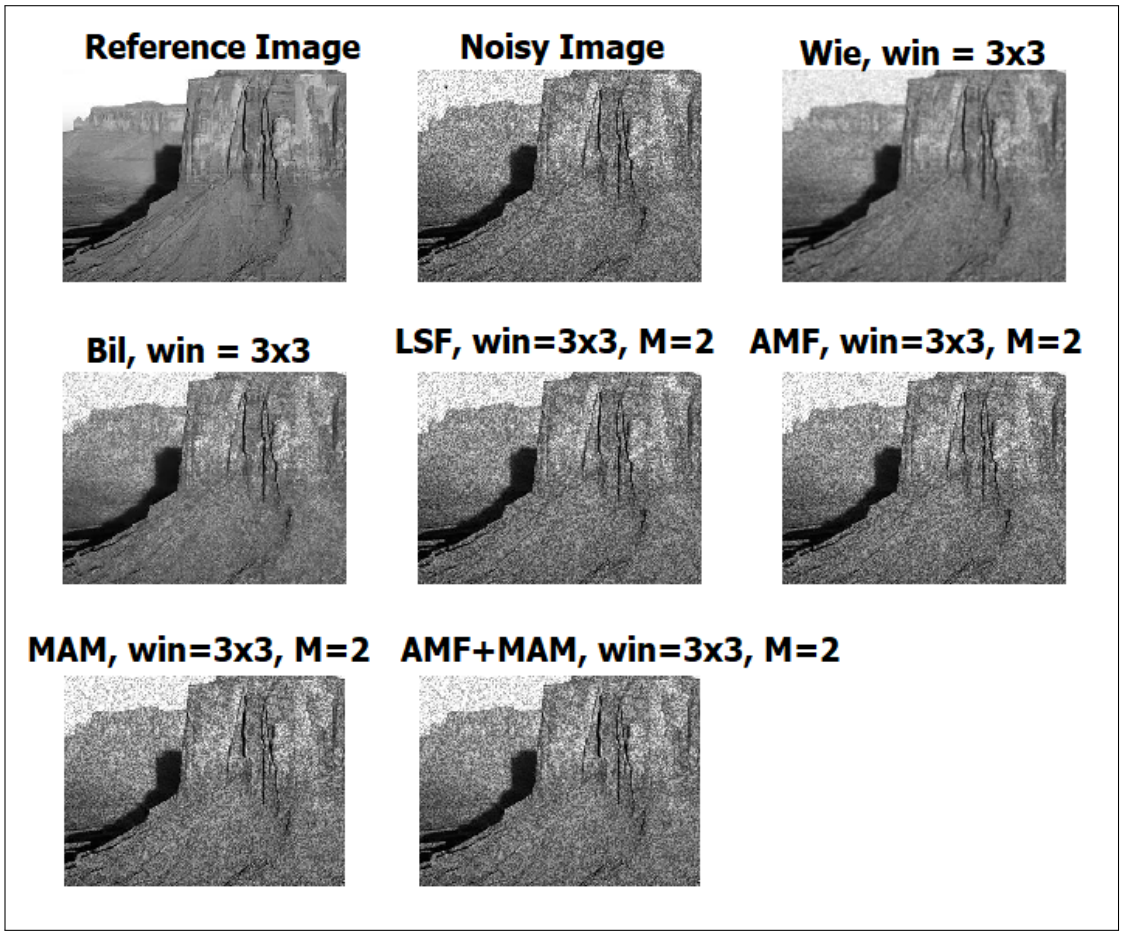

Figure 4.25: FQA Results for all the filters, with window size = 3x3 and Multiplier value = 2, for Sample RGB Image

4.4.3 Computation Time

In this section, the Computing time (in seconds) for the various filters described in sections 2.1.1 and 4.2.1, are shown. The various filters used for derivation of the FQA results are compared here, to form an overall perspective in terms of filter efficiency.

The processing times for the region filtering are not shown in the following sections, but understandably, it takes more time to compute the results, due to the calculations of FQA parameters required to decide if a region is filtered twice or not.

All the timing parameters shown in these following sub sections have been coded in Matlab 2018a software, running on a Macbook Pro with 2.3 GHz processor Intel Core i5, 8 GB RAM and macOS High Sierra v.10.13.3 operating system.

4.4.3.1 Sea Ice SAR Images

The computing time for SAR Sea Ice images is given in 4.13 and shown in the graph of Figure 4.26.

Table 4.13: Computing Time of SAR Sea Ice Images

Average of Different Noises									
	Window Size	Wie	Bil	LSF, M = 1	LSF, M = 2	AMF, M = 1	AMF, M = 2	MAMF, M = 1	MAMF, M = 2
Timing	3 x 3	**0.0084**	1.2397	1.0801	1.0668	0.5913	0.4806	2.4106	0.6014
	5 x 5	0.0086	1.6611	1.1234	1.1257	0.6697	0.5188	3.4123	0.7567
	7 x 7	0.0089	2.2393	1.3848	1.3763	0.8252	0.5968	4.1329	0.9382
	9 x 9	0.0101	2.8716	1.4836	1.4781	0.9863	0.6698	4.3847	1.0675
	11x11	0.0097	3.5346	1.6210	1.6086	1.1771	0.7707	8.1830	1.6370

From the Table 4.13 and Figure 4.26, it is seen how the slowest processing is by the MAMF with M = 1, followed by the Bilateral filtering. The MAMF with M = 2 is very slightly slower than that of the AMF with M = 2. The quickest result is produced by the in-built function in Matlab used for the Wiener filter results.

One important phenomenon noted from the values above, is the steep rise of computation times for the Bilateral filter, especially for window size 9x9 and 11x11. This is due to the use of exponential calculations done to compute the range and domain

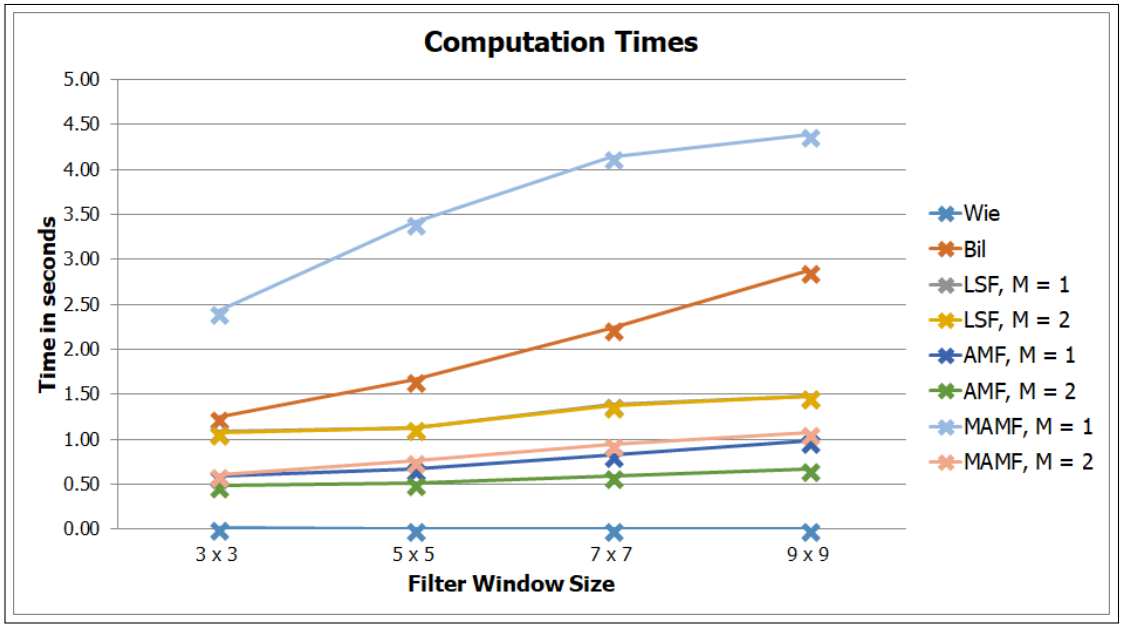

Figure 4.26: Graph of the Computing time for SAR Sea Ice Images

filtering values used for filtering. Lastly, the two LSF processes take almost identical amount of time.

4.4.3.2 Sentinel-1A SAR Images

The computing time for Sentinel-1A SAR images is given in Table 4.14 and shown in the graph of Figure 4.27.

Table 4.14: Computing Time of Sentinel-1A SAR Images

Average of Different Noises									
	Window Size	Wie	Bil	LSF, M = 1	LSF, M = 2	AMF, M = 1	AMF, M = 2	MAMF, M = 1	MAMF, M = 2
Timing	3 x 3	**0.1083**	15.9017	12.9198	12.8628	7.3204	5.6983	34.6414	6.6984
	5 x 5	0.1121	20.6348	13.9466	13.6208	8.6095	6.2358	44.1860	7.8701
	7 x 7	0.1180	28.5744	16.7837	16.6401	10.0978	7.1884	50.4737	9.2377
	9 x 9	0.1351	36.8006	18.8563	18.8652	12.7778	8.5795	55.3114	11.2310
	11x11	0.1181	43.8356	19.8263	19.6898	14.5383	9.3739	100.7155	16.5894

From the Table 4.14 and Figure 4.27 it is seen how, similar to the Sea Ice images performance, the slowest processing is by the MAMF with M = 1 followed by the Bilateral filtering. The MAMF with M = 2 is initially very slightly slower than that

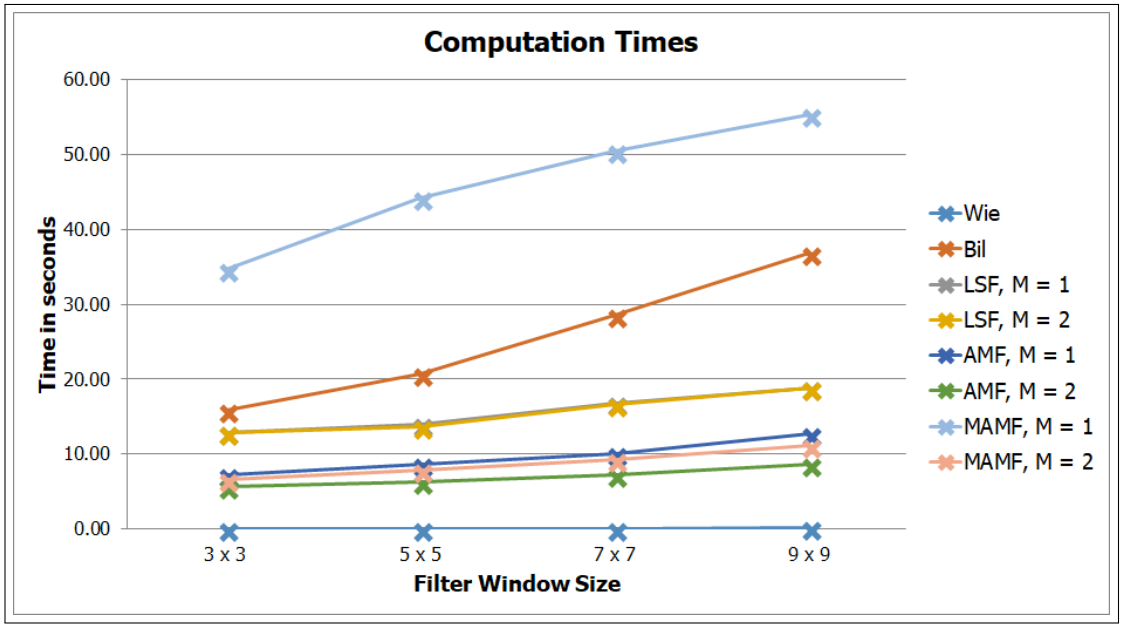

Figure 4.27: Graph of the Computing time for Sentinel-1A SAR Images

of the AMF filter with M = 2, but then becomes much slower with window sizes 9 and 11. The quickest result is produced by the in-built function in Matlab used for the Wiener filter results. However one noticeable difference is that the MAMF with M = 2, is now initially faster than the AMF with M = 1 with window sizes 3, 5, 7 and 9. The steep rise in the computation times for the Bilateral filter with window sizes 9 and 11, is similar as the one seen in section 4.4.3.1 and due to the similar circumstances mentioned. Lastly, the two LSF processes again take almost identical amount of time.

4.4.3.3 Simulated SAR Images

The computing time for Simulated SAR images is given in Table 4.15 and shown in the graph of Figure 4.28.

From the Table 4.15 and Figure 4.28, it is seen how the slowest processing is now by the Bilateral. The MAMF with M = 2 is very slightly slower than that of the AMF filter with M = 2 and M = 1, for window sizes 3, 5 and 7. The quickest result is produced by the in-built function in Matlab used for the Wiener filter results. The

Table 4.15: Computing Time of Simulated SAR Images

Average of Different Noises									
	Window Size	Wie	Bil	LSF, M = 1	LSF, M = 2	AMF, M = 1	AMF, M = 2	MAMF, M = 1	MAMF, M = 2
Timing	3 x 3	**0.0090**	1.2537	0.5025	0.4994	0.4243	0.4026	0.6150	0.5271
	5 x 5	0.0094	1.5088	0.5350	0.5340	0.4377	0.4235	0.6994	0.5953
	7 x 7	0.0102	1.8239	0.6233	0.6242	0.5009	0.4823	0.8131	0.6739
	9 x 9	0.0101	2.6088	0.6810	0.6949	0.5482	0.5271	0.8699	0.7366
	11x11	0.0103	3.1801	0.7316	0.7293	0.6051	0.5778	1.3054	1.0695

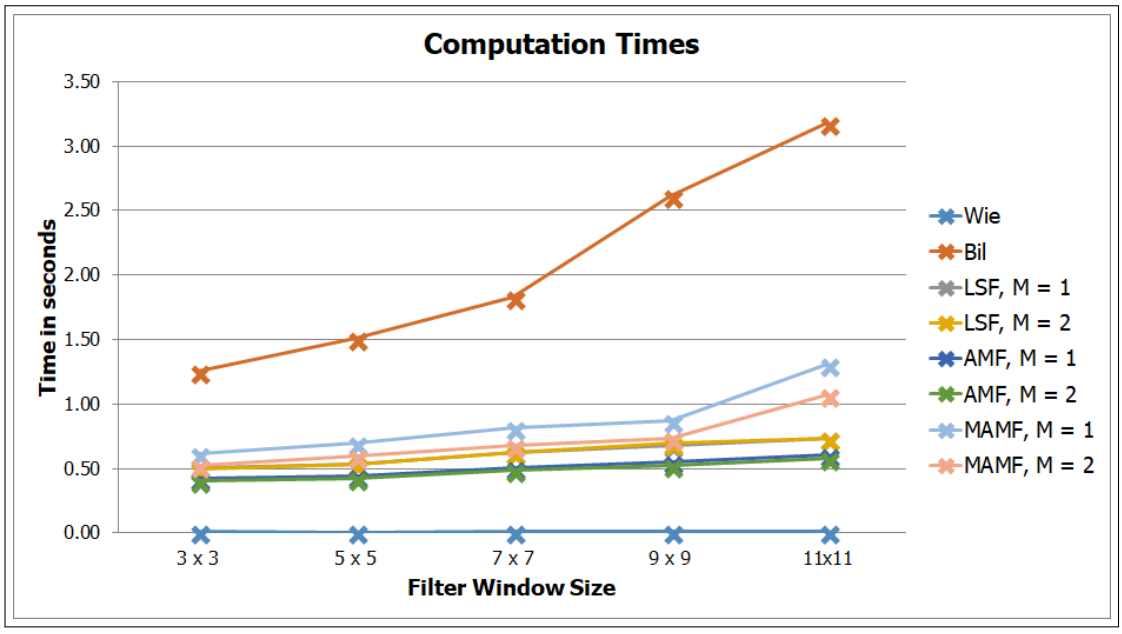

Figure 4.28: Graph of the Computing time for Simulated SAR Images

steep rise in the computation times for the Bilateral filtering is again similar as the one seen in section 4.4.3.1 and due to the similar circumstances mentioned. Lastly, the two LSF processes again take almost identical amount of time.

4.4.3.4 Sample RGB Images

The computing time for sample RGB images is given in Table 4.16 and shown in the graph of Figure 4.29.

From the Table 4.16 and Figure 4.29, it is seen how the results show almost identical outcome to that witnessed with the Sea Ice images. The slowest result is produced

Table 4.16: Computing Time of RGB Images

Average of Different Noises									
	Window Size	Wie	Bil	LSF, M = 1	LSF, M = 2	AMF, M = 1	AMF, M = 2	MAMF, M = 1	MAMF, M = 2
Timing	3 x 3	**0.0203**	2.7957	2.4566	2.4341	1.3552	1.0922	6.1932	1.5188
	5 x 5	0.0205	3.7834	2.6190	2.6140	1.5640	1.2305	8.1480	1.9053
	7 x 7	0.0208	5.0521	3.2263	3.2116	1.9145	1.4254	9.3511	2.2455
	9 x 9	0.0208	6.5437	3.4625	3.4563	2.2591	1.5776	9.5735	2.4268
	11x11	0.0212	8.0245	3.7629	3.7488	2.6679	1.7968	17.2513	3.6687

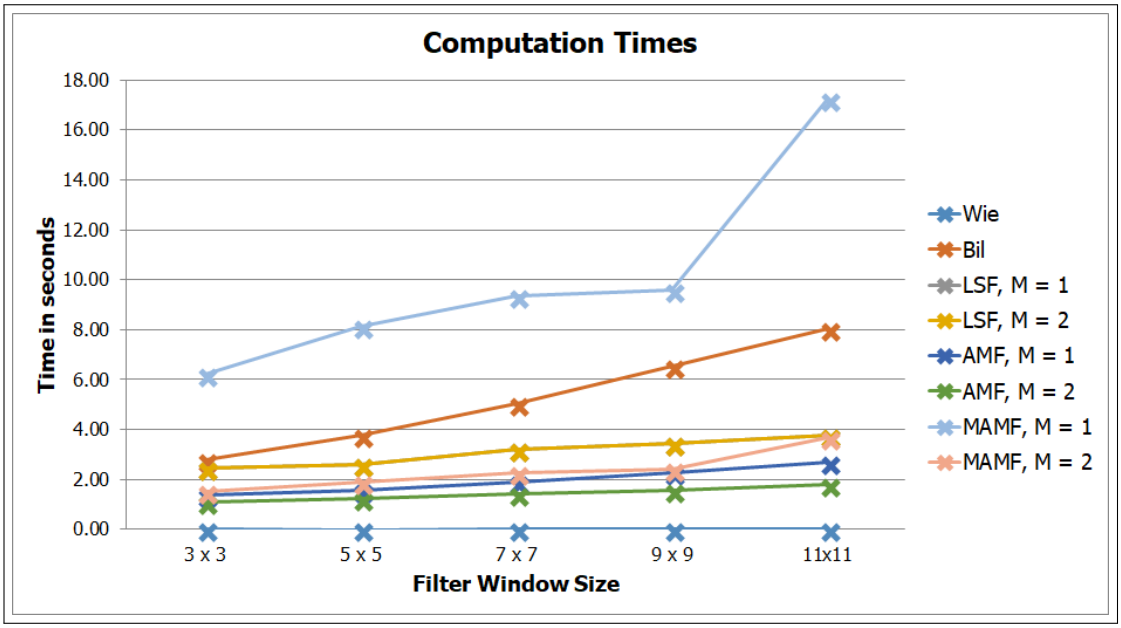

Figure 4.29: Graph of the Computing time for Sample RGB Images

the MAMF with M = 1, followed by the Bilateral filter. The MAMF with M = 2 is slightly slower than AMF M = 1 and even more slower than AMF M = 2 respectively. The LSF is slower than AMF and MAMF, apart from the MAMF M=1. The steep rise in the computation times is similar as the one seen in section 4.4.3.1 and due to the similar circumstances mentioned. Lastly, the two LSF processes again take almost identical amount of time.

4.5 Summary

A further modification is proposed to the AMF using the advantages of the MMSE filter used in the Wiener filtering. For the FQA, the proposed filter marginally outperforms the AMF for the SAR Sea Ice, the Sentinel-1A as well as the Simulated SAR images, especially in terms of edge and feature preservation. These are two vital properties which will be further exploited in the following chapter for the purpose of Sea Ice segmentation. For the subjective analysis, in some cases it can be seen that the Wiener filter produces a much better result. It can also be said that the differences between the proposed filter and the AMF are sometimes minimal. For the computation efficiency, the proposed filter is only marginally slower than the AMF filter.

Thus, by using the local statistics of the image, similar to that of the AMF and making use of the advantages of the Wiener filter in suppressing speckle noise, a MAMF is proposed. The proposed filter is effective in its desired purpose of maintaining the balance between speckle suppression and feature preservation, although future work can be done to even further improve the filter. Along with the proposed filter, a region and adaptive algorithm was proposed to further boost the performance of filters for improved results.

For the purpose of this research, the region-based filtering proposal with only the combination of AMF followed by the proposed MAMF has been shown, although several other variations have been tested and implemented. However, it can be noted that the combination of the two filters presented, have subsequently produced the best result, although this being minor improvement to the original MAMF. But these have lead to considerable increase in computation time and thus not used extensively in this research. The user-defined threshold used for the region-based filtering has been set high enough to detect enough regions as well as improving the FQA results by a small minority. Future work can be done with the region-based filtering, to further increase the efficiency of the various filtering algorithms.

CHAPTER 5

MULTI-STAGE SEGMENTATION OF SEA ICE IMAGERY

5.1 Introduction

Sea Ice which grows in the open seas like the Arctic, is formed when the sea water gets frozen. The presence of strong gale force winds and sea waves affects these sea ice regions, causing it to form varying size and shape. For example in the winter, the sea ice regions form a stronger and larger sea ice block/ floe due to the colder temperature and calmer winds. Whereas in the summer, they form smaller, weaker floes due to the melting of the sea ice regions caused by higher temperatures and the fracturing caused by adjacent sea ice floes due to wind. Figure 5.1 shows a typical example of the difference between the sea ice regions during the summer and winter.

In Figure 5.1, it can be seen the level of diversity of the sea ice regions during the various stages of sea ice growth/ shrinkage. Thus developing a robust technique which can be adjustable to these varying conditions is a challenging task that has been an active research field for than 25 years.

Over the years, many scientists have presented various algorithms, some of which are described in 2.1.2, for segmenting the Sea Ice images. Most of the techniques suggested in the literature are based on utilising the texture information within the image data, as has been used in this study. Each of these algorithms have their own merits and demerits. Some of them have been used for comparison with the technique chosen in

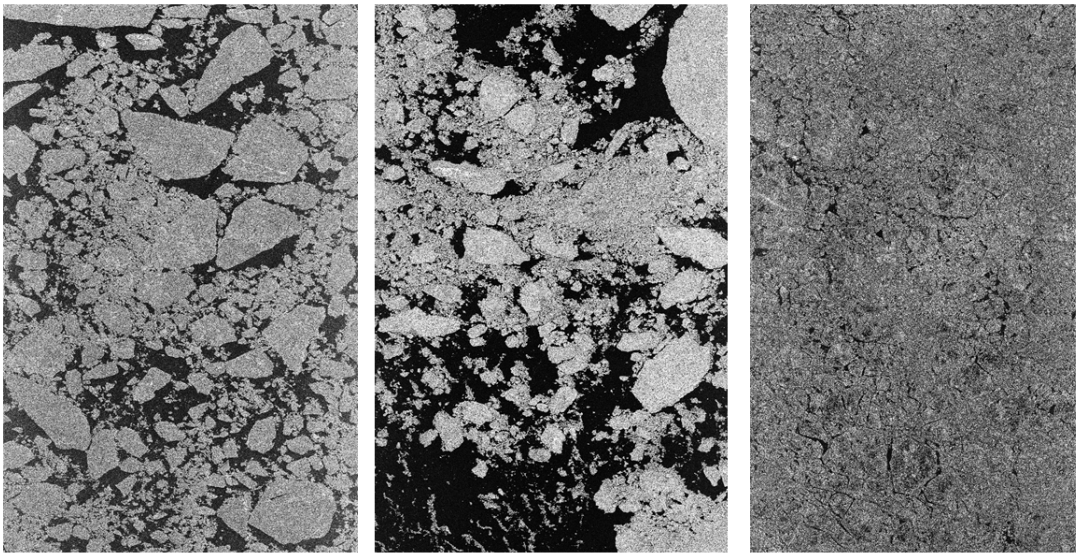

Figure 5.1: Sea Ice regions example: (a) Sea Ice region during early winter (b) Sea Ice region during mid-summer (c) Sea Ice region during peak winter season

this study, as well as for proposal of additional processing to aid the technique chosen.

This chapter is organised as follows; Section 5.2 gives information of the proposed Post-Processing algorithms for further increasing the quantitative efficiency of the segmented results acquired with the KGC algorithm. Dataset preparation, Evaluation criteria and the experimental results and analysis of the various images are given in Section 5.3, followed by summary of the findings and contributions given in section 5.4.

5.2 Refined Segmentation using Local Active Contours and Conditional Morphological Processing

Although the KGC algorithm, as seen from the previous section, has various advantages over other conventional image segmentation techniques, it still has few drawbacks which need to be enhanced using further processing, to make the algorithm more robust to the Sea Ice segmentation application. Even for the most robust image

segmentation algorithm, it is a challenging task to partition different sea ice regions and adapt to the varying ice conditions as seen in Figure 5.1. It is even more challenging when the sea ice regions are in so close proximity of each other and only separable by use of high-resolution visible image or through human perception. Hence for this purpose, an adaptive and condition based post processing algorithm is suggested to aid the KGC in getting even better segmentation accuracy.

The post processing algorithm involves a combination of several easy to implement algorithms such as Morphology [124], Skeletonisation [125] and local Active Contours [44]. These have been discussed in more detail in the following subsections and the Figure 5.2 shows how the Post Processing framework is implemented.

5.2.1 Region of Interest Extraction

In order to reduce the excess overload on the processing times, the "Regions of Interest" is extracted, in order to perform the post processing on only those regions that require further processing to split the overlapping regions. Furthermore, to automatically extract these regions, a combination of algorithms, Distance Transform and Skeletonisation is implemented [126–128].

The Distance Transform algorithm works with binary images and calculates the distance between the current pixel with the nearest non-white pixel. Of the various techniques the Distance Transform algorithm has, the *Chessboard* and *City-block* techniques are used for calculating these distances between the pixels. The result from both the techniques are then merged to get a combined result, which from experimentation has proven to be quite effective in getting the horizontal as well as vertical regions that need to be separated. Figures 5.3 and 5.4, give an example how the Distance Transform algorithm finds the Regions of Interest.

As seen from the Figures 5.3 and 5.4, it shows how the *Chessboard* technique of the Distance Transform algorithm is used to extract the Region of Interest that needs to be separated within the specific region within the Sea Ice image.

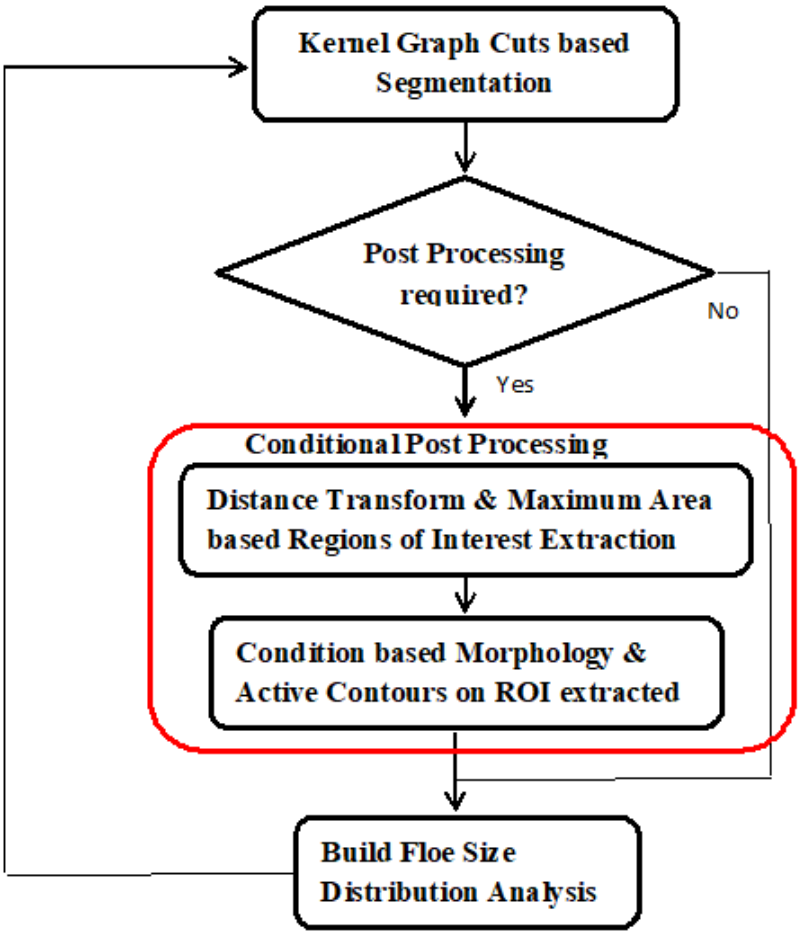

Figure 5.2: Post Processing Framework

The various techniques used in Distance Transform algorithm, available in Matlab software are; Euclidean, Quasi-Euclidean, City-block and Chessboard.

In Figure 5.5, (a) shows how the calculation for the Euclidean based distance transform technique. As seen, the Euclidean distance is basically a straight-line distance between two pixels. In a 2-D image, the Euclidean distance between pixels (x_1, y_1) and (x_2, y_2) is equal to $\sqrt{(x_1 - x_2)^2 + (y_1 - y_2)^2}$. Similarly (b) shows the City block based distance transform technique. As seen, the city block technique measures the path between the pixels based on a "4-connected" neighbourhood. In a 2-D image, the City block distance between pixels (x_1, y_1) and (x_2, y_2) is equal to $|x_1 - x_2| + |y_1 - y_2|$.

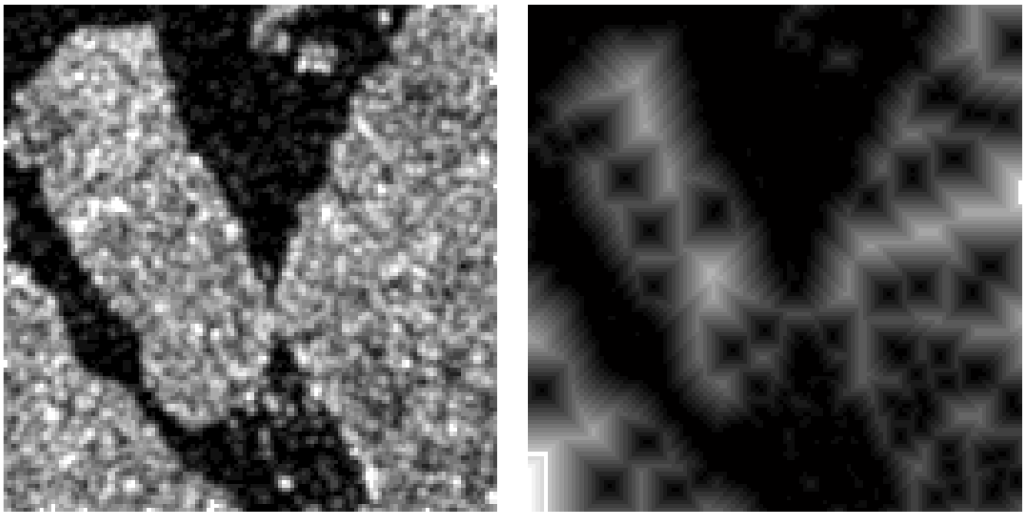

Figure 5.3: Distance Transform example

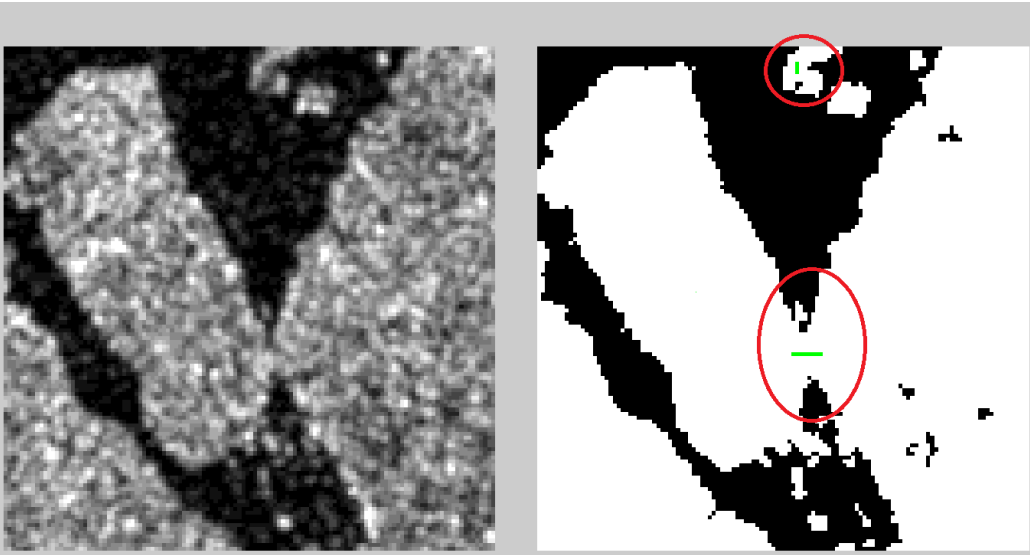

Figure 5.4: Region of Interest extracted using Distance Transform

In (c), the calculation for the Chessboard distance technique is shown. The Chessboard technique measures, unlike the City block technique, the path between the pixels on a "8-connected" neighbourhood. In a 2-D image, the Chessboard distance between

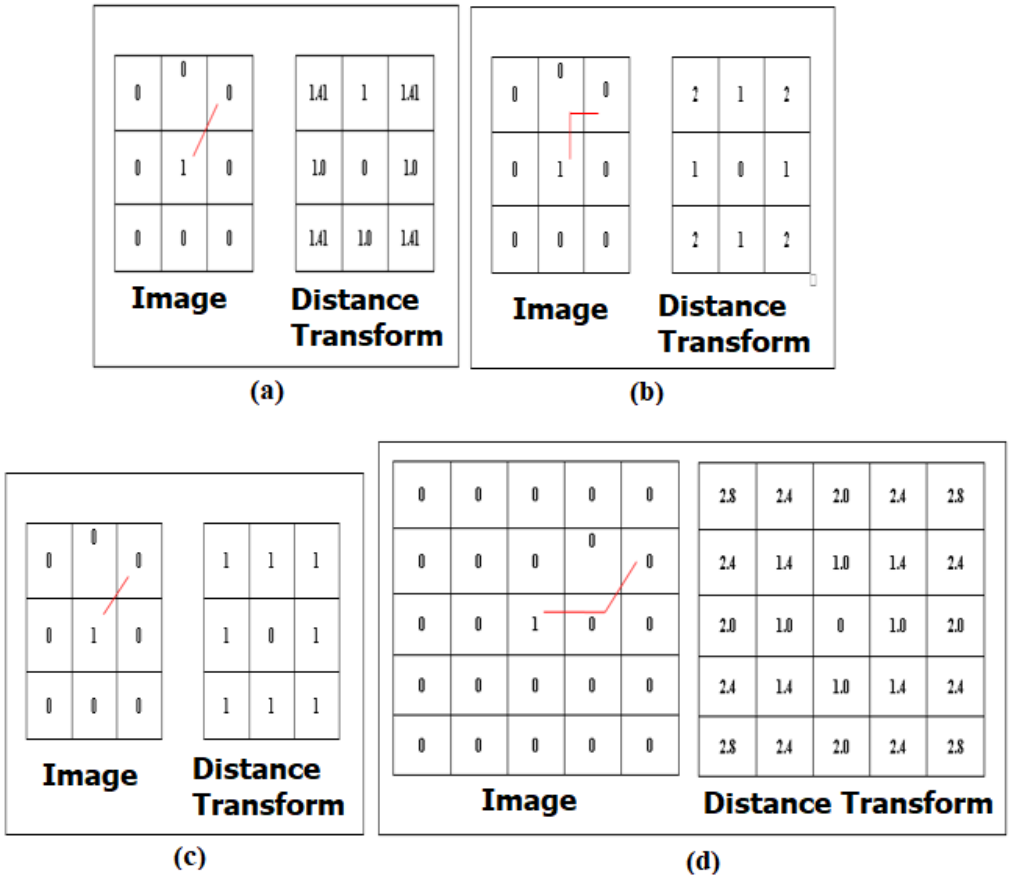

Figure 5.5: The four different Distance Transform techniques available in Matlab software package

pixels (x_1, y_1) and (x_2, y_2) is equal to $max(|x_1 - x_2|\ ,\ |y_1 - y_2|)$. Lastly in (d), the calculation for the Quasi-Euclidean based distance transform technique is shown. The Quasi-Euclidean technique measures the total Euclidean distance along a set of horizontal, vertical and diagonal segments.

In a 2-D image, the Quasi-Euclidean distance between pixels (x_1, y_1) and (x_2, y_2) is defined as follows,

$$\begin{aligned} |x_1 - x_2| \ + \ (\sqrt{2}-1)|y_1 - y_2|, \ If |x_1 - x_2| > |y_1 - y_2| \\ (\sqrt{2}-1)|x_1 - x_2| \ + \ |y_1 - y_2|, \ Otherwise \end{aligned} \tag{5.1}$$

5.2.2 Conditional Morphology

Another extremely popular technique used in most image processing is Morphology [124, 129, 130]. The two most popular Morphological operators are "Erosion" and "Dilation". The *Erosion* operator has been used for performing the Conditional Morphology used in the post-processing stage.

In terms of image processing, Erosion shrinks/ erodes the image features and even in some cases completely removes them, depending on the size of the *structuring element* chosen. Dilation on the other hand, is opposite to that of Erosion, i.e. it enlarges/ dilates the image features depending on the size of the *structuring element* chosen. More details on the Morphological operators can be found in [131]. Figure 5.6, shows an example of how the two most common Morphological operators work.

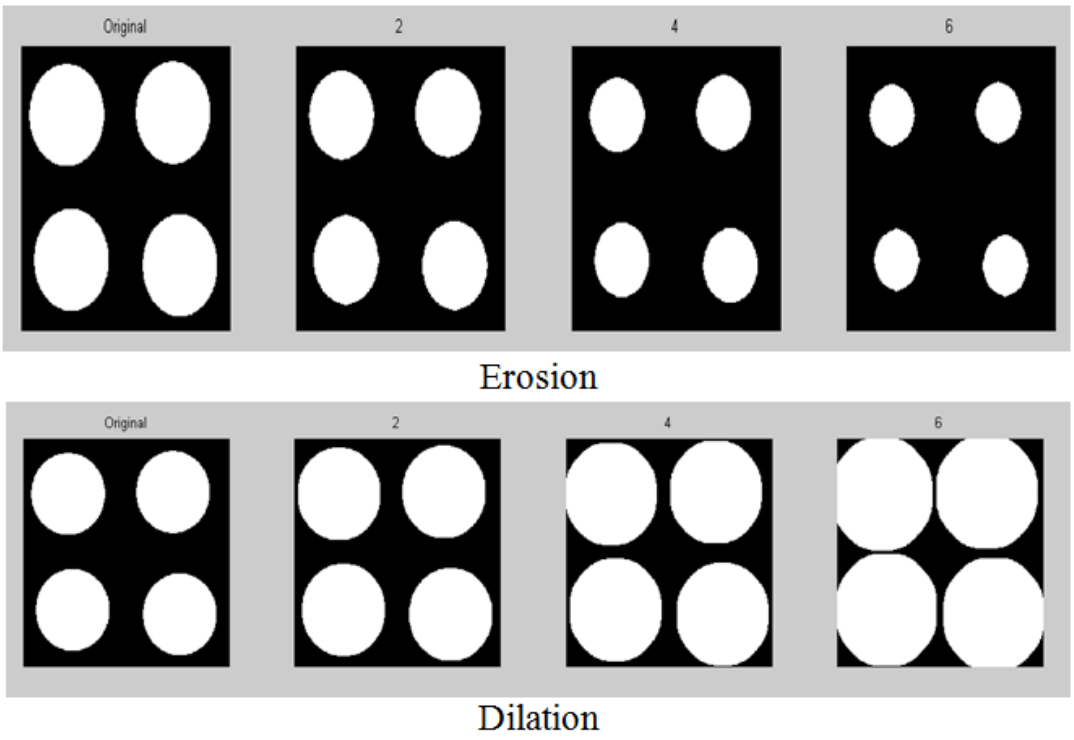

Figure 5.6: Example of Morphological operation

As seen in Figure 5.6, the original image is changed with increasing structuring

element sizes. It can be seen how Erosion makes the white region represented by the circles smaller and smaller with increasing structuring element size, whereas Dilation does the opposite and increases the white region.

Thus for the morphological operator to work properly, it is important to correctly choose the "*structuring element*". The structuring element is a binary-valued neighbourhood which is used to probe/ observe with a given image. It is used to identify how a shape "fits" or "misses" a particular object within the image. The central pixel, referred to as the "origin", identifies which pixels are *"true"* or *"false"* pixels that are included in the morphological computation. The structuring element used in Matlab software is usually a flat-based structuring element, which has different shapes that can be used such as; diamond, disk, line, octagon, rectangle, square etc. [132, 133] Figures 5.7 and 5.8, show two examples of these types of shapes used in creating the structuring element for morphological operation.

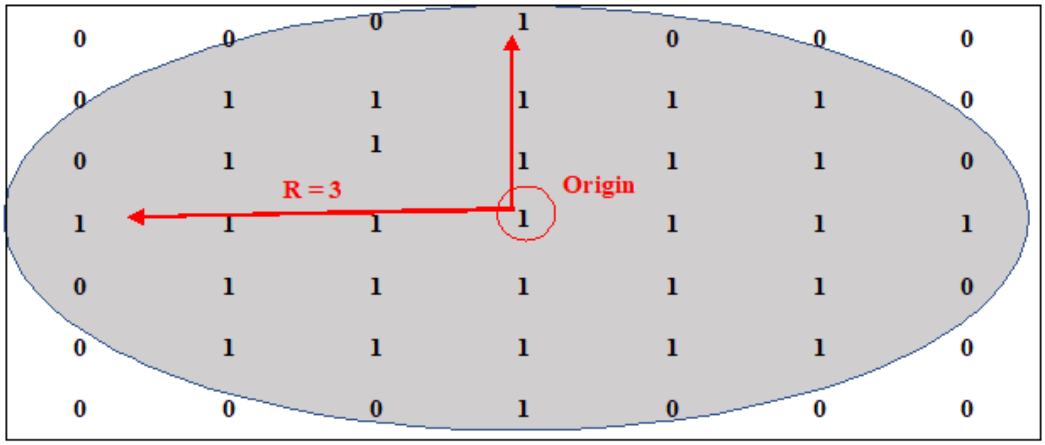

Figure 5.7: Disk type of Structuring element for Morphological operation

The line shaped structuring element, seen in Figure 5.8, has been used in the post-processing stage for performing the Conditional Morphology [134]. The angle for the structuring element has been chosen to be perpendicular to the orientation of the region of interest extracted in the previous stage. The distance is set to be double the size

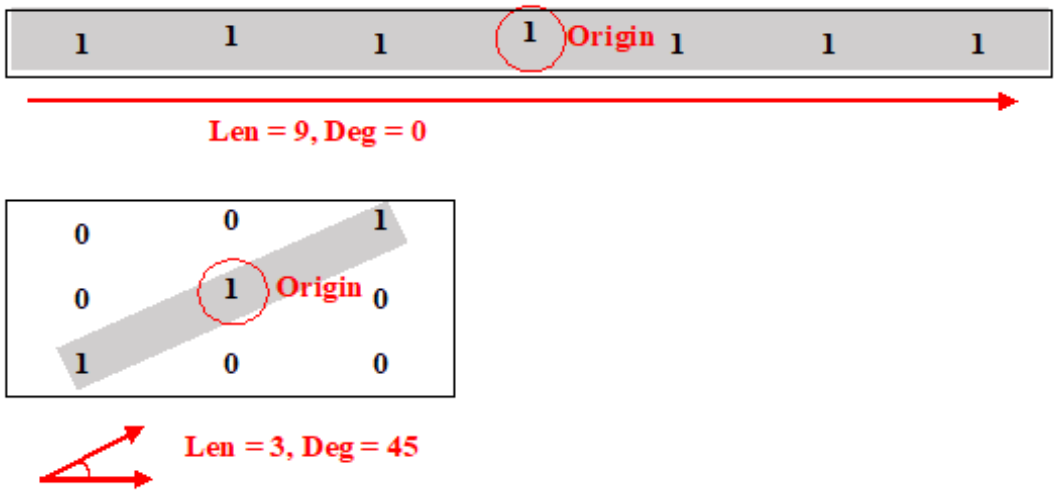

Figure 5.8: Line type of Structuring element for Morphological operation

of the of the Distance Transform value of the central pixel of that particular region of interest. The Figure 5.9, demonstrates how this is done.

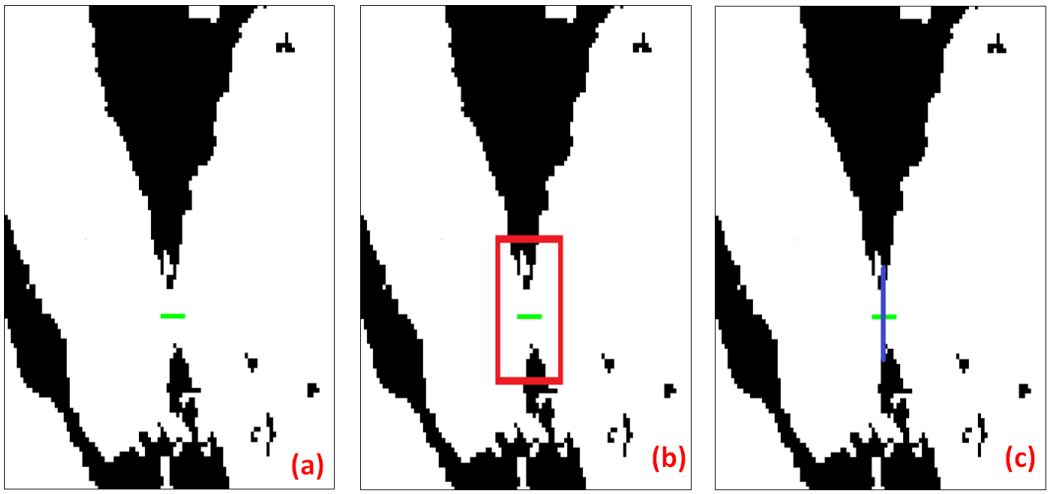

Figure 5.9: Structuring element and Size for Region of Interest selection

In Figure 5.9, the green line in (a) denotes the extracted Region of Interest from the Distance Transform calculations from the previous stage. The red box in (b) is the *bounding box* which specifies the area which is used for performing the post-

processing modification using Morphology and Active Contours. Finally in (c), the blue line shows the orientation of the structuring element and the length, which is twice the size of the central pixel of the Region of Interest extracted from the Distance Transform calculation.

Thus it can be seen how the Morphology performed on the image, is condition based, i.e. based on orientation and size of the Region of Interest extracted as well as regional, i.e. based on the size of the bounding box created using the Region of Interest extracted using Distance Transform.

5.2.3 Active Contours

Along with Conditional Morphology, the Chan-Vese based Active Contours (AC) algorithm [44] is used for the conditional post processing for separating the touching sea ice floes. The AC, similar to the KGC algorithm, is an energy minimization based algorithm, which is based on evolving a curve in and around an object in an image until it reaches the object's boundary, as seen in Figure 5.10.

The curve for the AC has the ability to either shrink or expand on the object's region, based on the intrinsic and extrinsic parameters, until it reaches the object's boundary. Equation 5.2 explains how these calculations for the AC are achieved.

$$\begin{aligned} F_1(C) + F_2(C) = & \int_{inside(C)} \left| u_0(x, y) - c_1 \right|^2 dydx \\ & + \int_{outside(C)} \left| u_0(x, y) - c_2 \right|^2 dydx \end{aligned} \tag{5.2}$$

Here C is the evolving curve around the object; $c1$ and $c2$ are the average energies inside and outside the curves respectively of the image u_0. Hence,

1. If the curve C is inside the object; $F_1(C) \approx 0$ and $F_2(C) > 0$.

2. If the curve C is outside the object; $F_2(C) \approx 0$ and $F_1(C) > 0$.

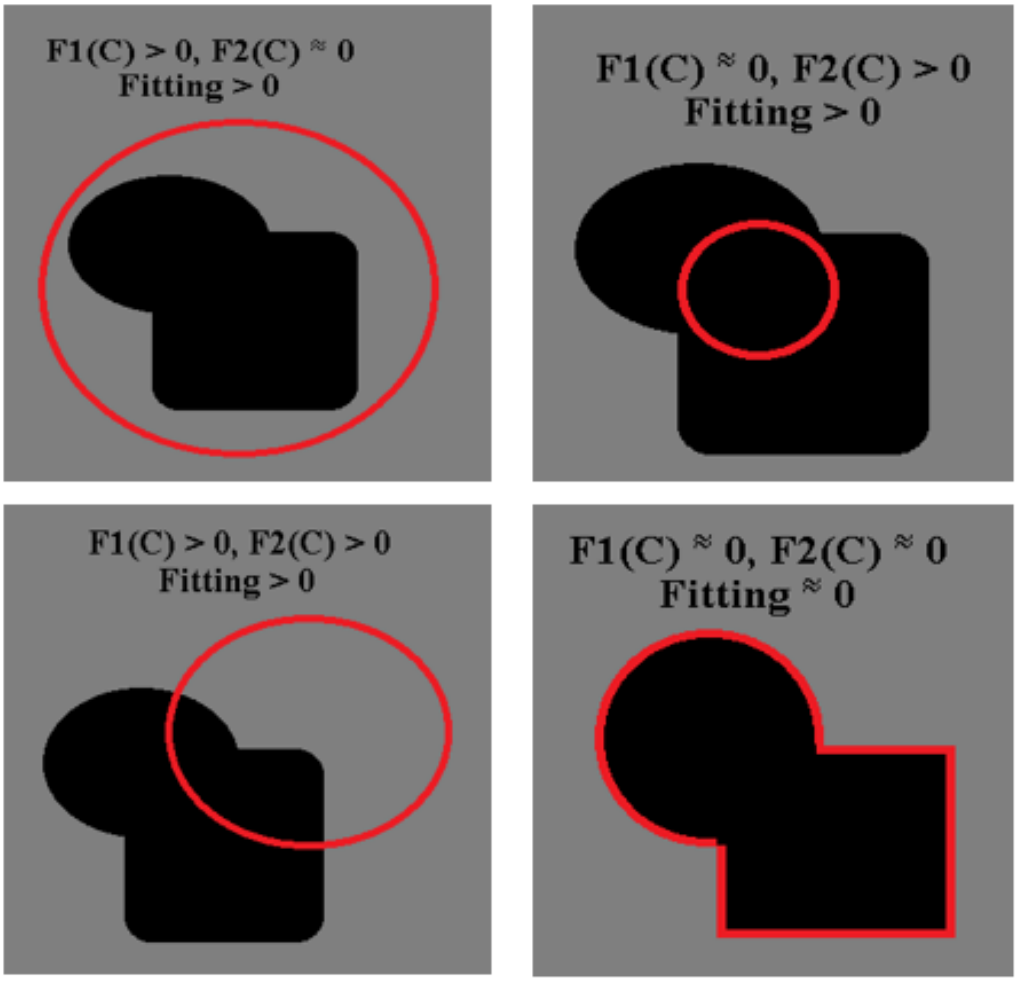

Figure 5.10: Chan Vese based Active Contours Operation

3. If the curve C is inside and outside the object; $F_2(C) > 0$ and $F_1(C) > 0$.

4. If the curve C is on the object boundary; $F_1(C) \approx 0$ and $F_2(C) \approx 0$.

The Chan-Vese based AC algorithm is chosen over any other algorithm, due to its region growing ability based on local statistics of the image, which in this case, have been modified by the conditional morphology. The penalty parameter for the AC, which decides the contour movement inside or outside the object, is chosen low enough so that even minute pixel changes are picked up for the partition to be possible.

5.3 Experimental results and analysis

The combination of the Post Processing techniques described in the previous section are compared with numerous real-world SAR Sea Ice images from various datasets downloaded and received for this study. This is done to test the perform of the Post Processing stage and set forth its efficacy. The dataset preparation and the evaluation criteria, followed by the quantitative as well as subject analysis is presented in this section in brief detail. Matlab software has been used to perform these analysis.

5.3.1 Dataset preparation

There have been in total 3 different datasets of TerraSAR-X satellite images that have been used in the Quantitative and Subjective analysis performed. This has been done to validate the performance of the proposed Post Processing algorithm to increase the efficacy of the KGC algorithm for the SAR Sea Ice images.

Similar to the analysis done for testing the adaptive filter proposed in the previous chapter, the primary dataset used is from the TerraSar-X satellite, acquired on 29 June 2012 from the northern Chukchi Sea. The images represent early summer breakup of the Sea Ice floes. The acquired SAR image has a dimension of 16303 by 16181 pixels. It has been cropped in the top right part of the image, as seen in Figure 4.3. This was primarily also done due to the availability of High-resolution SAR data from that particular region. Tests were performed on three subsequent images created with dimensions 570 by 620 pixels, 699 by 554 pixels and 610 by 694 pixels respectively, before applying the algorithm to the bigger image. For further reference purposes, we refer to this as dataset 1.

The second dataset is also from the TerraSAR-X satellite, acquired on 2nd and 12th August 2014, around the time when this study was started. It has been acquired with the Office of Naval Research (ONR) - Marginal Ice Zone (MIZ) Program's buoy cluster 1 and 2 respectively, located north of the Arctic region near the Beaufort Sea. Figure

5.11 shows the different cluster areas for the United States's Office of Naval Research - Marginal Ice Zone (ONR-MIZ) Program, having various autonomous multi-sensor buoy systems deloyed for tracking the Sea ice movement. This is particularly important region as it has shown the most Sea Ice volume decline than any other region, since the program began more than 45 years ago [6, 135, 136]. The image captured on 2nd August 2014 has dimensions of 25140 by 48158 pixels, whereas the image captured on 12th August 2014 has dimensions of 25479 by 44971 pixels. Both images were downsized 15 percent using Bilinear interpolation to new dimensions of 3771 by 7223 pixels and 3821 by 6745 pixels respectively. Figures 5.12 and 5.13 show the regions cropped from the two images to create Sample 1 and Sample 2 for this dataset.

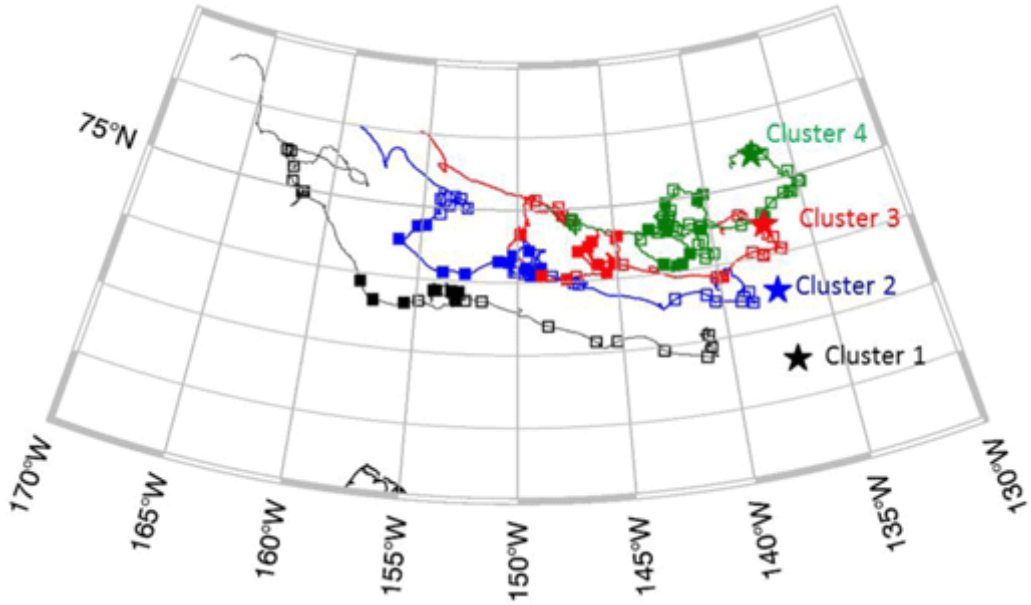

Figure 5.11: ONR-MIZ Program - Different Cluster areas with reference buoys

The third and final dataset is acquired by the TerraSAR-X satellite as well on 31st July 2014, couple of days before the two images from the previous dataset. Like the image captured on 12th August 2014, the image used in this dataset is also from Cluster 2 of the ONR-MIZ program's buoy cluster region. Figure 5.14 shows the part of the image which has been used to create the images used in this dataset. The cropped

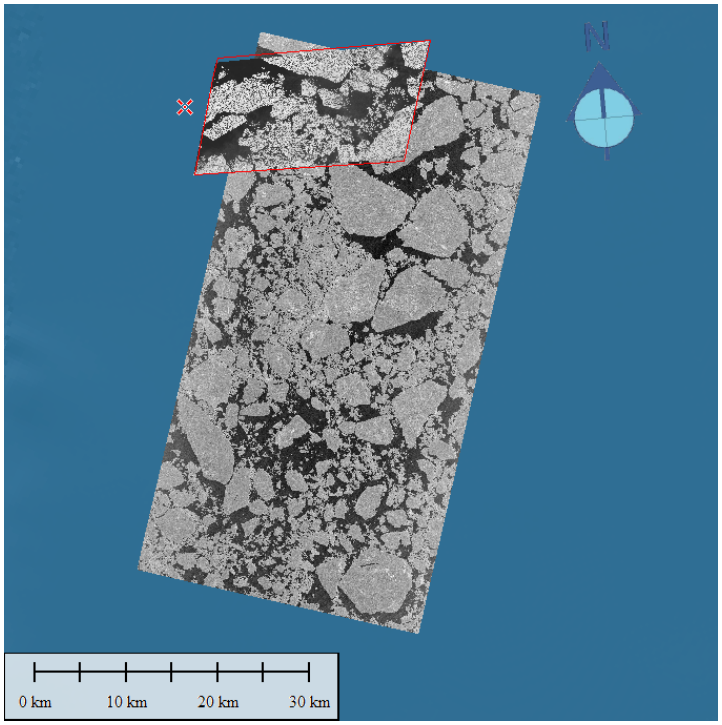

Figure 5.12: Sample TerraSar-X image acquired on 2nd August 2014

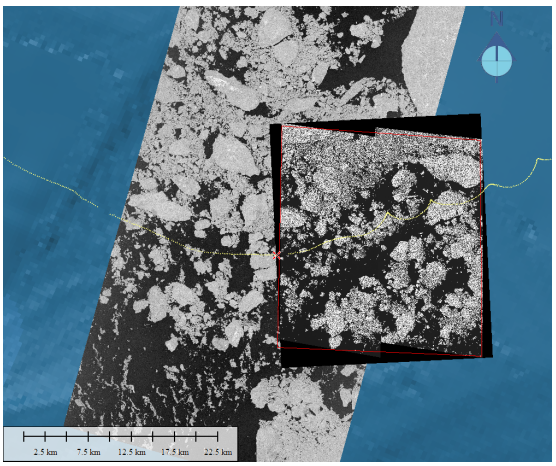

Figure 5.13: Sample TerraSar-X image acquired on 12th August 2014

region has dimensions of 3787 by 5027 pixels. The image is then divided into two parts to create the two sample images used in this dataset, having dimensions of 3787 by 2514 pixels and 3787 by 2513 pixels respectively.

Figures 5.15 and 5.16 show the regions which have been cropped from the cropped image captured on 31st July 2014.

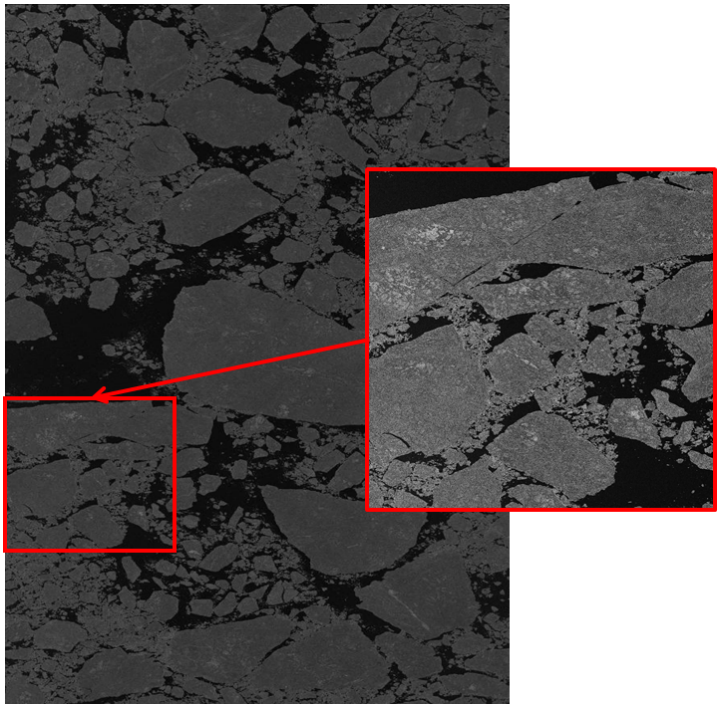

Figure 5.14: Sample TerraSar-X image acquired on 31st July 2014

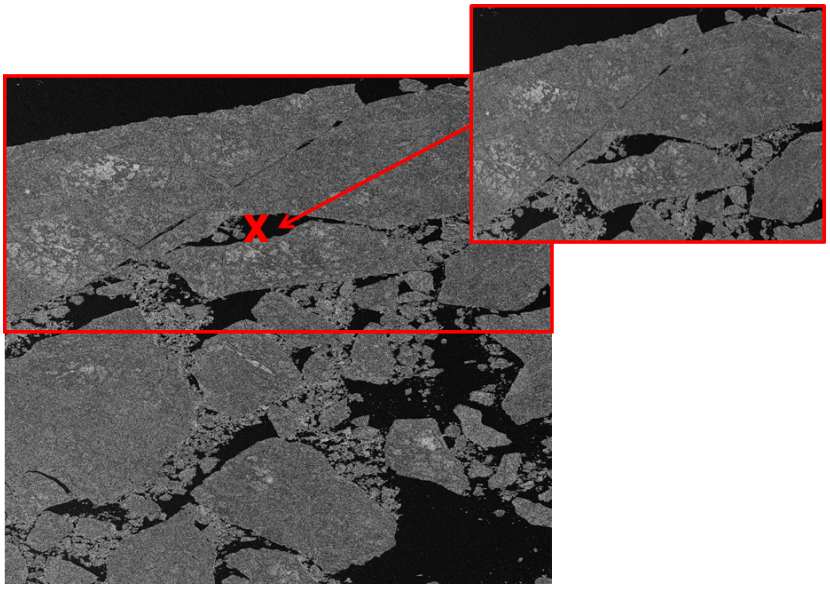

Figure 5.15: Cropped Region 1 from the original image captured on 31st July 2014

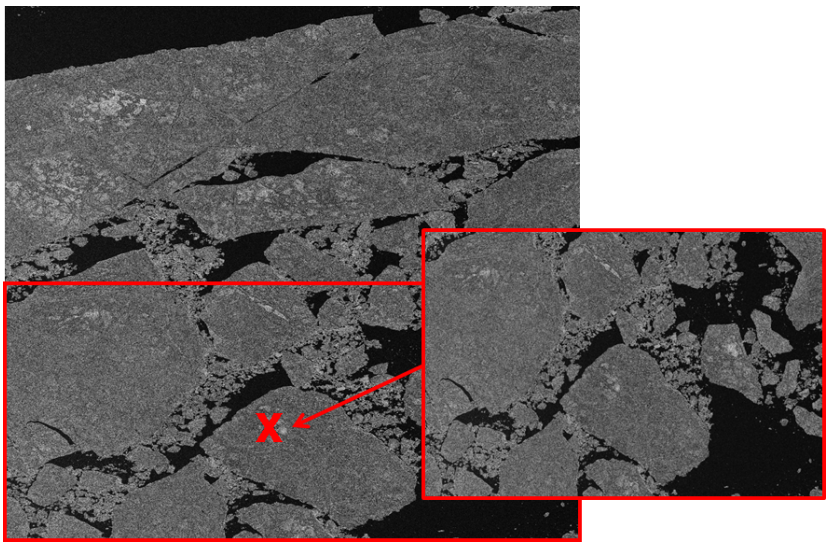

Figure 5.16: Cropped Region 2 from the original image captured on 31st July 2014

5.3.2 Evaluation Criteria

In this sub section, a new Region based Analysis is proposed that provides a highly accurate segmentation accuracy for the Sea Ice images. The Ground Truth Preparation is also discussed in this sub section, which provides more information on the difficulties and bias in producing a Ground Truth.

5.3.2.1 Region based Analysis

To propose the new Region based Accuracy measure, the ROC curve (mentioned in section 2.3.2) analysis is used and further modification is suggested to build a more accurate Segmentation Accuracy measurement. The new accuracy measurement has been simply referred to as ORA. It is a measurement of the percentage of similarity of regions between the GT image and the Segmented result and can be given by the equation,

$$ORA = \frac{1}{N} \sum_{i=1}^{N} RA_i \tag{5.3}$$

As seen in Equation 5.3, the ORA is the mean of the Regional Accuracies of each of the regions within the GT image. N in the equation is the total number of regions

identified in the GT image. Furthermore, the *RA* can be given by,

$$RA = \frac{GT_{Reg} \cap Seg_{Reg}}{GT_{Reg} \cup Seg_{Reg}} \tag{5.4}$$

In Equation 5.4, the numerator term measures the intersection of the regions between the GT and the Segmented Image, whereas the denominator term measures the union of these regions. In other terms, the Regional Accuracy is the measure of the regions which are present in both the GT and Segmented Image.

The proposed Segmentation Accuracy measure differs from other quantitative measures, as it measures the accuracy of the Segmentation algorithm to correctly identify the region in the GT image. It calculates the "intersection" of the regions between the GT image region and the Segmented image region, i.e. all the regions that are correctly identified by the Segmentation algorithm. It also calculates the "union" of all the regions that are occupied within the Segmentation algorithm with that particular GT image region. By comparing these values against each other, it calculates the exact regional accuracy of the Segmentation algorithm to correctly identify the GT image regions, rather than just the pixels correctly identified. This helps to identify the "Under Segmentation", "Over Segmentation" and "Correct Segmentation", which is later calculated using the boundary parameters. Equations 5.5, 5.6 and 5.7 show how the Under, Over and Correct Segmentation are calculated.

$$UnderSegmentation = \frac{GT_{Boundary} \setminus Seg_{Boundary}}{GT_{Boundary} \cup Seg_{Boundary}} \tag{5.5}$$

$$OverSegmentation = \frac{Seg_{Boundary} \setminus GT_{Boundary}}{GT_{Boundary} \cup Seg_{Boundary}} \tag{5.6}$$

$$CorrectSegmentation = \frac{2 \times \left[GT_{Boundary} \cap Seg_{Boundary} \right]}{GT_{Boundary} \cup Seg_{Boundary}} \tag{5.7}$$

The ORA also provides a weighted average for the accuracy based on the size of the GT image region, thus avoiding lower values if a large number of smaller regions

are present within the GT image. For the purpose of this work, the ORA is considered the most important parameter in comparison with the Under, Over or Correct Segmentation values.

Table 5.1: ROC versus ORA analysis for Sample Synthetic Images

Average								
Technique	Condition	Precision	Recall	Fmeasure	Overall Acc	Under Seg	Over Seg	Correct Seg
WaterShed	-	78.62	99.65	87.08	60.66	49.50	39.61	28.57
LevelSet	-	72.36	99.85	81.99	39.03	63.65	35.14	26.72
CDCut	-	79.38	99.24	85.58	45.18	54.22	41.47	34.86
KGC_Pen0.8	k=2	94.16	99.04	96.37	49.39	58.34	16.94	42.49
KGC_Pen0.2	k=2	94.07	98.93	96.24	49.54	43.73	35.87	52.72

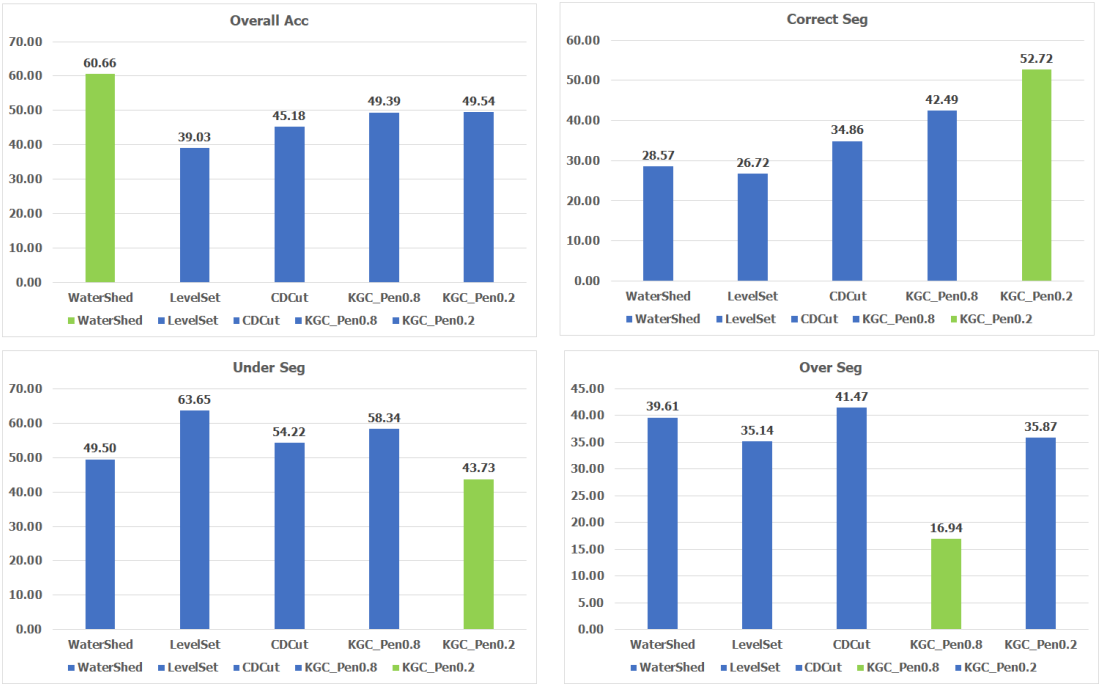

Figure 5.17: Graph of the ORA values for Sample Synthetic Images

Further differentiation between the ROC and the ORA are given by the Table 5.1 and Figures 5.17, 5.18. These results represent the average for the three (out of five) sample synthetic images used from the RGB database shown in section 4.3.1 and shown in Figure 5.19.

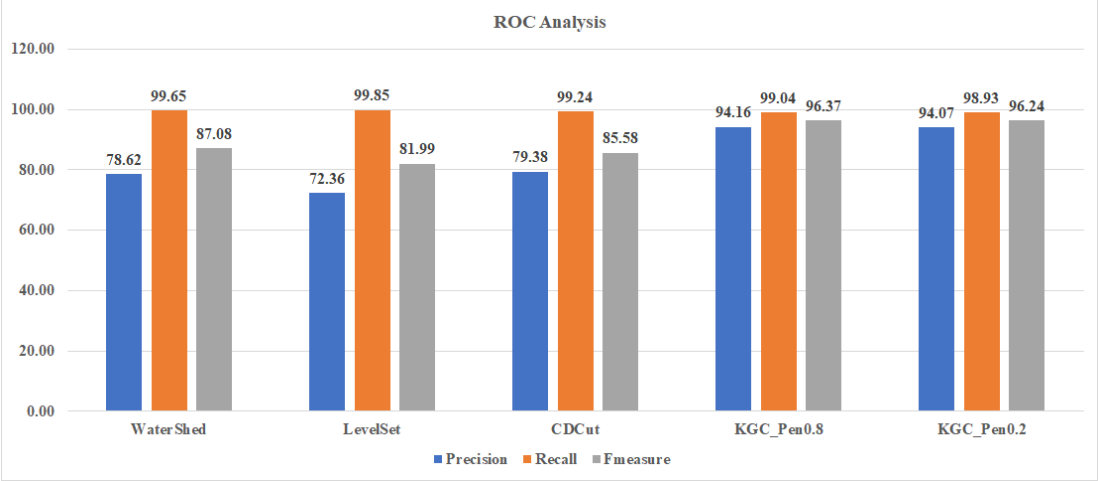

Figure 5.18: Graph of the ROC values for Sample Synthetic Images

Figure 5.19: Sample Synthetic Images used

As mentioned in the ROC, an algorithm with high Precision and low Recall tends to show a lot of results but most being incorrect. Whereas one with high Recall and low

Precision, gets fewer results but most being correct. Thus from the Table 5.1, all three algorithms; Watershed, LevelSet and CDCut produce fewer results but most being correct. Whereas the KGC produces a lot of results, most being incorrect. However, with the Boundary-based results, these produce highest Correct Segmentation rate and lowest Under and Over Segmentation rates. The worst results for the Boundary-based analysis are achieved by the LevelSet, followed by the CDCut and then the Watershed. The highest ORA results are produced by the Watershed, followed by the KGC results.

Thus it can again be highlighted, the key differences of calculation of Segmentation Accuracy by the ROC and the ORA. Whilst the ROC primarily focuses on the Positive Rate values [68], the ORA focuses on Positive and Negative rate values, to get a completely accurate Segmentation Accuracy for a specific algorithm. This is very crucial in the calculation of the FSD, to get an accurate understanding of the various social and environmental impacts on Sea Ice images.

5.3.2.2 Ground Truth Preparation

Generating a Ground Truth (GT) image for the SAR Sea Ice images is a difficult task, due to the existence of speckle, backscattering and other factors affecting the SAR images, as mentioned in the previous chapters. A human perception of the different regions also vary person to person and thus manually obtaining the GT image is also a difficult and biased operation. However experts have still, for the past 25 years of research, produced Sea Ice charts through manual interpretations of the SAR imagery [137].

For this research, the GT image has been created using the most popular technique "Watershed" mentioned in section 2.1.2.1. The Watershed algorithm has been known to produce highly over-segmented results but also lower under-segmented results. Thus utilising this advantage and with the use of limited High-resolution SAR data available, the GT image is created. The High-resolution SAR data hasn't been directly used to create the GT image as the data varies slightly, due to being few days

apart from the measurement, from the actual TerraSAR-X satellite data used in this research. Figure 5.20 shows an example of the High-resolution data available for the acquired TerraSAR-X satellite data.

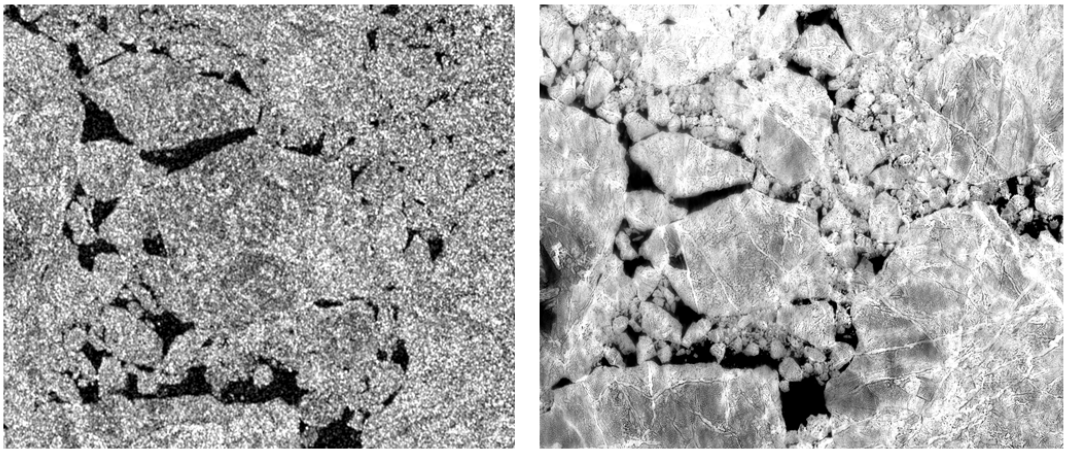

Figure 5.20: Sample TerraSAR-X image versus its equivalent High-Resolution Visible image available

From Figure 5.20, it can be seen how the High-resolution data varies slightly to that of the equivalent TerraSAR-X data used. Despite these variations, it is still a good way of understanding the boundaries to be performed for the variations Sea Ice regions while creating the GT image. In some cases however, even with the help of the available High-resolution data, it is difficult to trace the boundary for the TerraSAR-X data, especially in conditions with more complex ice conditions as in the case of dataset 2 image captured on 12th August 2014. In these cases, the GT image created may not be entirely accurate and represent the true shape of the sea ice floes in the SAR data.

For this research, the GT image is thus created by first obtaining the overly segmented result with Watershed algorithm, followed by manual separation and merging of the sea ice regions with the help of the High-resolution data available. This is thus a time consuming tasks and varies significantly per image, owing to its complexity of regions. It is still requires less time than complete manual preparation of the GT image

by a Sea Ice expert which has, in previous cases, required more than 2 days.

5.3.3 Quantitative Analysis

In this section, the Quantiative Analysis is done for the proposed algorithm, the original KGC [49] algorithm, the CDCut [48] and the Level Set [43] algorithm. The proposed ORA is used to validate the efficacy of the results by performing the analysis on the three dataset images mentioned in the previous section. Visual comparison as well as computing efficiency is also done for providing subjective analysis.

It should be noted that although the Watershed [42] has been shown in the results in this section, it has not been used to compare the results with the Post Processing algorithm proposed and the KGC on its own. This is primarily owing to the fact mentioned in the previous section, i.e. the Watershed algorithm has been used for preparing the GT images for the Quantitative Analysis.

All the timing parameters shown in these following sub sections have been coded in Matlab 2015b software, running on a Dell desktop with 3.2 GHz processor Intel Core i5-3470, 8 GB RAM and 64 bit Windows 7 Enterprise operating system.

5.3.3.1 SAR Sea Ice Images - Dataset 1

Overall Accuracy Assessment As with the FQA, the Quantitative analysis for the Segmentation were primarily done on the Sea Ice images of dataset 1. The average of the results for the images in the dataset is given in Tables 5.2 and 5.3, with the latter showing the simplified version of the best results. Figure 5.21 shows the graph representation of the values for better understanding. Table 5.4 and Figure 5.22 show the computing efficiency for these various algorithms.

From Tables 5.2 and 5.3, it can be seen how the proposed Post Processing algorithm has the best ORA for the images in the dataset. Although the increase in accuracy is not that high compared to the other two dataset image results. The best set of results

Table 5.2: Quantitative Analysis of SAR Sea Ice Images, data set 1

Average					
Technique	Criteria	Overall Region Acc	Under Seg	Over Seg	Correct Seg
Watershed	-	55.35	5.50	12.73	81.77
Level Set	-	22.07	31.79	31.61	36.60
CDCut	-	21.04	38.65	20.69	40.66
KGC only	k=2	21.21	31.20	19.81	48.99
	k=3	21.19	32.36	19.28	48.36
	k=4	20.91	33.31	**18.60**	48.10
	k=5	21.11	33.67	18.66	47.66
KGC + MAM filtering	k=2	22.03	33.76	19.88	46.37
	k=3	21.16	34.42	19.63	45.95
	k=4	20.88	35.97	19.38	44.64
	k=5	20.89	36.16	19.78	44.06
KGC + RMAM filtering	k=2	22.03	33.75	19.88	46.37
	k=3	21.16	34.53	19.55	45.92
	k=4	20.86	36.13	19.53	44.34
	k=5	21.11	35.47	19.41	45.11
KGC with PostPro only	k=2	22.30	**27.12**	24.34	48.54
	k=3	22.26	27.49	22.92	49.59
	k=4	21.37	28.02	21.77	**50.21**
	k=5	22.16	28.88	22.23	48.89
KGC + MAM filtering & PostPro	k=2	30.84	28.88	28.50	42.62
	k=3	**31.34**	29.07	27.67	43.25
	k=4	24.17	29.74	25.98	44.28
	k=5	24.79	29.65	26.62	43.73
KGC + RMAM filtering & PostPro	k=2	30.84	28.88	28.50	42.62
	k=3	28.46	29.20	27.75	43.04
	k=4	27.74	29.80	26.25	43.94
	k=5	28.15	29.90	26.94	43.16

for the KGC algorithms are produced with k equal to 3. It can be noticed how the MAMF, proposed in the previous chapter, gets the best result for the images in the dataset. The region based MAMF, also proposed in the previous chapter, is closely followed in second place.

In terms of boundary based analysis, the best Correct Segmentation and the Under

Table 5.3: Quantitative Analysis of SAR Sea Ice Images, data set 1 - Best results

Average					
Technique	Criteria	Overall Region Acc	Under Seg	Over Seg	Correct Seg
Watershed	-	55.35	5.50	12.73	81.77
Level Set	-	22.07	31.79	31.61	36.60
CDCut	-	21.04	38.65	20.69	40.66
KGC Only	k=3	21.19	32.36	**19.28**	48.36
KGC + MAM	k=3	21.16	34.42	19.63	45.95
KGC + RMAM	k=3	21.16	34.53	19.55	45.92
KGC with Post Pro only	k=3	22.26	**27.49**	22.92	**49.59**
KGC + MAM with PostPro	k=3	**31.34**	29.07	27.67	43.25
KGC + RMAM with PostPro	k=3	28.46	29.20	27.75	43.04

Table 5.4: Computing Times of SAR Sea Ice Images, data set 1

Average		
Technique	Criteria	Timing
Watershed	-	0.02
CDCut	-	0.70
Level Set	-	1.12
KGC only	k=2	0.07
	k=3	0.11
	k=4	0.22
	k=5	0.38
KGC with Post Process only	k=2	1.13
	k=3	0.94
	k=4	0.90
	k=5	0.87
KGC, MAM filtered & Post Process	k=2	1.40
	k=3	1.32
	k=4	1.14
	k=5	1.25
KGC, RMAM filtered & Post Process	k=2	1.38
	k=3	1.32
	k=4	1.16
	k=5	1.25

Segmentation are produced with the KGC algorithm with just the Post Processing algorithms, without the use of adaptive filtering. However it can be seen how the ORA

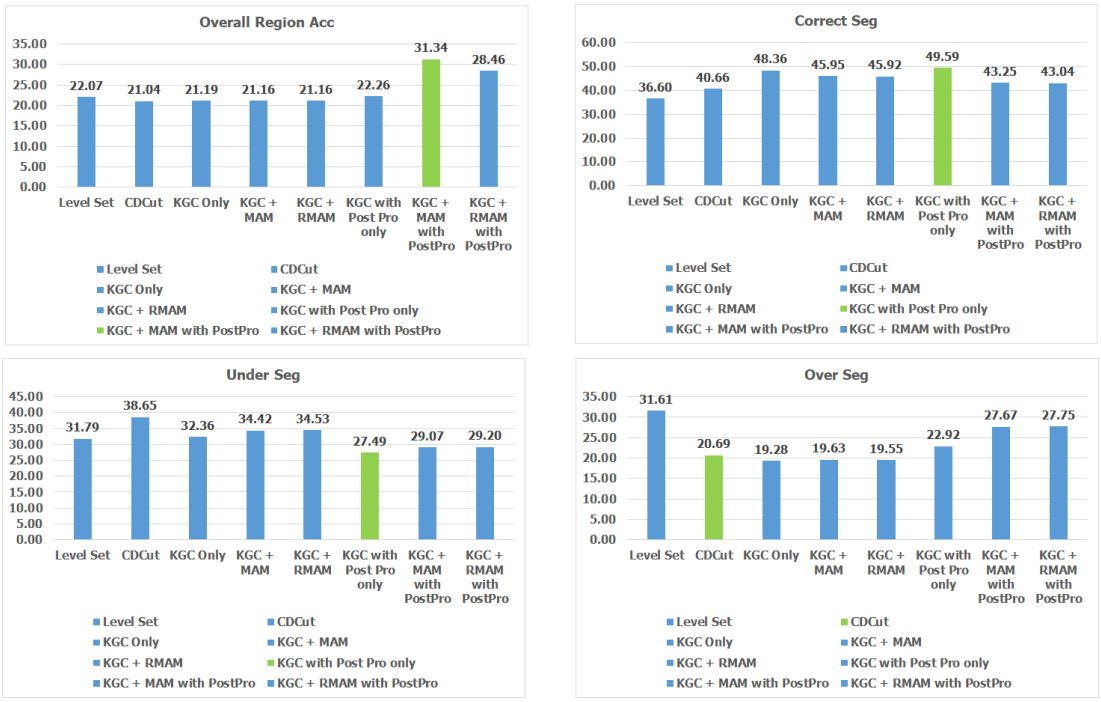

Figure 5.21: Graph of the Quantitative Analysis values for SAR Sea Ice Images, dataset 1

is also significantly lower for these cases. The lowest Over Segmentation rate is produced with the CDCut algorithm as seen in the other two dataset images. Graphical representation of the boundary based analysis and the ORA are shown in Figure 5.21.

The computing efficiency for the various algorithms is given in Table 5.4 and shown in Figure 5.22. The KGC algorithm on its own with k=2 is the quickest algorithm, closely followed by its equivalent value for k=3, which is of importance from above discussion. The impact of applying Post Processing algorithms for the images is not as significantly higher as compared to the images in dataset 2, which can be concluded from the complexity of images in this particular dataset.

Tables 5.5, 5.6 and 5.7 show the individual results for the three images in dataset 1. It can be seen how there is noticeable increase in the ORA in Sample 3 with the Post Processing addition along with adaptive filtering to improve the KGC result. The MAMF again is the best, closely followed by the region based MAMF for the ORA.

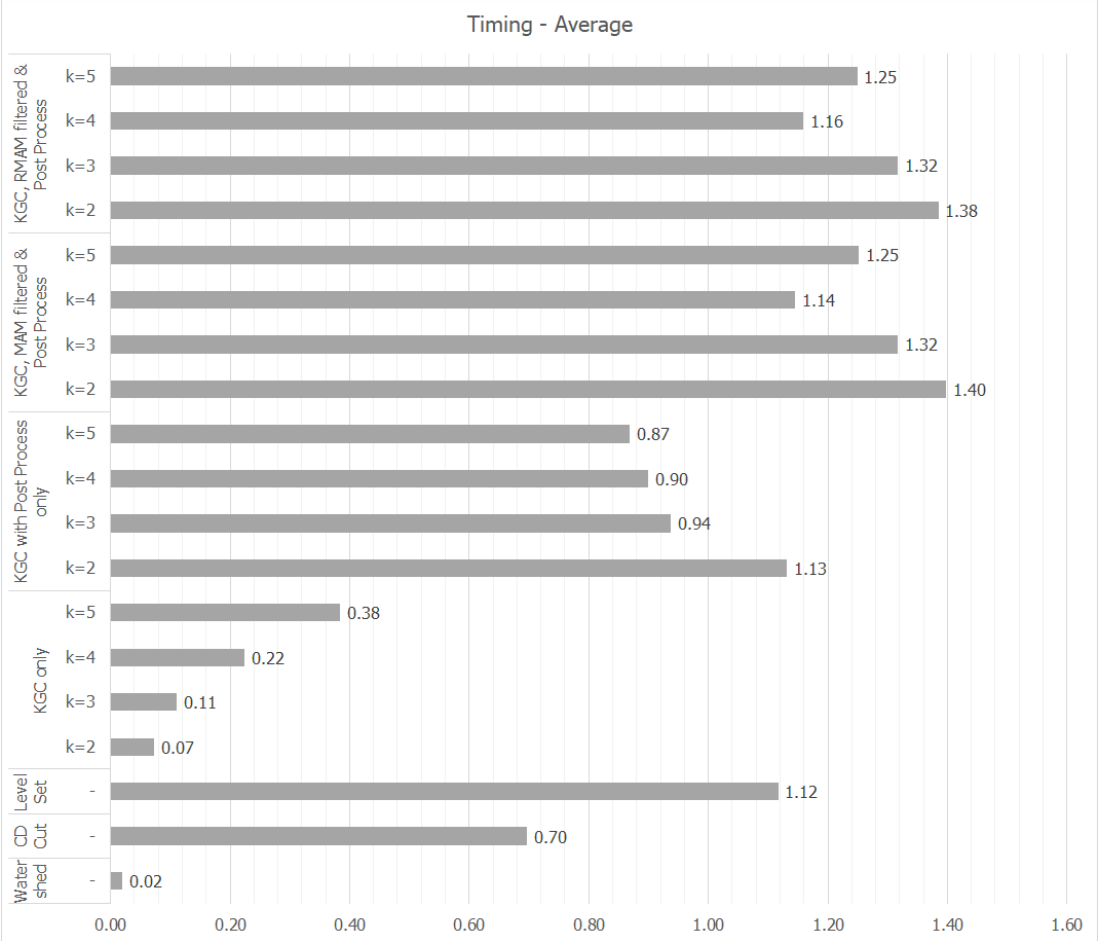

Figure 5.22: Graph of the Computing efficiency values for SAR Sea Ice Images, dataset 1

Table 5.5: Quantitative Analysis of Sample 3 of TS-X image captured on 31st July 2014

Sample 3							
Technique	Criteria			Overall Region Acc	Under Seg	Over Seg	Correct Seg
Watershed	-			69.01	6.28	8.62	85.10
Level Set	-			14.61	35.17	28.72	36.11
CDCut	-			11.74	38.29	**22.43**	39.28
KGC Only	No Pre/ Post Pro	KGC Pen = 0.2	k=3	11.95	27.57	26.22	**46.21**
KGC + MAM	Win 5x5, M = 1		k=3	11.94	28.85	26.22	44.93
KGC + RMAM	Win 5x5, M = 1		k=3	11.94	28.72	26.13	45.15
KGC with Post Pro	No Pre Pro	KGC Pen = 0.2, AC Pen = 0.05	k=3	14.74	23.16	31.70	45.14
KGC + MAM with PostPro	Win 5x5, M = 1		k=3	**36.63**	22.73	38.58	38.68
KGC + RMAM with PostPro	Win 5x5, M = 1		k=3	27.61	**22.70**	38.83	38.46

Table 5.6: Quantitative Analysis of Sample 4 of TS-X image captured on 31st July 2014

Sample 4						
Technique	Criteria			Overall Region Acc	Under Seg	Over Seg	Correct Seg
Watershed	-			45.75	4.93	15.97	79.10
Level Set	-			26.55	29.56	31.39	39.04
CDCut	-			26.37	38.06	17.80	44.14
KGC Only	No Pre/ Post Pro	KGC Pen = 0.8	k=3	26.49	32.57	**14.34**	**53.08**
KGC + MAM	Win 3x3, M = 1		k=3	26.46	33.90	14.59	51.51
KGC + RMAM	Win 3x3, M = 1		k=3	26.46	33.87	14.45	51.68
KGC with Post Pro	No Pre Pro	KGC Pen = 0.8, AC Pen = 0.05	k=3	26.85	**26.91**	21.43	51.67
KGC + MAM with PostPro	Win 3x3, M = 1		k=3	27.50	27.17	23.74	49.09
KGC + RMAM with PostPro	Win 3x3, M = 1		k=3	**27.53**	27.24	23.82	48.94

Table 5.7: Quantitative Analysis of Sample 5 of TS-X image captured on 31st July 2014

Sample 5						
Technique	Criteria			Overall Region Acc	Under Seg	Over Seg	Correct Seg
Watershed	-			51.28	5.28	13.61	81.11
Level Set	-			25.06	**30.64**	34.72	34.64
CDCut	-			25.02	39.60	21.84	38.56
KGC Only	No Pre/ Post Pro	KGC Pen = 0.8	k=3	25.12	36.93	17.27	45.80
KGC + MAM	Win 7x7, M = 1		k=3	25.09	40.52	18.07	41.41
KGC + RMAM	Win 7x7, M = 1		k=3	25.08	40.99	18.07	40.94
KGC with Post Pro	No Pre Pro	KGC Pen = 0.8, AC Pen = 0.8	k=3	25.19	32.40	**15.64**	**51.96**
KGC + MAM with PostPro	Win 7x7, M = 1		k=3	29.88	37.30	20.70	41.99
KGC + RMAM with PostPro	Win 7x7, M = 1		k=3	**30.23**	37.66	20.61	41.73

The Under Segmentation rate is also the lowest compared to other algorithm with region based MAMF marginally beating the MAMF on its own. The CDCut algorithm has the lowest Over Segmentation rate, whereas the KGC on its own has the highest Correct Segmentation rate.

In terms of Samples 4 and 5, the ORA doesn't show a great increase, although the region based MAMF still produces the best result. The Under Segmentation rate in Sample 4 is achieved with the KGC and Post Processing algorithm on its own, closely followed by the adaptive filtering introduced Post Processing results. For Sample 5, the Level Set algorithm surprisingly produces the lowest Under Segmentation rate. The Over Segmentation and Correct Segmentation rates in Sample 4 is achieved by the KGC algorithm on its own. In Sample 5, this is achieved by the KGC algorithm along

with Post Processing only.

Thus in conclusion, a mixed set of results are produced for the images in this dataset for the boundary based analysis, however for the ORA, the adaptive filtering and the Post Processing addition to the KGC produce the best results.

Table 5.8: ROC Analysis of SAR Sea Ice Images, data set 1

Average				
Technique	Criteria	Precision	Recall	Fmeasure
Watershed	-	99.67	99.40	99.54
Level Set	-	**98.45**	96.52	97.47
CDCut	-	97.70	99.15	98.42
KGC only	k=2	98.26	99.07	98.66
	k=3	98.11	99.38	98.74
	k=4	97.96	**99.63**	**98.78**
	k=5	97.78	99.52	98.64
KGC + MAM	k=2	98.20	99.06	98.63
	k=3	98.11	99.23	98.67
	k=4	97.91	99.51	98.70
	k=5	97.88	99.49	98.68
KGC + RMAM	k=2	98.21	99.06	98.63
	k=3	98.10	99.25	98.67
	k=4	97.87	99.52	98.69
	k=5	97.84	99.48	98.65
KGC with PostPro only	k=2	98.45	98.23	98.33
	k=3	98.40	98.53	98.46
	k=4	98.34	98.72	98.53
	k=5	98.09	98.70	98.39
KGC + MAM with PostPro	k=2	98.39	95.80	97.05
	k=3	98.36	96.19	97.25
	k=4	98.28	96.84	97.55
	k=5	98.28	96.59	97.42
KGC + RMAM with PostPro	k=2	98.39	95.80	97.05
	k=3	98.34	96.08	97.19
	k=4	98.24	96.84	97.53
	k=5	98.17	96.21	97.17

Table 5.9: ROC Analysis of SAR Sea Ice Images, data set 1 - Best results

Average				
Technique	Criteria	Precision	Recall	Fmeasure
Watershed	-	99.67	99.40	99.54
Level Set	-	**98.45**	96.52	97.47
CDCut	-	97.70	99.15	98.42
KGC Only	k=3	98.11	**99.38**	**98.74**
KGC + MAM	k=3	98.14	99.31	98.72
KGC + RMAM	k=3	98.14	99.33	98.73
KGC with Post Pro only	k=3	98.40	98.53	98.46
KGC + MAM with PostPro	k=3	98.38	96.76	97.54
KGC + RMAM with PostPro	k=3	98.38	96.65	97.49

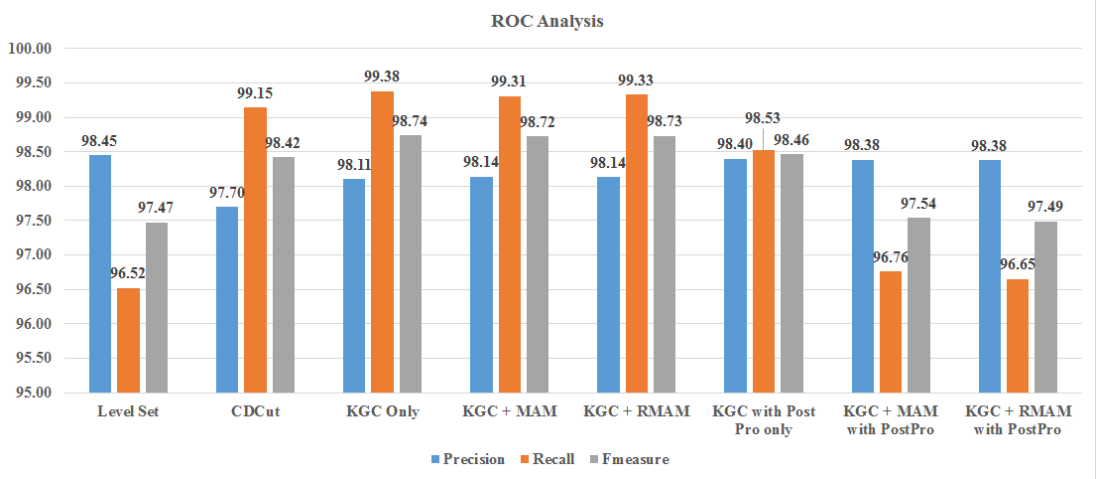

Figure 5.23: Graph of the ROC Analysis values for SAR Sea Ice Images, dataset 1

Receiver Operating Characteristic Assessment The equivalent ROC analysis for the ORA based quantitative assessment presented in Tables 5.2 and 5.3, is given in Tables 5.8 and 5.9 respectively. Table 5.8 presents the average of the results for the images in Dataset 1, with the best results (from table 5.3) presented in Table 5.9. Figure 5.23 shows the graphical representation of the values for better understanding and finally Figure 5.24 shows the ROC curve, which is the *True Positive Rate* versus the *False Positive Rate*, as shown in Figure 2.22.

As seen from the Tables 5.8 and 5.9 as well as figure 5.23, the Level Set algorithm

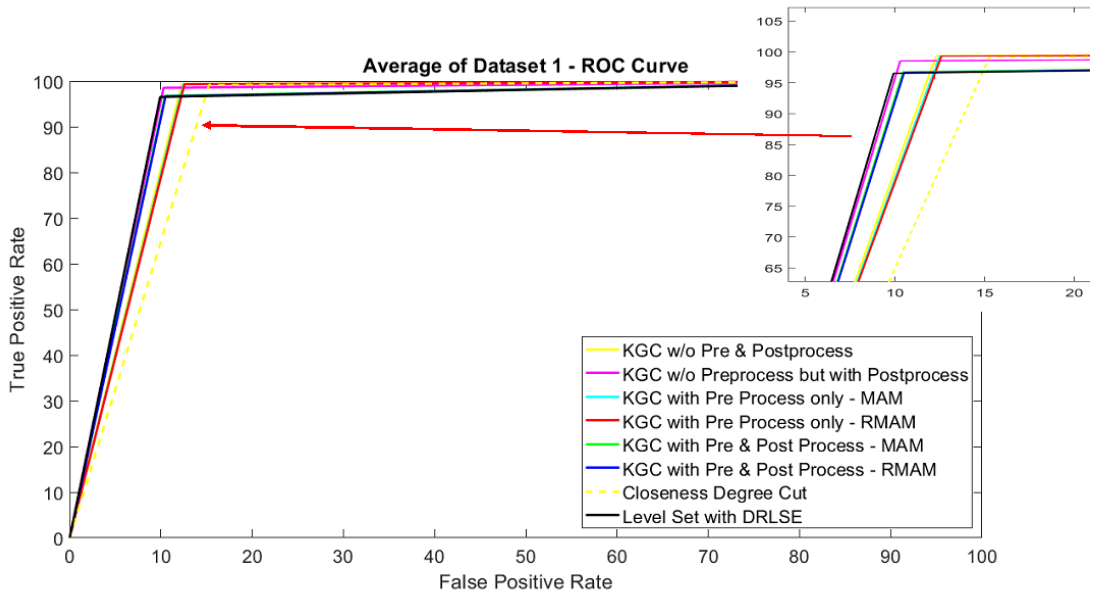

Figure 5.24: ROC Curve for SAR Sea Ice Images, dataset 1

has the best Precision, whereas the KGC algorithm on its own without any Pre or Post processing gives the best Recall and thus the Fmeasure. This indicates that the best result for this dataset, is produced by the KGC on its own, without the need of any Pre or Post processing. It can thus be said that the addition of Pre and Post processing lowers the accuracy of the result, which is contradictory as seen in the ORA assessment.

As per the ROC analysis described in section 2.3.2, higher Precision and lower Recall means the Segmentation algorithm produces high number of results, most of which are incorrect. A higher Recall and lower Precision means, lower number of results are produced but most of them are correct. Thus the ideal result is produced with algorithm having high Precision and high Recall, which from Table 5.8, is produced by KGC without pre or post processing. This is also evident from Table 5.2, where it produces the lowest Over Segmentation rate and higher Correct Segmentation.

Thus from Table 5.8, the KGC+MAM/ KGC+RMAM with post processing produces a lot of results, most of which are incorrect. This is contradictory to the results for the ORA shown in Table 5.2, where it produces the highest Regional Accuracy.

This highlights the differences of calculation between the ROC and the ORA in terms of finding the Correct Segmentation accuracy. Whilst the ROC only calculates the positive results, the ORA also calculates the negative along with the positive results to get an accurate Segmentation rate.

In Figure 5.24, the ROC curve is shown. It can be seen that the worst result is produced by the CDCut algorithm, while the best result is produced by the KGC algorithm on its own, close followed by the addition of Adaptive Filtering of the proposed MAMF and region based MAMF respectively.

5.3.3.2 SAR Sea Ice Images - Dataset 2

Overall Accuracy Assessment The next set of Quantitative analysis were done on images in dataset 2. Tables 5.10 and 5.11 show the average of the results for the images in this dataset, with the latter being the simplified version of the best results. Figure 5.25 shows the graphical representation of the Quantitative values. Table 5.12 and Figure 5.26 show the computing efficiency for these set of images in the dataset for the various algorithms.

From Tables 5.10 and 5.11, it can be seen how the ORA is significantly increased compared to CDCut and the Level Set algorithm. It is significantly improved compared to the original KGC algorithm without Pre or Post Processing, almost twice that of the original result. It can be seen how the Pre Processing increases the ORA result gradually, before it is drastically increased by the Post Processing algorithm. The Post Processing algorithm on its own without speckle filtering, applied to the KGC algorithm also increases the ORA, giving the basis for performing filtering and checking the result. It can be be seen how the optimum results are produced with the KGC algorithm parameter “k” equal to 2.

For the Boundary based analysis, it can be seen how all the KGC algorithm results have the least amount of Under Segmentation, the lowest being the Post Processed result. However, the Over Segmentation values are higher compared to the CDCut and

Table 5.10: Quantitative Analysis of SAR Sea Ice Images, data set 2

Average					
Technique	Criteria	Region Acc	Under Seg	Over Seg	Correct Seg
Watershed	-	87.92	0.76	1.98	97.27
Level Set	-	29.61	45.21	34.84	19.96
CDCut	-	17.19	42.78	**26.47**	30.75
KGC only	k=2	24.24	25.63	37.01	37.37
	k=3	24.15	27.22	37.05	35.74
	k=4	20.39	30.68	35.84	33.47
	k=5	11.63	37.69	35.21	27.11
KGC + MAM filtering	k=2	24.65	25.11	35.61	39.29
	k=3	21.05	26.91	35.66	37.44
	k=4	11.56	38.11	35.08	26.82
	k=5	20.61	30.57	34.96	34.48
KGC + RMAM filtering	k=2	24.65	25.04	35.57	**39.40**
	k=3	21.08	25.98	35.83	38.20
	k=4	20.15	34.19	34.95	30.86
	k=5	12.37	34.96	31.86	33.19
KGC with PostPro only	k=2	37.13	21.90	42.78	35.32
	k=3	37.17	22.17	42.23	35.60
	k=4	34.63	24.32	39.43	36.26
	k=5	24.73	27.62	38.94	33.45
KGC + MAM filtering & PostPro	k=2	56.64	20.93	46.17	32.91
	k=3	50.25	21.64	45.27	33.10
	k=4	41.44	27.27	40.95	31.78
	k=5	52.19	23.20	43.10	33.70
KGC + RMAM filtering & PostPro	k=2	**56.78**	**20.91**	46.11	32.99
	k=3	52.74	21.22	45.91	32.88
	k=4	47.24	26.08	40.67	33.26
	k=5	31.62	27.65	40.91	31.44

the Level Set algorithm, the lowest produced with the CDCut algorithm. Finally, the Correct Segmentation value also the highest compared to the CDCut and the Level Set results for all the KGC algorithm results. However it can be seen how the value is

Table 5.11: Quantitative Analysis of SAR Sea Ice Images, data set 2 - Best results

Average					
Technique	Criteria	Overall Region Acc	Under Seg	Over Seg	Correct Seg
Watershed	-	87.92	0.76	1.98	97.27
Level Set	-	29.61	45.21	34.84	19.96
CDCut	-	17.19	42.78	**26.47**	30.75
KGC Only	k=2	24.24	25.63	37.01	37.37
KGC + MAM	k=2	24.65	25.11	35.61	39.29
KGC + RMAM	k=2	24.65	25.04	35.57	**39.40**
KGC with Post Pro only	k=2	37.13	21.90	42.78	35.32
KGC + MAM with PostPro	k=2	56.64	20.93	46.17	32.91
KGC + RMAM with PostPro	k=2	**56.78**	**20.91**	46.11	32.99

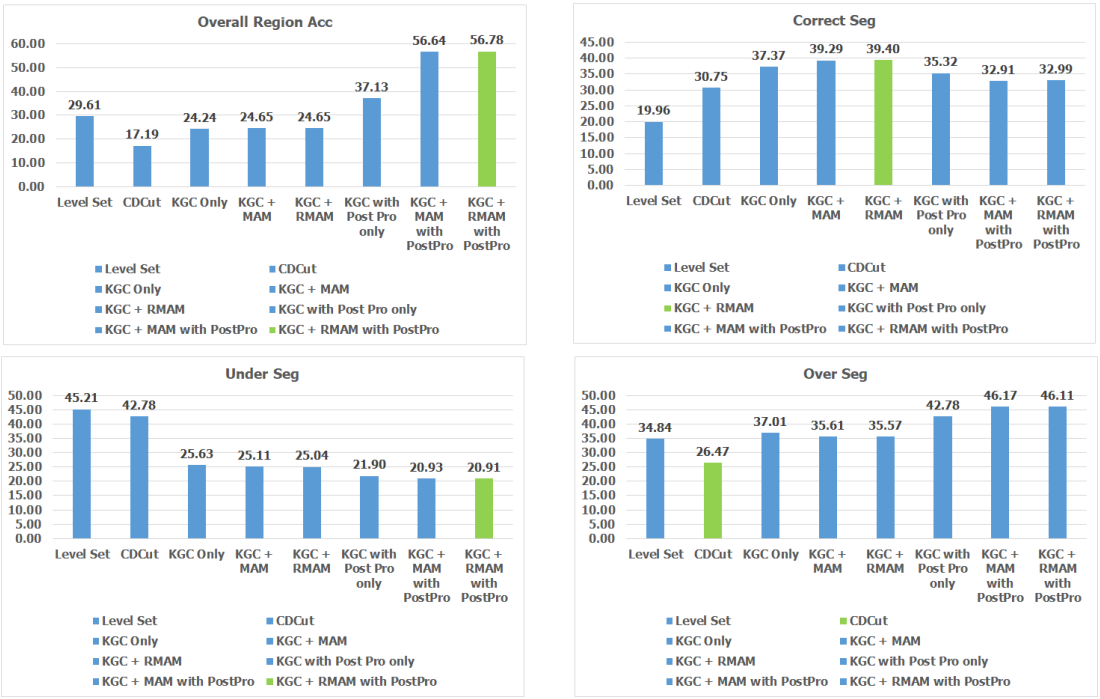

Figure 5.25: Graph of the Quantitative Analysis values for SAR Sea Ice Images, dataset 2

decreased slightly in the Post Processing result as opposed to the result produced with Pre Processing along with the KGC algorithm.

From Table 5.12, it can however be seen that even though the KGC algorithm on

Table 5.12: Computing Times of SAR Sea Ice Images, data set 2

Average		
Technique	Criteria	Timing
Watershed	-	0.02
CDCut	-	1.00
Level Set	-	1.36
KGC only	k=2	0.02
	k=3	0.13
	k=4	0.17
	k=5	0.26
KGC with PostPro only	k=2	4.87
	k=3	4.57
	k=4	3.80
	k=5	3.48
KGC + MAM with PostPro	k=2	13.20
	k=3	11.34
	k=4	7.56
	k=5	10.06
KGC + RMAM with PostPro	k=2	13.11
	k=3	11.98
	k=4	6.81
	k=5	6.74

its own for k=2 is the fastest, the processing times for the Post Processing algorithms require considerable amount of time. This is primarily due to the values used for the parameters for Post Processing algorithm for finding the partition of regions, especially the Active Contour iterations. It can however be noted that for segmenting the highly complex image captured on 12th August 2014 takes considerably longer time (3 times as much) as opposed to the image captured on 2nd August 2014. From the image shown in the previous section, it is easy to reason why.

In terms of the ORA and the boundary based analysis, it can be seen how the Region based MAMF proposed in the previous chapter produces the best result for dataset 2. The processing times are considerably increased but is justified with the increase in

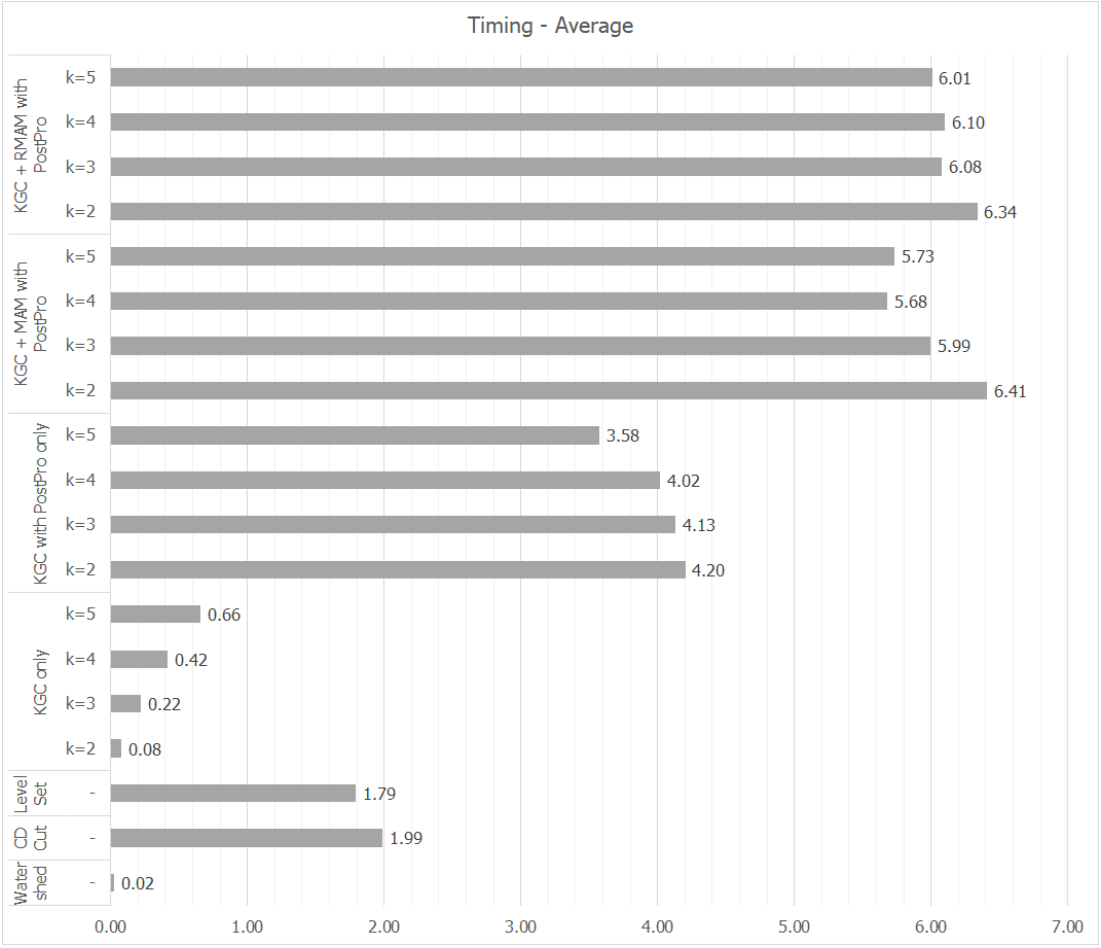

Figure 5.26: Graph of the Computing efficiency values for SAR Sea Ice Images, dataset 2

Table 5.13: Quantitative Analysis of TS-X image captured on 2nd August 2014

Sample 1							
Technique	Criteria			Overall Region Acc	Under Seg	Over Seg	Correct Seg
Watershed	-			92.95	0.72	1.55	97.74
Level Set	-			40.58	45.80	35.13	19.08
CDCut	-			17.39	41.54	**25.81**	32.64
KGC Only	No Pre/ Post Pro	KGC Pen = 0.05	k=2	31.18	24.73	36.15	39.12
KGC + MAM	Win 5x5, M = 1		k=2	31.74	23.32	33.95	42.73
KGC + RMAM	Win 5x5, M = 1		k=2	31.75	23.18	33.88	**42.94**
KGC with Post Pro	No Pre Pro	KGC Pen = 0.05, AC Pen = 0.05	k=2	46.96	22.85	39.39	37.76
KGC + MAM with PostPro	Win 5x5, M = 1		k=2	71.56	21.45	41.69	36.86
KGC + RMAM with PostPro	Win 5x5, M = 1		k=2	**71.85**	**21.40**	41.58	37.02

Segmentation Accuracy. Tables 5.13 and 5.14 show the individual results for the two different images in dataset 2. It can be noted, particularly for Sample 1 (TSX captured

Table 5.14: Quantitative Analysis of TS-X image captured on 12th August 2014

Sample 2						
Technique	Criteria			Overall Region Acc	Under Seg	Over Seg	Correct Seg
Watershed	-			82.89	0.80	2.40	96.80
Level Set	-			18.64	44.62	34.54	20.84
CDCut	-			16.98	44.02	**27.12**	28.86
KGC Only	No Pre/ Post Pro	KGC Pen = 0.2	k=2	17.30	26.52	37.87	35.61
KGC + MAM	Win 3x3, M = 1		k=2	17.55	26.89	37.26	**35.85**
KGC + RMAM	Win 3x3, M = 1		k=2	17.55	26.89	37.26	**35.85**
KGC with Post Pro	No Pre Pro	KGC Pen = 0.2, AC Pen = 0.05	k=2	27.29	20.95	46.17	32.88
KGC + MAM with PostPro	Win 3x3, M = 1		k=2	**41.71**	**20.41**	50.64	28.95
KGC + RMAM with PostPro	Win 3x3, M = 1		k=2	**41.71**	**20.41**	50.64	28.95

on 2nd August 2014), the significant increase in performance as opposed to any algorithm. The results in Sample 2 are also significant compared to any other algorithm.

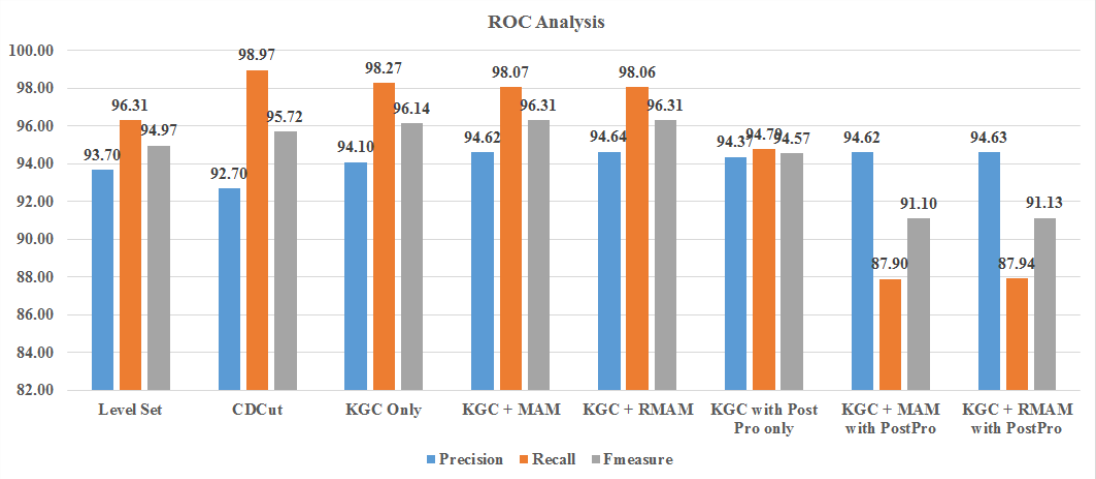

Figure 5.27: Graph of the ROC Analysis values for SAR Sea Ice Images, dataset 2

Receiver Operating Characteristic Assessment The ROC analysis for dataset 2 images is given in Tables 5.15 and 5.16 as well simplified by Figure 5.27. Figure 5.28 provides the ROC curve, which is the *True Positive Rate* versus the *False Positive Rate*.

Contradictory to the dataset 1, the best Precision results are produced by KGC algorithm aided by the proposed region based MAMF. The best Recall and thus the Fmeasure results are produced by KGC algorithm aided by the proposed MAMF. However, similar to dataset 1, the results indicate that the addition of Post processing lowers the

Table 5.15: ROC Analysis of SAR Sea Ice Images, data set 2

Average				
Technique	Criteria	Precision	Recall	Fmeasure
Watershed	-	99.90	99.83	99.86
Level Set	-	93.70	96.31	94.97
CDCut	-	92.70	98.97	95.72
KGC only	k=2	94.10	98.27	96.14
	k=3	93.69	98.73	96.14
	k=4	93.17	99.27	96.12
	k=5	89.54	99.78	94.34
KGC + MAM filtering	k=2	94.62	98.07	96.31
	k=3	94.11	98.68	96.34
	k=4	89.61	**99.79**	94.40
	k=5	93.61	99.35	**96.39**
KGC + RMAM filtering	k=2	**94.64**	98.06	96.31
	k=3	94.25	98.47	96.31
	k=4	92.62	99.54	95.95
	k=5	85.00	99.37	91.49
KGC with PostPro only	k=2	94.37	94.79	94.57
	k=3	94.31	94.78	94.54
	k=4	94.19	95.68	94.93
	k=5	91.27	95.70	93.41
KGC + MAM filtering & PostPro	k=2	94.62	87.90	91.10
	k=3	94.49	88.20	91.22
	k=4	92.32	90.89	91.59
	k=5	94.36	89.09	91.64
KGC + RMAM filtering & PostPro	k=2	94.63	87.94	91.13
	k=3	94.53	87.87	91.06
	k=4	93.96	91.66	92.79
	k=5	86.39	91.11	88.56

accuracy of the result, which is contradictory as seen in the ORA assessment.

As per the ROC analysis described in section 2.3.2, the ideal result is produced by KGC+MAM without post processing. This is also evident from Table 5.10, where it produces the highest Correct Segmentation rate and lower Over Segmentation.

Thus from Table 5.15, the KGC+MAM/ KGC+RMAM with post processing pro-

Table 5.16: ROC Analysis of SAR Sea Ice Images, data set 2 - Best results

Average				
Technique	Criteria	Precision	Recall	Fmeasure
Watershed	-	99.90	99.83	99.86
Level Set	-	93.70	96.31	94.97
CDCut	-	92.70	**98.97**	95.72
KGC Only	k=2	94.10	98.27	96.14
KGC + MAM	k=2	94.62	98.07	96.31
KGC + RMAM	k=2	**94.64**	98.06	**96.31**
KGC with Post Pro only	k=2	94.37	94.79	94.57
KGC + MAM with PostPro	k=2	94.62	87.90	91.10
KGC + RMAM with PostPro	k=2	94.63	87.94	91.13

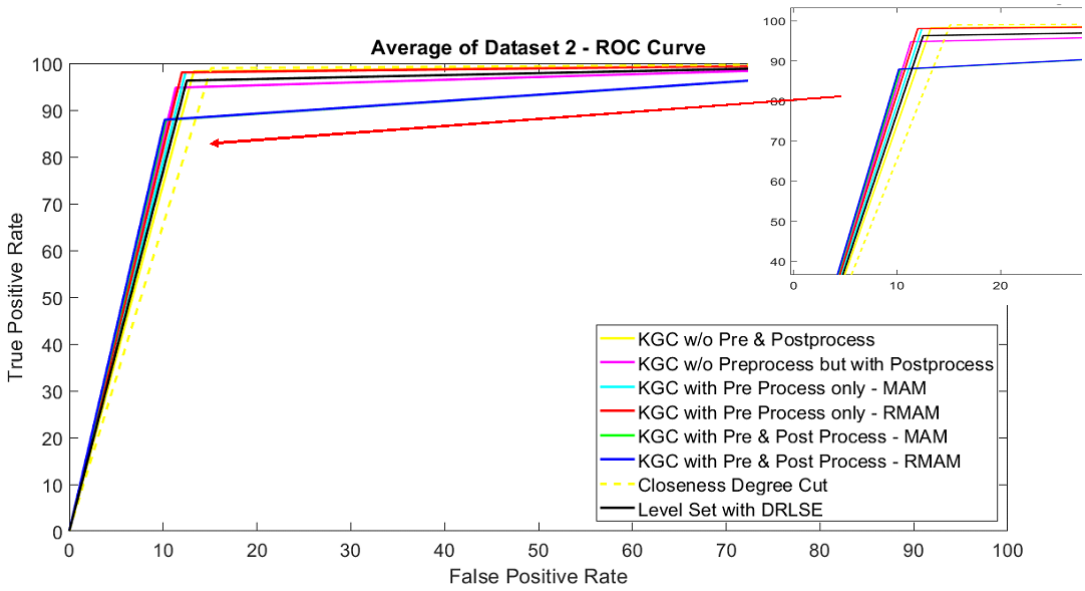

Figure 5.28: ROC Curve for SAR Sea Ice Images, dataset 2

duces a lot of results, most of which are incorrect. This is contradictory to the results for the ORA shown in Table 5.10, where it produces the highest Regional Accuracy. This again highlights the differences of calculation between the ROC and the ORA in terms of finding the Correct Segmentation accuracy.

In Figure 5.28, the ROC curve is shown. It can be seen that the worst result is produced yet again by the CDCut algorithm, while the best result is produced by the

KGC algorithm with the addition of Adaptive Filtering of the proposed region based MAMF. These are closely followed by the KGC algorithm with the addition of Adaptive Filtering of the proposed MAMF and the KGC algorithm without any Pre or Post Processing. These are very evident from the Precision, Recall and Fmeasure values from Table 5.15.

5.3.3.3 SAR Sea Ice Images - Dataset 3

Overall Accuracy Assessment The final set of Quantitative analysis were done on the images in dataset 3. Tables 5.17 and 5.18 show the average of the results for the images in this particular dataset, with the best set of results shown in the latter. Figure 5.29 shows the graphical results for the values in Table 5.18. Table 5.19 and Figure 5.30 show the average computing efficiency for the images in this dataset for the various algorithms used in comparison.

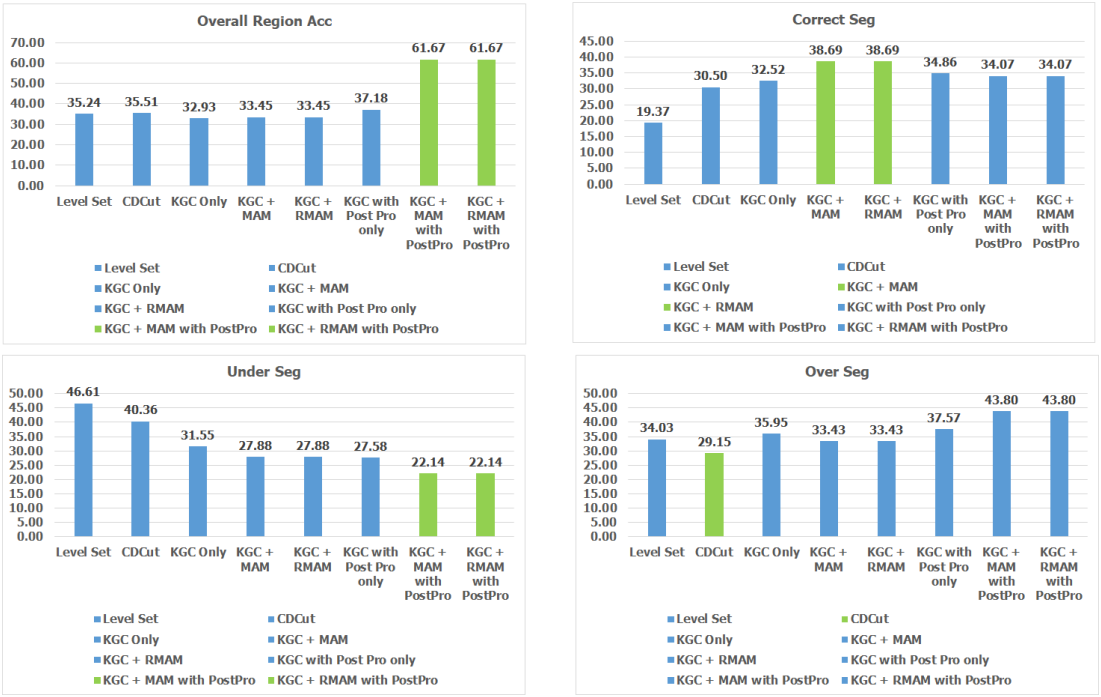

Figure 5.29: Graph of the Quantitative Analysis values for SAR Sea Ice Images, dataset 3

Table 5.17: Quantitative Analysis of SAR Sea Ice Images, data set 3

Average					
Technique	Criteria	Overall Region Acc	Under Seg	Over Seg	Correct Seg
Watershed	-	72.50	1.29	4.87	93.85
Level Set	-	35.24	46.61	34.03	19.37
CDCut	-	35.51	40.36	**29.15**	30.50
KGC only	k=2	32.93	31.55	35.95	32.52
	k=3	32.93	32.15	36.22	31.64
	k=4	32.90	32.12	36.01	31.87
	k=5	32.64	36.21	34.74	29.06
KGC + MAM filtering	k=2	33.45	27.88	33.43	**38.69**
	k=3	33.02	28.82	33.98	37.20
	k=4	32.88	30.33	34.10	35.58
	k=5	32.84	30.49	34.25	35.26
KGC + RMAM filtering	k=2	33.45	27.88	33.43	38.69
	k=3	33.01	29.01	34.00	36.99
	k=4	32.98	29.10	34.04	36.87
	k=5	32.96	29.93	34.19	35.88
KGC with PostPro only	k=2	37.18	27.58	37.57	34.86
	k=3	36.38	27.68	37.72	34.61
	k=4	37.95	27.74	37.47	34.79
	k=5	35.94	30.77	35.92	33.32
KGC + MAM filtering & PostPro	k=2	**61.67**	**22.14**	43.80	34.07
	k=3	59.44	22.75	43.52	33.74
	k=4	43.93	23.51	42.74	33.75
	k=5	52.07	23.48	43.01	33.51
KGC + RMAM filtering & PostPro	k=2	**61.67**	**22.14**	43.80	34.07
	k=3	59.52	22.79	43.57	33.65
	k=4	44.07	23.19	42.95	33.87
	k=5	44.77	23.21	43.18	33.62

From Tables 5.17 and 5.18, it can again be seen how the ORA is significantly increased compared to the CDCut and the LevelSet algorithms. The Post Processed results, with MAMF and the region based MAMF produce identical best results, but vary with increasing value of k for the KGC algorithm. The Post Processing result

Table 5.18: Quantitative Analysis of SAR Sea Ice Images, data set 3 - Best results

Average					
Technique	Criteria	Overall Region Acc	Under Seg	Over Seg	Correct Seg
Watershed	-	72.50	1.29	4.87	93.85
Level Set	-	35.24	46.61	34.03	19.37
CDCut	-	35.51	40.36	**29.15**	30.50
KGC Only	k=2	32.93	31.55	35.95	32.52
KGC + MAM	k=2	33.45	27.88	33.43	**38.69**
KGC + RMAM	k=2	33.45	27.88	33.43	38.69
KGC with Post Pro only	k=2	37.18	27.58	37.57	34.86
KGC + MAM with PostPro	k=2	**61.67**	**22.14**	43.80	34.07
KGC + RMAM with PostPro	k=2	**61.67**	**22.14**	43.80	34.07

with the adaptive filtering produce almost twice the increase in accuracy compared to the KGC algorithm on its own. The increase with the addition of filtering to the KGC algorithm and just the Post Processing aren't as much noticeable as seen in dataset 2.

The best set of results are again produced with KGC, k equal to 2, which have the best ORA as well the lowest Under Segmentation in terms of Boundary based assessment. As noted in dataset 2, the Over Segmentation, however, is increased and there is a slight drop in Correct Segmentation accuracy to compensate for the increase in the ORA. The CDCut algorithm again has the lowest Over Segmentation accuracy.

In terms of processing times, again the KGC on its own with k=2 is the fastest. But compared to the results in dataset 2, the processing times aren't as high for these particular images. This is again evident from the set of images used in this particular dataset and the settings used for the Post Processing algorithm to get maximum number of Sea Ice floe regions identified and separated.

Tables 5.20 and 5.21 show the individual results for the two images in the dataset. It is quite easily noticeable the difference in the ORA for both of the images apart from the Post Processing set of results which are almost similar to each other, Sample 12 being slightly lower. It can also be seen, for Sample 11, the ORA for the Post

Table 5.19: Computing Times of SAR Sea Ice Images, data set 3

Average		
Technique	Criteria	Timing
Watershed	-	0.02
CDCut	-	1.99
Level Set	-	1.79
KGC only	k=2	0.08
	k=3	0.22
	k=4	0.42
	k=5	0.66
KGC with PostPro only	k=2	4.20
	k=3	4.13
	k=4	4.02
	k=5	3.58
KGC + MAM with PostPro	k=2	6.41
	k=3	5.99
	k=4	5.68
	k=5	5.73
KGC + RMAM with PostPro	k=2	6.34
	k=3	6.08
	k=4	6.10
	k=5	6.01

Table 5.20: Quantitative Analysis of top half of TS-X image captured on 31st July 2014

Sample 11							
Technique	Criteria			Overall Region Acc	Under Seg	Over Seg	Correct Seg
Watershed	-			51.64	1.92	7.60	90.48
Level Set	-			45.07	46.33	33.68	19.99
CDCut	-			45.35	39.54	29.50	30.96
KGC Only	No Pre/ Post Pro	KGC Pen = 0.2	k=3	45.09	33.81	32.27	33.93
KGC + MAM	Win 7x7, M = 1		k=3	45.26	29.99	**28.33**	**41.67**
KGC + RMAM	Win 7x7, M = 1		k=3	45.26	29.99	**28.33**	**41.67**
KGC with Post Pro	No Pre Pro	KGC Pen = 0.2, AC Pen = 0.2	k=3	45.64	29.05	33.86	37.09
KGC + MAM with PostPro	Win 7x7, M = 1		k=3	**64.49**	**22.88**	39.63	37.49
KGC + RMAM with PostPro	Win 7x7, M = 1		k=3	**64.49**	**22.88**	39.63	37.49

Processed result is even higher than the Watershed result used to produce the GT. The ORA for the Post Processed result for Sample 11 is 1.5 times better than other other

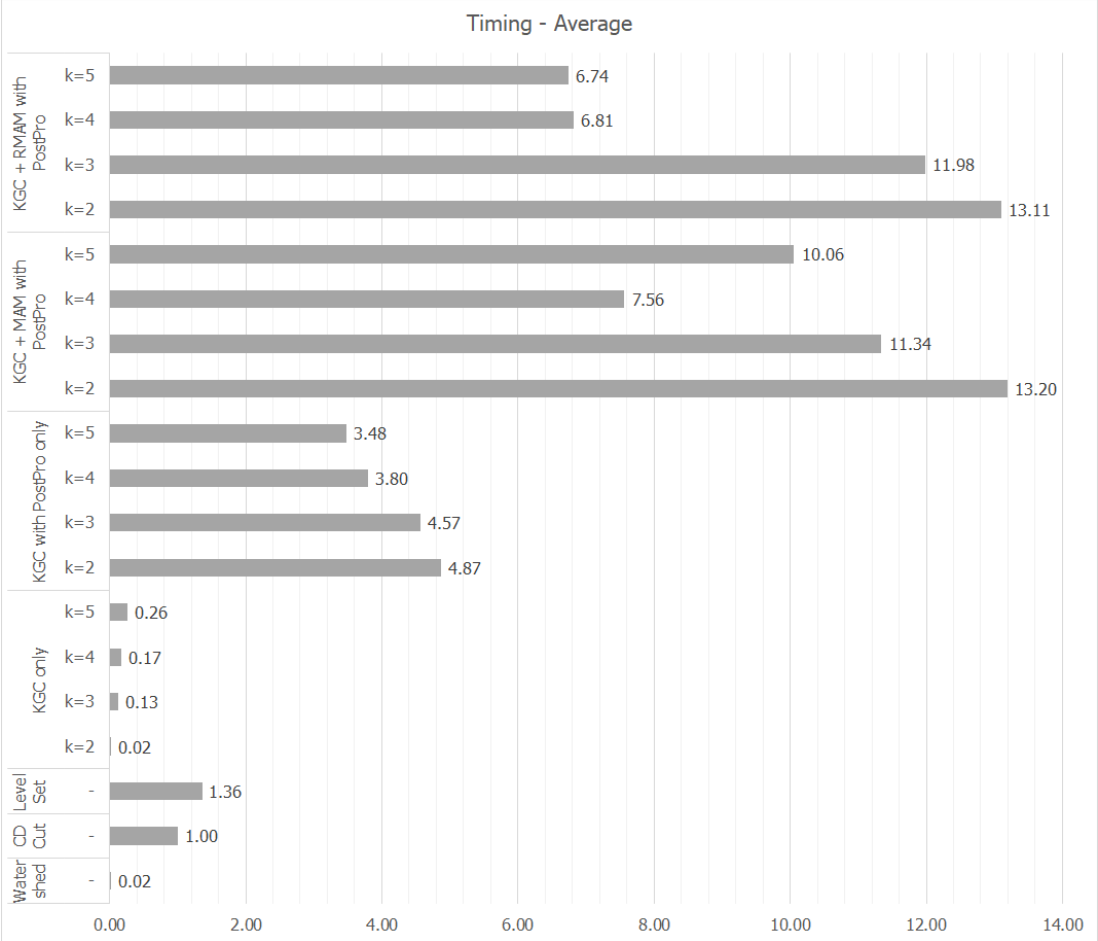

Figure 5.30: Graph of the Computing efficiency values for SAR Sea Ice Images, dataset 3

Table 5.21: Quantitative Analysis of bottom half of TS-X image captured on 31st July 2014

Sample 12							
Technique	Criteria			Overall Region Acc	Under Seg	Over Seg	Correct Seg
Watershed	-			93.35	0.65	2.14	97.22
Level Set	-			25.40	46.89	34.37	18.74
CDCut	-			25.67	41.17	**28.79**	30.03
KGC Only	No Pre/ Post Pro	KGC Pen = 0.05	k=2	20.87	28.60	39.87	31.54
KGC + MAM	Win 3x3, M = 1		k=2	21.62	26.23	39.38	**34.39**
KGC + RMAM	Win 3x3, M = 1		k=2	21.62	26.24	39.38	34.38
KGC with Post Pro	No Pre Pro	KGC Pen = 0.05, AC Pen = 0.05	k=2	26.96	25.92	41.94	32.14
KGC + MAM with PostPro	Win 3x3, M = 1		k=2	**61.20**	**21.75**	47.94	30.31
KGC + RMAM with PostPro	Win 3x3, M = 1		k=2	**61.20**	**21.75**	47.94	30.31

results, whereas for Sample 12, it is almost 3 times better.

Table 5.22: ROC Analysis of SAR Sea Ice Images, data set 3

Average				
Technique	Criteria	Precision	Recall	Fmeasure
Watershed	-	99.93	99.80	99.86
Level Set	-	96.20	98.69	97.43
CDCut	-	96.75	98.39	97.56
KGC only	k=2	96.57	99.44	97.98
	k=3	96.46	99.51	97.96
	k=4	96.45	99.53	97.96
	k=5	96.00	**99.72**	97.82
KGC + MAM filtering	k=2	96.91	99.27	**98.07**
	k=3	96.72	99.38	98.03
	k=4	96.45	99.53	97.96
	k=5	96.41	99.56	97.95
KGC + RMAM filtering	k=2	96.91	99.27	**98.07**
	k=3	96.69	99.40	98.02
	k=4	96.58	99.47	98.00
	k=5	96.53	99.52	98.00
KGC with PostPro only	k=2	96.91	98.43	97.66
	k=3	96.90	98.40	97.64
	k=4	96.89	98.45	97.66
	k=5	96.62	98.50	97.55
KGC + MAM filtering & PostPro	k=2	**97.18**	94.06	95.59
	k=3	97.10	94.62	95.84
	k=4	97.04	94.70	95.85
	k=5	97.03	94.80	95.90
KGC + RMAM filtering & PostPro	k=2	**97.18**	94.06	95.59
	k=3	97.10	94.57	95.81
	k=4	97.07	94.67	95.85
	k=5	97.04	94.83	95.92

Receiver Operating Characteristic Assessment The ROC analysis for dataset 3 images is given in Tables 5.22 and 5.23 as well simplified by Figure 5.31. Figure 5.32 provides the ROC curve, which is the *True Positive Rate* versus the *False Positive Rate*.

Table 5.23: ROC Analysis of SAR Sea Ice Images, data set 3 - Best results

Average				
Technique	Criteria	Precision	Recall	Fmeasure
Watershed	-	99.93	99.80	99.86
Level Set	-	96.20	98.69	97.43
CDCut	-	96.75	98.39	97.56
KGC Only	k=2	96.57	**99.44**	97.98
KGC + MAM	k=2	96.91	99.27	**98.07**
KGC + RMAM	k=2	96.91	99.27	**98.07**
KGC with Post Pro only	k=2	96.91	98.43	97.66
KGC + MAM with PostPro	k=2	**97.18**	94.06	95.59
KGC + RMAM with PostPro	k=2	**97.18**	94.06	95.59

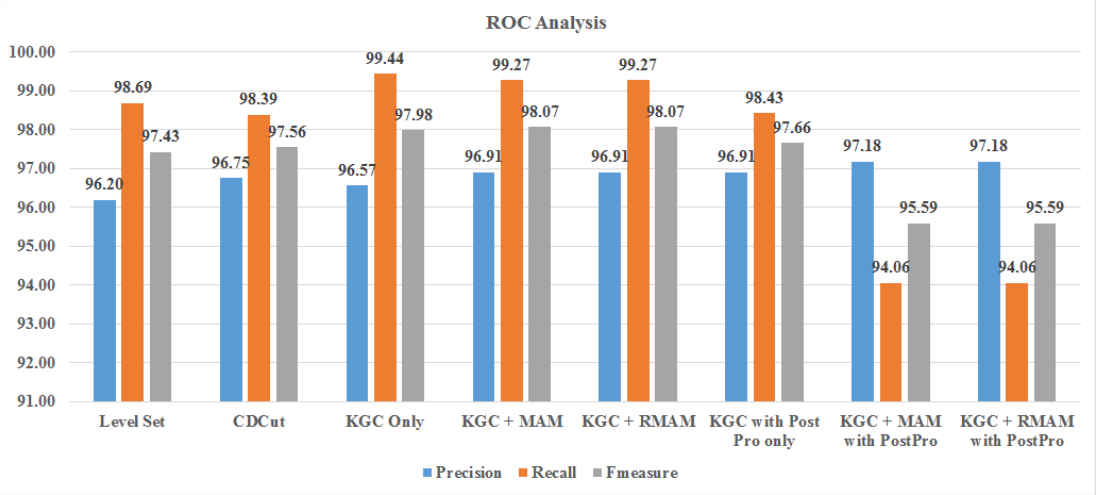

Figure 5.31: Graph of the ROC Analysis values for SAR Sea Ice Images, dataset 3

From Tables 5.22 and 5.23 as well as Figure 5.31, contrary to dataset 1 and 2 results, the best Precision rate is produced by the KGC with the combination of Pre and Post processing algorithms proposed. The best Recall rate is produced by the KGC without Pre and Post processing and finally the best Fmeasure results are produced, yet again by KGC algorithm aided by the proposed MAMF. However, similar to dataset 1 and 2, the results indicate that the addition of Post processing lowers the accuracy of the result, which is contradictory to the ORA assessment results seen earlier.

As per the ROC analysis described in section 2.3.2 the ideal result is produced by

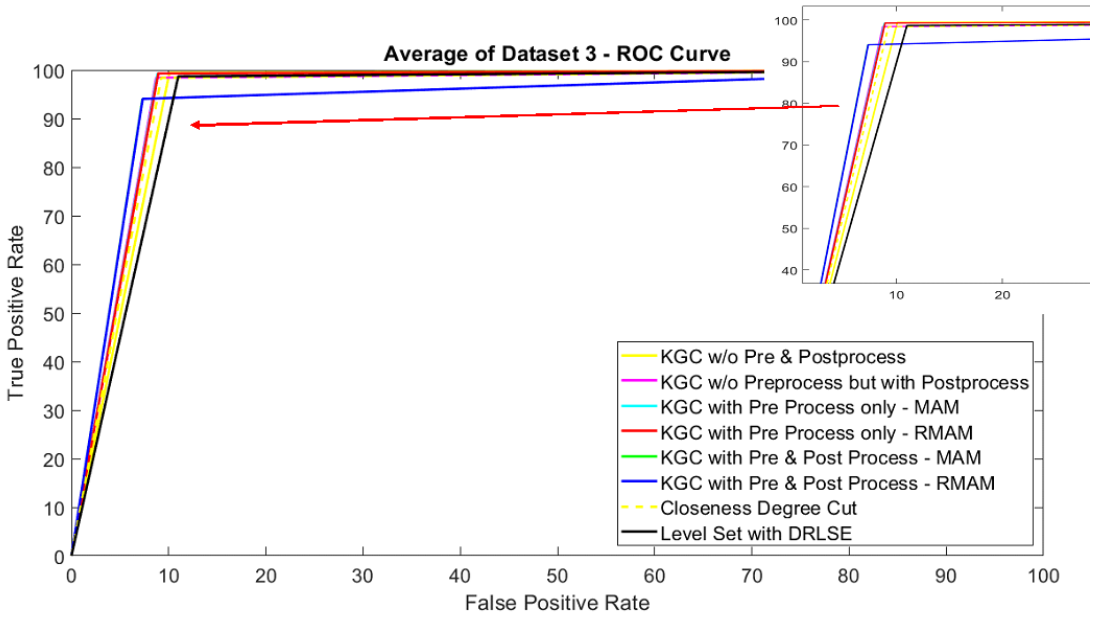

Figure 5.32: ROC Curve for SAR Sea Ice Images, dataset 3

KGC+MAM/ KGC+RMAM without post processing. This is also evident from Table 5.17, where it produces the highest Correct Segmentation rate and lower Over Segmentation.

Thus from Table 5.22, the KGC+MAM/ KGC+RMAM with post processing produces a lot of results, most of which are incorrect. This is contradictory to the results for the ORA shown in Table 5.17, where it produces the highest Regional Accuracy. This again highlights the differences of calculation between the ROC and the ORA in terms of finding the Correct Segmentation accuracy.

In Figure 5.32, the ROC curve is shown. It can be seen that the worst result is produced this time by the Level Set algorithm, while the best result is produced by the KGC algorithm with the addition of a combination of proposed Pre and Post processing algorithms. These are closely followed by the KGC algorithm with the addition of Adaptive Filtering of the proposed MAMF and then the CDCut algorithm. These are very evident from the Precision, Recall and Fmeasure values from Table 5.22.

5.3.4 Subjective Analysis

In this section, the effects of varying the key parameters of the KGC algorithm are given in Figures 5.33, 5.34, 5.35 and 5.36. This is followed by the visual analysis done for the various algorithms mentioned in the previous section and compared with the proposed Post Processing addition to improve the results produced with the KGC algorithm.

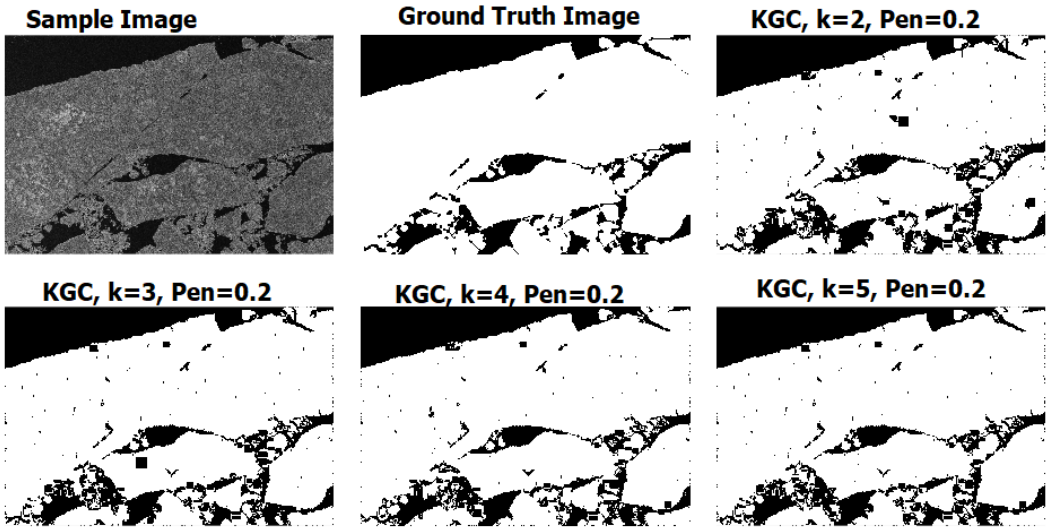

Figure 5.33: Effects of varying k parameter of the KGC for top part of TSX image captured on 31st July 2014

Figures 5.33 and 5.34 show the effects of varying the "k" parameter of the KGC algorithm. The k in the algorithm, determines the number of labels to assign to the various regions. From the figures, it can be seen how by varying this parameter has very minor changes noticeable, which is also noticeable from the ORA results shown in the previous section. However it can be seen how the spot errors in the bigger Sea Ice regions are gradually decreased with the increasing k value, thus resulting in fewer Over Segmented regions.

Figures 5.35 and 5.36 show the effects of varying the "alpha" parameter of the KGC algorithm. The $alpha$ in the algorithm, determines the data penalty cost which

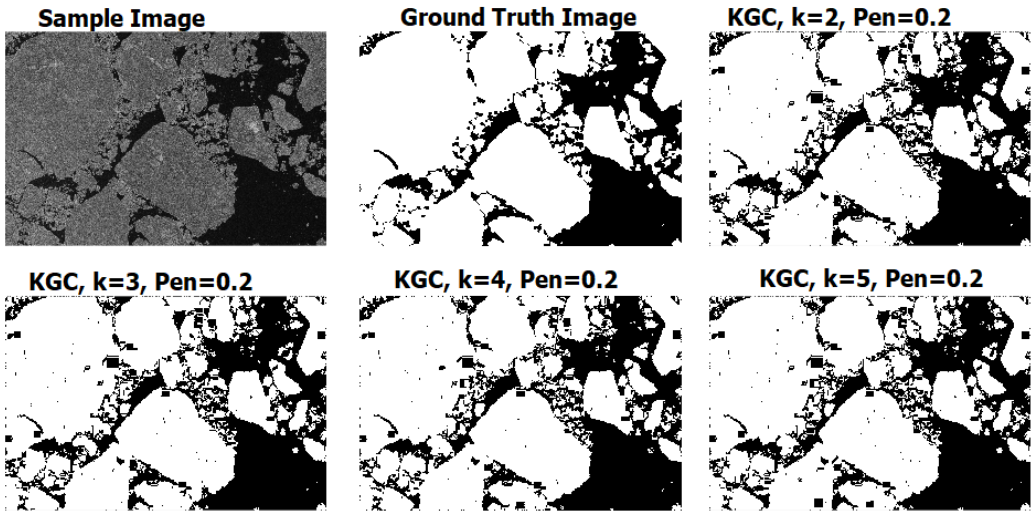

Figure 5.34: Effects of varying k parameter of the KGC for bottom part of TSX image captured on 31st July 2014

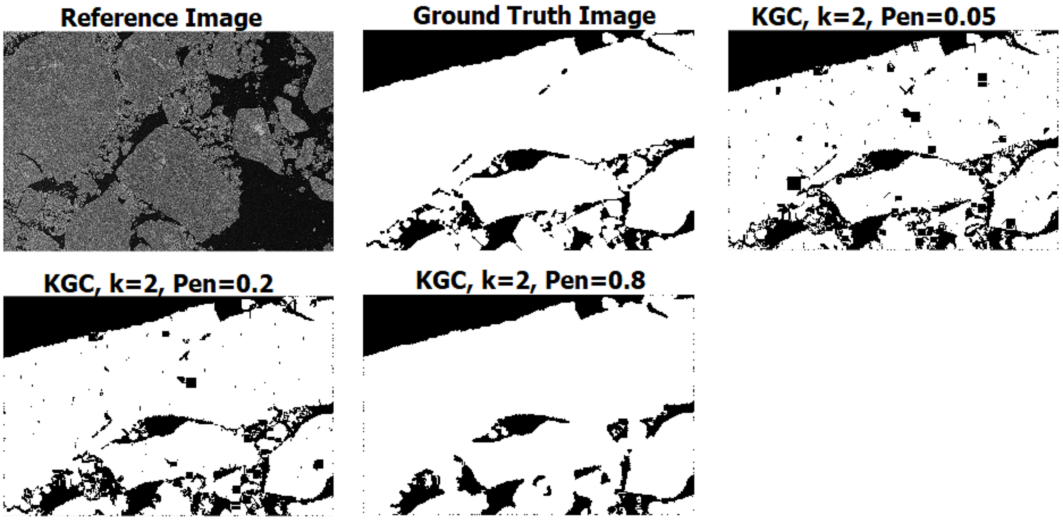

Figure 5.35: Effects of varying alpha parameter of the KGC for top part of TSX image captured on 31st July 2014

determines if a pixel is water or ice, in the case of Sea Ice images. It can be seen how varying this parameter varies the results quite drastically and producing more clearer results with the increasing $alpha$ value. However, this also reduces the correct Sea Ice regions extracted, as the neighbouring regions are merged with one another.

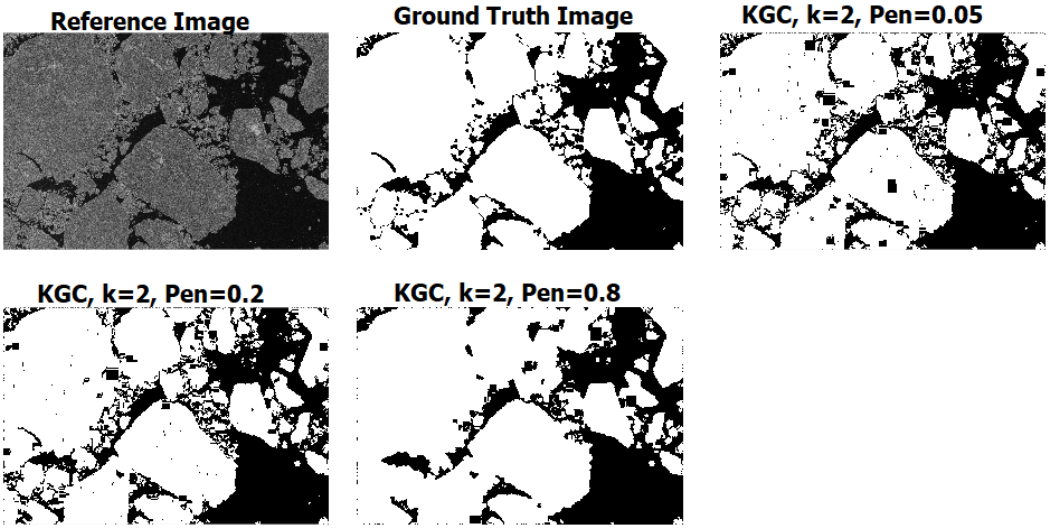

Figure 5.36: Effects of varying alpha parameter of the KGC for bottom part of TSX image captured on 31st July 2014

5.3.4.1 SAR Sea Ice Images - Dataset 1

Figures 5.37, 5.38 and 5.39 show the ORA results for each of the regions within the three images in dataset 1. The various Sea Ice regions with the most noticeable change have been highlighted to validate the advantages of the proposed Post Processing algorithm in improving the segmentation accuracy of the KGC algorithm.

In Figure 5.37, the various results for the Ground truth (a), KGC on its own (b), KGC with Post Processing only (c), KGC with MAMF and no Post Processing (d), KGC with region based MAMF and no Post Processing(e), KGC with MAMF and Post Processing (f), KGC with region based MAMF and Post Processing(g), Level Set(h) and lastly CDCut (i), are shown. Out of the four highlighted regions, it can be seen how for most cases where the accuracy as low as 0.8 or 1.2 percent, after Post Processing addition, it has been increased to more than 90 percent for those particular regions. There are various other regions with minor improvements, but the most significant increase in accuracy are highlighted in these four selected regions.

It can thus be seen, in validation to the Quantitative ORA results mentioned in the

Figure 5.37: Visual Analysis values for Sample 3 of TSX image captured on 29th June 2012

previous section, how the Post Processing significantly improves the segmentation accuracy and is the highest compared to any other algorithms compared.

Similar cases are noted for the remaining two images in the dataset, although not many regions with significant increase are noticeable for these particular images.

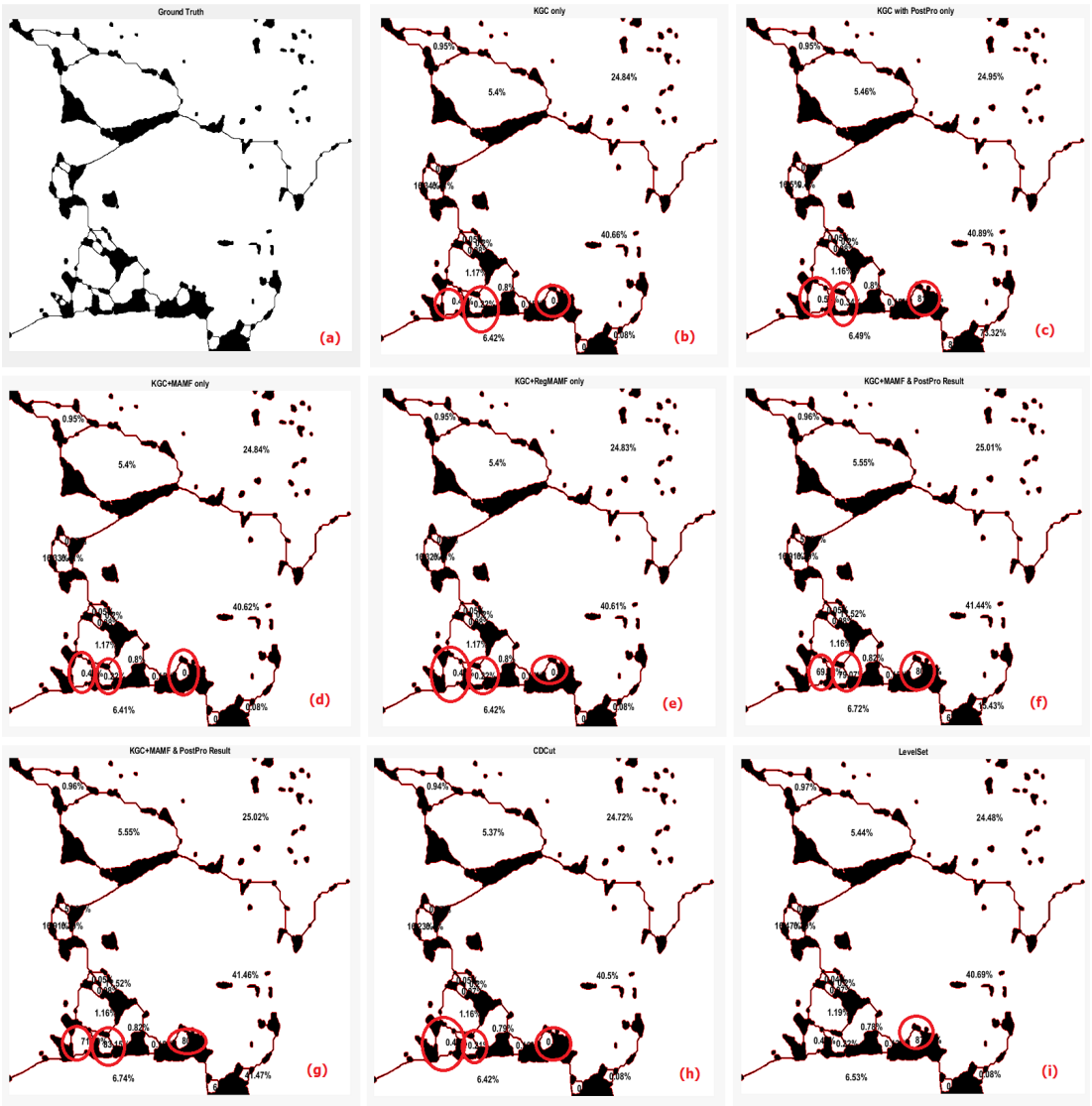

Figure 5.38: Visual Analysis values for Sample 4 of TSX image captured on 29th June 2012

These are also reflected from the ORA results shown in the previous section.

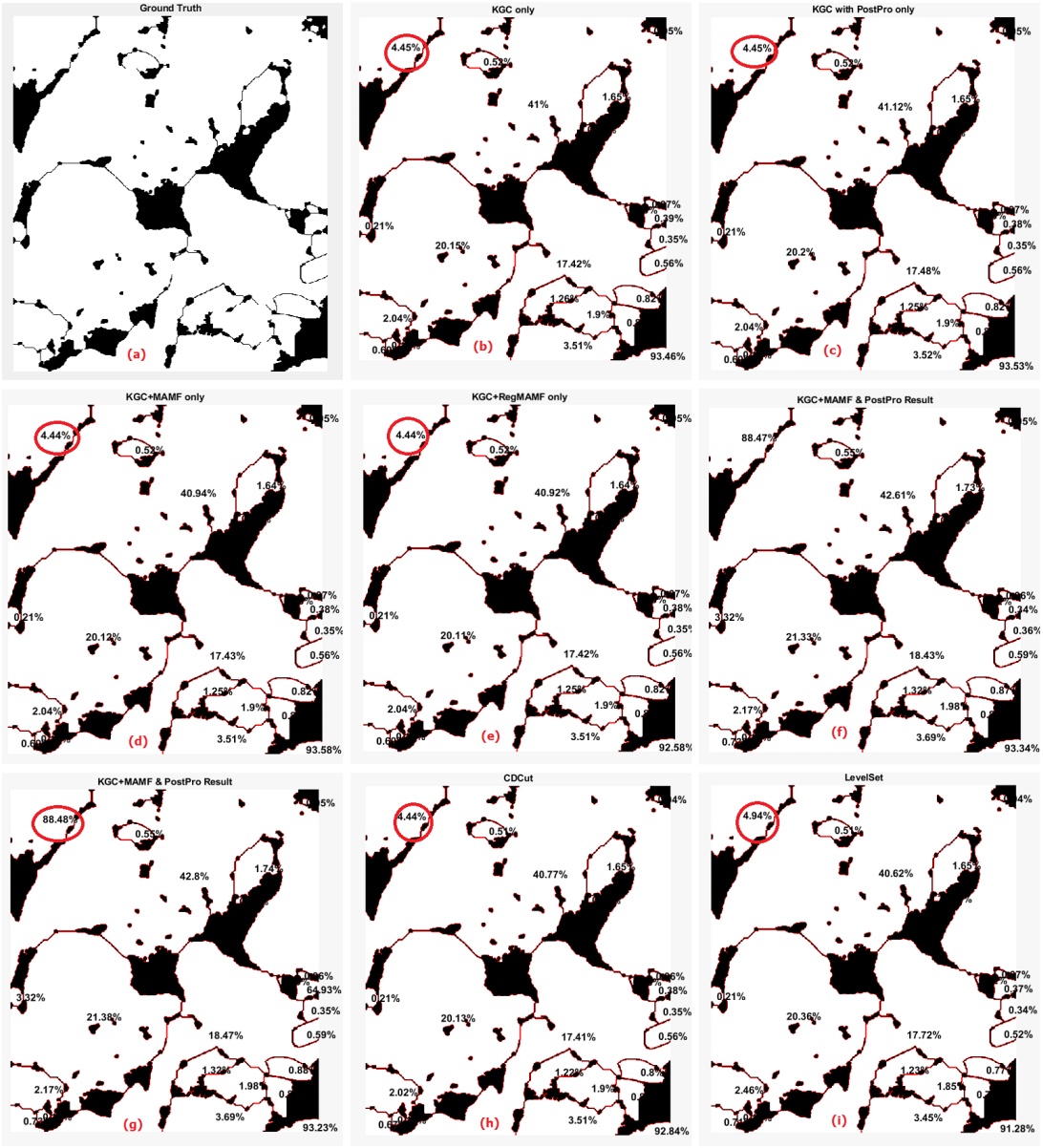

Figure 5.39: Visual Analysis values for Sample 5 of TSX image captured on 29th June 2012

5.3.4.2 SAR Sea Ice Images - Dataset 2

Figures 5.40 and 5.41 show the regional accuracy for the ORA for each of the regions within the two images in dataset 2. The various Sea Ice regions with the most noticeable change have been highlighted to validate the advantages of the proposed Post

Figure 5.40: Visual Analysis values for TSX image captured on 2nd August 2014

Processing algorithm in improving the segmentation accuracy of the KGC algorithm.

In Figures 5.40 and 5.41, the results are ordered in the form of Ground truth (a), KGC on its own (b), KGC with Post Processing only (c), KGC with MAMF and no Post Processing (d), KGC with region based MAMF and no Post Processing(e), KGC with MAMF and Post Processing (f), KGC with region based MAMF and Post Processing(g), Level Set(h) and lastly CDCut (i) respectively. Similar to that noticed in dataset 1, it can be seen how the Post Processed results with MAMF and region based

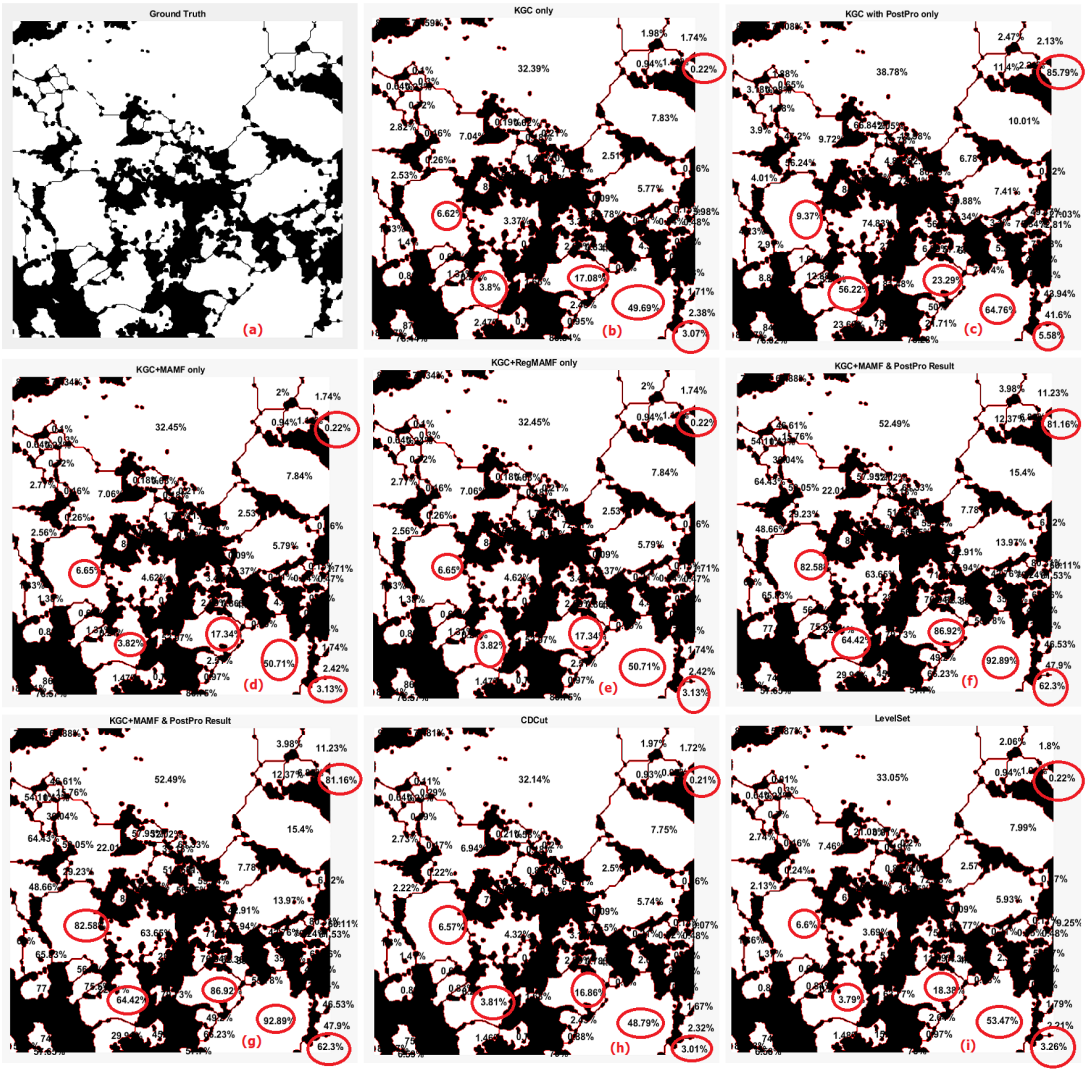

Figure 5.41: Visual Analysis values for TSX image captured on 12th August 2014

MAMF produce significant increase in accuracy for the most noticeable regions highlighted. However, as opposed to the images in dataset 1, it can be seen the sheer number of regions which are increased in accuracy for the images in this dataset 2. This is also owing to the huge number of Sea Ice regions present within the image as opposed to the images in dataset 1.

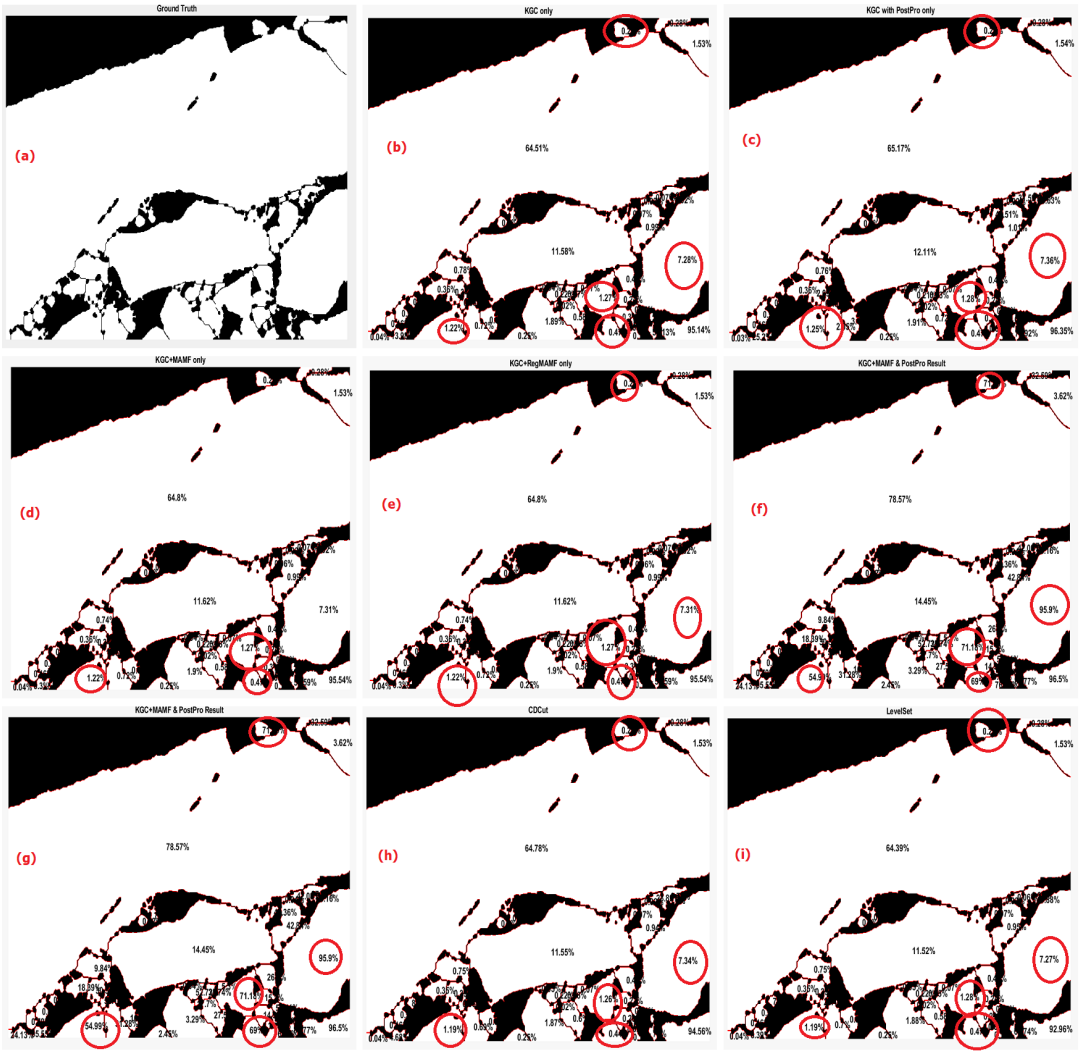

Figure 5.42: Visual Analysis values for top part of TSX image captured on 31st July 2014

5.3.4.3 SAR Sea Ice Images - Dataset 3

Figures 5.42 and 5.43 show the regional accuracy for the ORA for each of the regions within the two images in dataset 3. The Sea Ice regions with the most noticeable change have been highlighted to validate the advantages of the proposed Post Processing algorithm in improving the segmentation accuracy of the KGC algorithm.

In Figures 5.42 and 5.43, the results are ordered in the form of Ground truth (a),

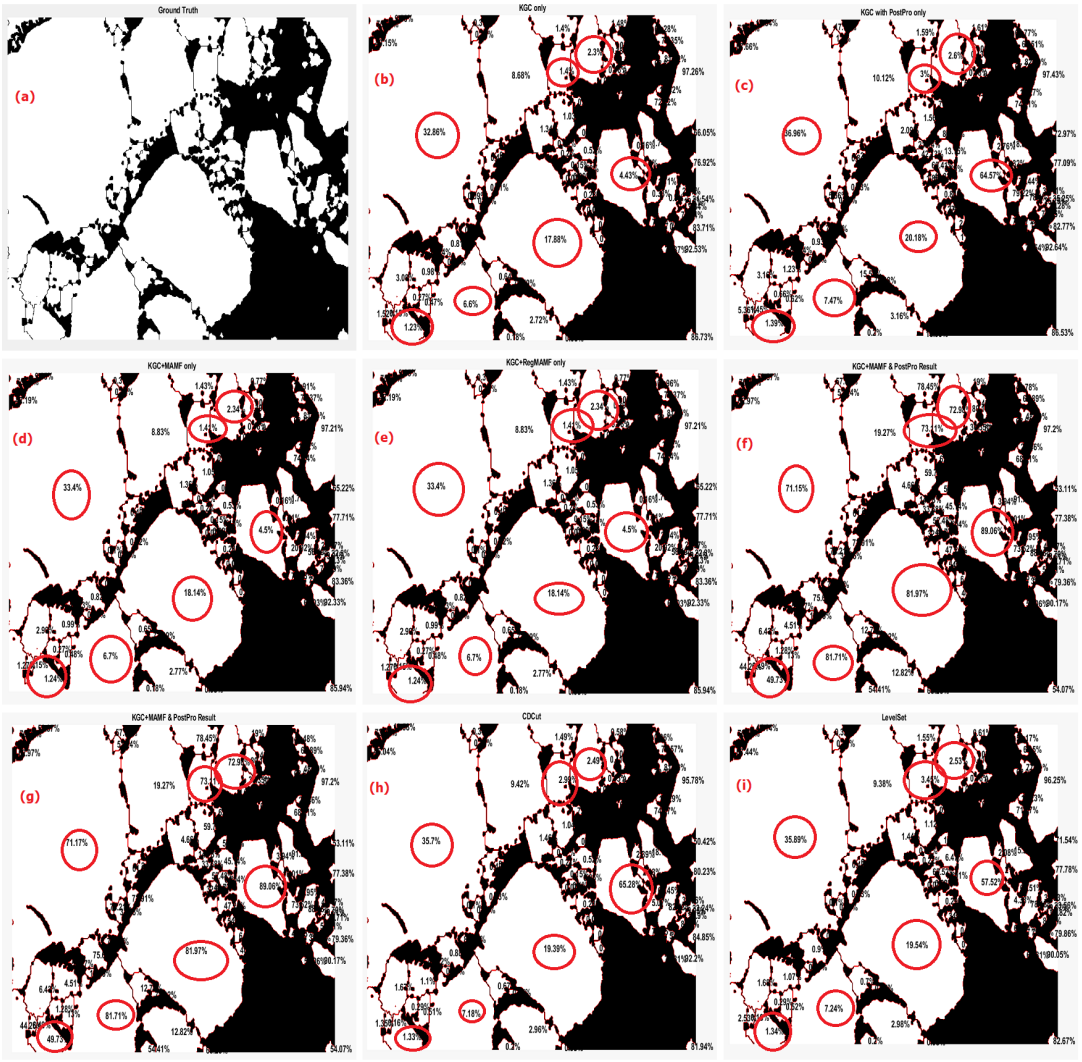

Figure 5.43: Visual Analysis values for bottom part of TSX image captured on 31st July 2014

KGC on its own (b), KGC with Post Processing only (c), KGC with MAMF and no Post Processing (d), KGC with region based MAMF and no Post Processing(e), KGC with MAMF and Post Processing (f), KGC with region based MAMF and Post Processing (g), Level Set(h) and CDCut (i). Similar to the findings for the images in dataset 2, numerous amount of Sea Ice regions with increased ORA can be witnessed within the images for the dataset 3. There are fewer noticeable regions in the first image unlike the second image, owing to the reduced number of Sea Ice regions.

5.4 Summary

A condition and region based Post Processing algorithm is proposed to improve the Segmentation Accuracy of the KGC algorithm proposed in [49]. The KGC algorithm on its own produces good results for the SAR Sea Ice images used in this research. However to further separate the touching Sea Ice floes, the Post Processing algorithm is proposed. The proposed adaptive filters, mentioned in chapter 4, are used along with the proposed Post Processing algorithm to the KGC.

In terms of the Quantitative Analysis done for the three dataset images, the proposed algorithm produces the best results when compared to popular and recent algorithms such as the DRLSE [43] and the CDCut [48]. In some cases, it even surpasses the Watershed algorithm [42] which has been used to generate the GT images for validating the efficacy of the various algorithms.

A region based analytical technique ORA was proposed which correctly calculates the true accuracy of all the Sea Ice regions within the image, by matching the intersection and union of the Segmented Image region with those of the GT Image. Boundary based analysis were also done, using only the edges derived from the Segmentation, to calculate the Under, Over and Correct Segmentation of the various Sea Ice regions.

The proposed Condition and Region based Post Processing algorithm incorporated a mixture of various easy to use algorithms such as the Distance Transform [126–128], Skeletonisation [125], Morphology [124] and Active Contours [44] in finding the various "Regions of Interest" and separating the touching Sea Ice floes using local statistics of the Image. From the results presented in the previous sections, it can be seen how the proposed addition to the KGC produces significant improvement and also getting the best results. It, however, compromises moderately in some cases for the computing efficiency but with further future work in this research and with modified settings for the Post Processing algorithm, this can be further minimised.

CHAPTER 6

CONCLUSIONS AND FUTURE WORK

6.1 Conclusions

The general objective of this thesis is to develop an adaptive and region based algorithms for effective segmentation of SAR Sea Ice images. These include various algorithms for Speckle Filtering, Image Segmentation and Sea Ice floe separation as presented in chapters 4 and 5 respectively. The main contributions of the thesis are summarised as follows.

1. In Chapter 4, an improved Adaptive Filtering algorithm is proposed for dealing with the speckle which is created in SAR images due to the backscattering of signals and coherent processing. The algorithm utilises the advantages of the two popular existing techniques; Adaptive Median filter and Wiener filter. Local statistics of the image such as mean and standard deviation are used for extracting the regions within the image which are identified as speckle. Speckle filtering is then only applied to those regions and not the whole image, thus avoiding the blurring of valid pixels as seen with most filters such as the Wiener filter. The AMF uses these local statistics to modify the speckle pixel as well, but the modified value is based on the median value of the identified valid pixels. However, the proposed MAMF filter utilises the advantages of the AMF and the Wiener filter to effectively combine and remove the speckle contained within the image. From experiments, it has been seen how the Wiener filter with the MMSE estimation produces the best Speckle Suppression and contrary to

that, the AMF produces the best Edge and Feature retention properties. Thus by combining these two advantages, the proposed MAMF is set to produce the best result, which is validated by the results in chapter 4. A further region based second stage filtering is also proposed, which effectively checks and compares the regions within the image with the user-specified FQA values. If the values are lower than the threshold, only a second stage of filtering is performed to those particular regions. The computation complexity of this stage is minimal, as seen by the results produced, as the first stage of the MAMF is itself able to deal with almost all of the speckle produced within the SAR image. The computational complexity of the proposed filter to that of the original AMF is also minimal, but with improved accuracy of the filtered image, which is beneficial for the SAR Sea Ice segmentation in Chapter 5.

2. In Chapter 5, an improvement to the KGC algorithm is proposed for producing further improved SAR Sea Ice segmentation results. The KGC on its own is a good algorithm to get SAR Sea Ice segmentation results, as it makes use of the local image statistics to find a partition, utilising K-means, Kernel mapping and Graph Cuts for achieving this. However, since the SAR images are always corrupted by speckle, the adaptive speckle filtering, proposed in Chapter 4, is used for improving the image itself. To separate the touching Sea Ice floes, which is a difficult for even the most robust algorithms, a region yet condition based Post Processing algorithm is used. It incorporates the use of easy to implement algorithms such as Distance Transform, Skeletonisation, Morphology and Active Contours. The Distance transform and Skeletonisation is used for finding the various "Regions of Interest", which are the various touching Sea Ice floes identified within the image, that need to be further separated. Thus by modifying the image first using Morphology, Active Contours is then used to regrow the modified pixels back to its original border, but this time with a separated edge separating the two regions. Based on the complexity of the image, in terms of

the number of Sea Ice floes needed to be separated and identified by the Region of Interest algorithm, the computing efficiency of this proposed algorithm is calculated. For more complex images, as seen in dataset 2 as opposed to dataset 1, the cost of the computing efficiency of the proposed addition is higher. But from the results produced, it also justifies the use of the algorithm, as high number of regions with increased accuracy are produced. The results produced have been higher than the CDCut, DRLSE and the KGC algorithm on its own, thus proving a case for the proposed algorithm. The results for some cases have even been higher than the highly over-segmented result produced using Watershed, which has been used for creating the GT image for validating the performance of the various algorithms. Furthermore, an accurate Region based Quantitative Analysis ORA is proposed. The ORA correctly calculates the true Segmentation Accuracy of the various Sea Ice floe regions by means of Intersection and Union of regions between the Segmented and the GT image. Boundary based analysis is also done for finding the Under, Over and Correct Segmentation, based only on the Segmentation edges produced for the various Sea Ice floe regions. From the results shown in Chapter 5, it can be seen how the proposed Post Processing addition produces the best ORA and the least Under Segmentation results.

6.2 Future Work

Followed by the conclusions of the various novel techniques proposed for SAR Sea Ice Segmentation in this thesis, the following directions for future work are discussed.

1. The Speckle filtering has been an active research problem for more than 25 years and over the years many researchers have proposed various ideas for tackling the speckle. Many of the recent literature suggests use of local statistics, as used in this thesis. However, it has been still an active problem in effectively identifying the various pixels/regions within an image which need to be filtered

out or suppressed. Future work can thus focus various algorithms for extraction of these regions, along with other emerging techniques such as Image Fusion, which incorporates the fusion of lower and higher resolution data to effectively get a high resolution SAR image, which has considerably lower effects from speckle.

2. The SAR Sea Ice Segmentation has also been active research problem for several decades, especially the Arctic region, owing to the fact that the region has increasingly produced lower levels of Sea ice floes with passing years. It is however still been increasingly difficult to extract the Sea Ice regions accurately for creating the Floe Size Distribution analysis used by scientists for comparing the data from past several years of study. It has also been increasingly difficult to get an accurate GT image without the need of human intervention and thus the data produced is biased in most cases. Thus future work can involve in researching algorithms which are able to help researchers and scientists get an accurate and automated GT image. Furthermore, it can be investigated to effectively process the SAR data which is very challenging, even for the most robust and fast operating systems. Downsizing the image for processing has been shown to produce not as accurate results as with processing the original image. This is evident as the pixels values are also modified considerably and this is particularly challenging in cases like this research, which require separation of Sea Ice floes, which depends on pixel values of the neighbouring pixels.

REFERENCES

[1] R. Korsnes, "Quantitative analysis of sea ice remote sensing imagery," *International Journal of Remote Sensing*, vol. 14, no. 2, pp. 295–311, 1993.

[2] D. Haverkamp, L. K. Soh, and C. Tsatsoulis, "A comprehensive, automated approach to determining sea ice thickness from sar data," *Geoscience and Remote Sensing, IEEE Transactions on*, vol. 33, no. 1, pp. 46–57, 1995.

[3] M. Fily and D. A. Rothrock, "Extracting sea ice data from satellite sar imagery," *Geoscience and Remote Sensing, IEEE Transactions on*, no. 6, pp. 849–854, 1986.

[4] H. Deng and D. A. Clausi, "Unsupervised segmentation of synthetic aperture radar sea ice imagery using a novel markov random field model," *Geoscience and Remote Sensing, IEEE Transactions on*, vol. 43, no. 3, pp. 528–538, 2005.

[5] A. Wong, D. A. Clausi, and P. Fieguth, "Sec: Stochastic ensemble consensus approach to unsupervised sar sea-ice segmentation." IEEE, 2009, Conference Proceedings, pp. 299–305.

[6] R. Kwok, G. Cunningham, M. Wensnahan, I. Rigor, H. Zwally, and D. Yi, "Thinning and volume loss of the arctic ocean sea ice cover: 2003–2008," *Journal of Geophysical Research: Oceans*, vol. 114, no. C7, 2009.

[7] J. Stroeve, M. Serreze, S. Drobot, S. Gearheard, M. Holland, J. Maslanik, W. Meier, and T. Scambos, "Arctic sea ice extent plummets in 2007," *Eos*, vol. 89, no. 2, p. 13, 2008.

[8] J. Maslanik, C. Fowler, J. Stroeve, S. Drobot, J. Zwally, D. Yi, and W. Emery, "A younger, thinner arctic ice cover: Increased potential for rapid, extensive sea-ice loss," *Geophysical Research Letters*, vol. 34, no. 24, 2007.

[9] G. Holloway and T. Sou, "Has arctic sea ice rapidly thinned?" *Journal of Climate*, vol. 15, no. 13, pp. 1691–1701, 2002.

[10] M. C. Serreze, M. M. Holland, and J. Stroeve, "Perspectives on the arctic's shrinking sea-ice cover," *science*, vol. 315, no. 5818, pp. 1533–1536, 2007.

[11] L. Xu, J. Li, A. Wong, and C. Wang, "A kpca texture feature model for efficient segmentation of radarsat-2 sar sea ice imagery," *International Journal of Remote Sensing*, vol. 35, no. 13, pp. 5053–5072, 2014.

[12] J.-S. Lee, "Speckle analysis and smoothing of synthetic aperture radar images," *Computer Graphics and Image Processing*, vol. 17, no. 1, pp. 24–32, 1981.

[13] T. D. Williams, L. G. Bennetts, V. A. Squire, D. Dumont, and L. Bertino, "Wave–ice interactions in the marginal ice zone. part 2: Numerical implementation and sensitivity studies along 1d transects of the ocean surface," *Ocean Modelling*, vol. 71, pp. 92–101, 2013.

[14] J. Zhang, A. Schweiger, M. Steele, and H. Stern, "Sea ice floe size distribution in the marginal ice zone: Theory and numerical experiments," *Journal of Geophysical Research: Oceans*, vol. 120, no. 5, pp. 3484–3498, 2015.

[15] D. Rothrock and A. Thorndike, "Measuring the sea ice floe size distribution," *Journal of Geophysical Research: Oceans*, vol. 89, no. C4, pp. 6477–6486, 1984.

[16] J. Zhang, H. Stern, B. Hwang, A. Schweiger, M. Steele, M. Stark, and H. C. Graber, "Modeling the seasonal evolution of the arctic sea ice floe size distribution," *Elem Sci Anth*, vol. 4, 2016.

[17] T. Toyota, C. Haas, and T. Tamura, "Size distribution and shape properties of relatively small sea-ice floes in the antarctic marginal ice zone in late winter," *Deep Sea Research Part II: Topical Studies in Oceanography*, vol. 58, no. 9-10, pp. 1182–1193, 2011.

[18] B. Hwang, J. Ren, S. McCormack, C. Berry, I. B. Ayed, H. C. Graber, and E. Aptoula, "A practical algorithm for the retrieval of floe size distribution of arctic sea ice from high-resolution satellite synthetic aperture radar imagery," *Elem Sci Anth*, vol. 5, 2017.

[19] D. Dumont, A. Kohout, and L. Bertino, "A wave-based model for the marginal ice zone including a floe breaking parameterization," *Journal of Geophysical Research: Oceans*, vol. 116, no. C4, 2011.

[20] T. D. Williams, P. Rampal, and S. Bouillon, "Wave–ice interactions in the nextsim sea-ice model," *The Cryosphere*, vol. 11, no. 5, p. 2117, 2017.

[21] E. Hervet, R. Fjortoft, P. Marthon, and A. Lopes, "Comparison of wavelet-based and statistical speckle filters," in *Remote Sensing*. International Society for Optics and Photonics, 1998, pp. 43–54.

[22] J.-S. Lee, "Digital image enhancement and noise filtering by use of local statistics," *IEEE transactions on pattern analysis and machine intelligence*, no. 2, pp. 165–168, 1980.

[23] J.-S. Lee, "Digital image smoothing and the sigma filter," *Computer Vision, Graphics, and Image Processing*, vol. 24, no. 2, pp. 255–269, 1983.

[24] J.-S. Lee, "A simple speckle smoothing algorithm for synthetic aperture radar images," *IEEE Transactions on Systems, Man, and Cybernetics*, no. 1, pp. 85–89, 1983.

[25] J.-S. Lee, "Speckle suppression and analysis for synthetic aperture radar images," *Optical engineering*, vol. 25, no. 5, pp. 255 636–255 636, 1986.

[26] J.-S. Lee, J.-H. Wen, T. L. Ainsworth, K.-S. Chen, and A. J. Chen, "Improved sigma filter for speckle filtering of sar imagery," *IEEE Transactions on Geoscience and Remote Sensing*, vol. 47, no. 1, pp. 202–213, 2009.

[27] J.-S. Lee, T. L. Ainsworth, Y. Wang, and K.-S. Chen, "Polarimetric sar speckle filtering and the extended sigma filter," *IEEE Transactions on Geoscience and Remote Sensing*, vol. 53, no. 3, pp. 1150–1160, 2015.

[28] A. Lopes, R. Touzi, and E. Nezry, "Adaptive speckle filters and scene heterogeneity," *IEEE Transactions on geoscience and remote sensing*, vol. 28, no. 6, pp. 992–1000, 1990.

[29] V. Frost, J. Stiles, K. S. Shanmugam, J. Holtzman, and S. Smith, "An adaptive filter for smoothing noisy radar images," *Proceedings of the IEEE*, vol. 69, no. 1, pp. 133–135, 1981.

[30] V. S. Frost, J. A. Stiles, K. S. Shanmugan, and J. C. Holtzman, "A model for radar images and its application to adaptive digital filtering of multiplicative noise," *IEEE Transactions on Pattern Analysis and Machine Intelligence*, no. 2, pp. 157–166, 1982.

[31] D. T. Kuan, A. A. Sawchuk, T. C. Strand, and P. Chavel, "Adaptive noise smoothing filter for images with signal-dependent noise," *IEEE Transactions on Pattern Analysis and Machine Intelligence*, no. 2, pp. 165–177, 1985.

[32] D. Kuan, A. Sawchuk, T. Strand, and P. Chavel, "Adaptive restoration of images with speckle," *IEEE Transactions on Acoustics, Speech, and Signal Processing*, vol. 35, no. 3, pp. 373–383, 1987.

[33] E. M. Eliason and A. S. McEwen, "Adaptive box filters for removal of random noise from digital images," *Photogrammetric Engineering and Remote Sensing*, vol. 56, no. 4, pp. 453–458, 1990.

[34] F. Qiu, J. Berglund, J. R. Jensen, P. Thakkar, and D. Ren, "Speckle noise reduction in sar imagery using a local adaptive median filter," *GeoScience & Remote Sensing*, vol. 41, no. 3, pp. 244–266, 2004.

[35] C. Tomasi and R. Manduchi, "Bilateral filtering for gray and color images," in *Sixth International Conference on Computer Vision*. Mumbai, India: IEEE, 1998, pp. 839–846.

[36] A. E. Bryson, *Applied optimal control: optimization, estimation and control*. CRC Press, 1975.

[37] N. Wiener, *Extrapolation, interpolation, and smoothing of stationary time series*. MIT press Cambridge, MA, 1949, vol. 7.

[38] J. S. Lim, *Two-dimensional Signal and Image Processing*. Englewood Cliffs, NJ: Prentice Hall, 1990.

[39] B. Burns, D. Cavalieri, M. Keller, W. Campbell, T. Grenfell, G. Maykut, and P. Gloersen, "Multisensor comparison of ice concentration estimates in the marginal ice zone," *Journal of Geophysical Research: Oceans*, vol. 92, no. C7, pp. 6843–6856, 1987.

[40] L.-K. Soh and C. Tsatsoulis, "Automated sea ice segmentation (asis)," in *Geoscience and Remote Sensing Symposium Proceedings, 1998. IGARSS'98. 1998 IEEE International*, vol. 2. IEEE, 1998, pp. 586–588.

[41] L.-K. Soh, C. Tsatsoulis, D. Gineris, and C. Bertoia, "Arktos: An intelligent system for sar sea ice image classification," *IEEE Transactions on geoscience and remote sensing*, vol. 42, no. 1, pp. 229–248, 2004.

[42] F. Meyer, "Topographic distance and watershed lines," *Signal processing*, vol. 38, no. 1, pp. 113–125, 1994.

[43] C. Li, C. Xu, C. Gui, and M. D. Fox, "Distance regularized level set evolution and its application to image segmentation," *IEEE transactions on image processing*, vol. 19, no. 12, pp. 3243–3254, 2010.

[44] T. F. Chan and L. A. Vese, "Active contours without edges," *Ieee Transactions on Image Processing*, vol. 10, no. 2, pp. 266–277, 2001. [Online]. Available: <GotoISI>://WOS:000167016400007

[45] L. A. Vese and T. F. Chan, "A multiphase level set framework for image segmentation using the mumford and shah model," *International journal of computer vision*, vol. 50, no. 3, pp. 271–293, 2002.

[46] J. A. Sethian *et al.*, "Level set methods and fast marching methods," *Journal of Computing and Information Technology*, vol. 11, no. 1, pp. 1–2, 2003.

[47] S. O. R. Fedkiw and S. Osher, "Level set methods and dynamic implicit surfaces," *Surfaces*, vol. 44, p. 77, 2002.

[48] W. Zhao, Z. Tian, L. Yang, and W. Yan, "Sar image segmentation based on closeness degree cut and minimum description length criterion," *Journal of the Indian Society of Remote Sensing*, pp. 1–11, 2014.

[49] M. B. Salah, A. Mitiche, and I. B. Ayed, "Multiregion image segmentation by parametric kernel graph cuts," *Image Processing, IEEE Transactions on*, vol. 20, no. 2, pp. 545–557, 2011.

[50] Y. Boykov, O. Veksler, and R. Zabih, "Fast approximate energy minimization via graph cuts," *Pattern Analysis and Machine Intelligence, IEEE Transactions on*, vol. 23, no. 11, pp. 1222–1239, 2001.

[51] S. Lloyd, "Least squares quantization in pcm," *IEEE Transactions on Information Theory*, vol. 28, no. 2, pp. 129–137, 1982.

[52] P. Berkhin, "A survey of clustering data mining techniques," Accrue Software, Report, 2002.

[53] D. Arthur and S. Vassilvitskii, "k-means++: The advantages of careful seeding," in *Proceedings of the eighteenth annual ACM-SIAM symposium on Discrete algorithms*. Society for Industrial and Applied Mathematics, 2007, pp. 1027–1035.

[54] K. Muller, S. Mika, G. Ratsch, K. Tsuda, and B. Scholkopf, "An introduction to kernel-based learning algorithms," *IEEE Transactions on Neural Networks*, vol. 12, no. 2, pp. 181–201, 2001.

[55] M. Girolami, "Mercer kernel-based clustering in feature space," *IEEE Transactions on Neural Networks*, vol. 13, no. 3, pp. 780–784, 2002.

[56] I. S. Dhillon, Y. Guan, and B. Kulis, "Weighted graph cuts without eigenvectors a multilevel approach," *Pattern Analysis and Machine Intelligence, IEEE Transactions on*, vol. 29, no. 11, pp. 1944–1957, 2007.

[57] M. D. Buhmann, *Radial basis functions: theory and implementations*. Cambridge: Cambridge university press, 2003.

[58] D. Z. S. Chen, "Fuzzy clustering using kernel method," *IEEE, Nanjing, China*, 2002.

[59] R. B. Potts, "Some generalized order-disorder transformations," in *Mathematical proceedings of the cambridge philosophical society*, vol. 48, no. 1. Cambridge University Press, 1952, pp. 106–109.

[60] C. H. Ding, X. He, H. Zha, M. Gu, and H. D. Simon, "A min-max cut algorithm for graph partitioning and data clustering," in *Data Mining, 2001. ICDM 2001, Proceedings IEEE International Conference on*. IEEE, 2001, Conference Proceedings, pp. 107–114.

[61] C. H. Ding, X. He, and H. D. Simon, "On the equivalence of nonnegative matrix factorization and spectral clustering," in *SDM*, vol. 5. SIAM, 2005, Conference Proceedings, pp. 606–610.

[62] S. Birchfield and C. Tomasi, "Depth discontinuities by pixel-to-pixel stereo," *International Journal of Computer Vision*, vol. 35, no. 3, pp. 269–293, 1999.

[63] J. Besag, "On the statistical analysis of dirty pictures," *Journal of the Royal Statistical Society. Series B (Methodological)*, pp. 259–302, 1986.

[64] S. Geman and D. Geman, "Stochastic relaxation, gibbs distributions, and the bayesian restoration of images," *IEEE Transactions on pattern analysis and machine intelligence*, no. 6, pp. 721–741, 1984.

[65] Y. Sheng and Z.-G. Xia, "A comprehensive evaluation of filters for radar speckle suppression," in *Geoscience and Remote Sensing Symposium, 1996. IGARSS'96.'Remote Sensing for a Sustainable Future.', International*, vol. 3. IEEE, 1996, pp. 1559–1561.

[66] J.-S. Lee, L. Jurkevich, P. Dewaele, P. Wambacq, and A. Oosterlinck, "Speckle filtering of synthetic aperture radar images: A review," *Remote Sensing Reviews*, vol. 8, no. 4, pp. 313–340, 1994.

[67] Z. Wang, A. C. Bovik, H. R. Sheikh, and E. P. Simoncelli, "Image quality assessment: from error visibility to structural similarity," *IEEE transactions on image processing*, vol. 13, no. 4, pp. 600–612, 2004.

[68] D. M. Powers, "Evaluation: from precision, recall and f-measure to roc, informedness, markedness and correlation," 2011.

[69] J. A. Richards and J. Richards, *Remote sensing digital image analysis*. Springer, 1999, vol. 3.

[70] "Nasa earth observatory: Remote sensing introduction and history," https://earthobservatory.nasa.gov/Features/RemoteSensing/, accessed: 2017-06-01.

[71] T. L. Roush, "Mars: Remote sensingmars: Remote sensing," in *Encyclopedia of Planetary Science*. Springer, 1997, pp. 459–461.

[72] M. Montopoli, P. Tognolatti, F. S. Marzano, M. Pierdicca, and G. Perrotta, "Remote sensing of the moon sub-surface from a spaceborne microwawe radiometer aboard the european student moon orbiter (esmo)," in *Geoscience and Remote Sensing Symposium, 2007. IGARSS 2007. IEEE International*. IEEE, 2007, pp. 4451–4454.

[73] "Satellite missions: Landsat-1 to landsat-3," https://directory.eoportal.org/web/eoportal/satellite-missions/l/landsat-1-3, accessed: 2017-06-01.

[74] "Satellite missions: Sentinel-1," https://directory.eoportal.org/web/eoportal/satellite-missions/c-missions/copernicus-sentinel-1, accessed: 2017-06-01.

[75] "Satellite missions: Terrasar-x," https://directory.eoportal.org/web/eoportal/satellite-missions/t/terrasar-x, accessed: 2017-06-01.

[76] M. I. Skolnik, "Radar handbook," 1970.

[77] Y. K. Chan and V. C. Koo, "An introduction to synthetic aperture radar (sar)," *Progress In Electromagnetics Research B*, vol. 2, pp. 27–60, 2008.

[78] F. Yamazaki, "Applications of remote sensing and gis for damage assessment," *Structural Safety and Reliability*, pp. 1–12, 2001.

[79] "Wikipedia upload (commons)," https://upload.wikimedia.org/wikipedia/commons/6/61/Remote_Sensing_Illustration.jpg, accessed: 2017-06-01.

[80] "Electro-magnetic sensors - nasa," https://science.nasa.gov/ems/01_intro, accessed: 2017-06-01.

[81] "Satellite missions: Ikonos," https://earth.esa.int/web/guest/missions/3rd-party-missions/current-missions/ikonos-2, accessed: 2017-09-03.

[82] "Satellite missions: Spot," https://earth.esa.int/web/guest/missions/3rd-party-missions/current-missions/spot, accessed: 2017-09-03.

[83] "Satellite missions: Alos," https://earth.esa.int/web/guest/missions/3rd-party-missions/historical-missions/alos, accessed: 2017-09-03.

[84] "Satellite missions: Quickbird," https://directory.eoportal.org/web/eoportal/satellite-missions/q/quickbird-2, accessed: 2017-09-03.

[85] "Environment and climate change canada," https://www.ec.gc.ca/glaces-ice/default.asp?lang=En&n=D5F7EA14-1&offset=1&toc=show, accessed: 2017-07-23.

[86] "Environment and climate change canada," https://www.ec.gc.ca/glaces-ice/default.asp?lang=En&n=F2358C10-1, accessed: 2017-07-23.

[87] D. Isleifson, B. Hwang, D. G. Barber, R. K. Scharien, and L. Shafai, "C-band polarimetric backscattering signatures of newly formed sea ice during fall freeze-up," *IEEE Transactions on Geoscience and Remote Sensing*, vol. 48, no. 8, pp. 3256–3267, 2010.

[88] B. Oliver, "Sparkling spots and random diffraction," *Proceedings of the IEEE*, vol. 51, no. 1, pp. 220–221, 1963.

[89] J. W. Goodman, "Some fundamental properties of speckle," *JOSA*, vol. 66, no. 11, pp. 1145–1150, 1976.

[90] E. N. Leith, "Quasi-holographic techniques in the microwave region," *Proceedings of the IEEE*, vol. 59, no. 9, pp. 1305–1318, 1971.

[91] B. Oliver, "Sparkling spots and random diffraction," *Proceedings of the IEEE*, vol. 51, no. 1, pp. 220–221, 1963.

[92] J. Rigden and E. Gordon, "The granularity of scattered optical maser light," *SPIE MILESTONE SERIES MS*, vol. 133, pp. 213–213, 1997.

[93] L. Gagnon and A. Jouan, "Speckle filtering of sar images: a comparative study between complex-wavelet-based and standard filters," in *Optical Science, Engineering and Instrumentation'97*. International Society for Optics and Photonics, 1997, pp. 80–91.

[94] A. Achim, P. Tsakalides, and A. Bezerianos, "Sar image denoising via bayesian wavelet shrinkage based on heavy-tailed modeling," *IEEE Transactions on Geoscience and Remote Sensing*, vol. 41, no. 8, pp. 1773–1784, 2003.

[95] S. Parrilli, M. Poderico, C. V. Angelino, and L. Verdoliva, "A nonlocal sar image denoising algorithm based on llmmse wavelet shrinkage," *IEEE Transactions on Geoscience and Remote Sensing*, vol. 50, no. 2, pp. 606–616, 2012.

[96] L. Xu, J. Li, Y. Shu, and J. Peng, "Sar image denoising via clustering-based principal component analysis," *IEEE transactions on geoscience and remote sensing*, vol. 52, no. 11, pp. 6858–6869, 2014.

[97] K. Dabov, A. Foi, V. Katkovnik, and K. Egiazarian, "Image denoising by sparse 3-d transform-domain collaborative filtering," *IEEE Transactions on image processing*, vol. 16, no. 8, pp. 2080–2095, 2007.

[98] D. D. Muresan and T. W. Parks, "Adaptive principal components and image denoising," in *Image Processing, 2003. ICIP 2003. Proceedings. 2003 International Conference on*, vol. 1. IEEE, 2003, pp. I–101.

[99] L. Zhang, W. Dong, D. Zhang, and G. Shi, "Two-stage image denoising by principal component analysis with local pixel grouping," *Pattern Recognition*, vol. 43, no. 4, pp. 1531–1549, 2010.

[100] D. A. Clausi and B. Yue, "Comparing cooccurrence probabilities and markov random fields for texture analysis of sar sea ice imagery," *Geoscience and Remote Sensing, IEEE Transactions on*, vol. 42, no. 1, pp. 215–228, 2004.

[101] J. A. Karvonen, "Baltic sea ice sar segmentation and classification using modified pulse-coupled neural networks," *IEEE Transactions on Geoscience and Remote Sensing*, vol. 42, no. 7, pp. 1566–1574, 2004.

[102] B. Dezso, R. Giachetta, I. László, and I. Fekete, "Experimental study on graph-based image segmentation methods in the classification of satellite images," *EARSeL eProceedings*, vol. 11, no. 1, pp. 12–24, 2012.

[103] C. T. Zahn, "Graph-theoretical methods for detecting and describing gestalt clusters," *IEEE Transactions on computers*, vol. 100, no. 1, pp. 68–86, 1971.

[104] R. Urquhart, "Graph theoretical clustering based on limited neighbourhood sets," *Pattern recognition*, vol. 15, no. 3, pp. 173–187, 1982.

[105] C. Rother, V. Kolmogorov, and A. Blake, "Grabcut: Interactive foreground extraction using iterated graph cuts," *ACM Transactions on Graphics (TOG)*, vol. 23, no. 3, pp. 309–314, 2004.

[106] Y. Boykov and G. Funka-Lea, "Graph cuts and efficient nd image segmentation," *International journal of computer vision*, vol. 70, no. 2, pp. 109–131, 2006.

[107] S. C. Zhu and A. Yuille, "Region competition: Unifying snakes, region growing, and bayes/mdl for multiband image segmentation," *IEEE Transactions on Pattern Analysis and Machine Intelligence*, vol. 18, no. 9, pp. 884–900, 1996.

[108] V. Caselles, R. Kimmel, and G. Sapiro, "Geodesic active contours," *International journal of computer vision*, vol. 22, no. 1, pp. 61–79, 1997.

[109] B. Schölkopf, A. Smola, and K.-R. Müller, "Nonlinear component analysis as a kernel eigenvalue problem," *Neural computation*, vol. 10, no. 5, pp. 1299–1319, 1998.

[110] B. Scholkopf, S. Mika, C. J. Burges, P. Knirsch, K.-R. Muller, G. Ratsch, and A. J. Smola, "Input space versus feature space in kernel-based methods," *IEEE transactions on neural networks*, vol. 10, no. 5, pp. 1000–1017, 1999.

[111] M. Filippone, F. Camastra, F. Masulli, and S. Rovetta, "A survey of kernel and spectral methods for clustering," *Pattern recognition*, vol. 41, no. 1, pp. 176–190, 2008.

[112] B. Miles, I. B. Ayed, M. W. Law, G. Garvin, A. Fenster, and S. Li, "Spine image fusion via graph cuts," *IEEE Transactions on Biomedical Engineering*, vol. 60, no. 7, pp. 1841–1850, 2013.

[113] Q. Luo, W. J. Qin, and J. Gu, "Kernel graph cuts segmentation for mr images with intensity inhomogeneity correction," *Applied Mechanics and Materials*, vol. 333-335, pp. 938–943, 2013.

[114] Q. Luo, W. Qin, T. Wen, J. Gu, N. Gaio, S. Chen, L. Li, and Y. Xie, "Segmentation of abdomen mr images using kernel graph cuts with shape priors," *Biomedical engineering online*, vol. 12, no. 124, 2013.

[115] R. Harini and C. Chandrasekar, "Efficient pattern matching algorithm for classified brain image," *International Journal of Computer Applications (09758887)*, vol. 57, no. 4, pp. 5–10, 2012.

[116] D. Xiang, T. Tang, C. Hu, Y. Li, and Y. Su, "A kernel clustering algorithm with fuzzy factor: Application to sar image segmentation," *Geoscience and Remote Sensing Letters, IEEE*, vol. 11, no. 7, p. 1291, 2014.

[117] S. Balla-Arab, X. Gao, B. Wang, F. Yang, and V. Brost, "Multi-kernel implicit curve evolution for selected texture region segmentation in vhr satellite images," *Geoscience and Remote Sensing, IEEE Transactions on*, vol. 52, no. 8, pp. 5183–5192, 2014.

[118] M. Ma, J. Liang, M. Guo, Y. Fan, and Y. Yin, "Sar image segmentation based on artificial bee colony algorithm," *Applied Soft Computing*, vol. 11, no. 8, pp. 5205–5214, 2011.

[119] Y. Gui, X. Zhang, and Y. Shang, "Sar image segmentation using mser and improved spectral clustering," *EURASIP Journal on Advances in Signal Processing*, vol. 2012, no. 1, p. 83, 2012.

[120] D. Karaboga, "An idea based on honey bee swarm for numerical optimization," Technical report-tr06, Erciyes university, engineering faculty, computer engineering department, Tech. Rep., 2005.

[121] D. Karaboga and B. Basturk, "A powerful and efficient algorithm for numerical function optimization: artificial bee colony (abc) algorithm," *Journal of global optimization*, vol. 39, no. 3, pp. 459–471, 2007.

[122] D. Karaboga and B. Akay, "A survey: algorithms simulating bee swarm intelligence," *Artificial intelligence review*, vol. 31, no. 1-4, p. 61, 2009.

[123] "Alaska space facility's vertex," https://vertex.daac.asf.alaska.edu/, accessed: 2017-03-01.

[124] J. Serra, *Image analysis and mathematical morphology*. Academic press, 1982, vol. 1.

[125] C. J. Hilitch, "Linear skeletons from square cupboards," 1969.

[126] D. W. Paglieroni, "Distance transforms: Properties and machine vision applications," *CVGIP: Graphical models and image processing*, vol. 54, no. 1, pp. 56–74, 1992.

[127] A. Rosenfeld and J. L. Pfaltz, "Sequential operations in digital picture processing," *Journal of the ACM (JACM)*, vol. 13, no. 4, pp. 471–494, 1966.

[128] C. R. Maurer, R. Qi, and V. Raghavan, "A linear time algorithm for computing exact euclidean distance transforms of binary images in arbitrary dimensions," *IEEE Transactions on Pattern Analysis and Machine Intelligence*, vol. 25, no. 2, pp. 265–270, 2003.

[129] G. Matheron, *Random sets and integral geometry*. New York: Wiley, 1975, vol. 1.

[130] E. R. Dougherty and R. A. Lotufo, *Hands-on morphological image processing*. Bellingham: SPIE press, 2003, vol. 71.

[131] W. Gonzalez and R. E. Woods, "Eddins, digital image processing using matlab," *Third New Jersey: Prentice Hall*, 2004.

[132] R. Adams, "Radial decomposition of disks and spheres," *CVGIP: Graphical Models and Image Processing*, vol. 55, no. 5, pp. 325–332, 1993.

[133] R. Jones and P. Soille, "Periodic lines: Definition, cascades, and application to granulometries," *Pattern Recognition Letters*, vol. 17, no. 10, pp. 1057–1063, 1996.

[134] J. Ren, B. Hwang, P. Murray, S. Sakhalkar, and S. McCormack, "Effective sar sea ice image segmentation and touch floe separation using a combined multi-stage approach," in *Geoscience and Remote Sensing Symposium (IGARSS), 2015 IEEE International*. IEEE, 2015, pp. 1040–1043.

[135] A. Schweiger, R. Lindsay, J. Zhang, M. Steele, H. Stern, and R. Kwok, "Uncertainty in modeled arctic sea ice volume," *Journal of Geophysical Research: Oceans*, vol. 116, no. C8, 2011.

[136] C. M. Lee, S. Cole, M. Doble, L. Freitag, P. Hwang, S. Jayne, M. Jeffries, R. Krishfield, T. Maksym, and W. Maslowski, "Marginal ice zone (miz) program: Science and experiment plan," WASHINGTON UNIV SEATTLE APPLIED PHYSICS LAB, Tech. Rep., 2012.

[137] J. Karvonen, "A sea ice concentration estimation algorithm utilizing radiometer and sar data," *The Cryosphere*, vol. 8, no. 5, pp. 1639–1650, 2014.

APPENDIX A

PUBLICATIONS BY AUTHOR

1. Sakhalkar, S., Ren, J., Hwang, P. and Murray, P., 2015. Effective SAR image segmentation and sea-ice floe distribution analysis via kernel graph cuts based feature extraction and fusion. In 4th International Conference on SENSOR NETWORKS (pp. 28-37).

2. Ren, J., Hwang, B., Murray, P., Sakhalkar, S. and McCormack, S., 2015, July. Effective SAR sea ice image segmentation and touch floe separation using a combined multi-stage approach. In Geoscience and Remote Sensing Symposium (IGARSS), 2015 IEEE International (pp. 1040-1043).